University of Sussex

Daniel Warren Lester

Submitted for the degree of PhD

Creation of a semiconductor system for the removal of volatile organic compounds from biogas

August 2013

I hereby declare that the studies described in this thesis are the sole work of the author, and have not been previously submitted, either in the same or any other form, for a degree to this or any other university.

Daniel Warren Lester

Acknowledgements

I am very grateful to the many people who have made this PhD possible. First and foremost I would like to thank my three supervisors; Dr. Qiao Chen, Dr. Gerry Lawless and Dr. John Turner, and industrial sponsors PpTek, for believing in me and giving me the opportunity and guidance to complete my studies. I would further like to thank Professor Norman Billingham for discussions about differential scanning calorimetry and polymers. I am grateful to Dr. Alaa Abdul-Sada and to Chris Dadswell for their great help with gas chromatography-mass spectroscopy and inductively coupled plasma analysis respectively. A special mention goes to Mick and Fran of the teaching lab for their infinite patience with my use of their equipment and labspace. I would like to thank all of my colleagues including, but not limited to, the nano-group. Thank you to Raaz, who has been my partner in crime, both literal and metaphorical, for the last four years, you have made this PhD infinitely more interesting and fun. To Laura, for sharing a lab and all of its fires and water leaks with me (why do they not cancel each other out?). Ben and Steve, for sharing an office, comparing facial hair and conquering the internet. JK, for helpful discussions relating to whisky, gin and data analysis (in that order). Joy, for once upon a time teaching me how to do lab research and survive living on my own. As a segue, to the several lucky souls who have had the pleasure to live with me, putting up with my ranting, hangovers and the occasional fire alarm. To all my friends, John, Joe, Tony, James and the many others who have given me a whole host of stories I can never tell my grand-children (or the authorities). Despite what many will think, my PhD wasn't all hard work so a big thank you to Falmer Bar, East Slope Bar, The London Unity and The Duke of Beaufort for keeping me well lubricated and, much like my housemates, putting up with my rants, hangovers

and the occasional disconap. In return you can thank me for almost single-handedly keeping you in profit. Last but not least, thank you Vicki and my family, without your support, both moral and tangible, I would never have survived this PhD.

Abstract

This thesis is concerned with the preparation, and subsequent investigation of, titanium dioxide (TiO_2) nanomaterials and their ability to remove phenol from gas streams for application towards the abatement of polluted land fill gas (LFG). Using the well documented ability of TiO_2 to excite an electron by UV light, phenol was removed from gas streams to investigate the efficacy of TiO_2 nanomaterials. Phenol was chosen as a representative VOC but the catalysts were proven to also remove four other organic compounds during gas phase photocatalysis. It was found that in loadings of 1 mol % the degradation of phenol could be increased relative to pristine TiO_2 nanofibres. The activity of six metal oxide dopants were fairly compared to one another where it was found that cobalt doped TiO_2 showed very high activity, more so than P25 powder. Furthermore, mono-metallic cobalt nanomaterials were shown to degrade phenol in the gas phase, however, more studies are required on these materials.

Supports for TiO_2 were investigated in order to provide a more practical catalyst for industrial continuous flow reactors. These included novel zeolite:titania composites which were fibrous, non-woven mats of these materials were prepared by electrospinning and were shown to effectively remove phenol from polluted gas stream.

Contents

List of Abbreviations

Å	Angstrom(s) = 10^{-10} m
AcAc	Acetyl acetonate
AES	Auger electron spectroscopy
AFM	Atomic force microscope
ATR	Attenuated total reflection
BIS	Bremsstrahlung *iso*chromat spectroscopy
CB	Conduction band
CBM	Conduction band minimum
CVD	Chemical vapour deposition
DMF	n,n – dimethyl formamide
DRS	Diffuse reflectance spectroscopy
DSC	Differential scanning calorimetry
EDX	Energy dispersive X-ray
EELS	Electron energy loss spectroscopy
EXAFS	Extended X-ray absorption fine structure
FTIR	Fourier transform infra-red
LDOS	Local density of states

M	Undefined metal
MB	Methylene blue
Me	Methyl
nm	Nano-meter(s)
PCVD	Physical chemical vapour deposition
PDOS	Projected density of states
PMMA	Poly(methyl methacrylate)
ps	Pico-second(s)
PVD	Physical vapour deposition
SEM	Scanning electron microscope
STEM	Scanning transmission electron microscope
STM	Scanning tunnelling microscope
TEM	Transmission electron microscope
TEOS	Tetra ethyl *ortho*silicate
TTiB	Titanium tetraisobutoxide
TTIP	Titanium tertaisopropoxide
UPS	Ultra-violet photoelectron spectroscopy
UV-Vis	Ultra-violet visible

VB	Valence band
VBM	Valence band minimum
VOC	Volatile organic compound
XES	X-ray emission spectroscopy
XPS	X-ray photoelectron spectroscopy
XRD	X-ray diffraction

1. Introduction

1.1 General Introduction

In recent years environmental concerns have been a hot topic, with governments worldwide under pressure to reduce chemical emissions, conserve natural resources and protect the land. The need for technology for the reduction of toxic emissions, especially from industrial manufacturers and automobiles, has been particularly prevalent. A component of these chemical emissions are classified as Volatile Organic Compounds (VOC), defined as "any organic compound having an initial boiling point less than or equal to 250 °C measured at a standard pressure of 101.3 kPa."[1] Industries are under pressure to reduce their emissions as controlled by The Volatile Organic Compounds in Paints, Varnishes and Vehicle Refinishing Products Regulations of 2005 and amendments in 2009, 2010 and 2012.[2]

One specific source of VOCs, and a target area for remediation, is landfill waste gas (LFG). LFG is biogas composed of ~55 % CH_4 and 45 % CO_2, with impurities such as H_2S, siloxanes and VOCs.[3] Due to the ability to combust methane for fuel, there is the potential for landfill sites to function as a renewable energy source.[4] However, the quality of the LFG must be improved by removing the impurities before it can be used as an energy source.

At present, only limited technology exists to remove some of these impurities from the waste gas emitted, where improvements can be made in areas such as selectivity and catalyst regeneration. Present systems focus on filtering: for example Siemens advocate the use of granulated activated carbon to trap VOCs in both the liquid and gas phase.[5] Another system, used by PpTek of Sussex, is polystyrene beads which

adsorb incoming VOCs in the gas phase.[6] There is a draw back in that these beads can be blocked by siloxane compounds, deactivating the catalyst. A large drawback for both of these methods is that the filtration medium requires either expensive regeneration by thermal oxidation or inefficient disposal. Biofilters have been used as alternatives to VOC degradation, where the pollutants are trapped by a medium either coated in bio-organisms, or transferred to a compartment containing bio-organisms. These organisms, which can be bacteria or fungi, naturally decompose the VOCs, however, in order to degrade a large breadth of VOCs, multiple species of organisms are required. Furthermore, because of the living nature of these organisms they can suffer from deactivation by certain harmful compounds and changes in pH.[7]

Focusing on the points made above, I aim to develop an energy efficient technology to remove a variety of target VOCs from biogas through a catalytic process. I focus on the demonstration of the application of TiO_2 based nanomaterials as the catalysts for photoexcited oxidation of VOCs. In this work, phenol was chosen as an example of a typical VOC. Long term goals of the project include further improving the reactivity and selectivity of the catalysts, specifically towards siloxanes and the conversion of biogas into fuel, such as butanol. This would render the catalytic reactor self-sufficient and would put energy back into the electrical grid.

This thesis is composed of the following chapters: Chapter one is a literature review of the chemistry and physics of nanomaterials and a review of the most common methods used to analyse them. Sections 1.3-1.7 were written with the help of the literature referenced in the bibliography.

Chapter two focuses on the preparation of TiO_2 nanofibres, including preparation of electrospinning solutions, electrospinning and calcination. The variables

affecting electrospinning have been investigated with respect to their effect on nanofibre diameter and diameter distribution. This has been published in the Journal of Polymer Engineering (2013, 33, 5, 453-461). An analysis of calcination was performed with reference to X-ray diffraction, differential scanning calorimetry, infra-red and ultra-violet spectroscopies and links drawn between crystal phase and photocatalytic activity.

Chapter three introduces photocatalysis in earnest and describes the photocatalytic processes and the efficiencies of TiO_2 nanofibres compared to P25. The role of light was investigated as a function of catalyst efficiency and additionally, the activation of TiO_2 by heat was explored.

Chapter four investigates the differences in activity and possible explanations for these changes with respect to six different d-block metals: chromium, cobalt, copper, iron, nickel and vanadium.

Chapter five explores the application of silica and titania supports of TiO_2, to increase the applicability to industrial applications. Dip-coated and fibrous zeolites were prepared as were dip-coated glass fibres and P25 doped nanofibres. These series of catalysts showed excellent activity and are promising for the future.

Chapter six addresses the success of the project with respect to the goals set out in the general introduction of this thesis.

1.2 The Chronicle of Nanomaterials

It is often thought that Richard Feynman inspired what later became known as nanotechnology after his 1959 lecture entitled "*There's plenty of room at the bottom*", during which he envisioned the manipulation of individual atoms.[8] However, research into the field of nanomaterials with sub-micron dimension was only dramatically enhanced by the development of high resolution microscopy techniques, such as the scanning electron microscope (SEM),[9] transmission electron microscope (TEM),[10] atomic force microscope (AFM)[11,12] and scanning tunnelling microscope (STM), the last of which led to the award of the Nobel Prize in physics to Binnig and Rohrer in 1986.[13]

Modern nanomaterials were bench marked by the discovery of C_{60}, part of a class of carbon compounds named fullerenes, in 1985 by Kroto, Curl and Smalley, who were awarded the Nobel Prize in chemistry in 1996.[14] Fullerenes are closed spheres composed of five and six carbon rings that are sp^2 hybridised. In a similar synthetic process, elongated fullerenes, in the form of nanotubes, were discovered in 1991.[15] The significance of the finding of tubular structures has lead to a wider application of nanomaterials in different areas, which in turn, has stimulated the development of a variety of nanostructured materials. The most common of these nanomaterials are: powders, metal oxide fibres (the focus of this research), metal oxide rods and tubes, numerous silicon morphologies and quantum dots, the most common of which are CdS and CdSe.

The combined effect of these 20th century discoveries was the beginning of what are now known as nanomaterials: these are currently defined as “a natural, incidental or manufactured material containing particles, in an unbound state or as an

aggregate or as an agglomerate, and where, for 50% or more of the particles in the number size distribution, one or more external dimensions is in the size range 1 nm~100 nm."[16]

1.2.1 Applications of Nanomaterials

Nanomaterials of a given composition display very different properties when compared to the bulk material of the same composition. For example, Zsigmondy found that a colloidal gold solution was red, not yellow as is observed in the bulk material.[17] The fundamental reason for the disparity between the bulk and nanomaterials is found in the quantum mechanical description of the material at these length scales (Section 1.4). This can be observed in quantum dots where an increase in energy is observed as size decreases (Section 1.8.4). This disparity between bulk and nanomaterials offers new opportunities in the applications of nanomaterials. For example, in the field of nanoelectronics, carbon nanotubes have been shown to act as single electron transistors at room temperature[18] and radio frequency mixers for use in electromagnetic wave processing.[19] Later, it was found that the use of carbon nanotubes is limited by the reproducibility therefore Ge/Si nanowires were developed for the same application.[20] Nanomaterials are also of importance to medicine where biologically compatible nanofibres have been used to replace damaged cardio tissue.[21] Semiconductor quantum dots (QD) are excellent candidates in biomedical applications since their fluorescence is tuneable by adjusting the size of the QDs.[22] CdSe quantum dots, encapsulated in poly ethylene glycol (PEG), have been used to detect prostate cancer cells in mice.[23] As fluorescence is easily tracked by spectroscopy, it has given rise to an effective technique for diagnosis.[24]

Of great importance are metal oxide semiconductor (MOS) nanomaterials, the focus of this project. They have been used for highly selective, high sensitivity gas sensors.[25.26] The photocatalytic properties of semiconductor nanomaterials have made them excellent photocatalysts for applications in green chemistry, namely environmental remediation and renewable energy. For example water splitting with doped TiO_2, as first discovered by Fujishima and Honda, developed hydrogen fuel production by UV light activation, a potential source of clean, renewable energy, converting solar energy into chemical energy.[27,28] Since then, TiO_2 has been regularly used for the photocatalytic splitting of water with a standard three electrode set-up shown in Figure 1.1. Under illumination of the TiO_2 photoanode, electrons will be excited to the conduction band and transfer to the counter electrode (platinum) which will leave holes in the valence band. The holes will oxidise water to oxygen and the electrons on the platinum counter electrode will reduce water to hydrogen. To facilitate the redox, an electrolyte is added between the cathode and anode, which determines the nature of the redox reactions. If using a base, the OH^- rather than H^+ is involved in the redox reactions.

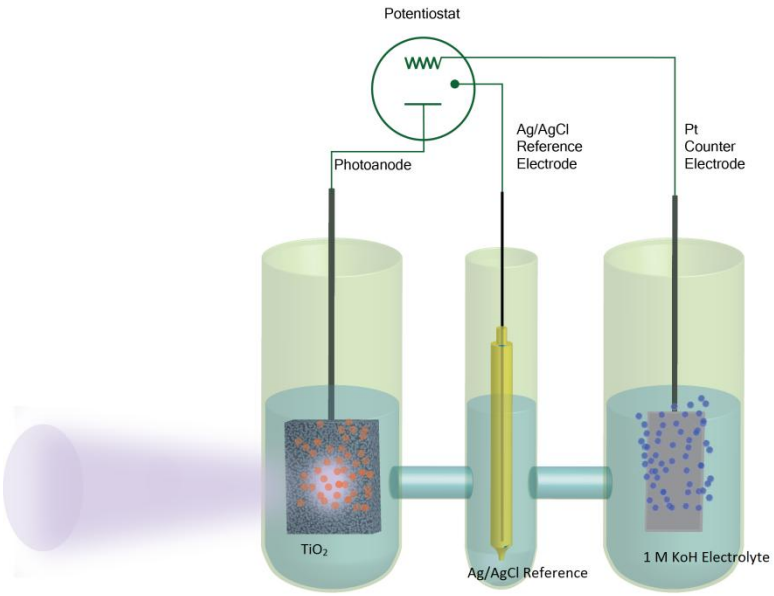

Figure 1.1. Diagram of a typical water splitting set-up. In the left-hand cell the TiO_2 anode produces electrons by photoexcitation. These electrons are carried to the platinum counter electrode (right-hand cell). The electrons in the right-hand cell will reduce water to hydrogen and the holes left behind in the left-hand cell will oxidise water to oxygen. Picture courtesy of Rantej Kler.[29]

$$2H_2O_{(l)} + 2e^- \rightarrow H_{2(g)} + 2OH^-_{(aq)} \qquad (a)$$

$$4OH^-_{(aq)} \rightarrow O_{2(g)} + 2H_2O + 4e^- \qquad (b)$$

$$2H_2O_{(l)} \rightarrow 2H_{2(g)} + O_{2(g)} \qquad (c)$$

Scheme 1.1. Splitting of water using a basic electrolyte where (a) is the reduction of water at the platinum counter electrode, (b) is the oxidation at the anode and (c) is the overall equation of water splitting.

The reverse of water-splitting takes place in an electrochemical fuel cell, which converts the stored chemical energy, from hydrogen, into electricity with mechanical

power. A fuel cell consists of an anode and a cathode with an electrolyte layer between the two (Figure 1.2). A fuel, most commonly H_2, is pumped into the cell and split into an electron and a proton. The proton can travel through the electrolyte but the electron instead is transferred to the cathode through an external circuit, creating a direct current for as long as fuel is being supplied.[30]

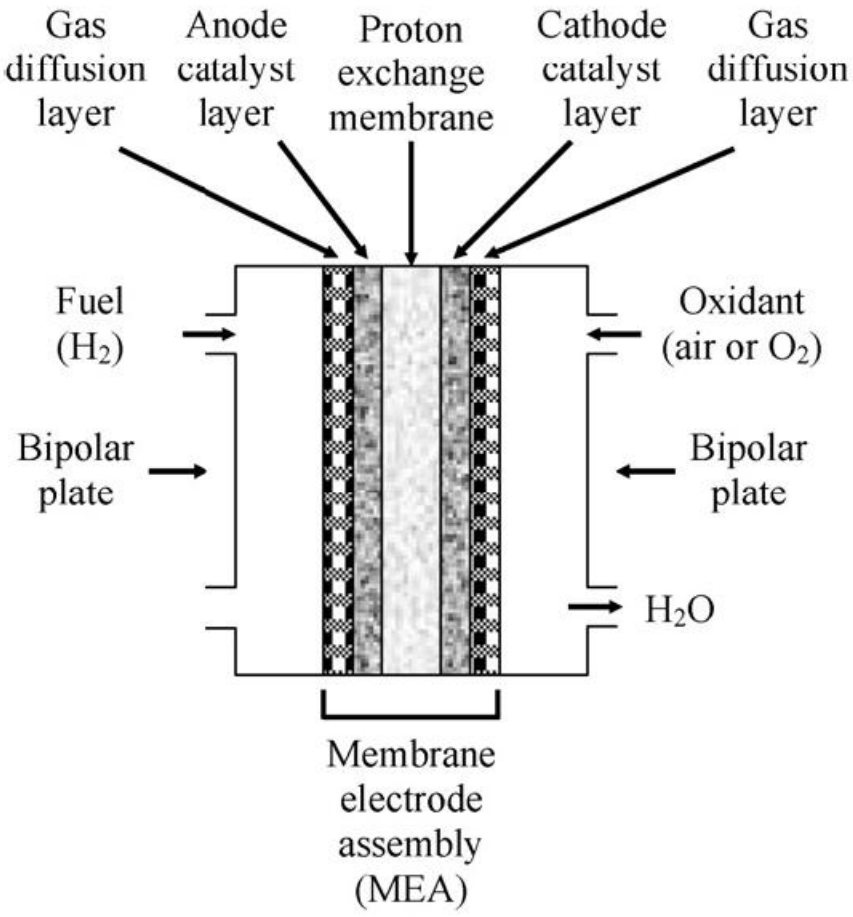

Figure 1.2. Diagram of an electrochemical fuel cell. This fuel cell demonstrates the opposite of water-splitting, where H_2 is supplied as the fuel source to be converted by redox to H_2O.[30]

MOS nanomaterials are also suitable as photocatalysts for the abatement of pollutants in the gas and liquid phases. The former is of particular relevance to this project, which details the removal of VOCs from biogas using UV illuminated titania.

The use of nanomorphologies of TiO_2 to reduce the concentration of pollutants from the gas phase is discussed in detail in Sections 3, 4 and 5. The by-products of these reactions are inorganic acids, water and carbon dioxide. Here, the carbon cycle can in theory be closed if the generated carbon dioxide can be further converted to hydrocarbons and alcohols as a renewable fuel source. This process occurs naturally in photosynthesis, therefore research has been ongoing towards synthetic replication. Although bio-organisms are frequently used to facilitate these transformations,[31] nanomaterials have also shown promise in this field.[32] Both cobalt and copper based nanostructures have been activated with UV light in the presence of CO_2, producing hydrogen, and a complex mixture of alkanes, alkenes and alcohols.[33] Figure 1.3 summarises some of the possible applications of photoactivated titanium dioxide, the metal oxide semiconductor used in this project.[34]

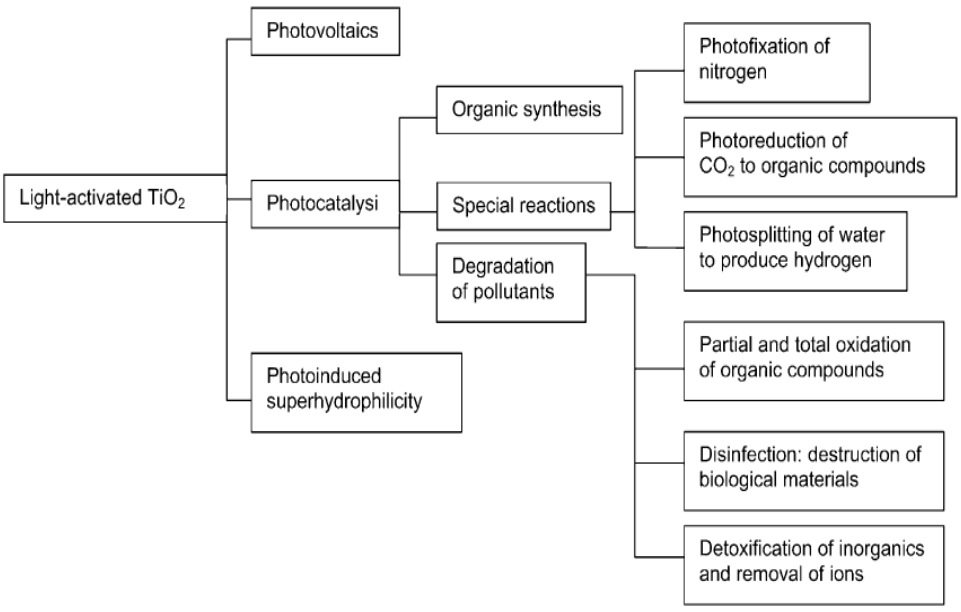

Figure 1.3. Applications of photoactivated TiO_2.[34]

1.3 Structure of Materials

1.3.1 Crystal Structure

A lattice is an infinite, 3D array of points each with identical symmetry and properties. The lattice is the basic structure of a crystal and is a 'scaffold' on to which a structural basis, or motif, can be set. The imposition of this structural motif on a 3D lattice yields the crystal structure of the material. The example of the convolution of motif and lattice is illustrated in Figure 1.4.

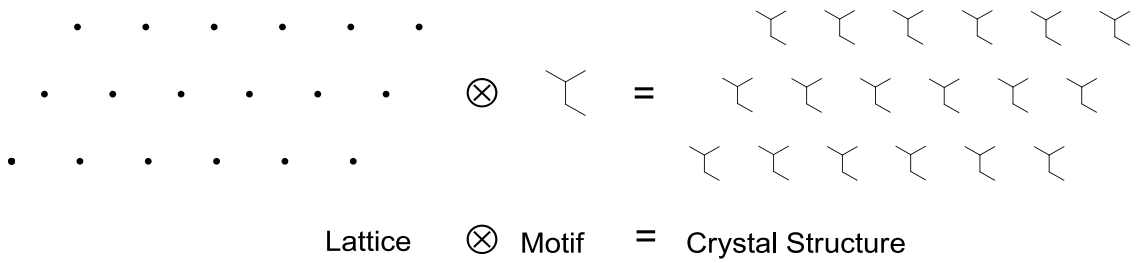

Figure 1.4. Convolution of the lattice (left) and structural motif (middle) to yield the crystal structure.

A unit cell can be formed by drawing lines between adjacent points of the lattice to form a parallelepiped (Figure 1.5). There are many possibilities of parallelepiped that can be drawn that contain the entire motif, but the one that has the shortest sides which are nearest to perpendicular is usually chosen as the representative unit cell.

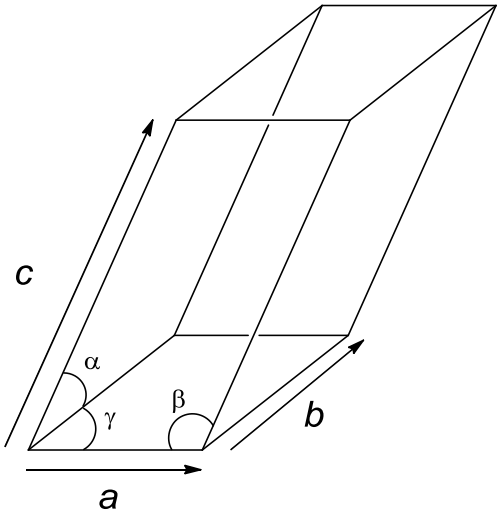

Figure 1.5. Example of a parallelepiped unit cell, derived from the crystal structure.Vector *b* and angle β are located on the opposite side for clarity.

The vectors of the unit cell are labelled *a*, *b* and *c* and the angles between them are labelled α, β and γ, defined as the lattice parameters. This unit cell has translational symmetry to all other cells. The translations of the unit cell are of the form, $R = xa + yb + zc$, where $x, y,$ and z are integers. Using these translations of the unit cell the entire crystal structure can be built with no loss of information. The unit cell is repeated to fill all of the space in the crystal lattice, making it an example of tessellation in 3D space.

The shape of the unit cell can be classified into fourteen 3D crystal lattices that can be sub-divided into seven crystal systems as a function of their symmetry, where their symmetry is determined by the relationship between the lattice constants and angles between lattice vectors (Table 1.1). This gives rise to fourteen 3D crystal lattices, known as the Bravais lattices.

Table 1.1. Structural classifications of the seven types of crystal system, with respect to their symmetry and physical parameters.

System	Rotational Symmetry	Conditions	Bravais Lattices
Triclinic	C_1	$a \neq b \neq c$ $\alpha \neq \beta \neq \gamma$	1
Monoclinic	One C_2	$a \neq b \neq c$ $\alpha = \beta = 90^o \neq \gamma$	2
Orthorhombic	Three C_2	$a \neq b \neq c$ $\alpha = \beta = \gamma = 90^o$	4
Tetragonal	One C_4	$a = b \neq c$ $\alpha = \beta = \gamma = 90^o$	2
Cubic	Four C_3	$a = b = c$ $\alpha = \beta = \gamma = 90^o$	3
Trigonal Rhombohedral	One C_3	$a = b = c$ $\alpha = \beta = \gamma \neq 90^o$	1
Hexagonal	One C_6	$a = b \neq c$ $\alpha = \beta = 90^o$ $\gamma = 120^o$	1

These seven 3D crystal systems can be further divided based on where the lattice points are in the parallelepiped (Figure 1.6). When the lattice points are in the corner of the cell it is a primitive unit cell (p). When this cell has a further point at its centre, it is a body-centred unit cell (i). Where the cell has the corner points plus a point at the centre of each of its faces it is described as a face-centred unit cell (f). When the cell has points at its corners and at the centre of two opposite faces it is a side-centred unit cell (a, b or c depending on the side that the points are on). The monoclinic crystal unit cell can be either primitive or base-centred, meanwhile, the cubic crystal unit cell can be a

primitive, face centred or body centred unit cell. Therefore, there are two types of crystal lattice in a monoclinic crystal and three types of crystal lattice in a cubic crystal. The symmetry and shape of the unit cell lattice for a particular crystal is determined by the nature of the bonding.

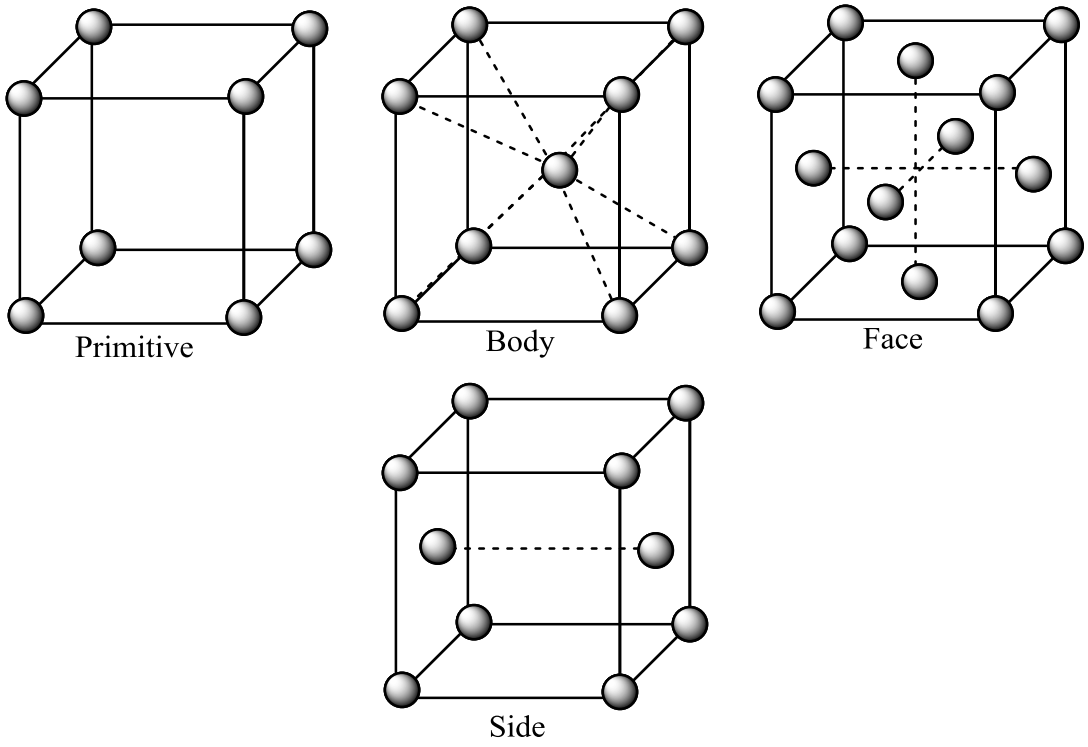

Figure 1.6. Bravis lattices for cubic 3D crystal structure types, showing the position of atoms that give rise to these distinctions.

A reciprocal lattice can be constructed from the Fourier transformation of the real space lattice into momentum space. It is called momentum space as momentum (p) is directly proportional to the wave vector (k) and inversely proportional to wavelength (λ), where $\hbar$ is the reduced Planck's constant.

$$p = \hbar k \tag{1.1}$$

$$\lambda = h/p \tag{1.2}$$

The vectors between the momentum space lattice points are the Fourier transforms of the real space lattice point distances. The primitive vectors of reciprocal space are given by the lattice vectors of the real space cell,

$$2\pi \frac{a \times b}{a \cdot (b \times c)} = c^* \tag{1.3}$$

$$2\pi \frac{a \times c}{a \cdot (b \times c)} = b^* \tag{1.4}$$

$$2\pi \frac{b \times c}{a \cdot (b \times c)} = a^* \tag{1.5}$$

where a^*, b^* and c^* are the basis vectors of reciprocal space, *a*, *b* and *c* are the real space vectors and $a \cdot (b \times c)$ is the volume of the real space cell. The formulae shown in Equations 1.3-1.5 specify that if two of the real space lattice vectors increase, the reciprocal vector that is perpendicular will also increase.

Crystal unit cells are formed with lattice points which also form crystal planes. The crystal planes are classified in relationship to lattice constants through Miller indices, which are defined as the reciprocals of the intersection distance of a plane though the real space vectors. The Miller indices quantify and assign the orientation of these planes with respect to the cell axis, using *hkl* notation. In reciprocal space, infinity becomes 0, and fractions become their reciprocal. This allows for *hkl* values to all be integers. For example 1⁄2, 1, ∞ becomes 210; this plane is shown in Figure 1.7.

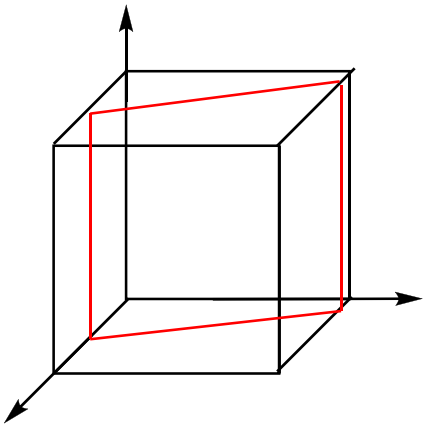

Figure 1.7. The 210 plane of a cell.

When written as (*hkl*) this refers to a plane going through a specified axis. When depicted as {*hkl*} this refers to a family of equivalent planes, for example {100} is (100), (010) and (001). An entire crystal can be described in terms of the distance and vector of the *hkl* planes in the reciprocal lattice, $d_{hkl}$and $\hat{n}_{hkl}$ respectively. These can be combined to describe the lattice in terms of a unit vector *G*, where

$$G_{hkl} = 2\pi\hat{n}_{hkl}/d_{hkl} \tag{1.6}$$

In a cubic lattice,

$$d_{hkl} = \frac{a}{(h^2+k^2+l^2)^{1/2}} \tag{1.7}$$

The Miller indices are the lowest possible integers of plane intersections, where higher indices describe planes of increasingly small divisions. For example the (200) plane will have half the spacing of the (100) plane. In powder X-ray diffraction, the low index planes will appear at lower d-values, where d is the plane spacing. It should be noted that the Miller indices represent the relative distances and orientations of the planes in reciprocal space, where the reciprocal space planes do not necessarily coincide with lattice points in real space.

1.3.2 Electronic Structure of Crystals

Due to the very large number of atoms present in a material, the number of orbitals in energy space is also very large, thus forming a continuum of states, referred to as bands, where many of these will have only negligible differences in the energy continuum. Figure 1.8 shows the electronic structures as a function of number of atoms within a cluster. For an isolated atom (Figure 8(a)), only the atomic orbitals are observed. Upon forming a diatomic molecule (Figure 8(b)) the atomic orbitals overlap to form the molecular bonding (lower energy) and anti-bonding (higher energy) orbitals. As the number of atoms increases to form a cluster (Figure 8(c), the number of bonding and anti-bonding orbitals remains consistent with those present in the individual atoms, but can still be observed as distinct orbitals. As the number of atoms further increases to the bulk (Figure 8(d), the number of molecular orbitals becomes large, and due to the similarity of their energy, form bands rather than distinct orbitals. The highest occupied band is called the valence band (VB) and the lowest unoccupied band is called the conduction band (CB).

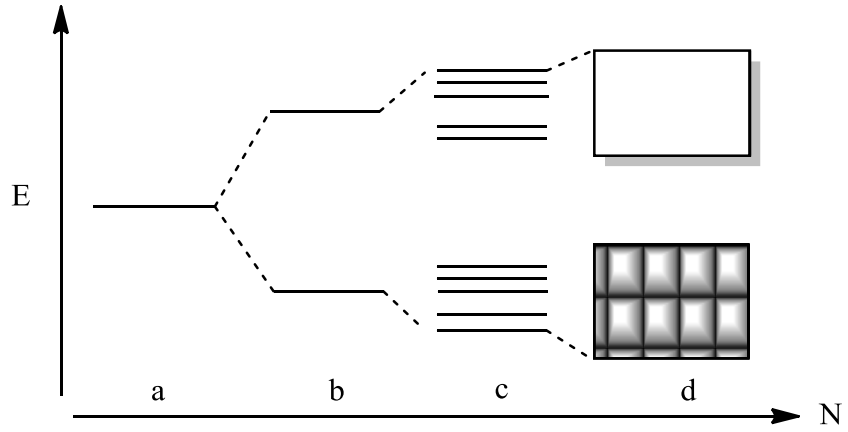

Figure 1.8. Graphic representation of the evolution from the quantum level to the classical level, with regard to the electronic structure of a material. Where; (a) atom, (b) small molecule, (c) cluster and (d) bulk. When the number of atoms, and therefore orbitals increases (a-d), the difference in energy between the orbitals becomes less well defined and give rise to band-structure (d).

The highest point of the top band in the valence band is called the valence band maximum (VBM). The lowest point of the lowest band in the conduction band is called the conduction band minimum (CBM). The distribution of the molecular orbitals as a function of energy is called the density of states, where some energy levels are forbidden and therefore will be empty of electron density. When this region extends through all *k* vectors, it is called the band gap, where *k* is the crystal wavevector and must obey the selection rule $\Delta k = 0$, in order to conserve crystal momentum. If the promotion of an electron from the VBM to the CBM requires no change in vector (*k*) then the bandgap is considered direct. An indirect bandgap is where $\Delta k \neq 0$ (Figure 1.9).

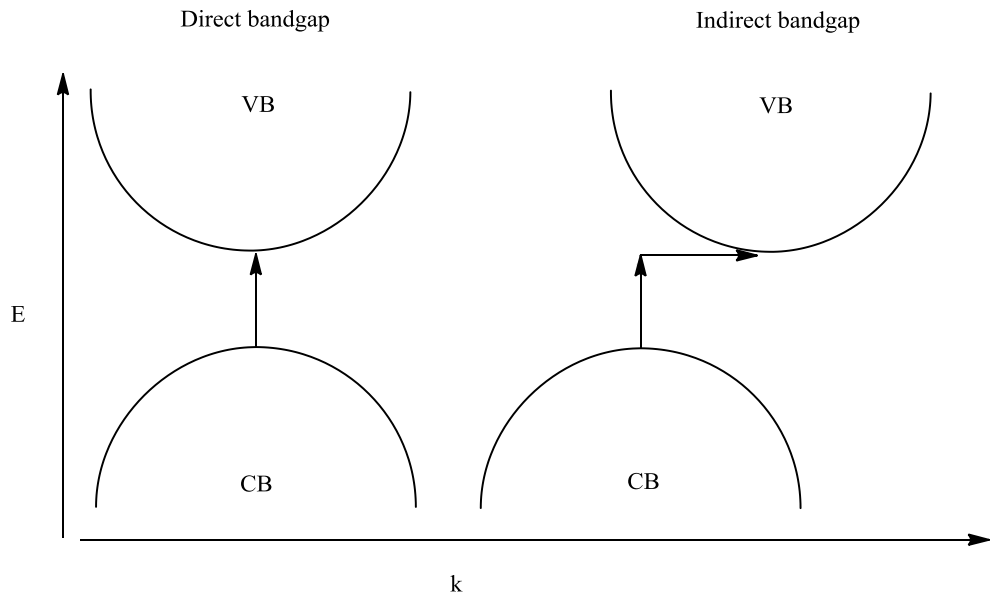

Figure 1.9. Direct and indirect bandgaps, where the direct band-gap shows no change in wave-vector of the excitation (shown as one straight line) and the indirect band-gap shows a change in wave-vector (shown as two perpendicular lines).

1.4 Properties of Nanomaterials

1.4.1 Quantum Size Effects

As the physical size of nanomaterials are of the nanometer scale, they contain a relatively small number of atoms compared to bulk materials. With such a size domain, the electronic structure of the materials becomes a direct function of the crystal size. The effects that arise from the reduced lattice size are called quantum size effects, which are related to the energy changes caused by the quantisation of the electrons in the nanomaterial. This quantisation can be simulated using the particle in the box model, which describes the energy changes of an electron when placed under physical boundaries. A particle is placed in a 'box', of width x and potential V, where there is infinite potential for all values of x except for a portion of length L, for which $V(x)=0$

where $0 \leq x \leq L$ (Figure 1.10). Because the walls have infinite potential energy, the particle has zero probability of existing outside of the box.

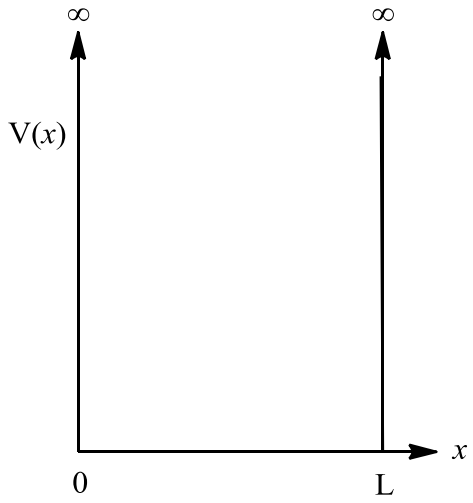

Figure 1.10. Schematic representation of the box into which the particle is confined. Where 0 and L and the box edges and x is the distance between these boundaries. V is the potential of the box, which reaches infinity at the edges (0 and L)

Through the Schrödinger equation we can determine the energy of a free particle,

$$\frac{\hbar^2}{2m}\frac{d^2\psi}{dx^2} = E\psi \tag{1.8}$$

This can be solved for,

$$\psi = A\cos\alpha x + B\sin\alpha x \tag{1.9}$$

Where A and B are constants. As the wavefunction is zero at the edges of the box, $\psi = 0$ at $x = 0$ and $x = L$, $A=0$, so the cosine term is removed, and $\alpha = n\pi L$. These are the boundary conditions. B then becomes,

$$B = \sqrt{2/L} \tag{1.10}$$

When the Schrödinger equation acts upon the wavefunction,

$$\psi = \left(\sqrt{2/L}\right)\sin(n\pi x/L) \tag{1.11}$$

then the value for the energy in terms of *n* is returned as,

$$E_n = \frac{n^2h^2}{8mL^2} \tag{1.12}$$

Because of the dependence on the value of *n*, an electron can only possess discrete wavefunctions and therefore discrete energies. Due to this only certain energy levels are permitted. At *n=1* the wavefunction is distributed over all *L*. At higher values of *n* there are nodes along *L*. However, as *n* tends towards infinity the number of nodes ensures that the probability distribution becomes smooth, leading towards the classical behaviour of an electron in a potential.

As $E \propto \frac{1}{L^2}$, the reduction of length of the box increases the energy of the bands. This is shown in Figure 1.11 which is a simulation of electron energy values as a function of box lengths. These energies have been calculated for lengths of 1-100 nm using 9.11×10^{-31} kg for the mass of an electron. It can be seen that the energy of the electron increases dramatically as the length decreases. Also shown is how these energies increase as the quantum number *n* is also increased.

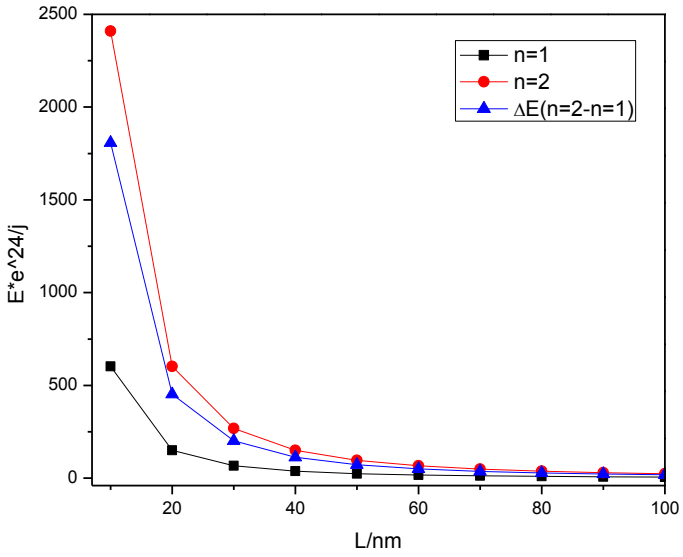

Figure 1.11. Simulation of the energy of a particle as a function of length. The black line shows the energy decreasing as box length increases when quantum number n=1. The red line depicts the decrease in energy of a particle in a box when n=2. It can be seen that for n=2 the starting energy is greater than that of n=1.

The quantisation of energy and its subsequent reliance on material size is also observed experimentally. For example, Figure 1.12 shows how the energy of optical absorption of CdSe increases as the cluster size decreases.

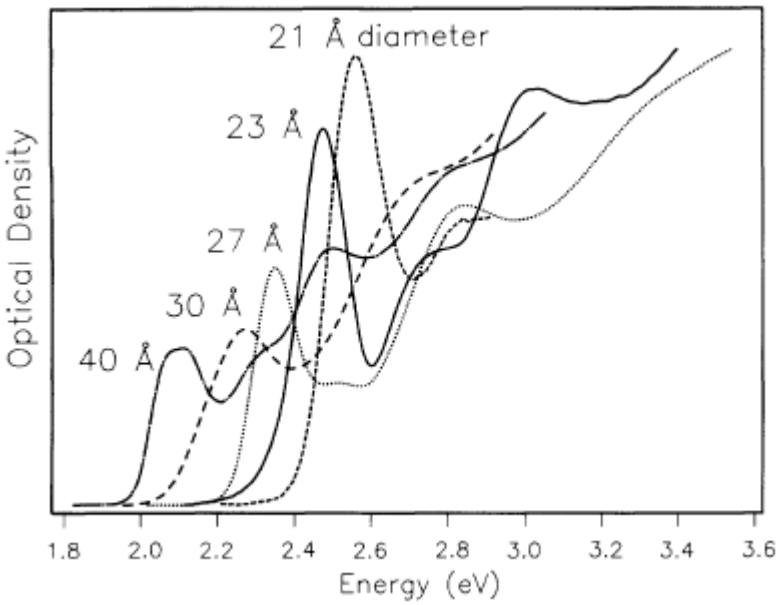

Figure 1.12. Optical density of CdSe as a function of size. As the size of the clusters decreases, the associated energies increase, due to quantisation of the electrons within the material.[35]

1.4.2 Surface to Volume Effects

Due to the small dimension of nanomaterials, their density of surface area is large compared to bulk materials. This is of great importance in chemical reactions as the reactions between gas molecules on a solid surface will occur at a faster rate when there are a larger number of surface atoms. The surface area density is a function of volume and surface area. They do not scale linearly. If a cubic structure has an edge of length *L*, then the area of the surface of a face is L^2 and the total volume of the cube is L^3. The density of the surface area is proportional to 1/L, therefore, smaller particle sizes will help to achieve large surface area. As the number of atoms (*n*) increases the, volume of the cube increases at a higher rate than the surface atoms. This is demonstrated in Figure 1.13 where a cube of *n* atoms has been plotted against its

surface atoms. As *n* tends towards infinity the number of atoms present on the surface is insignificant compared to the number of internal atoms. Conversely, in a nanomaterial, where *n* is small, a large fraction of the total atoms are found at the surface. As surface atoms are more likely to be coordinatively unsaturated compared to internal atoms, materials with a lower value of *n* will have a lower associated stability.

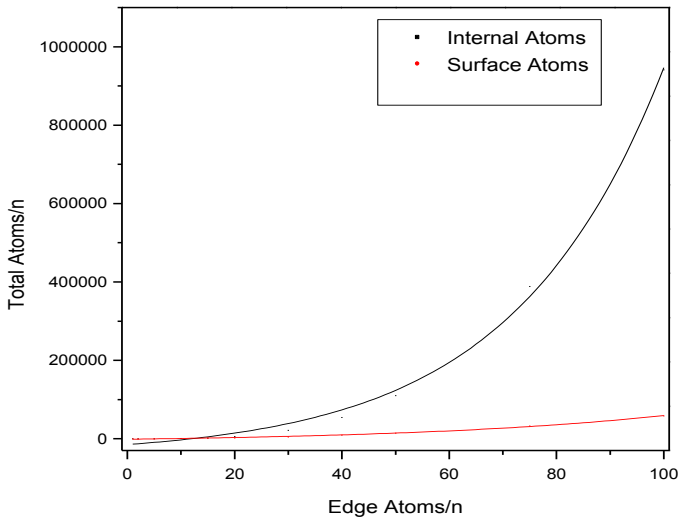

Figure 1.13.The dependence of surface and volume atoms on the number of surface atoms in a cube. It can be observed that the surface atoms form a far smaller percentage of the composition for large clusters.

The implication of surface atoms stability can be seen in the melting points of CdS, where melting point increases with crystal size. As Figure 1.14 shows, as the atomic radius decreases, the melting temperature of CdS decreases. As the radius increases the melting point becomes closer to that of the bulk material.

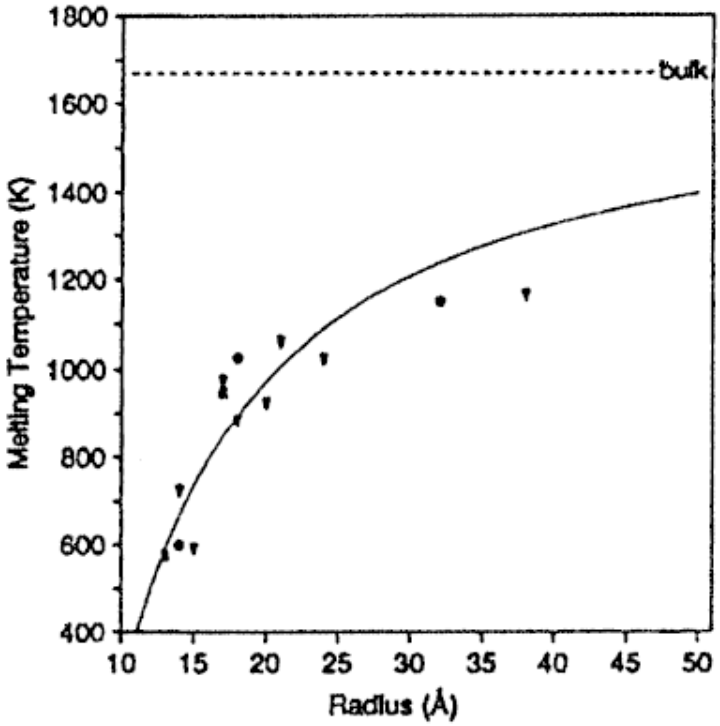

Figure 1.14. Melting point of CdS is shown to decrease as the particle radius decreases due to quantum size effects.[36]

This relationship was mathematically explained by the Gibbs-Thomson equation,[37]

$$\frac{\Delta T_m}{T_m^*} = \frac{2V_m(l)\gamma_{sl}}{\Delta H_m r} \tag{1.13}$$

Where; ΔT_m is the reduction of the melting temperature of the cluster, r is the radius of the cluster, T_m^* is the melting temperature of the bulk material, $V_m(l)$ is the molar volume of the liquid, γ_{sl} is the interfacial surface tension at the liquid-solid boundary and ΔH_m is the bulk enthalpy of melting. Equation 1.13 demonstrates that the reduction of the melting point is inversely proportional to the size of the clusters, as the surface energy is increased for smaller clusters.

1.5 Analysis of Nanomaterials

The properties of materials are strongly influenced by their physical and electronic structure, therefore it is necessary to be able to analyse both of these facets accurately and reliably. For materials chemists, X-ray diffraction and SEM imaging are often the first instruments used, yielding information about the crystal structure and morphology of a material respectively. However, further analysis by additional techniques will yield even more information about a material, such as elemental composition, oxidation state, bandgap distance or even density of states. A brief description of the most common of these analyses is presented below including their applications towards the investigation of nanomaterials.

1.5.1 Structural Analysis

Diffraction

Diffraction is the elastic scattering of radiation from a material. It is an effective, non-destructive method for structural determination and estimation of particle size in solids. Diffraction is a perturbation of an incident wave, with interference, by the periodic electron density (ρ) of atoms in a crystal which gives information on the spacing and relative orientations of the electron density in a material. The incident radiation is considered a wave, where the wavelength for X-rays is of the order ~10^{-10} m, and does not change in wavelength when they are scattered. The necessity of a wavelength of this scale is that it must be of the same order as the distribution of scattering density. When the wave strikes the electron density, it causes it to oscillate at the same frequency as the incident radiation. These scattered waves are spherical and will overlap with oscillations from nearby electrons. In almost all directions there will

be destructive interference, however, in very few directions there will be constructive interference and a wave will exit the sample. When an X-ray is shone directly at a crystal with a screen placed behind it, the rays from constructive interference will scatter in a regular pattern on the screen, as shown in Figure 1.15.

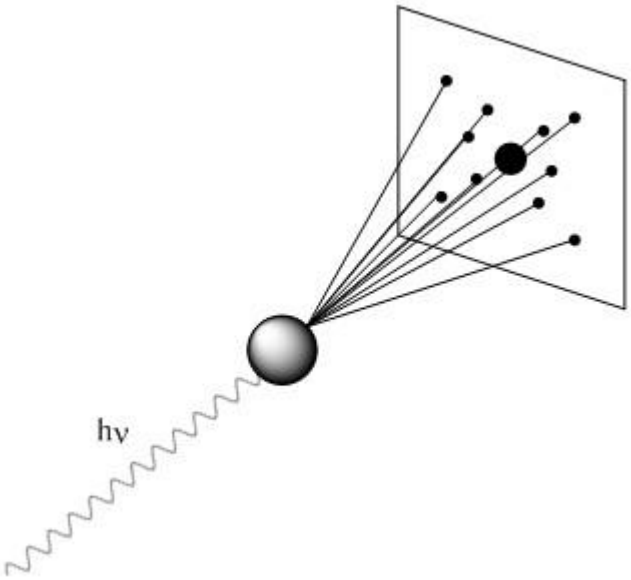

Figure 1.15. Scattering pattern of X-rays from a single crystal, showing the regular pattern of spots on the screen due to the long-range order in a single crystal.

The diffraction pattern is collected for a range of angles by either rotating the crystal or rotating the beam around the crystal. The scattering pattern is the Fourier transform of the object. Once collected, the diffraction pattern is Fourier transformed to provide the electron density map of the object.

As discussed in Section 1.3, a crystal is periodic with translational symmetry in all directions. It is this facet of the crystal that makes structural determination possible. The diffraction pattern is a direct result of the symmetry of the crystal. Harvesting scattering data is possible because of the large number of regularly aligned atoms present in a crystalline sample. The symmetry of the diffraction yields information on

the symmetry of the unit cell, while the intensities provide information on the complete molecular structure. As all the information of the crystal is contained within the unit cell, information on the entire crystal can be extracted from analysis of just the unit cell. The diffraction pattern contains the amplitude of all the diffracted waves, however, the relative phases of the waves are lost which is known as the phase problem. This is overcome by a process called structure solution, which shall be discussed later in this section.

Structural Determination *via* X-ray Diffraction

X-ray diffraction can be divided in to two main sub classes based on sample type, single crystal and powder. Single crystal X-ray diffraction is primarily used for determining inter-atomic distances and molecular structure. This is possible because single crystals have long range structure. From the shape factor, F_{hkl}, the electron density, and therefore the atomic positions, can be determined within a unit cell. In practice this cannot be achieved by a direct Fourier transform of the scattering pattern due to the phase problem, so it is performed with either the Patterson or direct methods, which account for the phase problems in different mathematical ways. In the direct method, statistical relationships between the electron density of the atoms are exploited, and in the Patterson method the structure and phase factors are squared to give rise to inter-atomic vectors within the crystal.[38] This is called the Patterson function and yields information on the atomic number of the atoms, making this a useful method for the determination of structures containing heavier elements.

In powder diffraction the sample is poly-crystalline; it is made up of many small crystals arranged in a random order. All Miller planes will be equally represented in the diffraction pattern. In the diffraction pattern, what were seen as sharp spots for single crystals are now seen as cones. Figure 1.16 shows a typical powder diffraction pattern from TiO_2 nanofibres taken in our lab. These cones are arranged in a spacing determined by the spacing between the crystal planes.

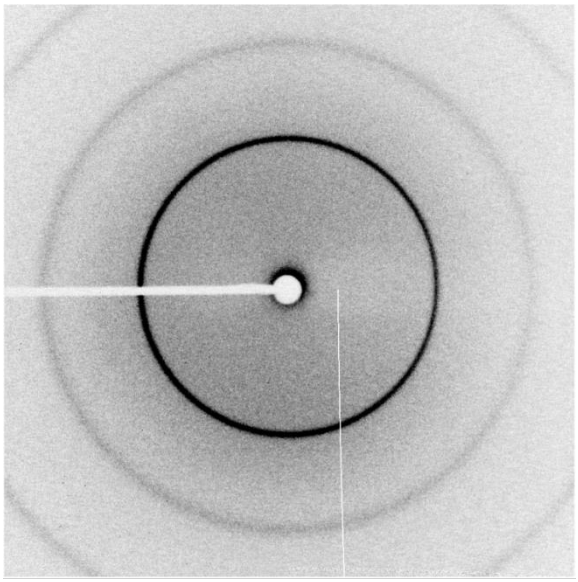

Figure 1.16. Powder diffraction pattern observed from pristine TiO_2 nanofibres, where the cones respresent the Bragg planes of the material. From the centre, the cones are the 110, 004 and 200 anatase planes. The slightly higher intensity on the left of the pattern infers preferential alignment. Collected on a Rigaku 007HF at University of Sussex, 2011.

These are called Bragg peaks, where the constructive interference is predicted by

$$n\lambda = 2d\sin\theta \tag{1.15}$$

where d is the spacing between the crystal planes and θ is the angle of the incident X-ray (Figure 1.17). It defines that for two equal incident X-rays, one reflecting off the surface and one from the inside of the material, the distance the internal X-ray travels is

twice that of the plane separation. In order to be in phase with the surface reflected X-ray, the internal X-ray must have travelled a whole number of wavelengths.

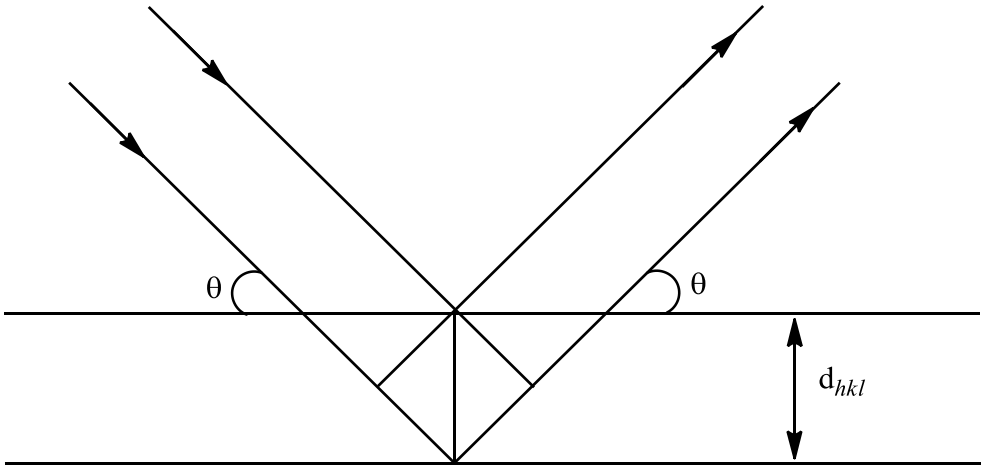

Figure 1.17. Bragg diffraction showing two incoming waves reflecting from consecutive planes, exiting the sample with constructive interference.

When trying to ascertain a crystal structure from a sample, the main difference between single crystal and powdered samples is that for a single crystal the structure can be solved but for a powder it is modelled, the most common method to do so being the Rietveld method. The Rietveld method is a least squares analysis that mathematically separates the diffraction peaks, which become overlapped in powdered samples.

The diffraction observed in an experiment can be compared to those in a database, such as ICDD (International Centre for Diffraction Data, formally called Joint Committee on Powder Diffraction Standards) for chemical and phase analysis, for example differentiating between CuO and Cu_2O or between rutile, anatase or brookite TiO_2. Figure 1.18 shows a typical powder XRD pattern of P25, collected in our lab. In the pattern both the anatase and rutile indexes can be clearly distinguished from one

another. Furthermore, the percentage composition of each of the present components can be calculated *via* the relative intensities of the peaks.

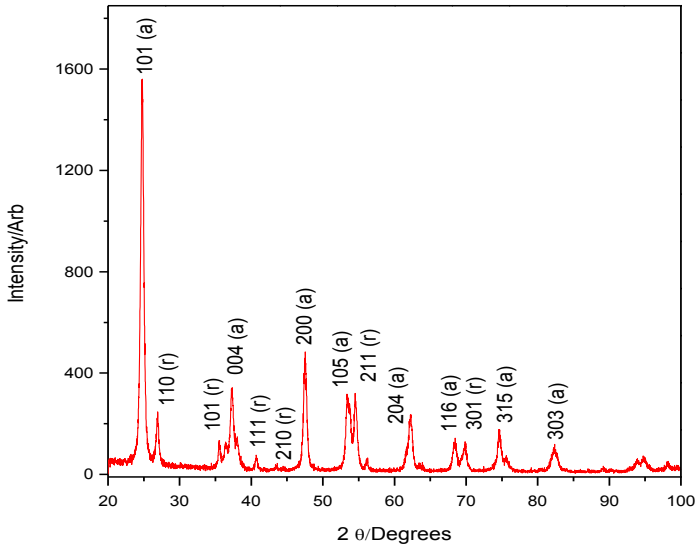

Figure 1.18. Powder diffraction pattern of P25 TiO_2, where the rutile (r) and anatase (a) phases can be distinguished from each other. Obtained at University of Sussex, 2012, Wei Cheet Lee and indexed from ICDD.

In an amorphous sample the diffraction pattern is far harder to interpret as there is no long range periodic structure, therefore the diffraction patterns will no longer be regular, resulting in less intense, broader peaks.

Particle Size Determination *via* X-ray diffraction

The crystallite size in a nanomaterial can be determined using the X-ray data and applying the Scherrer equation,

$$\tau = \frac{K\lambda}{\beta cos\theta} \tag{1.16}$$

where τ is the crystallite size, K is the shape factor, β is the line broadening at FWHM (full width half maximum, the width at half the maximum intensity) and θ is the Bragg angle. As defined by Equation 1.16, as the crystallite size decreases, line broadening increases, therefore sharp diffraction peaks imply large crystallite size. When K is unknown and cannot be determined, 0.9 is used as a good estimate. A disadvantage of using the Scherrer equation to determine crystallite size is that it is only applicable for particles in the range of ~5-200 nm. This is because as the crystallite size increases, diffraction peak broadening decreases and peak broadening from other sources becomes significant. Significantly, the Scherrer equation can only estimate mean crystallite size, not particle size.

The crystallite size of P25 of the sample presented in Figure 1.18 was estimated to be 16.5 nm, close to the particle size of ~21 nm, as stated by the suppliers (Sigma-Aldrich). The lower estimated value is because the Scherrer equation only calculates a lower limit on crystallite size, as line broadening can come from other factors than the shape factor, such as lattice defects.

1.5.2 Morphological Analysis

Microscopy is often the first point of call for morphological analysis of nanomaterials due to its quick analysis time. The four most common microscopes used are the scanning tunnelling microscope (STM), atomic force microscope (AFM), transmission electron microscope (TEM) and the scanning electron microscope (SEM). STM and AFM allow for atomic resolution analysis by scanning a needle over the

material surface. In STM electrons quantum tunnel through the surface whereas in AFM the needle tip is repulsed by the electrons on the material surface. STM has been used to observe the 2x1 reconstructed surface of TiO_2 (Figure 1.19).[39]

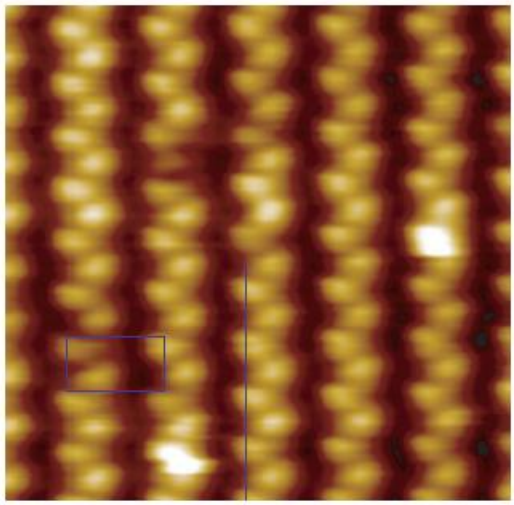

Figure 1.19. STM image of rutile TiO_2 011 2x1 reconstructed surface.[39]

AFM has been applied to the 3D surface mapping of materials, such as titanium dioxide. Figure 1.20 shows the surface morphology of TiO_2 nanoparticles on a silicon substrate, from which particle size can also be determined.[40]

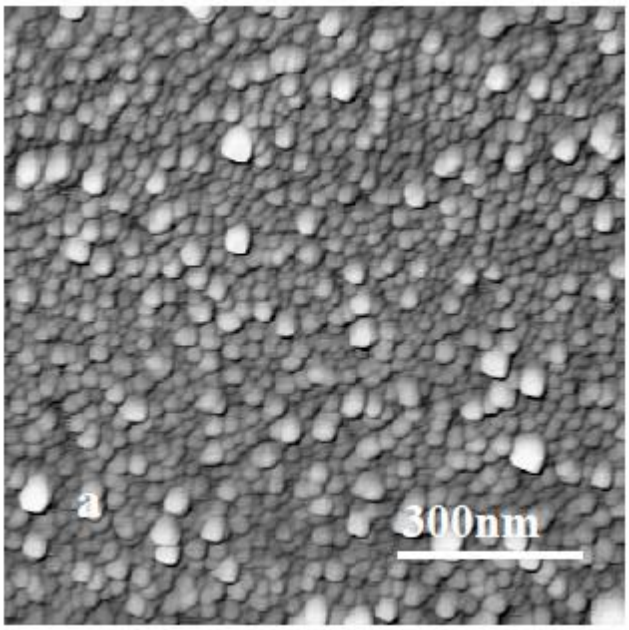

Figure 1.20. AFM image of TiO_2 nanoparticles on a silicon substrate, where it would be possible to estimate crystallite size from the image.[40]

Like STM, AFM can reach atomic scale resolution, but is disadvantaged by its slow analysis time and the relatively small surface area that can be analysed.

Electron Microscopy

The resolution of an image is of the order of the wavelength of radiation used to analyse the sample. For nanomaterials, the wavelength of visible light is too long to observe any features. A beam of electrons, often shortened to e-beam, have a wavelength of less than 1 Å, and therefore, theoretically it can be used to observe a material down to the atomic scale, however, in practice this depends on the precise microscope used. The resolution is typically in the region of 1-100 nm, which is a suitable scale for the analysis of nanomaterial morphology. The electron source is usually a heated filament, often tungsten, and accelerated through a potential (*E*) which

monochromates the beam into a single wavelength. The electron beam can be controlled by electrostatic or magnetic fields, allowing for analysis of particular regions of the observed sample.

A drawback is that the sample is commonly placed under vacuum to increase the mean free path of the electrons, making the analysis of volatile materials problematic. The two most common electron microscopes are the transmission electron microscope (TEM) and the scanning electron microscope. The principle difference between the two is the interaction of the e-beam with the sample. In TEM, the electrons pass through the sample and are diffracted whereas in SEM the interactions are from either backscattered or secondary reflected electrons. Figure 1.21 shows the primary interactions of the e-beam with the sample in electron microscopy.

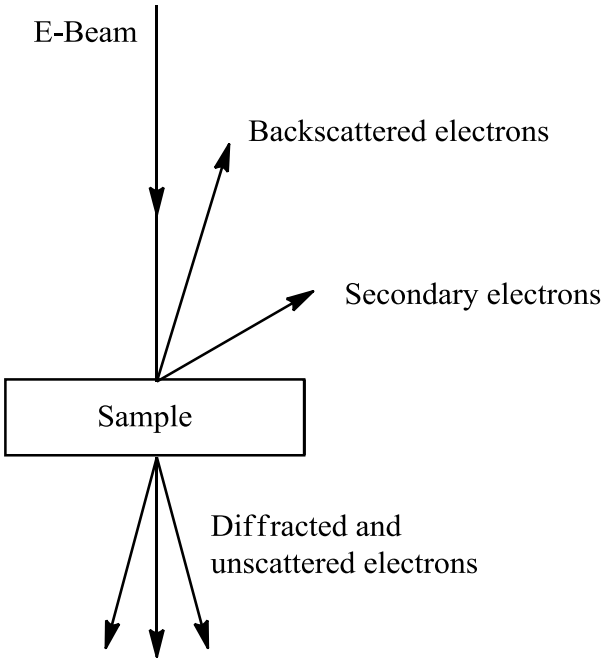

Figure 1.21. The interactions of an electron beam with a specimen. Backscattered and secondary electrons are associated with SEM and diffracted electrons are associated with TEM.

Transmission Electron Microscopy

In TEM the electron beam is scattered by electrons in the sample with a strong scattering factor, as electron-electron interactions are strong. The diffraction pattern can be shown as the un-processed pattern or converted to an image of the sample. Figure 1.22 shows the diffraction pattern of calcium carbonate taken by TEM, where the regular diffraction pattern can be observed.[41]

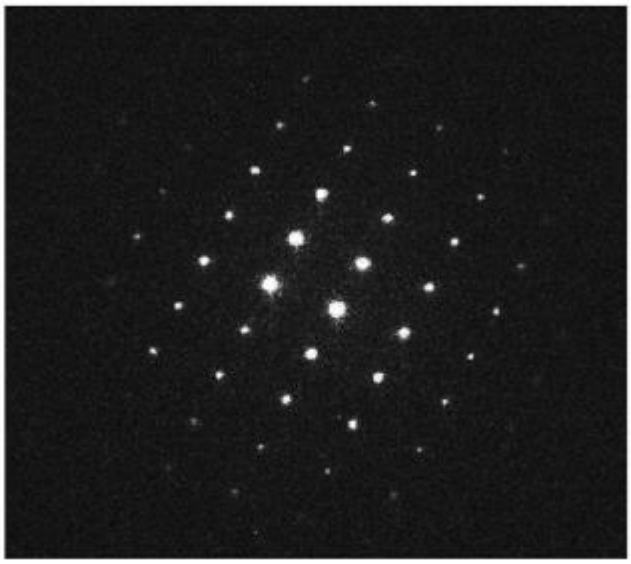

Figure 1.22. Diffraction pattern of calcium carbonate taken with a TEM, showing the regular patterns of spots, indicating a single crystal sample.[41]

A major disadvantage of TEM is that the sample can only have a maximum thickness, as the electrons must pass through the material. The maximum thickness is often in the region of 1 mm. However, a major advantage is that the high resolution of TEM allows for very short length scales to be observed. For example, Thamaphat *et al.* have estimated particle size from TEM images of TiO_2, shown in Figure 1.23.[42]

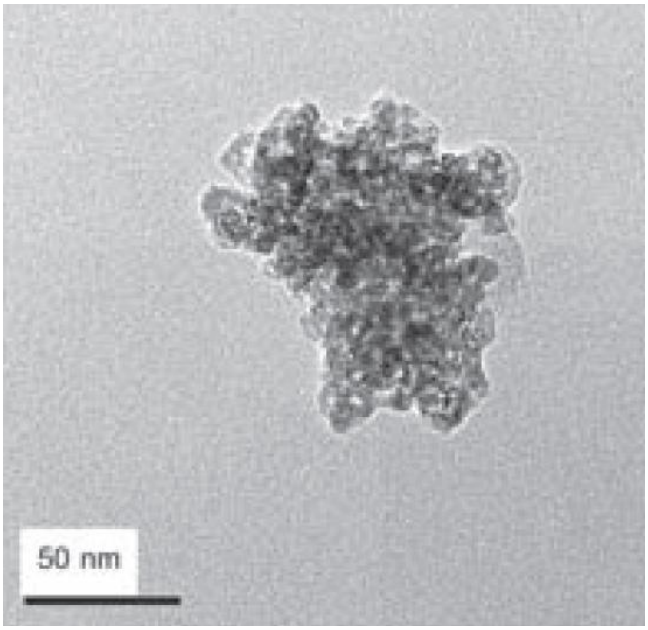

Figure 1.23. TEM image of anatase TiO_2 nanopowder.[42]

Scanning Electron Microscopy

SEM can make use of back scattered or secondary electrons, where secondary electron imaging is the most commonly used method. Secondary electrons are Auger electrons (See Figure 1.30), detected by a scintillator, named an Everhart-Thornley detector, where intensity as a function of position is projected onto a video screen. Back scattered electrons are elastic with regard to the incident e-beam therefore they can be analysed as a function of Z, atomic number. This gives rise to a boost in contrast, as heavier nuclei will give more intense images.

SEM is efficiently able to analyse a relatively large sample, but with much lower resolution than STM or AFM. The fast analysis time by SEM leads to it frequently being the first point of analysis for nanomaterials.

In this project secondary electron imaging has been used extensively in the analysis of both the morphology and dimensions of nanomaterials, including titania powder, fibres and particulated fibres, titania loaded zeolites and cobalt oxide and phosphate nanomorphologies. Figure 1.24 shows an SEM image of typical cobalt oxide nanofibres prepared in this project. From this image both the morphology and fibre diameter were estimated; they were found to be defect free and ~1000 nm diameter. Furthermore using SEM imaging of PMMA nanofibres, the relationships between morphology and electrospinning variables were determined (Section 2.3).

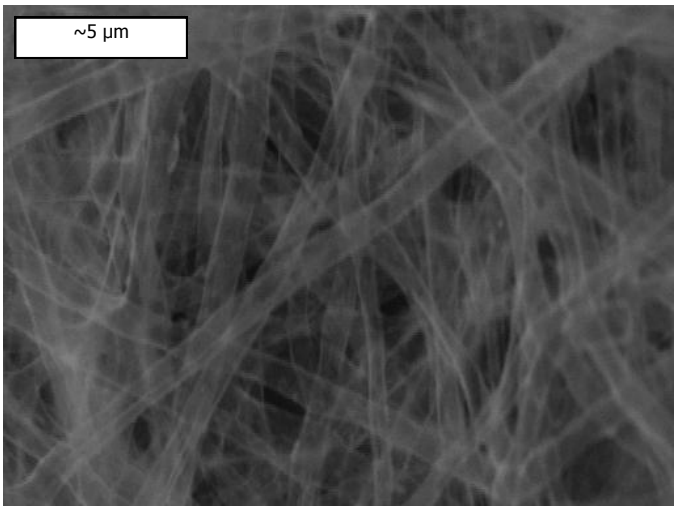

Figure 1.24. Typical SEM image of cobalt oxide nanofibres produced in our lab. Collected 2012. The diameter of the nanofibres was determined from these images (~1000 nm).

1.5.3 Chemical and Oxidation State Analysis

A further advantage of electron microscopes is that they can have integrated analytical methods, namely energy dispersive X-ray (EDX) and electron energy loss spectroscopy (EELS). These allow for elemental, and some electronic, analysis to complement the morphological information gained from electron microscopy. X-ray

photoelectron spectroscopy (XPS) and Auger electron spectroscopy (AES) are related techniques that yield similar information.

Both EELS and EDX require an incident beam of electrons. In EELS the e-beam is of a narrow de Broglie wavelength, where some of the electrons of the material will be inelastically scattered from processes such as core electron ionisation and valence band excitation. The energy difference from the inelastic scattering can be measured and will give details of the electronic structure of a material. For example, Akita *et al.* used an STEM with an integrated EELS to map the dispersion of gold across a titania surface (Figure 1.25).[43]

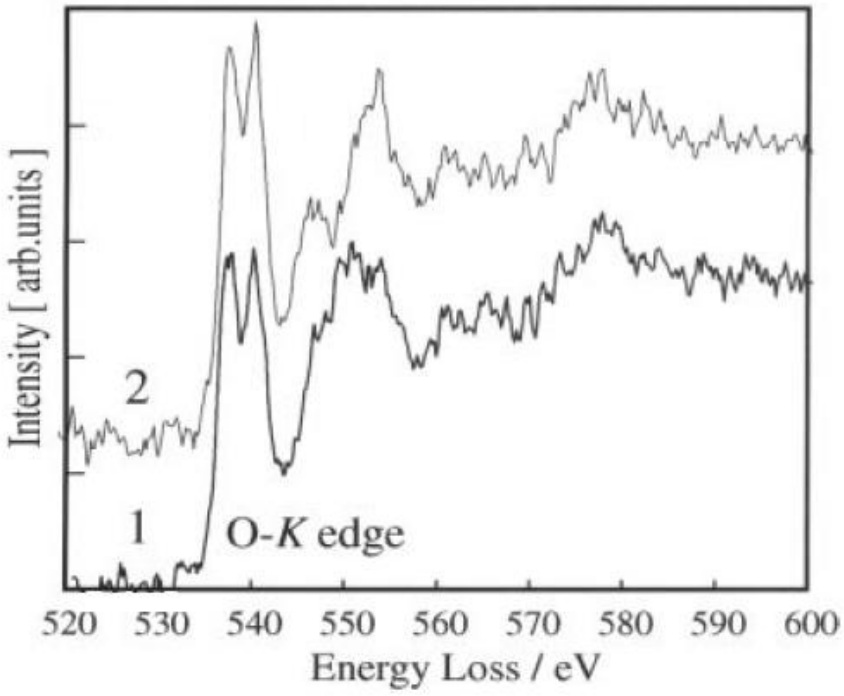

Figure 1.25. EELs spectrum of Au coated TiO_2 showing the O-*K* edge of two samples, where 1 is a titania sample with a high density of Au and 2 is a titania sample with low density of Au.[43]

Furthermore, EELS has seen application in oxidation state determination,[44] valence band density of states[45] and elemental analysis.[46]

In EDX, a core electron is ionised by the e-beam, where a higher energy electron fills the hole with the subsequent release of X-ray radiation, this can be seen in Figure 1.26. This radiation is a function of the element that is being investigated, allowing for elemental analysis. However, a drawback of EDX is that it is difficult to analyse elements of low effective charge (~Z <10), due to overlap of heavier element L and M lines with lighter element's K lines. EELS performs better for elements of low Z, making them complementary techniques. In order to obtain quantitative elemental analysis, the sample must be compared to a known standard of the element in question.

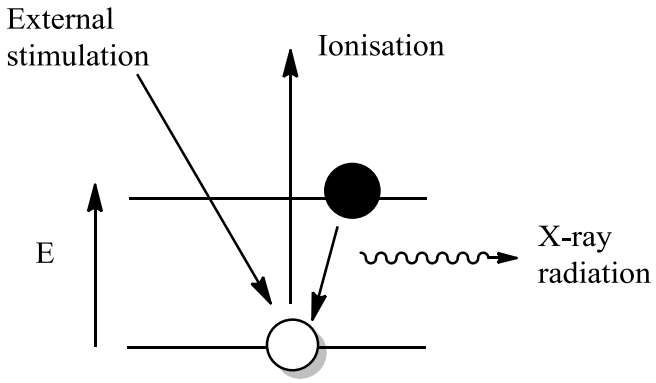

Figure 1.26. Mechanism of EDX showing the ionisation of an electron by external simulation and then a second electron falling into its place with the subsequent release of radiation. The energy of the radiation is of wavelength of X-rays.

The X-rays are detected by a Si(Li) diode. When an X-ray hits the diode a number of electron-hole pairs are created which causes a change in voltage. The number of electron hole pairs created is proportional to the energy of the detected X-ray. The Si(Li) diode necessitates the presence of liquid nitrogen cooling, in order to keep the conductivity suitably low. The number of voltage pulses for a given detected X-ray,

called counts, is recorded. Combined with the raster scanning ability of SEM, EDX yields the concentration of an element in a particular area. Using mapping, the dispersion of an element over a given material can be recorded. In this project, extensive use has been made of an SEM with integrated EDX for elemental analysis of doped TiO_2 nanofibres, cobalt oxide and phosphate nanomaterials and TiO_2 loaded zeolites. Figure 1.27 shows a typical EDX spectrum of TiO_2 loaded MCM41-S zeolite, where the silicon content of the alumina silicate zeolite is compared to the titanium content of TiO_2, to determine their relative concentrations.

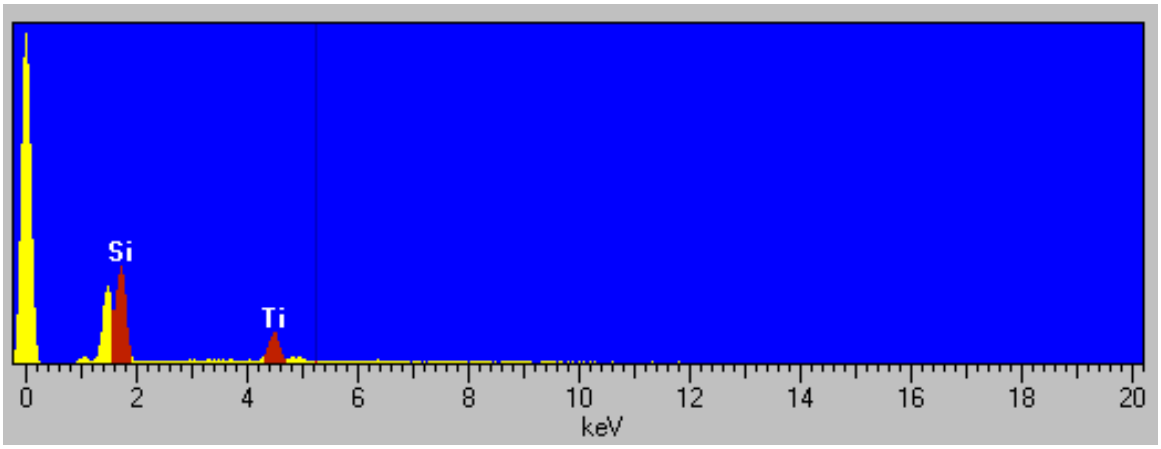

Figure 1.27. Typical EDX spectrum of P25 loaded MCM41-S zeolite, where the intensities of the Si and Ti peaks can be used to determine the composition of the material. Obtained at University of Sussex from our experiments, 2012.

X-ray Photoelectron Spectroscopy (XPS)

Closely related to EDX is X-ray photoelectron spectroscopy. In XPS a sample is irradiated with an incident X-ray beam, where the radiation is of sufficiently high energy that the core electrons of an element are ionised. The counts of ionised electrons are recorded as a function of energy. A general mechanism of XPS is shown in Figure 1.28, from the incident X-ray to the spectrum. Because of the low mean free path of

electrons, XPS must be performed under ultra high vacuum and is only suitable for surface analysis.

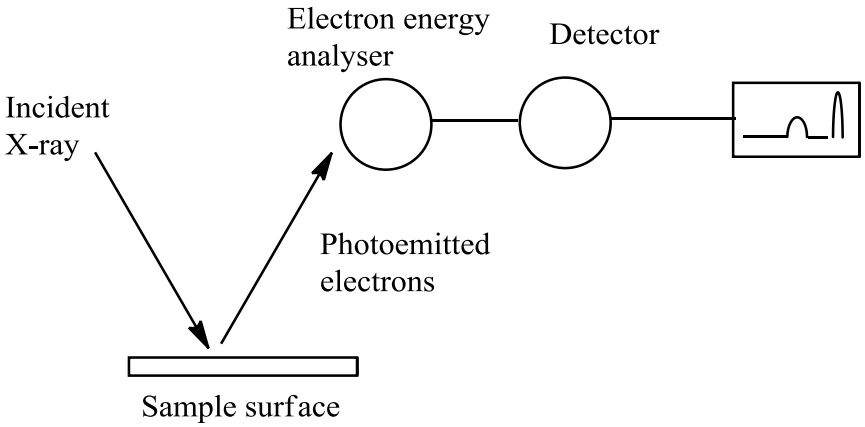

Figure 1.28. Diagram of XPS. Arrows indicate the pathway of incident X-rays and emitted electrons.

The energy of these emitted core electrons is characteristic of the parent element, rendering XPS useful for elemental analysis. The electron ionisations indicate a valence band edge which can, when combined with another spectroscopic technique, can measure the band gap of a material. For example, combined with bremsstrahlung *iso*chromat spectroscopy (BIS) the band gap of NiO was determined to be 4.3 eV, in agreement with local cluster computations at 5 eV (Figure 1.29).[47]

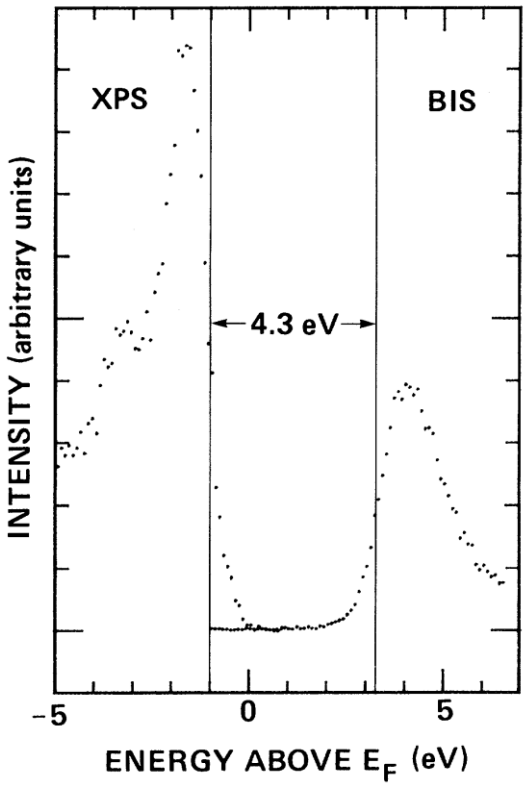

Figure 1.29. Combined XPS and BIS spectrum of NiO. The left-hand side (low energy) shows the valence band as determined by XPS. The right-hand side (high energy) shows the conduction band as determined by BIS.[47]

Furthermore, XPS also has applications in the analysis of oxidation states of metals, for example determining that in $SrFeO_3$ the iron is composed of Fe^{3+} and Fe^{4+} ions.[48]

Auger Electron Spectroscopy (AES)

During AES, a solid is irradiated with a type of radiation higher than the binding energy for an electron in a particular core. This leaves a hole that a higher energy electron can relax in to. This energy can be released as a photon, however; it could also transfer to a third electron, which will then be emitted from the sample. The ionisation

of these Auger electrons is shown in Figure 1.30. The second ionised electron is called the Auger electron. The mechanism of AES is similar to that of secondary electrons produced during SEM imaging.

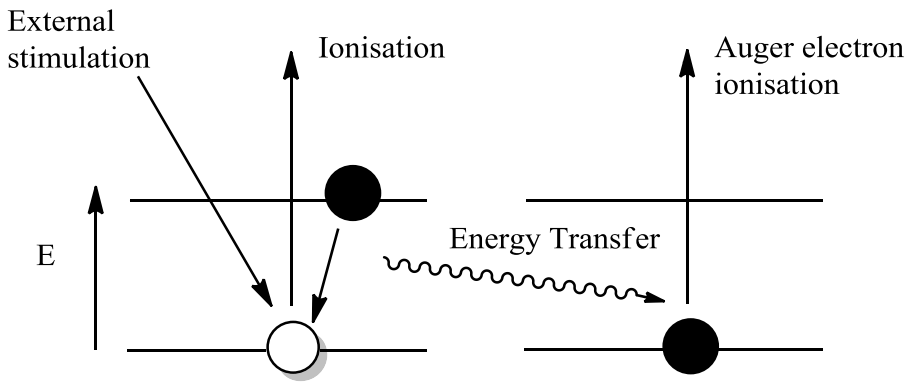

Figure 1.30. Diagram of AES. The external stimulation causes an initial ionisation. Another electron drops from a higher energy state into the hole left by the ionisation, releasing energy which is transferred to 3rd electron. This 3rd electron is the Auger electron.

Auger transitions are characteristic of an atom therefore they can be used in elemental analysis, however, it also has applications in surface defect analysis, as surface defects lead to a noticeable difference in the spectrum (Figure 1.31).[49]

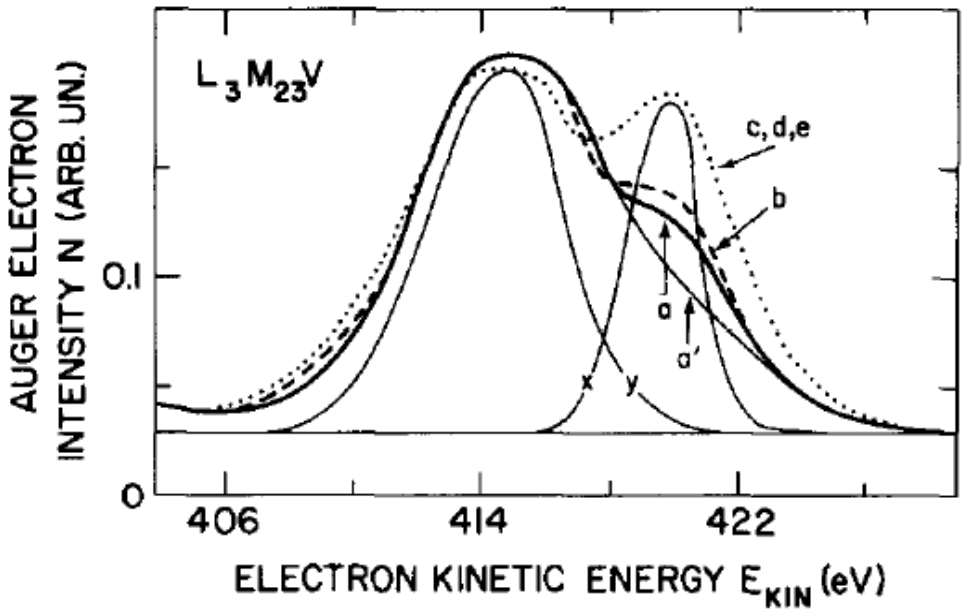

Figure 1.31. AES spectrum of the 110 plane of TiO_2, where a-e indicate differing degrees of surface defects. As the degree of defects increases (a-e) the energy of the Auger electron is observed to increase.[49]

As with XPS, this technique is usually run under ultra high vacuum and is only suitable for top layer analysis because of the low mean free path of the Auger electron.

1.5.4 Energetic Determination

The ground state energies of electrons are quantised in a way determined by quantum mechanics. When these electrons are provided with sufficient energy from a radiation source, promotions can occur. The energy of a transition is a function of the difference in the gap between the ground and excited state energies therefore, if the energy is known, the gap between energy levels can be determined. Figure 1.32 demonstrates the general transitions that can be measured between energy gaps. E_g is the energy gap between the highest occupied energy level and lowest unoccupied level.

IP is the ionisation potential of removing an electron to vacuum. EA is the electron affinity of the material obtaining an electron.

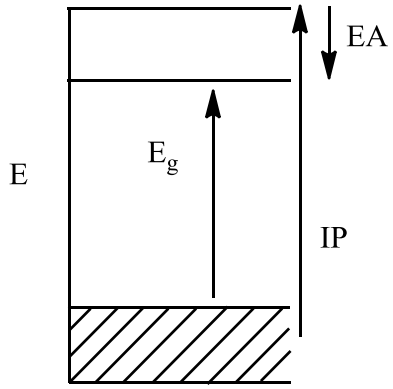

Figure 1.32. Energy diagram showing the fundamental transitions of an electron. EA = electron affinity, E_g = energy gap and IP = ionisation potential.

While no single technique exists that will suitably measure all of the transitions possible in a material, using a combination of techniques, a useful description of the electronics of a system can be discerned.

Both X-ray and optical spectroscopies can be used to elucidate the electronic structure of a material, where the principle difference between the two is the different energies of the radiation. In practice this means that optical spectra are derived from the energy changes of outer electrons and X-ray spectra are derived from energy changes of the core electrons of an atom.

X-ray Emission (Fluorescent) Spectroscopy (XES)

During XES an electron is excited using X-ray radiation or an electron source. An electron from a higher energy state can then relax into the vacancy, releasing the

energy as a photon or as a soft X-ray. Mechanistically XES is analogous to luminescence but uses higher wavelength incident radiation and therefore has higher energy emissions.

XES provides information of the local partial density of states for the valence band which, when combined with X-ray absorption spectroscopy (XAS), can elucidate the structure of the highest occupied and lowest unoccupied electronic regions.[50] By superimposing the spectra from X-ray absorption and emission spectroscopies the band gap energy can be calculated. Figure 1.33 shows the superimposition of X-ray absorption and emission spectra of ZnO where the bandgap was determined to be ~3 eV.[51]

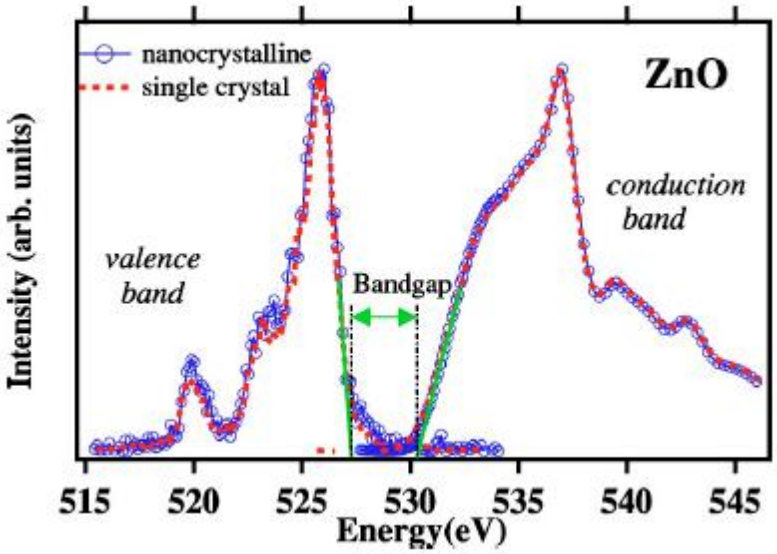

Figure 1.33. The difference between the valence band, determined by XES and conduction band, determined by XAS, are combined to determine that the band gap of ZnO is ~3 eV.[51]

Optical Spectroscopy

Optical spectroscopy is spectroscopy that is concerned with the use of radiation in the region of 10^{-4}-10^{-7} m. This includes infra-red, visible and ultra-violet radiation, where the visible and ultra-violet regions are often recorded together. Compared to X-ray radiation, these sources are low energy and, therefore, are regularly used in the analysis of lower energy transitions, such as measuring vibrational states or outer-shell excitations.

Fourier Transform Infra-Red (FT-IR)

Infra-red spectroscopy is often used to analyse the vibrational states of a material. These vibration energies are indicative of a particular bond, for example, the C=O band appears at 1740-1630 cm^{-1}. Because of these characteristic peaks, IR spectroscopy is used intensely in functional group analysis. In order for a vibration to be IR active it has to obey the selection rule that there must be a change in the dipole moment between the two bonding atoms. Figure 1.34 shows a typical FT-IR spectrum of PMMA, where the modes of the PMMA functional groups can be observed. The intensitiy of the C=O stretch was recorded as a function of calcining temperature to elucidate the degradation pathway of PMMA during calcination.

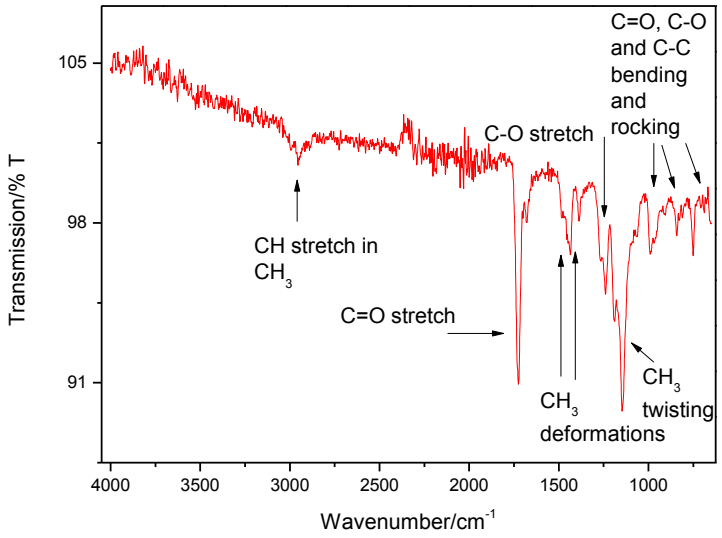

Figure 1.34. Typical FT-IR spectrum of PMMA nanofibres, obtained in our lab. Assignments were taken from Haris *et al*..[52]

Visible Light Spectroscopy

Visible light spectroscopy is concerned with transitions that either occur due to excitations *via* visible light (photoexcitation) or emit visible light (photoluminescence).Photoluminescence is perhaps the most well known visible light spectroscopic technique for nanomaterials as it is used in the analysis of quantum dots.

In the analysis of quantum dots, the emitted photon energy can be used to determine particle size, as energy increases inversely with particle size.[16] This can be observed in Figure 1.35, where the particle size of CdSe quantum dots has been determined by their fluorescence.[53] It can be observed that as the particle size increases the intensity and energy of the fluorescence decrease. The reasons for this relationship is due to quantum size effects, which were discussed in detail in Section 1.4.1.

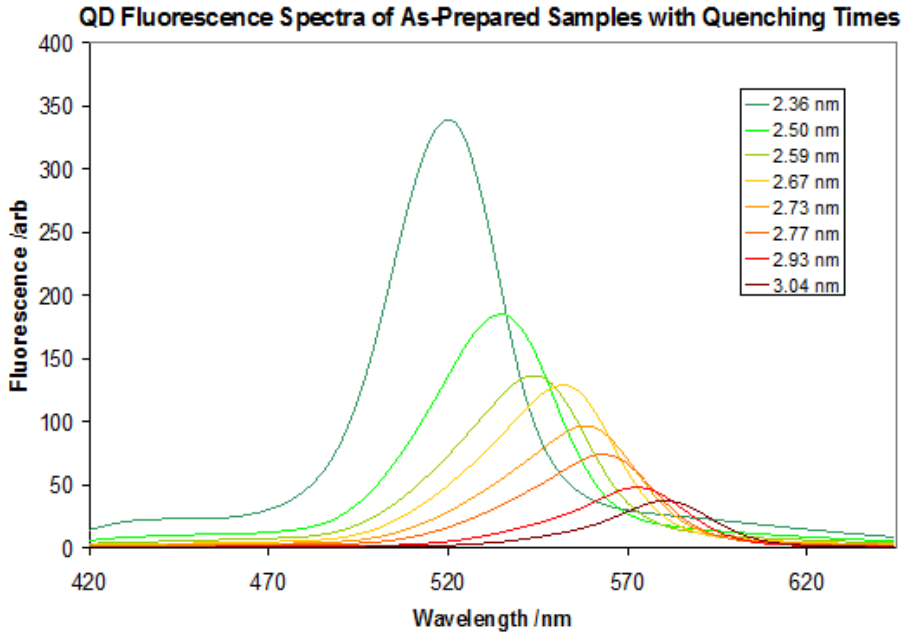

Figure 1.35. Fluorescence spectra of CdSe quantum dots and the particle size of each sample. It is observed the smaller the QD (green colours), the larger the absorbance.[53]

Ultra-Violet Visible (UV-Vis) Spectroscopy

UV-Visible spectroscopy refers to absorbance and reflectance techniques where the incident radiation is from the UV-Vis region of the electromagnetic spectrum. It is commonly used to determine the concentration of solutions by their absorbance, using the Beer-Lambert law,

$$A = \varepsilon CL \tag{1.17}$$

where A is the absorption, ε is the absorptivity, or molar extinction coefficient, C is the concentration and L is the path length of the cell. As Equation 1.17 shows, as the concentration of the solution increases, the absorbance also increases. Therefore, UV-

Vis absorption spectroscopy is useful for the determination of concentration of analytes. It has been used extensively in this project to determine the rate of increase in concentration of phenol during photocatalysis by measuring the intensity of λ_{max} of sodium phenolate (Sections 3, 4 and 5).

When analysing solids, UV-Vis absorption can be impractical so reflectance is often used as an alternative. A sample is irradiated where the light scatters back to the detector. When the reflectance is symmetric with respect to the incident radiation it is titled specular reflection, however, when the reflectance is over all allowed angles it is titled diffuse reflectance (DRS) (Figure 1.36). An integrating sphere can be used alongside diffuse reflectance UV-Vis to uniformly scatter all reflected light, allowing for an average over all scattering angles.

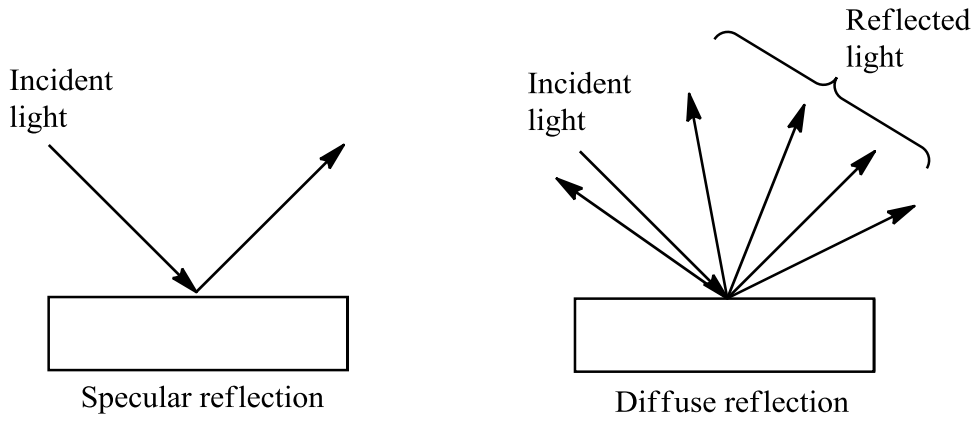

Figure 1.36. Specular and diffuse reflection. In specular reflection, the light is only reflected symmetrically with respect to the incoming radiation. In diffuse reflection the light is reflected over all allowed angles.

The wavelength of UV-Vis light is sufficient to excite electrons across a bandgap, therefore it is used regularly in bandgap analysis of un-doped and doped nanomaterials, for example it has been successfully used in the determination of the

band gap in bulk and nano TiO_2 materials.[54] It is often used to measure any change in band-edge caused by the loading of dopants into TiO_2 , where, as the loading of Cr increases (a→d), the band edge shifts towards the visible region of the electromagnetic spectrum (Figure 1.37).[55]

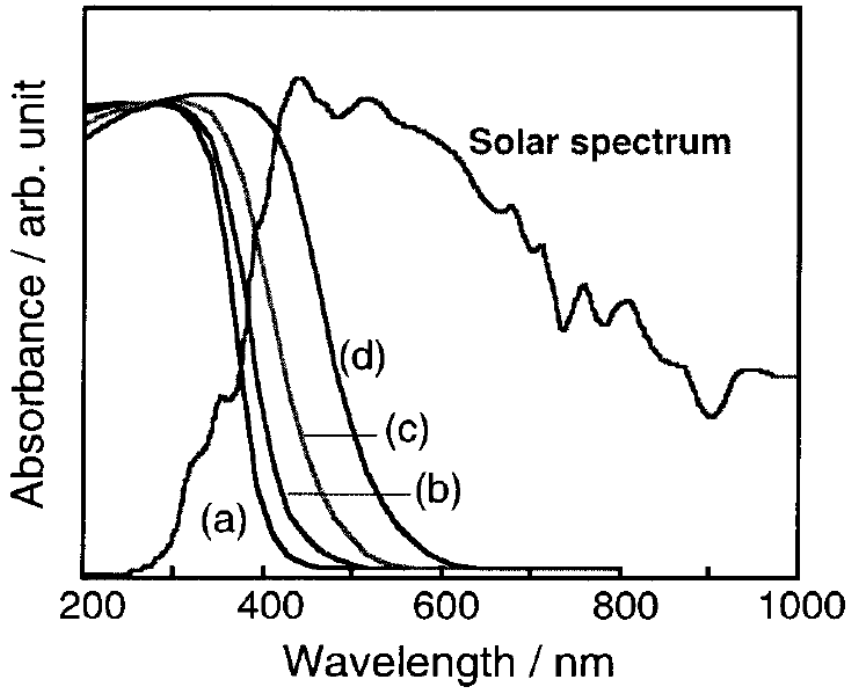

Figure 1.37. Diffuse reflectance UV-Vis spectrum of chromium loaded TiO_2. The band edge can be observed moving towards the visible region as Cr loading increases (a→d), due to the dopant altering the electronic structure.[55]

UV radiation can also be used to ionise electrons in a technique analogous to XPS, termed ultraviolet photoelectron spectroscopy (UPS), where an outer shell electron is ionised by the relatively low energy UV radiation. UPS is most often applied to the determination of the valence band edge,[56,57] however, Gall *et al.* used UPS in tandem with XPS to elucidate the valence band structure of ScN (Figure 1.38).[58]

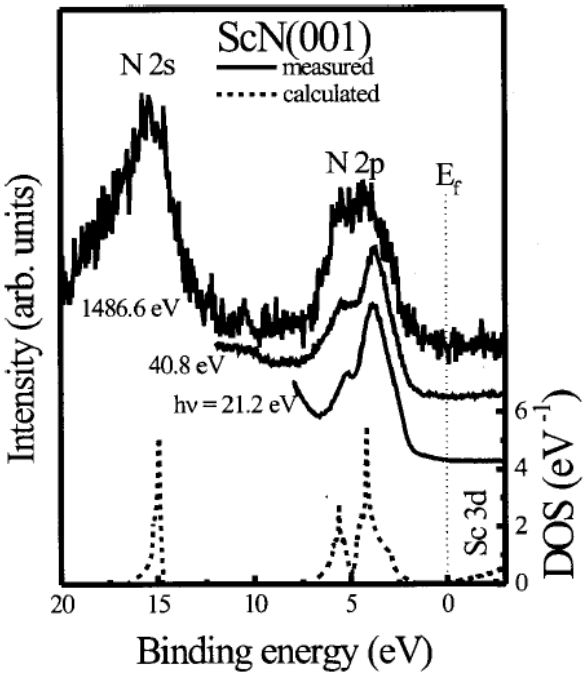

Figure 1.38. Combined UPS and XPS spectrum of the valence band structure of ScN. The calculated valence band structure is shown by the dotted lines.[58]

The application of some of these techniques will be discussed throughout the remainder of this thesis, with particular reference to doped TiO_2 nanomaterials.

1.6 Semiconductors

All materials can be classified by the size of the gap between the valence band and the conduction band, as conductors, semiconductors or insulators. The simplified band structures of the three materials are shown in Figure 1.39. In a conductor, the bandgap is non-existent, such as in metals, due to the overlap of the VB and CB. This allows for the flow of electrons without a potential barrier, which in turn gives rise to the conductive properties of metals. In insulators the bandgap is large (~> 4 eV) and cannot be easily surmounted. A semiconductor has a smaller bandgap (~< 4 eV) and,

when they are provided with a sufficient excitation energy, the energy gap can be bridged. Historically semiconductors have been called thermally dependent conductors, as thermal energy can be used to excite the electrons from VB to CB (discussed in Section 3.3), but the activation energy can also be supplied by photons through quantum transitions (discussed in Section 3.2). Photon activation of semiconductors is of great interest to green chemistry research as the quantum excitation process could be highly energetically effective as a free and unlimited supply of photons are available from the sun.

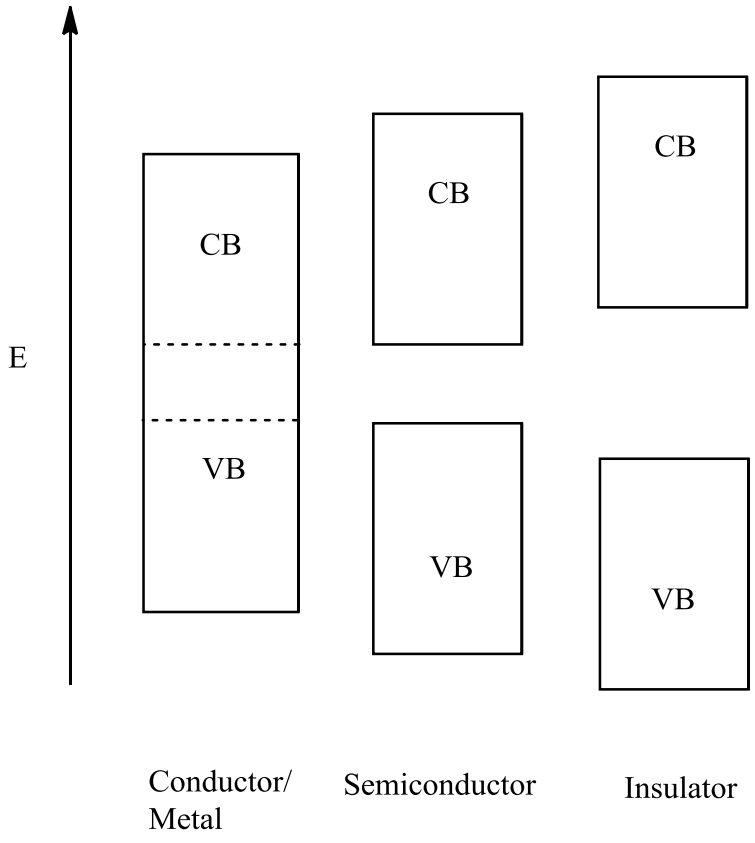

Figure 1.39. Bandgaps of insulators, semiconductors and conductors/metals. On the left the valence and conduction bands overlap, giving rise to high conductivity. On the right the gap between the CB and VB is large, making the excitation of electrons across the gap difficult, resulting in an insulator. In the middle, the semi-conductor has a small band-gap,

where electron transitions are possible with the input of energy, allowing for conductivity under activation conditions.

Within a semiconductor, the promotion of an electron creates a vacancy in the valence band and an electron in the conduction band. These are known as electron–hole pairs, also called the charge carriers, and can be used in various applications. The electron can be used for reductions and the hole can be used as an oxidant for chemical compounds. At any time, a number of electron–hole pairs are created while an amount will recombine, with a subsequent release of energy. At a given temperature formation and recombination will be in equilibrium, as determined by statistical mechanics, called the charge carrier concentration. This statistical distribution is the Fermi-Dirac distribution,

$$n_i = \frac{1}{e^{(ei-\mu)/kt}+1} \tag{1.14}$$

Where n is the population of electrons, e^i is the energy of a single electron, μ is the electrochemical potential, k is the Boltzman constant and t is the temperature. An increase in temperature shifts the equilibrium to further populate the conduction band with electrons. When the population of electrons in the conduction band reaches a critical point, a significant electrical current will be generated.

Fermi level and Fermi Energy

The Fermi energy is the energy where there is a 50 % chance that *fermions*, electrons in this case, will have the required energy to populate the conduction band. Figure 1.40 shows how the Fermi level changes with temperature. The Fermi level is a

hypothetical concept and as such does not have to be an allowed energy state. In insulators and semiconductors the Fermi level is found in the bandgap, where the density of states is zero. Fermi energy on the other hand is the highest occupied energy state at absolute zero temperature. The energy difference between the Fermi level and the vacuum level is defined as work-function which represents the energy cost for creating a free electron.

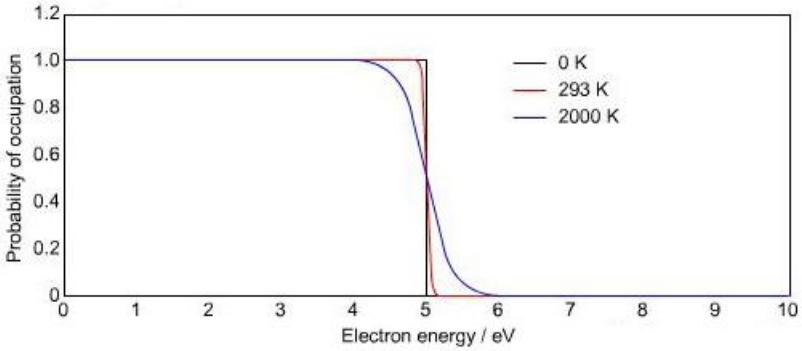

Figure 1.40. Fermi-Dirac distribution at several temperatures. This graph shows how the energy distribution of Fermions changes as the temperature increases. At higher temperatures (blue line) the distribution of Fermion energies is greater than at lower temperatures (red and black lines).[59]

1.7 History, Physics and Chemistry of TiO_2

TiO_2, or titania, is a well known and often used white pigment. The natural white colour is due to the fact that TiO_2 does not absorb in the visible light spectrum. Titania's use as a white pigment is, to this day, still one of its most common usages, being present in materials such as paints. Furthermore, titania's very low toxicity allows it to be used in food products, such as tablets and tooth whiteners; and is currently known as food number E-171.[60]

Paints containing TiO_2 were observed to be “flaky”, which prompted scientists to investigate the reasons why.[61] This flaking was due to the photocatalytic properties of TiO_2, absorbing light and photooxidising the polymer filler of the paint. This occurred because TiO_2 is a semiconductor and, in the presence of light of a suitable energy ($h\nu$), will excite an electron from the valence band to the conduction band.

Research into the field of TiO_2 photocatalysis did not take off majorly until 1972 when Fujishima and Honda discovered the photocatalytic splitting of water on TiO_2 electrodes.[62] Since then research has expanded in many areas including self-cleaning glass,[63] water purification[64] and degradation of organic compounds, the focus of this research.[65]

1.7.1 Crystal Phases of Titanium Dioxide

TiO_2 has three major phases: rutile, anatase and brookite. The rutile phase is both the most stable[34] and the most common naturally occurring polymorph, however, anatase and brookite are found in some deposits and can be produced synthetically. All three contain six-coordinate titanium; where rutile and anatase form tetragonal crystal structures while brookite is orthorhombic (Figure 1.41). Anatase and rutile are both distorted structures, with two of their six Ti-O bonds having longer lengths. The name anatase is derived from the Greek 'anatasis', meaning extension, because of its extended vertical axis. Brookite has a more complex structure with six different Ti-O bond lengths.[66,67]

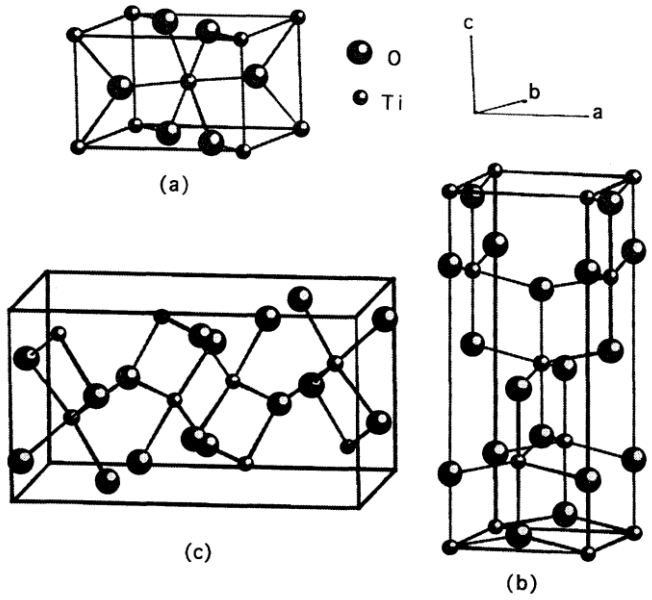

Figure 1.41. Crystal structures of TiO_2 phases. (a) Rutile, (b) Anatase and (c) Brookite. It can be seen that rutile and anatase have more regular crystal strctures than brookite. Anatase and rutile are orthorhombic with two lengths of Ti-O bond whilst brookite is tetrahedral with 6 different Ti-O bond lengths.[68]

Rutile is present in the ore ilmenite ($FeTiO_3$), where TiO_2 can be extracted, with up to 90 % purity by the Becher process (Scheme 1.2).[69] In this process, $FeTiO_3$ is oxidatively decomposed into TiO_2, forming Fe and CO_2 as side products.

$$4FeTiO_{3(s)} + O_{2(g)} \rightarrow 2Fe_2O_3 \cdot TiO_{2(s)} + 2TiO_{2(s)}$$

$$Fe_2O_3 \cdot TiO_{2(s)} + 3CO_{(g)} \rightarrow 2Fe_{(s)} + 2TiO_{2(s)} + 3CO_{2(g)}$$

Scheme 1.2. Extraction of TiO_2 from ilmenite in the Becher process. Ilmenite is decomposed under oxygen into Fe_2O_3.TiO_2 and TiO_2. The Fe_2O_3.TiO_2 is further purified under CO to produce pure TiO_2.

Anatase transforms into rutile, either directly or through brookite with an energy of -3.26 $kJmol^{-1}$ for a particle size of the mm order,[70] where the transformation energy is size dependent, due to surface free energy being a function of particle size.[71] The energy differences of the three polymorphs are small, due to their similar structures, and therefore they convert relatively easily. At macroscopic particle sizes, the stability is of the order rutile > brookite > anatase, however, at sub 11 nm sizes, rutile and anatase reverse stabilities and between 11 and 35 nm crystal size brookite is the most stable. Anatase will not transform into rutile at room temperature as it is kinetically stable; while exact temperatures depend on a variety of parameters including particle size, heating to 400-600 ℃ is often sufficient energy to facilitate this change.[34,72]

Table 1.2. -Ti-O bond lengths of the three polymorphs of TiO_2.

Scheme	Anatase	Rutile	Brookite
Ti-O Bond Length	1.949 (4)	1.937 (4)	1.87~2.04
(Å)	1.980 (2)	1.965 (2)	

The addition of dopants to TiO_2 has been observed to alter the transitions between the titania phases.[73] Adding dopants can provide more oxygen vacancies in a lattice, favouring the transition to rutile, whose less dense oxygen structure can more readily accommodate oxygen vacancies. Lattice substitution of Ti^{4+} with an M^{n+} dopant has been observed to mediate this change, where $n < 4$,[74–76] where such dopants include Li^{+}, Mg^{2+}, Co^{2+}, Ni^{2+} and Cu^{2+}. On the other hand if one were to decrease the oxygen vacancies, substituting with dopants with a valency $n > 4$, then the reverse would be

true. For example, in a phosphorous doped sample the onset of the phase change is delayed up to 900 °C.[77]

The measured band gaps for the rutile, anatase and brookite phases are slightly different at 3.00 eV, 3.2 eV and 3.4 eV for rutile, anatase and brookite respectively.[78] While rutile and brookite show direct bandgaps, the bandgap of anatase is indirect as there is a change in crystal momentum (*k*-vector).

In TiO_2, the top of the valence band is composed of O_{2p} orbitals and the bottom of the conduction band is two Ti_{3d} bands coming from the t_{2g} and 2_g states.[79] Theoretical calculations also imply that there is significant interaction between the O_{2p} and Ti_{3d} states.[73] Figure 1.42 shows the calculated density of states of the rutile, anatase and brookite phases of TiO_2.

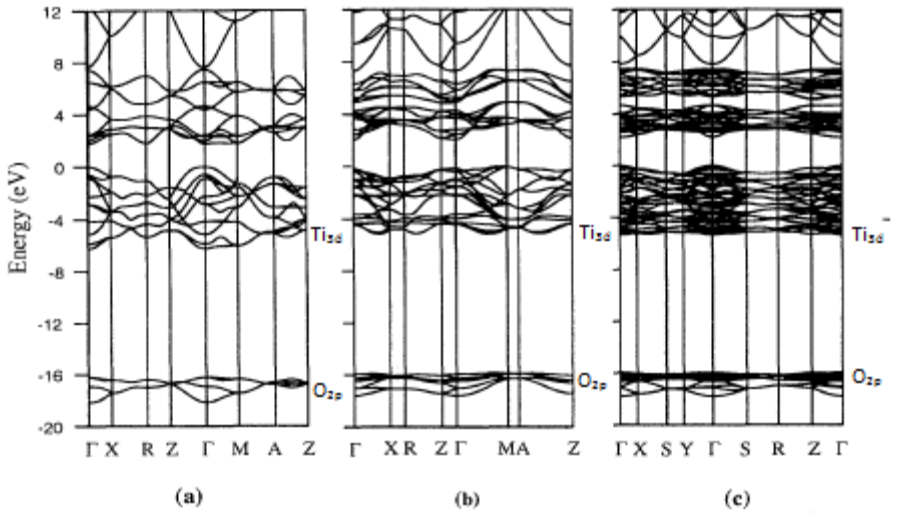

Figure 1.42. Density of states in (a) rutile, (b) anatase and (c) brookite. The DOS of brookie (c) is more dense due to the increase in regularity of the crystal structure.[68]

Anatase has been argued as the most photoactive of the three TiO_2 crystal phases,[68,80] and that the higher the composition of anatase phase the higher the

photocatalytic activity will be.[77] This may be due to the decreased rate of recombination arising from the indirect bandgap, however, the indirect bandgap could result in less efficient electron excitations, compared to rutile, as crystal momentum is not conserved.[81] Conversely, the smaller, direct bandgap of rutile may lead to increased efficiency of electron promotions but also increased recombination. Therefore, it is argued that the mixing of rutile with anatase, such as P25 (anatase 75%: rutile 25 %) offers the highest efficiency as a photocatalytic semiconductor, such as P25.[82] In these cases it is thought that the electron promotion occurs at the rutile phase, due to the lower excitation energy, and transfers to anatase, where the charge separation is stabilised.

1.7.2 Mechanism of TiO_2 Photocatalysis

During photocatalytic oxidation reactions involving TiO_2, radiation splits the electron–hole pair, where the hole creates OH radicals from hydroxyl groups and the electron reduces titanium from $Ti^{4+} \rightarrow Ti^{3+}$. Both of these reactions must take place simultaneously for the process to be considered catalytic. The bound OH radical can then proceed to oxidise organic compounds, and the Ti^{3+} species can react with O_2 to form super oxide, regenerating Ti^{4+}. Figure 1.43 shows a graphical representation of TiO_2 photooxidation, where the splitting of the electron-hole pair is observed under illumination corresponding to 3.2 eV (385 nm). The electron in the CB is then transferred to an oxidant and the hole accepts an electron from a reductant, resulting in its degradation.

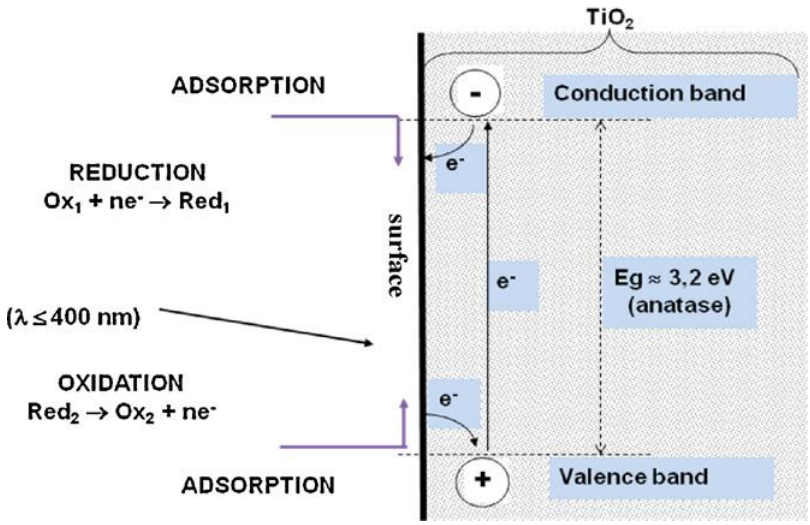

Figure 1.43. Diagram of TiO_2 energy plot showing its use as a photocatalyst. Upon radiation of a sufficient wavelength an electron is excited from the CB to the VB, leaving a hole in the former and an electron in the latter. The electron can be used for reductions and the hole can be used for oxidation of compounds, such as VOCs.[83]

Scheme 13 is the mechanism proposed by Hoffman of the steps that occur when TiO_2 is irradiated by light of a sufficient wavelength.

$$TiO_2 + h\nu \rightarrow TiO_2h^+ + e^- \qquad (a)$$

$$h^+ + Ti^{iv}OH \rightarrow [> Ti^{iv}OH \cdot]^+ \qquad (b)$$

$$e^- + Ti^{iv}OH \leftrightarrow [> Ti^{iii}OH] \qquad (c)$$

$$e^- + > Ti^{iv} \rightarrow Ti^{iii} \qquad (d)$$

$$h^+ + [> Ti^{iv}OH \cdot]^+ \rightarrow Ti^{iv}OH \qquad (e)$$

$$e^- + [> Ti^{iii}OH] \rightarrow Ti^{iv}OH \qquad (f)$$

$$[> Ti^{iv}OH \cdot]^+ + VOC \rightarrow > Ti^{iv}OH + VOC \cdot^+ \qquad (g)$$

$$Ti^{iii}OH + O_2 \rightarrow Ti^{iv}OH + O_2^- \cdot \qquad (h)$$

Scheme 1.3. Hoffmann's proposed mechanism of photooxidation by TiO_2. > denotes surface groups.[4] Scheme 1.3(a) is the charge-carrier separation, creating the electron-hole pair. Scheme 1.3(b), (c) and (d) are the trapping processes of the electron and the hole at the surface of TiO_2, on surface bound hydroxyl groups. Steps (b) and (c) are shallow electrons traps, and (d) is a deep electron trap from the reduction of Ti^{4+} to Ti^{3+}. Scheme 1.3(e) and (f) are the recombination reactions of the electron-hole pair, regenerating the initial TiO_2. Scheme 1.3(g) and (h) are the interfacial charge transfer reactions, where the electron and hole reduce and oxidise compounds respectively.

The inherent drawback in these processes is that the charge trapping and charge recombination processes are fast (ps-ns) compared to the charge transfer processes (ns-ms). To keep the charges separated for as long as possible, an electron acceptor is usually required, which is often dioxygen. Because of the role it plays in delaying recombination, the electron acceptor has an effect on the activity of the catalyst.[84]

It is currently unclear whether the oxidation occurs *via* a surface hydroxyl group, a free hydroxyl group[85] or by direct band oxidation. TiOH radicals have been observed by EPR,[86] which gives credit to a mechanism involving surface hydroxyl radicals, however, Mao *et al.* found no abstractable OH groups from which to create surface hydroxyls,[87] evidence for direct bandgap oxidation.

During the charge separation process hydrogen peroxide can be formed, from the CB electron and the VB hole, which will propagate the creation of more hydroxyl radicals (Scheme 1.4),[88] as it can be split by UV light.[89] However, not only can H_2O_2 be formed from O_2, it can also act as an O_2 source[4] and trap electrons on the surface of the catalyst, retarding recombination.[90]

$$O_2 + 2e^- + H^+ \rightarrow H_2O_2 \qquad (a)$$

$$2H_2O + 2h^+ \rightarrow H_2O_2 + 2H^+ \qquad (b)$$

Scheme 1.4. (a) Creation of H_2O_2 from the electron. (b) Creation of H_2O_2 from the hole.

To be an efficient photocatalyst for photooxidation of VOCs the CBM must be of a more negative potential than the species to be reduced and the VBM must have a more positive oxidation potential than the species to be oxidised. As Figure 1.44 shows, the CBM and VBM of TiO_2 lie at ~ -0.25 eV and ~ 3.00 eV respectively at pH 0, referenced to normal hydrogen electrode (NHE). In comparison, H^+/H_2 and H_2O/O_2 lie at 0.00 and 1.20 eV respectively, *vs.* NHE.

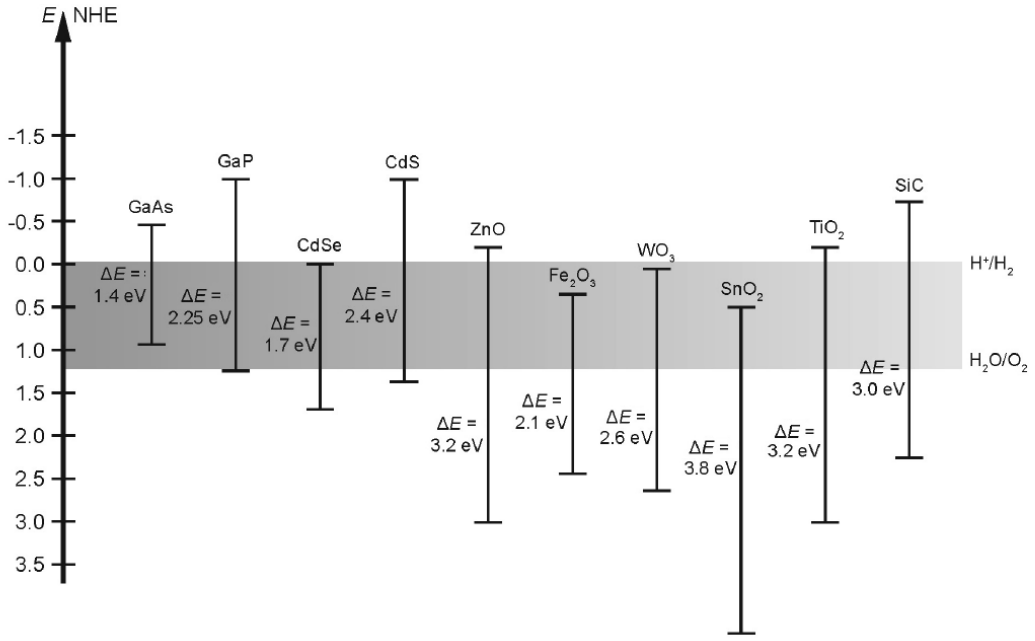

Figure 1.44. The bandgaps and VBM and CBM of the most common semiconductors referenced to normal hydrogen electrode (NHE). Measurements were made in an aqueous solution of pH 1.[91]

1.8 Practical Considerations and Applications of TiO_2 Photocatalysis

A suitable photoreactor is required in order to investigate the photocatalytic efficiencies of TiO_2. These reactors can either be designed for liquid phase or gas phase reactions, where each are discussed in the following sections. During both applications a catalyst is exposed to a pollutant and the change in concentration over time is measured. This can be accomplished in several ways: by directly following the decrease in concentration of the target VOC, or indirectly by recording the different rates of VOC build-up when the system is activated and deactivated, as applied in this research. Another indirect measurement is to follow the increase of the mineralisation products CO_2 and H_2O. The measurement methods can be split into two groups; in line sampling and periodic sampling, where the most frequently used are; FT-IR spectroscopy, UV-Vis spectroscopy, GC-MS or HPLC. Typical VOCs used in photocatalysis include ethanol, toluene, acetone, nitric oxide and organic dyes. Decisions of VOC are based on toxicity, ease of availability, ease of degradation and ease of following the photooxidation.

1.8.1 Liquid Phase

Photoactive catalysts are often used to treat water for environmental remediation and the provision of clean drinking water to communities where it is otherwise unavailable, for example the Stream Cleaner, an applicant for the 2012 James Dyson award that uses photocatalysed semi-conductors to provide safe drinking water.[92] The first documented example of water treatment with photoilluminated TiO_2 was in 1976[93] and then again in 1983 by Ollis,[94,95] however, many other research groups have also shown the efficacy of TiO_2 in this application.[96,97] A typical set-up is composed of a

glass container containing a polluted solution, into which a nanomaterial catalyst is placed. The solution will be irradiated, and the concentration of the pollutant measured as a function of time during catalyst activation, in order to calculate the rate of removal of the pollutant. Data from liquid phase reactors can be readily obtained as the contents of the reactor are static, and the initial concentration is constant and known. Furthermore, good contact between pollutant and catalyst can be achieved by good mixing of the reactor, however, this leads to issues of separation at the end of the remediation, usually involving a filtration step to remove the catalyst from the solution.

1.8.2 Gas phase

In this project only gas phase decomposition of VOCs was investigated. There are several differences between liquid phase and gas phase heterogeneous catalysis. In research, liquid phase reactors are static while gas phase are continuous flow. Continuous flow reactors have several additional disadvantages compared to liquid phase catalysis such as pressure drop and catalyst/pollutant contact time; however, there is little need for a separation step at the conclusion. In gas phase catalysis the challenge is to create a reactor that maximises the contact between the polluted gas stream and the catalyst. To achieve this reactor designs often contain a bottle neck where the gas is forced to flow over or through the catalyst. However, creating a catalyst bottle neck that is too dense will change the pressure on either side of the reactor leading to a stymied flow of gas – a pressure drop. Because of this, reactor design is paramount to catalytic success.

Numerous research groups have designed gas reactors for use in photocatalytic degradation.[98–106] Although scales and details change, the typical design is the same. A

gas supply is used to carry the VOC through the reactor (sometimes this is the VOC itself), a VOC reservoir, a reactor bed containing the catalyst, a UV light source and a detection method. Oxygen needs to be supplied to the reaction to allow for mineralisation, this can be from an O_2 or compressed air source, but other oxygen sources, such as H_2O_2, can be used. Catalyst beds come in many designs all of which attempt to provide the maximum catalyst surface and VOC contact. Figure 1.45 shows two examples of such reactors. A. is a coaxial, two tube system, with a minimum gap between the inner and outer tubes, and B. is a packed flat bed reactor.

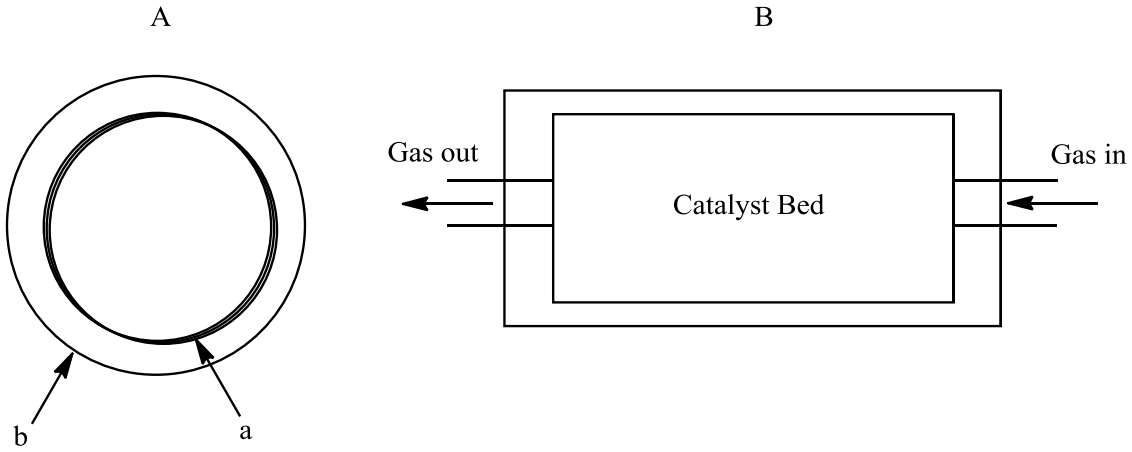

Figure 1.45. A. Coaxial design reactor. a. is the inner tube with an outside coating of the catalyst and b. is the outer tube. There is a gap of *ca*. 3 mm through which the polluted gas flows. B. Generic flat bed reactor design whereby the VOC is forced to run through the catalyst.

In this thesis a quartz tube reactor bed loaded with the catalyst and fixed in placed with glass wool has been used. This set-up was chosen as it offered the benefits of complete transparency to UV light in addition to high contact between catalyst and gas stream due to the efficient loading of catalyst forcing the gas stream to flow through it. A detailed description of the photoreactor used in this work is discussed in Section

7.3. In the following chapters the photocatalytic reactor was used to analyse the efficiency of TiO_2, CoO and $Co_2(PO_4)_3$ nanomaterials in the degradation of a target VOC. The efficacy of the catalysts is assessed based on the electronic and morphological structure of the catalysts, as determined by analytical techniques such as XRD, SEM and FT-IR.

2. Preparation of Nanostructured Materials *via* Electrospinning

Morphologically, powders are the simplest nanomaterial. The most well-known powdered, metal oxide semiconductor nanomaterial, with high photoactivity, is P25, which exists as a 75 % anatase: 25 % rutile mix. While nanopowders will most often give rise to the largest surface area, the possibility of precise control of the electronic properties and chemical reactivities has offered greater opportunity for other nanomorphologies.

In this chapter, the most common preparation methods of nanomaterials are reviewed with particular respect to their ability to produce consistent nanomaterials, with a high level of control of the morphology and loading of dopants. I then present my results on the investigation of extrinsic and intrinsic electrospinning variables, which have been systematically investigated as a function of mean fibre diameter. As the size can dramatically change the activities of nanomaterials, the mean fibre diameter is an appropriate measurement of quality of production. The metal oxide fibres were synthesised using a polymer solution as a carrier for the metal oxide precursors through the electrospinning process. Once formed, the polymer metal ion fibres were calcined at high temperatures to give rise to metal oxide nanofibres.

Here, I have investigated the degradation process of PMMA by FT-IR and UV-Vis spectroscopies and DSC. Through these techniques, the conversion and polymer decomposition processes were monitored in order to elucidate the details of the temperature dependent formation mechanism of metal oxide nanofibres.

Finally, the photocatalytic activity of the metal oxide fibres has been investigated as a function of calcining temperature, by powder X-ray diffraction. The

setup for the photocatalytic activity measurements is detailed in Section 7.3 and the details of the quantitative analysis are discussed in Section 7.4.

2.1 Overview of the Preparation of Nanomaterials

Due to the strong correlation between the length scale and morphology of nanomaterials and their electronic properties, the desire to effectively control their physical parameters becomes essential. There are many different morphologies of nanomaterials aside from the aforementioned powders. Spheres and crystals are morphologically similar to powders. Nanotubes, nanorods and nanofibres are all morphologies that are elongated along one axis. Novel nanomorphologies have also been observed, for example flowers. To produce these morphologies there are many methods available with three types of method, bottom-up, top-down and templating. The most common preparation methods are discussed below, with respect to the morphologies that they can produce and their ability to produce uniformly doped materials. The importance of doping is that the addition of an extra atom can alter the electronic properties, and therefore reactivities, of the material, giving rise to enhanced activity, as discussed in Section 1.4.

2.1.1 Anodisation

Anodisation is a top-down method of nanomaterial preparation which can yield highly ordered, closed bottom nanotubes. Because of the vertical alignment, nanotubes have applications as electrodes and for electron transport. Anodisation allows for control of the physical dimensions of the nanotubes by altering variables such as

electrolyte, current, current stability, voltage and pH.[107] Careful control of these variables is required to produce consistent tubes. In our laboratory, it has been shown that altering the voltage over the course of preparation can result in novel, tapered morphologies, such as nanobottles.[108]

Anodisation, or anodic oxidation, is an electrolytic process for the formation of metal oxides on a surface, whereby the substrate surface becomes the anode in an electrical circuit. A titanium cathode is placed into a fluoride containing electrolyte with an organic solvent (often ethylene glycol) where a current is passed though, creating TiO_2 on the cathode surface. A typical experimental set-up for anodisation is depicted in Figure 2.1. The purpose of the fluoride ion is to create nanotubes by electrically directed etching into the surface (anode) of the created 3D structures.[109] The purpose of using ethylene glycol is to reduce the overall anodisation speed and to balance the kinetics between the dissolution of the metal oxide and the oxidation process. Because of this mechanism nanotubes can be made from only certain materials, based on the stability of the metal oxide formed.

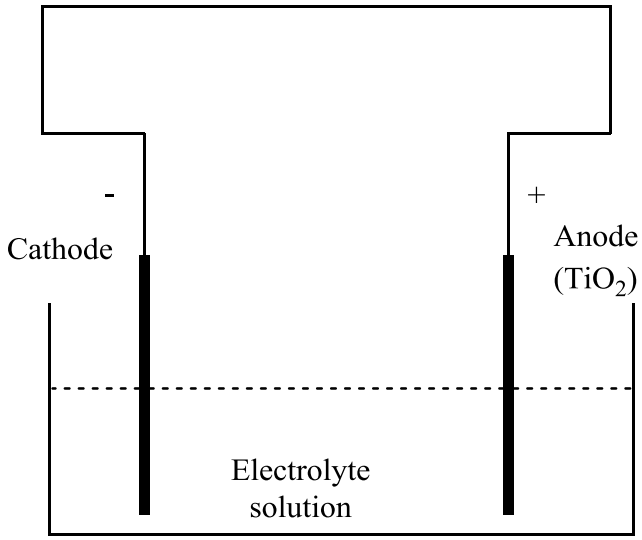

Figure 2.1. Diagram of a two electrode electrochemical cell for the anodisation of TiO_2 nanotubes. The TiO_2 anode and the cathode create an electrical circuit where the electrolyte completes the cicuit. This causes etching into the TiO_2 surface, creating nanotubes.

The electronic structure of the formed TiO_2 nanotubes can be adjusted by introducing a dopant. Such dopants can, in principle, be introduced by adding relevant chemical elements into the anodisation solution. During the anodic oxidation the dopants, Al, Si, Cr, Mn, Mo and Sn, were each incorporated into TiO_2 nanotubes, *via* the electrolyte solution. Despite identical initial concentrations, XPS analysis revealed that the dopants were not present in the nanotubes in the same concentration, highlighting that controlled doping is still a technical challenge for anodisation.[110]

2.1.2 Hydrothermal

The relatively low production rate of nanomaterials by anodisation can be overcome by using hydrothermal synthesis. Hydrothermal synthesis, a bottom-up approach for creating nanomaterials, can be used for bulk synthesis. It can not only

produce large, well defined crystals, but can also be used in the formation of nanorods,[111] nanotubes,[112] nanospheres[113] and nanowires.[114] Furthermore, hydrothermal synthesis can be used to produce meso- and micro-porous materials, such as zeolites.[115] While there is no agreement on the exact definition of hydrothermal synthesis, in general it is the crystallisation of a material from a solvent at higher than ambient temperature and pressure, by auto-clave. Figure 2.2 depicts a typical auto-clave. Inside the auto-clave, the crystal material is dissolved in a solvent and a heat gradient is applied, which forces the material to crystallise at the cooler end.

Figure 2.2. Photograph of a typical autoclave, taken at University of Sussex 2013.

This technique is exceedingly useful for producing large quantities of crystalline material. It is commonly seen forming naturally occurring ores, and has been used to synthetically produce 100 kg of quartz.[116] As well as crystals, sodium titanate and TiO_2-β, a meta-stable polymorph of TiO_2, nanorods have been produced, from $TiO_2 \cdot nH_2O$ in aqueous NaOH at up to 200 ˚C, in an autoclave.[111]

The hydrothermal method can also be used for introducing dopants as they can be well dispersed in the solvent. This allows for control of bulk dopant loading. Metal

ions of cerium, copper, iron, manganese, silver and zinc were dissolved in a hydrothermal precursor and annealed after reaction in an autoclave.[117] Similar methods have been used to create highly dispersed tungsten[118] and iron[119] loaded TiO_2. Doping by the hydrothermal method can also be performed post-formation in order to coat the surface. Nanotubes, nanorods and nanowires prepared by hydrothermal treatment were doped by the intercalation of methanol into the samples, followed by annealing under a nitrogen atmosphere.[120] The lack of oxygen forced the methanol to decompose into carbon rather than complete mineralisation. It was found that the carbon had doped into the titania lattice but with a clear difference between surface and bulk composition, highlighting the incomplete control of doping using this method.

It is the necessity of the auto-clave as specialist equipment which is the largest disadvantage of this production method. However, for the synthesis of metal oxide nanomaterials, a low temperature range (150-350 ˚C) is required, much lower than for other preparation techniques, such as CVD.

2.1.3 Chemical and Physical Vapour Deposition

Chemical vapour deposition (CVD) is used to make a variety of nanomaterials including tubes,[121] wires[122] and flowers.[123] A chemical precursor is heated to evaporation and deposited on a hot substrate (Figure 2.3), which will then decompose and form thin films on the substrate. Furthermore because of the high temperatures used and the gas flow, any volatile by-products are often removed, allowing the production of high purity nanomaterials, which is essential for good control of the electronic structure. This method was used by Pilkington to prepare Pilkington Activ self-cleaning windows,[124] where TiO_2 is distributed over a large surface area in a consistent coating.

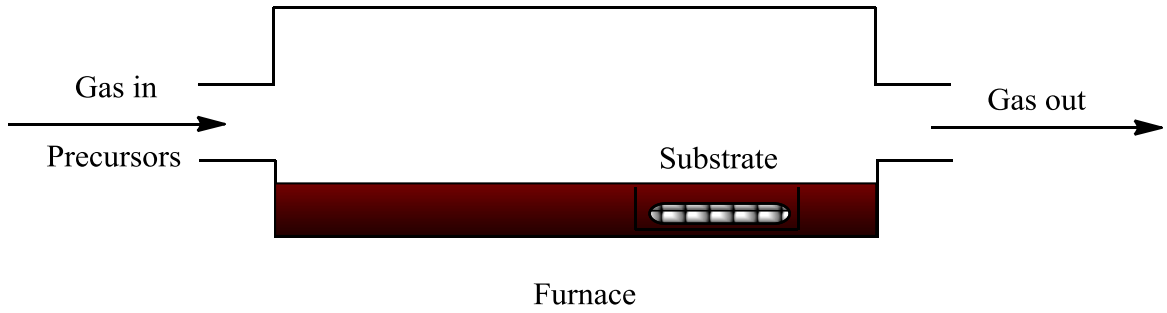

Figure 2.3. Diagram of chemical vapour deposition. In the tube is a substrate contained within a crucible. The tube is heated an a precursor is added by carrier gas, and is then deposited onto the substrate. This can create novel morphologies, such as flowers, aswell as thin films.

Sarantopolous found that controlled nitrogen doping of TiO_2 could be achieved by using TTiP and NH_3 as metal organic precursors, and controlling the mole fraction of NH_3 and temperature of reaction.[125] Nitrogen has also been employed in titania doping by using an organometallic precursor, such as titanium-amide guanidinates.[126] This intrinsic doping allows for only one precursor and enhanced control of the loading.

Similar to CVD, is physical vapour deposition (PVD), which uses a thermally stable precursor so that there is no chemical transformation after evaporation. The lack of chemical transformation allows for the use of lower temperatures, reducing the risk of product decomposition[127] and permits the use of temperature sensitive materials as substrates. The low temperature can decrease the adhesion between the substrate and the product.[128]

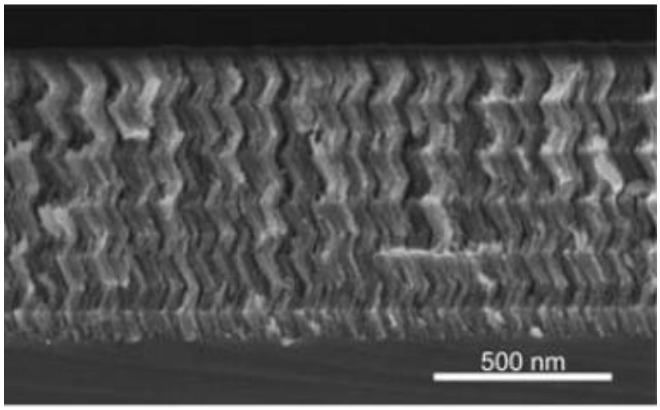

Figure 2.4. SEM image of alternate TiO_2 and SiO_2 layers.[129]

Both CVD and PVD allow for the preparation of large quantities of thin film nanomaterials, and can create layered products, such as alternating layers of TiO_2 and SiO_2 (Figure 2.4). However, CVD and PVD are not without their disadvantages as both can only produce a limited number of morphologies. Moreover they also require laborious control of both extrinsic and intrinsic variables such as; temperature, vacuum system, concentration, substrate, initiation method and reaction time, all of which will affect the resultant product.

2.1.4 Sol-Gel

The sol-gel methodology is a templating method for the production of a multitude of nanomaterials. A sol-gel is a biphasic system of a solid in a solution, resulting in a gel (contracted to sol-gel). The mixture of a solid in a solution allows the formation of 3D polymer networks, from which porous materials can be created. Once the 3D polymer network is formed the liquid phase must be removed, where methods commonly used for removal are; evaporation, centrifugation, supercritical drying or simply decanting. Once the solid phase has been isolated a thermal treatment is

typically required, to stabilise the structure, remove unwanted side-products and to crystallise the product.

Sol-gels were first reported in 1845 by Ebelman[130] and were further developed by Berger and Geffen in 1939.[131] The first known use of sol-gels for the production of fibres was in 1982, when Sakka produced fibres of glass from TEOS, a common precursor for the preparation of glass materials from sol-gels.[132] At around the same time, Barringer and Bowen showed that nanoscale TiO_2 can be made from these precursors.[133] Since then sol-gels have been used extensively as they are a desirable way to produce a range of materials including glasses,[134–136] ceramics[137] and metal oxides.[138] More recently sol-gels have been used to produce a wide range of materials including nanorods,[139] nanowires,[140] nanotubes[141] and nanofibres.[142] To form metal oxide nanomaterials, typically metal alkoxides or chlorides are used, for example TiO_2 nanorods were created by dipping anodic alumina membranes into a titanium tetra isopropoxide (TTiP) sol-gel before being dried and heat treated.[139] Using the same technique it can in principle form rods with any metal oxide composition with the correct precursor. The only limitation is that it can only form rod-like structures with random orientation.

Because of the liquid precursor, homogenous distribution of dopants can be achieved making them an excellent precursor for the investigation of doped nanomaterials. For example it has been shown that a multitude of metals can be impregnated into nano-TiO_2 by the sol-gel process, including copper, iron and aluminium.[143]

2.2 Preparation of Nanofibres by Electrospinning

In this project, we used electrospinning of a polymer solution (PMMA in DMF) to create metal oxide nanofibres. This morphology was chosen because nanofibres offer the possibility of mechanical strength, large surface area to volume ratio and the possibility of forming nonwoven mats with good gas penetration, which is an advantage for industrial gas-solid reactors. The electronic properties, and therefore reactivities, of nanofibres can be easily adjusted by control of the electrospinning variables and the doping concentration in the original polymer solution, which will be homogeneously dispersed.

2.2.1 History, Chemistry and Physics of Electrospinning

Electrospinning is an evolution of electrospraying that uses more viscous solutions, where the surface tension is greater than the electric field, so that fibres are produced instead of the mist that is generated when the surface tension is low. The first documented example of electrospraying was in the early 20th century, where it was noticed that in the presence of an electric field liquid surfaces behave strangely.[144]

Taylor described the equilibrium extracting force, *P*, as shown in Equation 2.1.[145]

$$P = 2\pi RT\cos\phi + w - \pi R^2 p \qquad (2.1)$$

Where *w* is the weight of the fluid above the nozzle, *p* is the pressure applied on the solution within the nozzle, *T* is the surface tension, ϕ is the angle between the fluid surface and nozzle wall, which defines the shape of the meniscus, and *R* is the radius of the nozzle. It defines the relationship between surface tension and applied pressure. In

our experiments, *w* becomes negligible as the syringe is horizontal, and *p* is determined by the rate flow of the syringe pump.

Electrostatic pressure (*p*) is balanced with the surface tension of a droplet. When an electric field of high enough strength is applied, it causes a rupture in the liquid surface which alters the radius of the droplet. This draws out a fibre which, because of its instability, breaks down into minute droplets. In the presence of an electrical field the equilibrium position of a liquid drop will become cone shaped, called a Taylor cone.[146]

When the voltage at the drop exceeds a critical value related to the surface tension, a liquid jet will start at the vertex of the cone. To maintain the Taylor cone, more solution needs to be supplied at the same rate as the expulsion of matter from the jet. The reason for the difference between fibre formation and spray formation is that the surface tension of a liquid is low enough that the jet is broken down into a fine spray by the applied voltage. When electrospinning the surface tension is high enough that the jet does not get broken down by the electric field, only warped, and the expulsion remains as a jet.[147] Hendricks *et al.* calculated the minimum spraying potential for a system where, above this potential, the droplet becomes unstable and can be spun into fibres.[148] Equation 2.2 describes the relationship between the voltage bias, surface tension and droplet radius.

$$V = \sqrt{200\pi\gamma R} \tag{2.2}$$

Where V is voltage in volts, γ is surface tension in dynes/cm and R is the droplet radius in cm. From Equation 2.2 it is clear that a large bias voltage will draw large solution droplets, resulting in larger diameter fibres. Once the solution is extruded from the syringe, it will be stretched into nanofibres due to the electrical field. The stretching

process follows the mass, charge and momentum conservation laws in agreement with steady state fluid dynamic theory as established by Feng.[149] Mass conservation requires that

$$\pi r^2 v = Q \tag{2.3}$$

where v is the linear stretching rate, r is the diameter of the fibre and Q is the volume flow rate. Q is assumed to be constant because of the force of the syringe pump, however, this may not be true if the delivery rate is higher than the flow rate determined by the stretch rate. If this is the case, then excess solution can accumulate at the nozzle tip, where the concentration will increase due to the solvent evaporation, leading to nozzle blockages and control of the solution composition may be lost.

The fibres become spun as, after the initial electrical potential has been exceeded, perturbations in the charges in the jet cause the fibres to repulse each other constantly, in a manner that forces the fibres to spiral away from the preceding fibres. As the jet gets longer and thinner, these spirals become more spaced out. Electrospinning is an example of Earnshaw's theorem as a collection of point charges cannot be held together by electrostatic forces alone.[150] After the formation of the original droplet, it was found that because of the electrical forces at work, very little depends on aerodynamics or the gravity of the Earth.

Since the technique has been well established, many research groups have focused their efforts towards investigating the effects of the parameters on the morphology and formation of nanofibres. Correlation between the variables has been observed as early as 1955, where a change in morphology of the jet was observed as voltage was increased.[151] The increase in fibre diameter with increasing solution viscosity was first observed by Baumgarten in 1917,[147] and expanded on by Beck-Tan

et al. and Gupta *et al.* who both established a link between solution concentration and fibre diameter.[152] Both investigations showed a power law increase of fibre diameter with concentration, Gupta *et al.* suggested that the exponent was 3.1 for PMMA in DMF[153] and Beck-Tan quoted 0.5 for PEO (poly ethylene oxide) in water.[152] There is also a strong link between polymer concentration and viscosity, where a power law dependence is observed, however, a biphasic system is usually observed, where the dividing point is called the critical chain overlap concentration c*. The critical chain overlap concentration is the concentration where the polymer solutions transition from dilute to semi-dilute un-entangled (Figure 2.5), and can be estimated by

$$c^* \sim \frac{1}{[\eta]} \tag{2.4}$$

where $[\eta]$ is the intrinsic viscosity, as is calculated from the Mark-Houwink-Sakurada relationship for a given molecular weight.

$$[\eta] = KM^{a} \tag{2.5}$$

Where *M* is the molecular weight and *K* and α are the Mark-Houwink parameters.

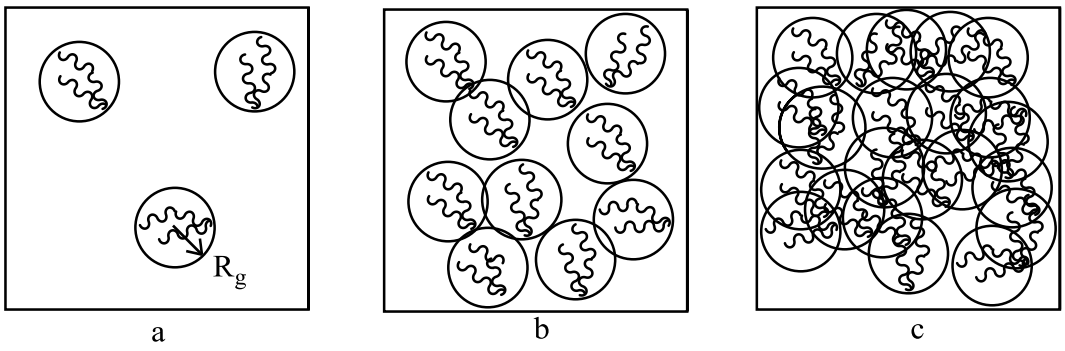

Figure 2.5. The different polymer concentration regions are shown in boxes a, b and c. Wavy lines are polymer chains and the spheres are the radius of gyration for the chains, a) dilute, $c < c^*$, b) semi-dilute un-entangled, $c > c^* > c_e$, c) semi-dilute entangled, $c > c_e$.

Gupta *et al.* found the critical chain overlap concentration to occur at 3.5 %, while Beck-Tan *et al.* found this concentration to be 4 wt. %.[150,151] Gupta *et al.* proposed that critical chain entanglement is observed when $c/c^* > 6$. Gupta *et al.* and McKee *et al.* published exponents of 0.65 and 1.5 respectively for the semi-dilute un-entangled region,[153,154] while Gupta *et al.* and Colby *et al.* published exponents for the semi-dilute entangled region as 5.3 and 4.8 respectively.[153,155]

The increase in viscosity of solution as the polymer concentration increases is due to certain properties of polymers that set them apart from non-polymers, these are all related to the fact they have large molecular weights.[156,157] These properties are: 1) Chain entanglement, where the polymer chain can entwine with either another part of the same chain or a separate chain, this makes the polymer more rigid in the solid state. 2) Summation of intermolecular forces, whereby the force interaction that polymers experience is amplified by the size of the chain. 3) Time scale motion, which is the polymer slowing the flow of the solvent. It is the interactions, overlap and

entanglement, of the polymer chains that determines the solution viscosity, where low levels of interaction are expected not to form fibres during electrospinning.

2.3 Controlling the Parameters of Electrospinning

PMMA in DMF was chosen as a model system to analyse the extrinsic processing variables of nozzle diameter, applied voltage and nozzle tip to collector distance, and the intrinsic variables of viscosity and concentration. As the morphology of metal oxide nanofibres is determined by the PMMA nanostructure, a deeper understanding of the formation of titanium dioxide nanofibres is gained from knowledge of the effects of the parameters. The intrinsic variables are those that depend on the solution, such as concentration and viscosity, while the extrinsic variables are processing parameters, such as applied electric field, nozzle diameter and nozzle tip to collector distance. To understand the individual influence of the parameters, only one was altered at a time, keeping the rest constant. These parameters were investigated with respect to the homogeneity of the morphology, fibre diameter, and the distribution of fibre diameters. The error bars in the fibre diameter plots correspond to the fibre diameter distribution.

The viscosity of the solutions at different concentrations was measured at room temperature using an Ostwald viscometer (PSL tube viscometer, BS/U type) with a 4 mm capillary. Glycerol was used to calibrate the viscometer. To determine the reproducibility and the consistency of the observed viscosity, measurements were repeated twice. From this, the kinematic viscosity (the ratio of viscosity to density) was calculated,

$$\eta_x = \eta_g(\frac{t_x\rho_x}{t_g\rho_g}) \quad (2.6)$$

where ρ is density (g ml^{-1}), η is viscosity (mPa·s) and t is time in seconds. Pure DMF was used as the zero measurement and glycerol (g) was used as the standard.

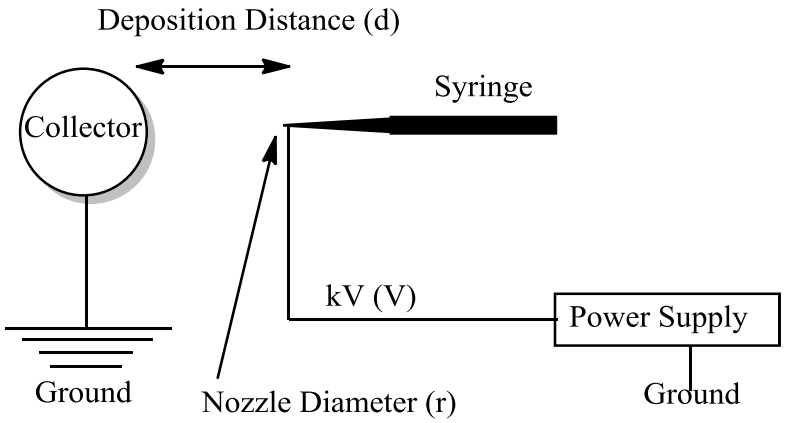

Figure 2.6. Schematic representation of electrospinning apparatus. The extrinsic variables which are examined are labelled on the diagram.

Our electrospinning experiments were performed using the set-up shown in Figure 2.6. We used a syringe nozzle diameter of 1.0 or 1.5 mm, with a volume flow rate of 1 ml/hr. Unless specified otherwise a 7 wt. % PMMA in DMF solution was used, with 0.15 wt. % acetyl acetone to encourage uniform spinning. Acetyl acetone is a chelating agent, which occupies any vacant sites on the metal precursor, raising the coordination number of TTiP from four to six. The titanium acetyl acetone complex is more soluble in organic solvents than TTiP, and therefore more likely to remain in the liquid phase. This results in the reduction of blockages in the nozzle and ensures that all the titanium precursor is used.[158,159] This viscosity of a typical electrospinning solution was 9.9 mPa.s. Unless specified otherwise, the applied voltage was set at 25 kV and nozzle tip to collector distance was set at 25 cm.

Post electrospinning the fibres were steam treated to convert any remaining titanium precursor to low vapour pressure titanium hydroxide in order to minimise loss of titanium components during the subsequent drying at 100 °C. The details of the calcination process are discussed in Section 2.4.

2.3.1 Extrinsic Variables

Nozzle diameter

Fibre diameter was investigated as a function of the diameter of the syringe nozzle diameter (*r*). The results show that as nozzle diameter increased, the mean fibre diameter increased (Figure 2.7), although there is a large variation in fibre diameter until the nozzle diameter was reduced to 0.5 mm. Using a 0.3 mm diameter nozzle, the average fibre diameter was found to be 420 ± 97 nm. The largest deviation was observed when electrospinning from a 0.5 mm nozzle, where the mean fibre diameter was found to be 605 ± 297 nm, evidencing that little control of fibre size is obtained using that nozzle size. Mean fibre diameters were found to be 875 ± 198 and 805 ± 212 nm for 1.0 and 1.5 mm nozzle diameters respectively. This is in contrast to Macossay *et al.* who found no correlation between nozzle diameter and fibre diameter, however, they did agree that the deviation of fibre diameter decreases for smaller nozzle diameters.[160]

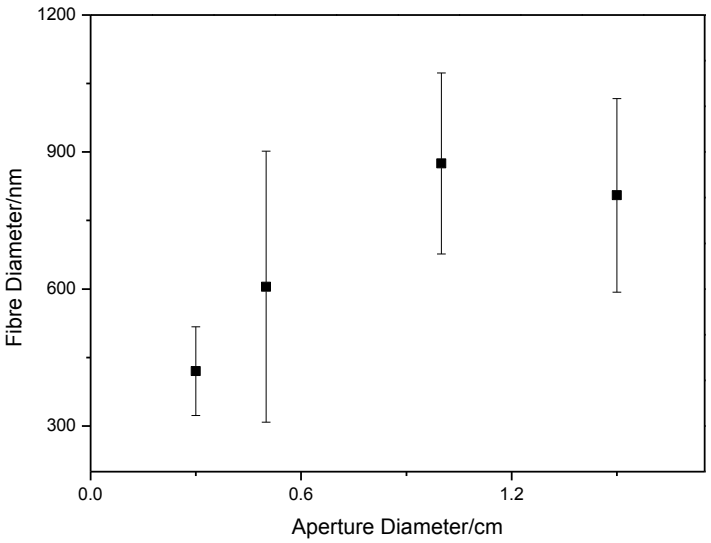

Figure 2.7. Mean fibre diameter as a function of nozzle diameter. The error bars represent the distribution function of the fibres.

When the nozzle diameter is large, the volume rate of extrusion of the polymer solution is increased leading to a large range of fibre diameters being produced. There is also less physical size restriction from the apparatus, which leads to less control of fibre diameters. This physical restriction explains the narrower distribution of fibre diameters when nozzle diameter decreases to 0.5 mm. It is also found that with a nozzle diameter larger than 1.0 mm with a solution of 7 wt. % PMMA and 10 wt. % TTiP resulted in minimum blockages during the electrospinning.

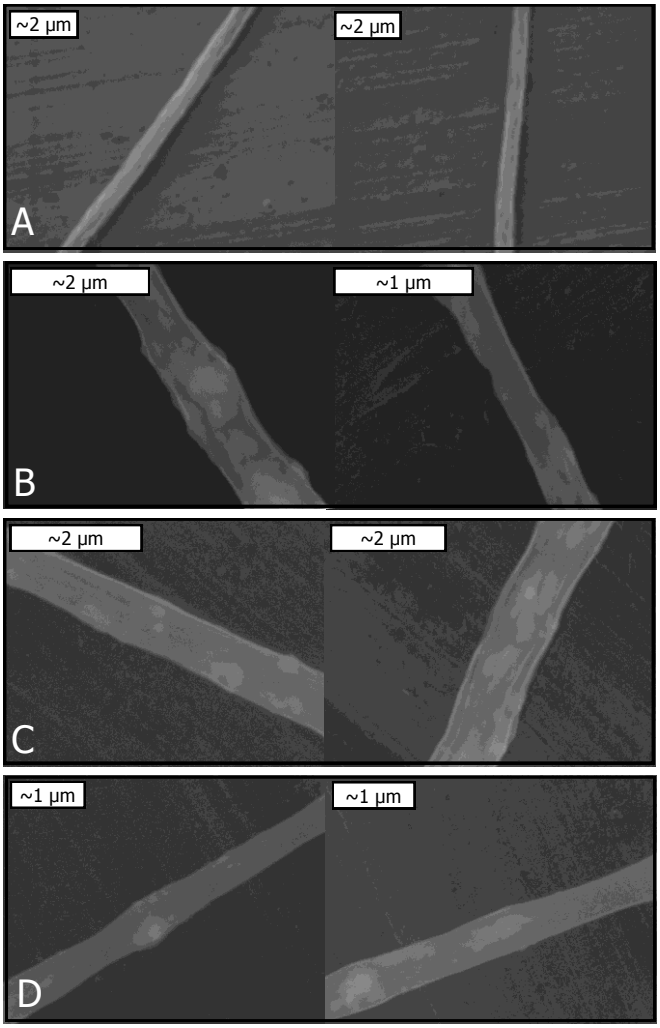

Figure 2.8. SEM images taken of nanofibres electrospun using different nozzle diameters. A: 0.3 mm. B: 0.5 mm. C: 1 mm. D: 1.5 mm.

In all cases the nanofibres produced were observed to be long and thin with some minor defects, such as nodules. The nodules were caused by aggregation of the polymer solution in the nozzle. As can be observed in Figure 2.8, these facets are more prominent when using larger diameter nozzles, as the larger size allows for a greater pooling of polymer solution. The morphology of the electrospun nanofibres will also be affected by other processing parameters, such as voltage bias and working distance between the nozzle tip and the collector. Both will affect the strength of the electrical field for electrospinning. Voltage (V) and deposition distance (d) were both investigated

using 1.0 mm and 1.5 mm diameter nozzles to analyse the difference in trends observed when electrospinning from differing nozzle diameters.

Applied Voltage

The voltage applied to the electrospinning solution was investigated using both 1.0 mm and 1.5mm nozzle diameters. From Figure 2.9 it can be seen that the mean fibre diameter does not deviate much between 5 kV and 25 kV when using a 1.5 mm nozzle diameter. The range of diameters varies between a minimum of 433 ± 91 nm, at 20 kV, and a maximum of 507 ± 130, at 10 kV. As the applied bias reaches 30 kV, the fibre diameter drops to 221 ± 97, about half the diameter of the fibres electrospun < 30 kV. Between 25 and 30 kV there is a critical point where the electric field draws the fibres out of the nozzle before they have time to grow to a large size.

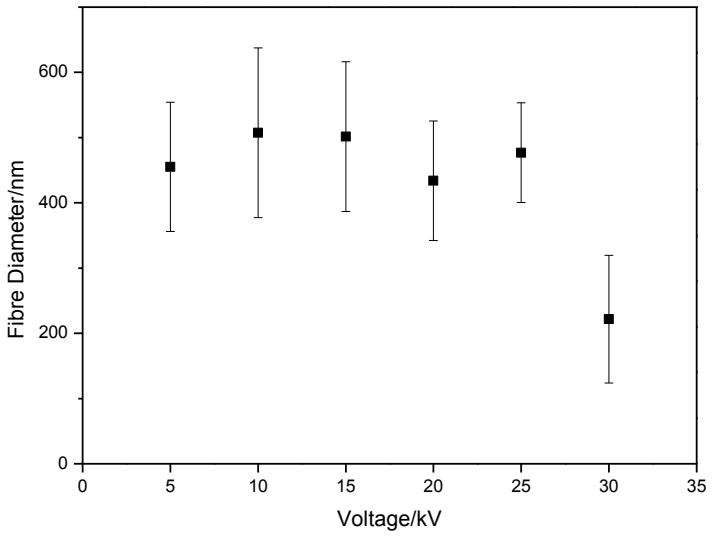

Figure 2.9. Voltage as a function of mean fibre diameter using a 1.5 mm diameter nozzle. The error bars represent the distribution function of the fibres.

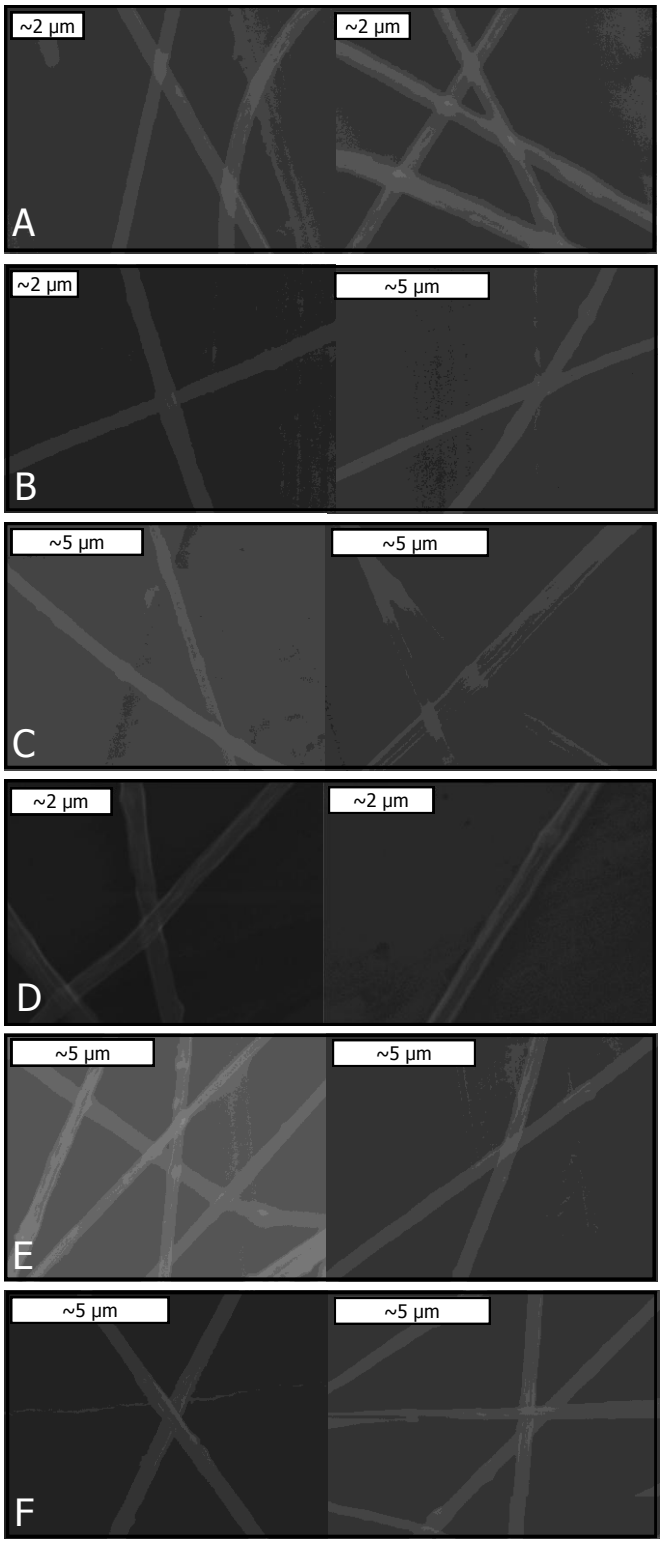

Figure 2.10. SEM images of TiO_2 nanofibres at increasing applied voltage using a 1.5 mm diameter nozzle. A: 5 kV, B: 10 kV, C: 15 kV, D: 20 kV, E: 25 kV and F: 30 kV.

SEM images show the nanofibres electrospun from a 1.5 mm diameter nozzle to be long and thin with no defects (Figure 2.10). As the applied bias increased, only the fibre diameter was seen to change, with no observable difference in morphology. This shows that when using a large nozzle diameter (1.5 mm), the applied voltage has little effect on morphology, only on the fibre size.

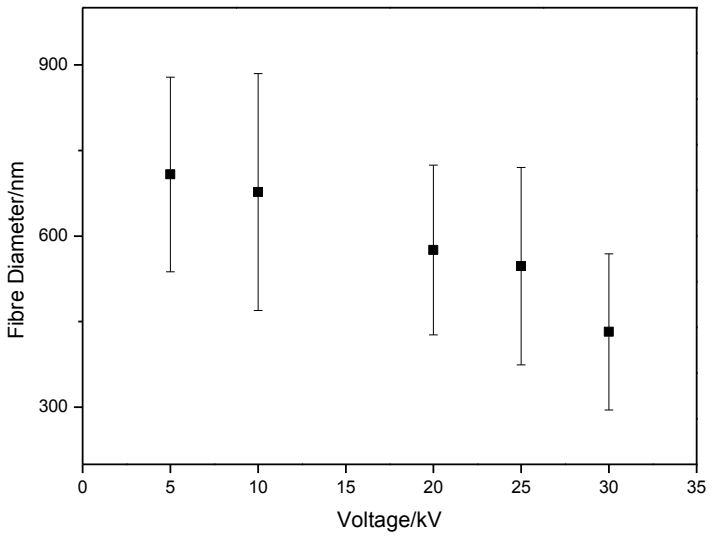

Figure 2.11. Fibre diameter as a function of voltage using a 1.0 mm diameter nozzle. The error bars represent the distribution function of the fibres. The mean fibre diameter is observed to decrease with voltage due to the increased rate of evaporation of the polymer solution.

When the nozzle diameter was decreased to 1.0 mm it can be observed that the fibre diameter decreased with increasing voltage (Figure 2.11). At 5 kV a maximum mean fibre diameter of 707 ± 170 nm was observed. There was a linear decrease in fibre diameter to 432 ± 136 at 30 kV. The deviation of fibre diameter from the mean changed negligibly as applied voltage increased implying voltage has consistent control of fibre diameter.

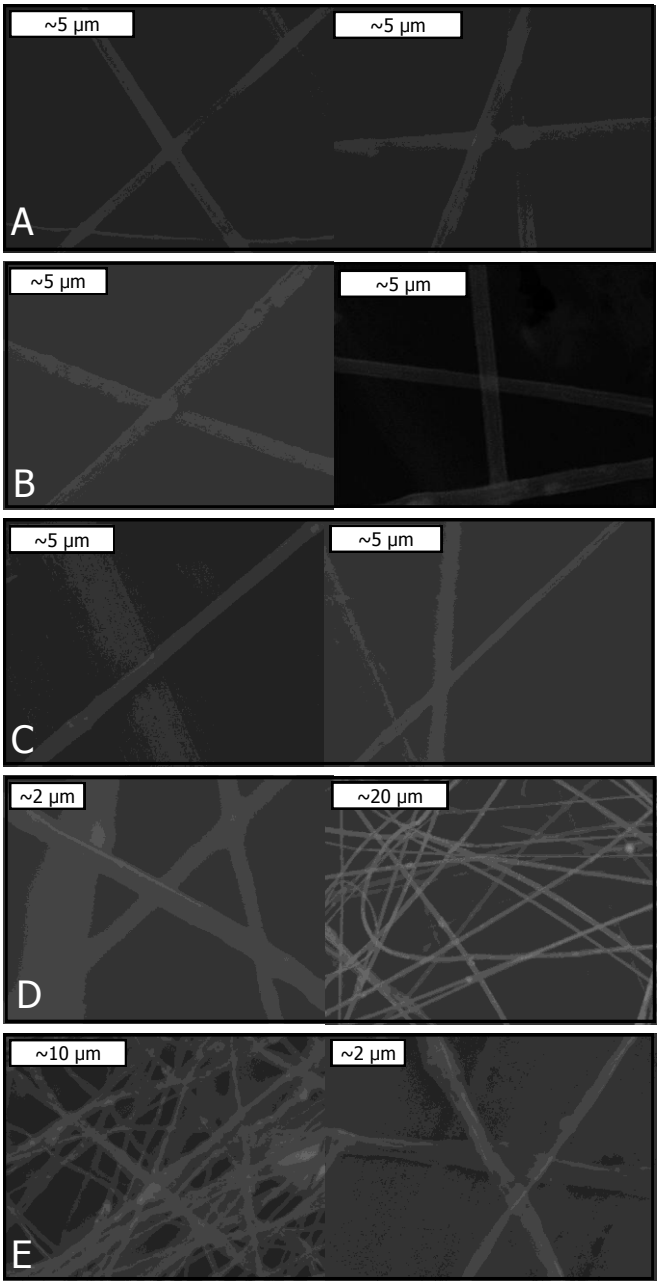

Figure 2.12. SEM images of TiO_2 nanofibres as a function of applied voltage using a 1.0 mm diameter nozzle. A: 5 kV, B: 10 kV, C: 20 kV, D: 25 kV and E: 30 kV.

The fibres were found to be long and thin and showed increased defects as the applied voltage increased (Figure 2.12). At 20 kV nodules had begun to appear in the fibres and by 30 kV several nodules were seen on each fibre. This is in agreement with Kanjanapongkul *et al.,* who found that above 21 kV DMF evaporated at a rapid rate which decreased the homogenity of the fibres produced.[161] At this critical voltage they

observed an increase of beads in the product. The higher voltage increases the rate that the solution is removed from the nozzle. It increases the extrusion so that the solvent is removed faster than solution from the syringe can be supplied to the tip which reduces the stability of the electrospinning. In our work high numbers of beads are not observed up until 30 kV, which is thought to be due to the increased flow rate from the syringe pump, which supplies solution to the tip at an increased rate, maintaining the tip stability.

Nozzle Tip to Collector Spinning Distance (Deposition Distance)

The influence of the nozzle tip to collector spinning distance parameter was also investigated with respect to fibre diameter and morphology. Deposition distance showed no control over fibre diameter when electrospinning using a 1.5 mm diameter nozzle (Figure 2.13).

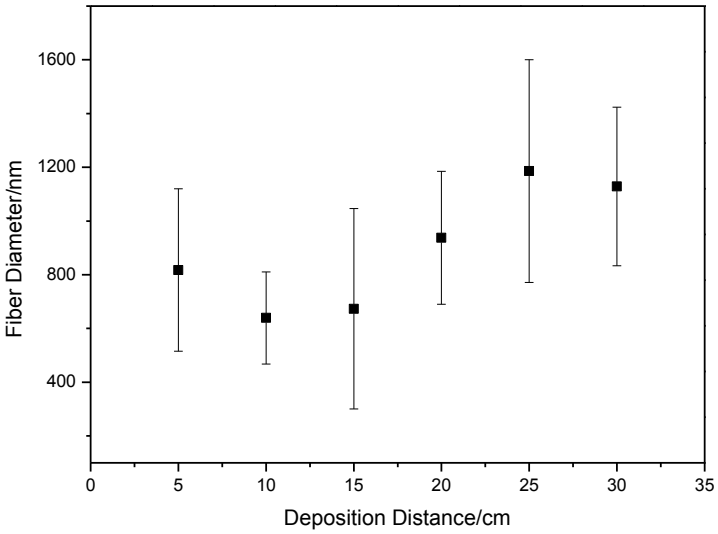

Figure 2.13. Fibre diameter as a function of deposition distance when electrospinning from a 1.5 mm diameter nozzle. Little correlation was observed between nozzle to collector distance and fibre diameter using a 1.5 mm aperture diameter. The error bars represent the distribution function of the fibres.

Diameters were in the range of 639 ± 171 nm, at 10 cm, to 1186 ± 414 nm, at 25 cm deposition distance. The large deviations of the fibre diameters further evidence a lack of control by deposition distance. The largest deviation was observed at 25 cm deposition distance of 1186 ± 414 nm.

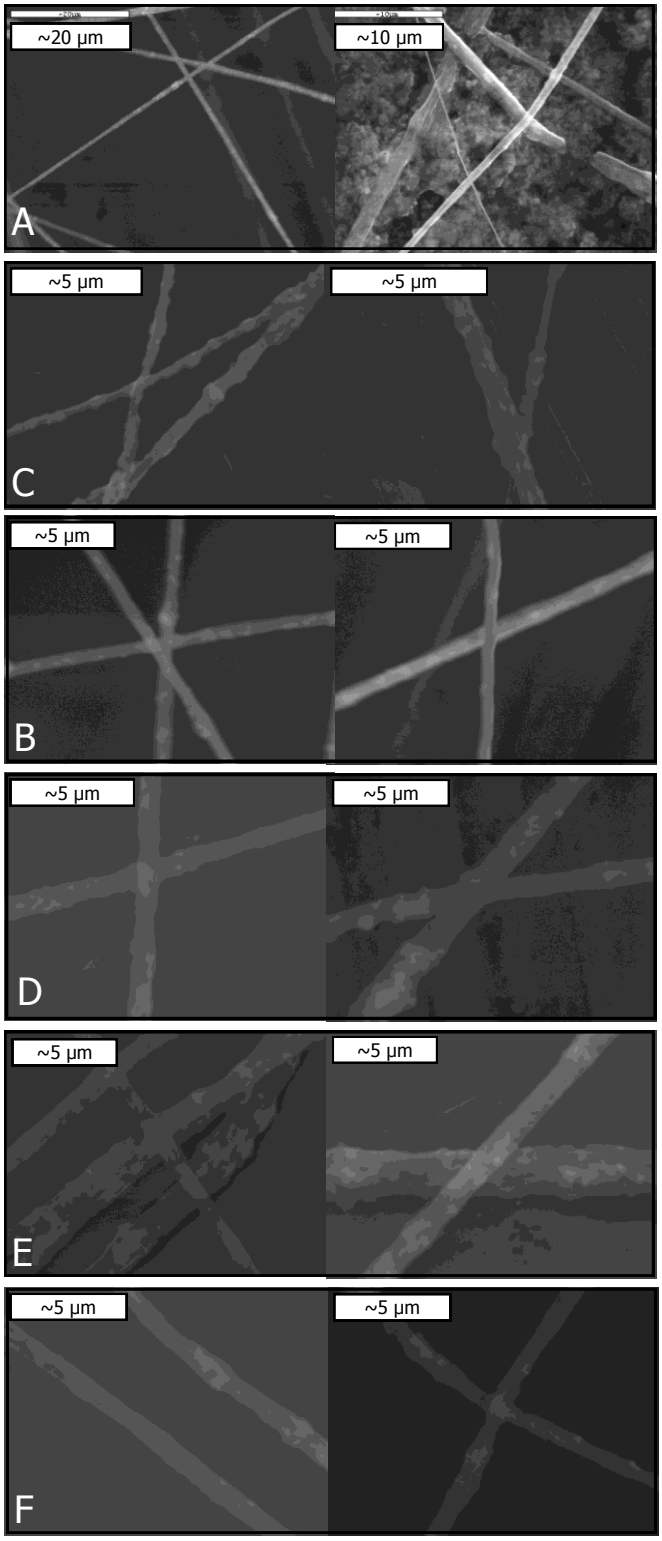

Figure 2.14. SEM images of TiO_2 nanofibres electrospun as a function of nozzle tip to collector distance, using a 1.5 mm diameter nozzle. A: 5 cm, B: 10 cm, C: 15 cm. D: 20 cm, E: 25 cm and F: 30 cm.

The nanofibres electrospun using a 1.5 mm diameter nozzle were observed to be of fibrous nature with defects appearing as a function of nozzle tip to collector distance (Figure 2.14). At short distances, 5 cm, a large amount of particulate was observed owing to the electric field not having sufficient time to draw out nanofibres. The fibres spun had a large number nodules present up until 20 cm deposition distance, where they began to recede, resulting in smoother nanofibres. At increased distance the electric field and deposition distance were balanced, maintaining the tip stability, resulting in consistent electrospinning.

When the nozzle diameter was reduced to 1.0 mm, a clearer relationship between deposition distance and fibre diameter was observed: the mean fibre diameter decreased with increasing nozzle tip to collector distance (Figure 2.15). The diameter at 2 cm was 676 ± 346 nm, reducing to 442 ± 102 at 30 cm deposition distance, indicating that using a 1.0 mm diameter nozzle, fibre diameter can be controlled by nozzle tip to collector distance. Furthermore it was observed that as the deposition distance increased, the deviation of fibre diameter decreased. This is evidenced by the deviation decreasing by three times on increasing the deposition distance from 2 cm to 30 cm, highlighting that the spread of fibre diameters can also be controlled by altering the nozzle tip to collector distance. At deposition distances above a critical value, 5-10 cm, the range of diameters drops rapidly as the electric field is not strong enough to support the weight of larger diameter (and therefore heavier) fibres, therefore only smaller diameter fibres were collected.

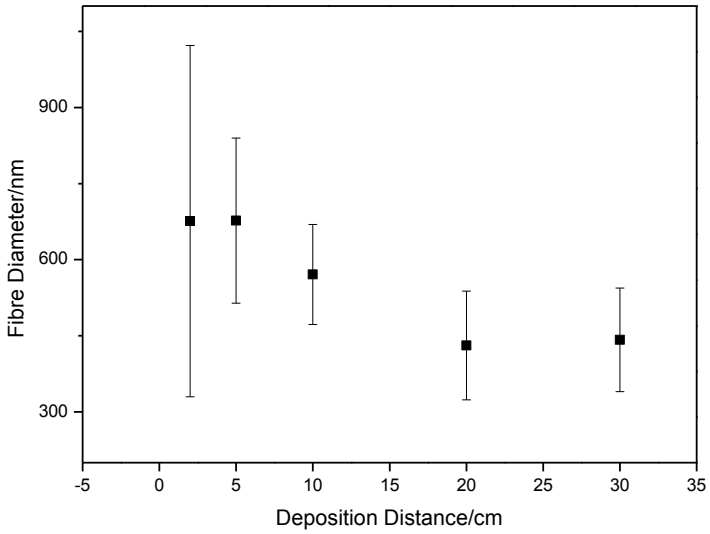

Figure 2.15. Fibre diameter as a function of deposition distance using a 1.0 mm diameter nozzle. A trend is observed of longer distances resulting in smaller diameter fibres which is attributed to the electric field being weaker at longer distances, and therefore, unable to support larger diameter fibres. The error bars represent the distribution function of the fibres.

Analysis by SEM showed that fibres electrospun using a 1.0 mm diameter nozzle did not consistently form until above a 2 cm deposition distance, where large amounts of particulate were observed below that distance (Figure 2.16). Above 2 cm nozzle tip to collector distance, smooth fibres were observed with little to no defects. Using a 1.0 mm diameter nozzle, deposition distance has little effect on fibre morphology above this critical distance.

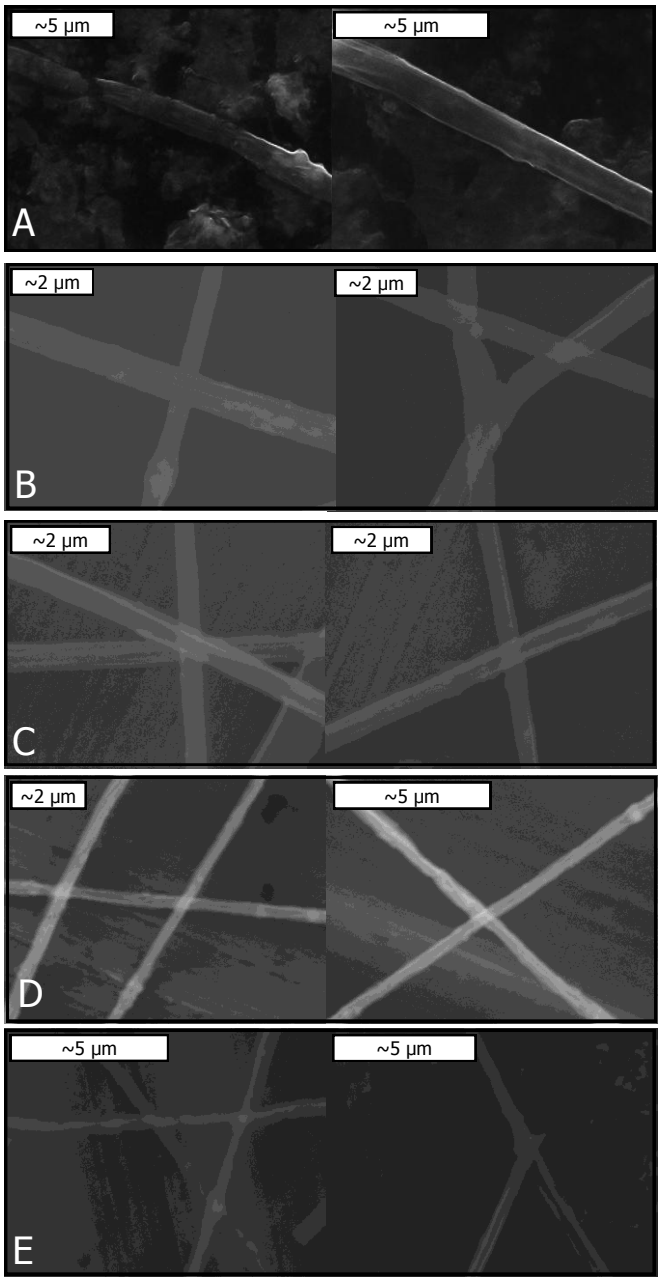

Figure 2.16. SEM images of TiO_2 nanofibres as a function of nozzle tip to collector distance, using a 1.0 mm diameter nozzle. A: 2 cm, B: 5 cm, C: 10 cm, D: 20 cm and E: 30 cm.

The polymer solution must be drawn out into a fibre by the electric field it is subjected to. When the deposition distance is small, there is not enough time for the field to adequately draw out a fibre before the pressure exerted on the solution has forced the solution out of the nozzle. As the distance increases, the electric field has

increased time to draw out the polymer solution as fibres. At shorter distances there is a greater amount of deviation from the mean fibre size, with the converse being true for an increased distance. This gives rise to a critical distance for fibre formation, which was observed above 5 cm when using a 1.5 mm diameter nozzle and above 2 cm for a 1.0 mm diameter nozzle. This shows that low deposition distances can be compensated for by using a smaller diameter nozzle, which lowers the rate of extrusion of solution.

2.3.2 Intrinsic variables

Concentration, viscosity and fibre diameter

In order to determine the relationships between concentration, viscosity and fibre diameter for our model system, both fibre diameter and viscosity were measured for PMMA concentrations of 0.2-15 wt. %, electrospun using a 1.5 mm diameter nozzle. Plotting mean fibre diameter as a function of concentration revealed a power law relationship (Figure 2.17). The fibre diameters increased from 127 ± 49 nm, at 3 wt. % PMMA, to 3190 ± 236 nm, at 10 wt. % PMMA. The deviations of the fibre diameters increased with mean fibre diameter.

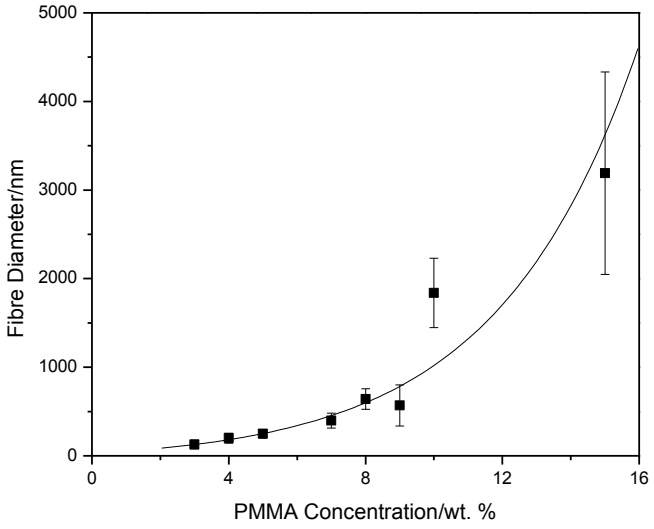

Figure 2.17. Fibre diameter as a function of PMMA concentration. The error bars represent the distribution function of the fibres.

Plotting the log of mean fibre diameter against the log of concentration revealed a linear line with an exponent of 2.0 and an R^2 of 0.90 (Figure 2.18).

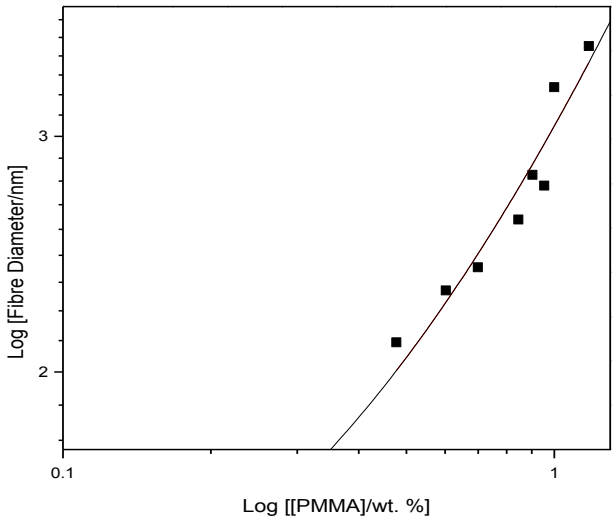

Figure 2.18. Logarithmic plot of fibre diameter as a function of PMMA concentration revealing that fibre diameter increases at faster rate than PMMA concentration.

Analysis of the SEM images revealed no fibres were formed below 5.0 wt. % PMMA. Above this concentration the fibres were found to be smooth and defect free (Figure 2.19). These images show a critical point where the concentration of PMMA is high enough for fibres to form. At low concentrations the polymer interactions are too few, resulting in little to no formation of nanofibres.

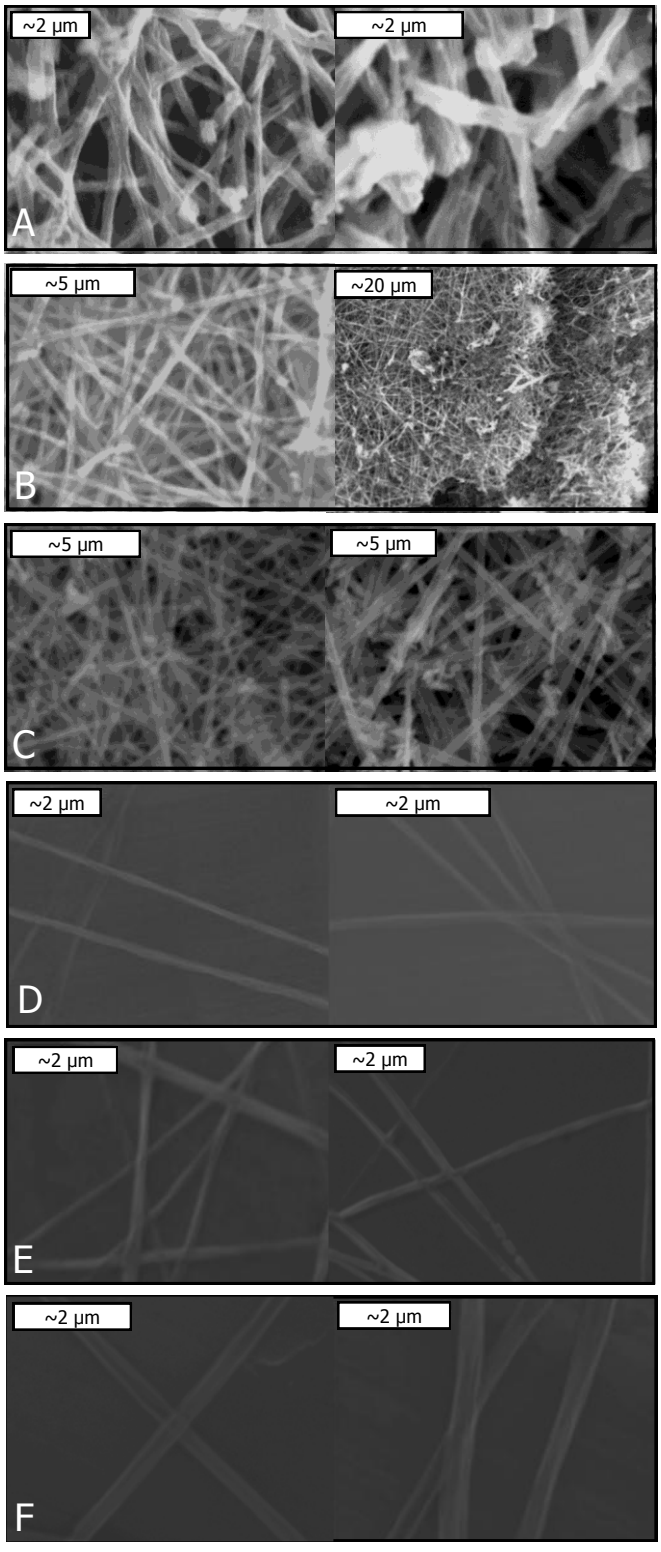

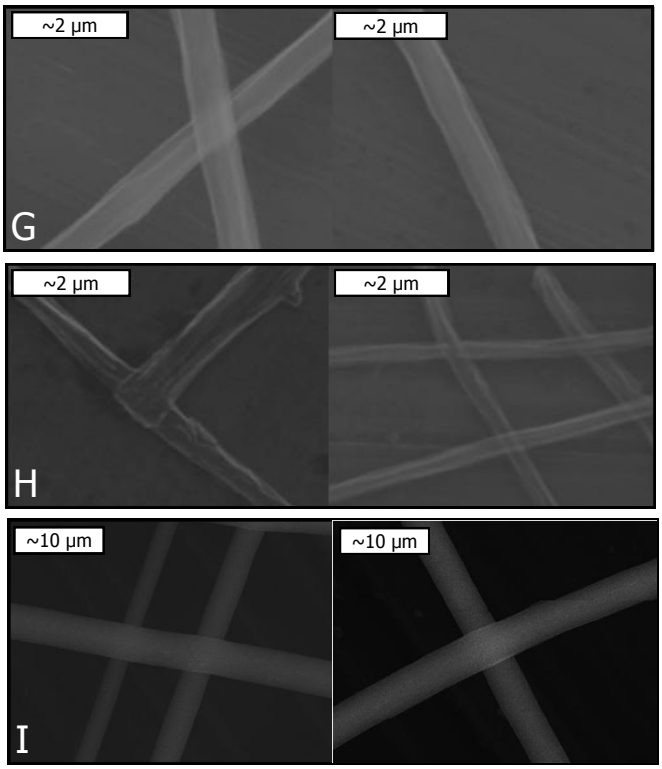

Figure 2.19. SEM images of fibres electrospun using a 1.5 mm diameter nozzle, as a function of increasing PMMA concentration. From top: 0.3, 2.0, 3.0, 4.0, 5.0, 7.0, 8.0, 9.0 and 15.0 wt. % PMMA in DMF.

Analysis of SEM images from increasing PMMA concentrations electrospun using a 1.0 mm diameter nozzle revealed a similar trend (Figure 2.20). Only limited fibre formation was observed below a critical concentration, however, this concentration was found to be below 2.0 wt. % when using a 1.0 mm nozzle.

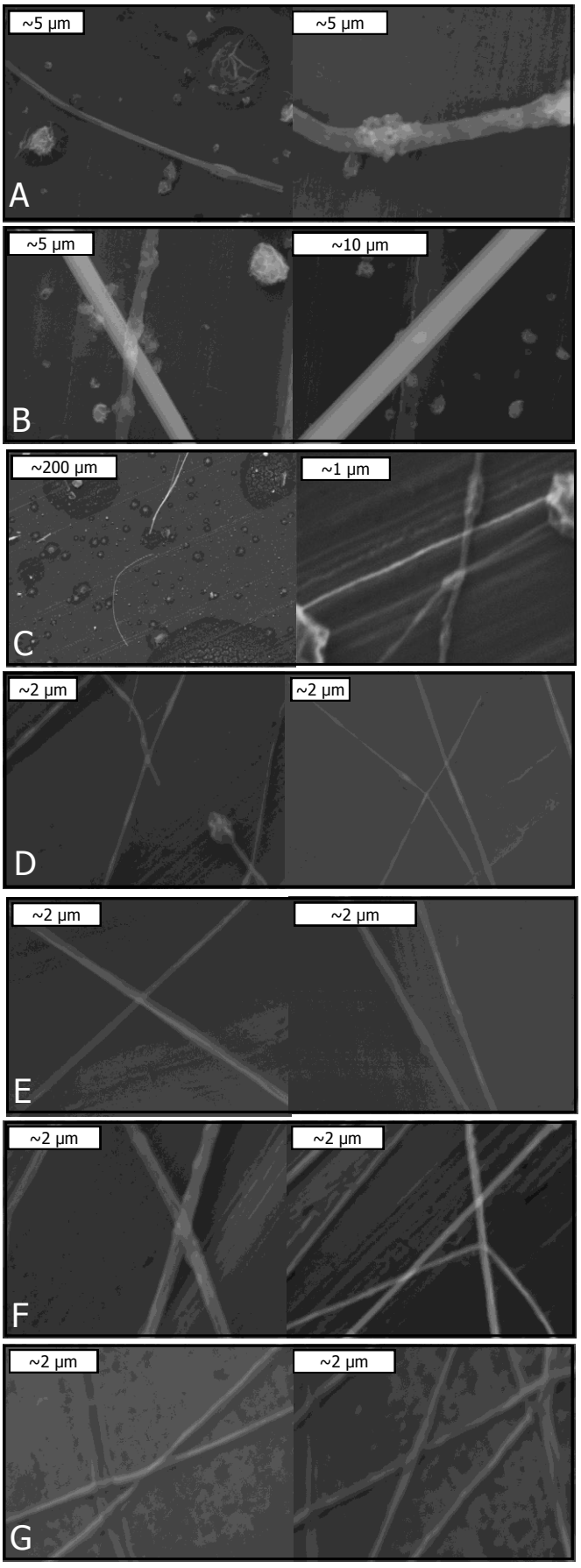
~5 µm
~5 µm
A
~5 µm
~10 µm
B
~200 µm
~1 µm
C
~2 µm
~2 µm
D
~2 µm
~2 µm
E
~2 µm
~2 µm
F
~2 µm
~2 µm
G

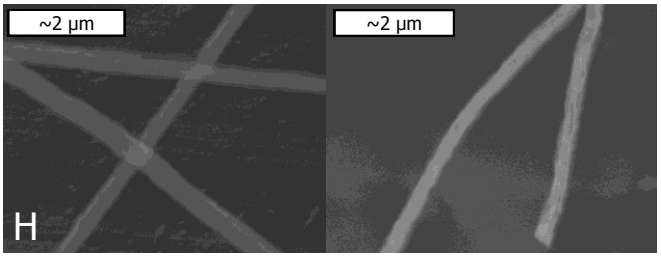

Figure 2.20. SEM images of TiO_2 nanofibres electrospun as a function of polymer solution concentration (wt. %), using a 1.0 mm diameter nozzle. A: 0.3, B: 1.0, C: 2.0, D: 3.0, E: 4.0, F: 5.0, G: 6.0, H: 7.0 and I: 8.0.

Electrospinning fibres requires a solution with surface tension higher than the electric field. The surface tension increases with viscosity,[147] which increases with concentration. It can be inferred that below 2.0 % PMMA concentration using a 1.0 mm diameter nozzle and below 5.0 % PMMA concentration using a 1.5 mm diameter nozzle, the surface tension is below the critical point for electrospinning. This is the critical chain overlap concentration (c^*), and was calculated from Equations 2.4 and 2.5. For PMMA in DMF, K = 0.015 g/cm^{-1} and a = 0.667. The average molecular weight of PMMA was 93,000 g/mol therefore, $[\eta]$= 30.9. Using the specific gravity of DMF, 0.95 g/cm^3, a value of 3.2 wt. % was calculated for the critical chain overlap concentration. This is in good agreement with Gupta *et al.* and Beck-Tan *et al.*, who found c* values of 3.5 and 4.0 % respectively.[152,153] When c is larger than c*, the viscosity will balance the surface tension resulting in fibres not droplets. Experimentally c^* was found to be 2.0 and 5.0 % for 1.0 and 1.5 mm diameter nozzles respectively, taking the average yields an estimated experimental c^* as 3.5 % wt. %, in good agreement with the calculated estimate.

Viscosities for increasing concentration PMMA solutions were calculated using Equation 2.6. The two were plotted against each other revealing an exponential trend, as

shown in Figure 2.21. The viscosity of the polymer free solvent, pure DMF, was measured to be 2.3 mPa.s. This increased to 236.7 mPa.s at 10 wt. % PMMA. The viscosity at critical chain overlap concentration was determined to be ~7.7 mPa.s.

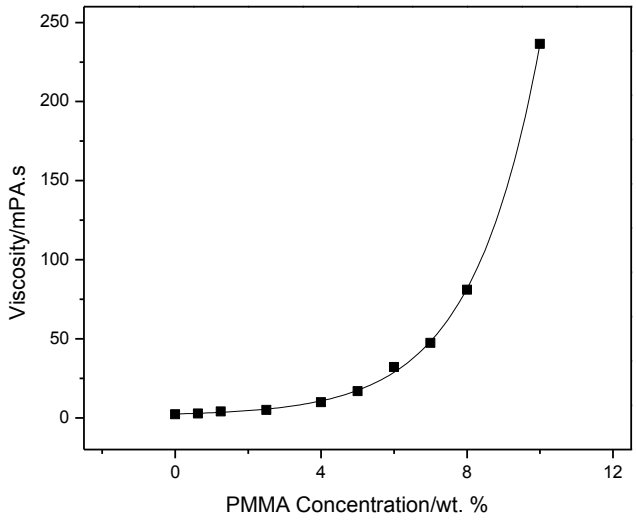

Figure 2.21. Viscosity as a function of PMMA concentration.

By plotting the logarithmic values, a biphasic trend was observed (Figure 2.22). The exponents of these trends were 0.4 and 3.4, with R^2 values of 0.94 and 0.98 respectively. These correspond to the semi-dilute un-entangled and semi-dilute entangled regions of polymer overlap (Figure 2.5). Gupta *et al.* found these exponents to be 0.65 and 5.3 for the semi-dilute un-entangled and semi-dilute entangled concentration regions respectively, close to experimental values obtained in our lab.[153]

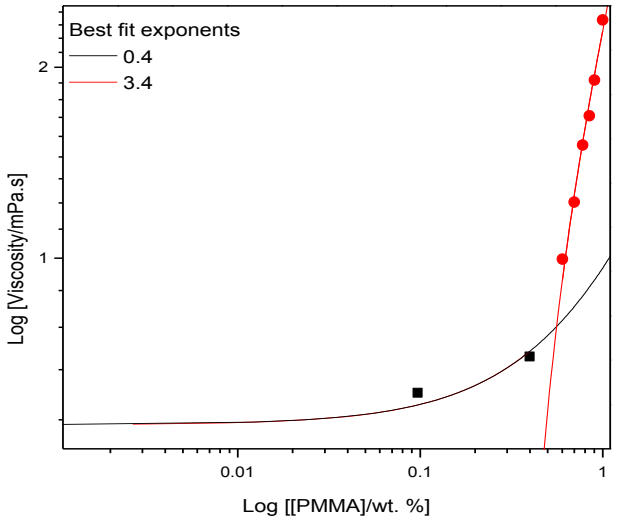

Figure 2.22. Logarithmic plot of solution viscosity as a function of PMMA concentration. The graph reveals two distinct regions of polymer concentration. The more horizontal trend is semi-dilute un-entangled region and the more vertical trend is the semi-dilute entangled region. The dividing point of these two trends is the critical chain overlap concentration.

To better understand the quantitative relationship of solution viscosity, fibre diameter was plotted against the measured viscosity. This revealed a linear relation with a slope corresponding to 6.5 nm/mPa.s and a R^2 of 0.979, indicating that viscosity is a large factor in dictating the diameter of fibres produced (Figure 2.23).

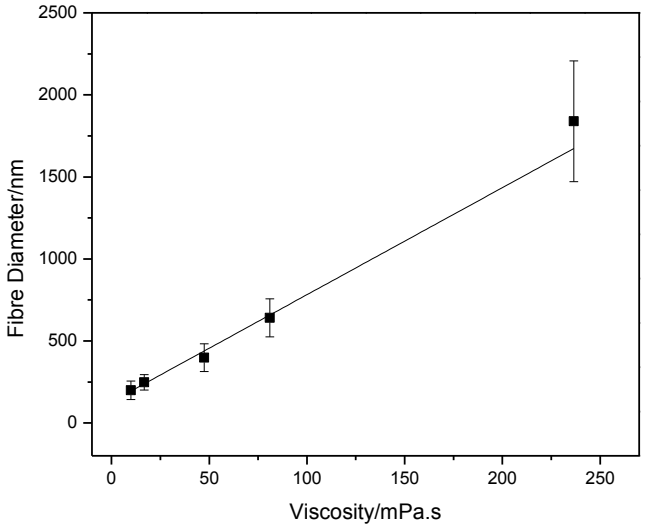

Figure 2.23. Viscosity as a function of mean fibre diameter. The graph reveals a linear correlation between viscosity and fibre diameter indicating the two variables are intrinsically linked. The error bars represent the distribution function of the fibres.

Gupta *et al.* observed an exponential relationship, with an exponent of 0.75, however, this was found to be the case only for PMMA with molecular weights of above 100,000 g/mol.[153]

2.4 Mechanism of Poly(Methyl Methacrylate) Degradation and Crystallinity of TiO_2 Nanofibres

Post electrospinning, it is typically necessary to remove the polymer scaffold. In some cases this is not required as the polymer is the desired product, for example in biological applications where the fibres are biopolymers.[21,163,164] However, when preparing metal oxide nanofibres by electrospinning, a polymer removal step is essential. This can be achieved *via* chemical,[164] oxidation,[165] UV or thermal methods.[166,167] For metal oxide materials thermal treatment has the dual purpose of

polymer removal and crystallisation of the metal oxide in to the desired phase. In the interests of green chemistry, keeping the conditions for polymer removal as close to standard ambient conditions (298 K and 1 bar) and minimising chemical use is desirable. This is often not trivial to accomplish because, despite the water solubility of many polymers,[168] the solvent must be compatible with the precursors.

In this section, the investigation of the thermal degradation of PMMA in DMF using differential scanning calorimetry (DSC), UV-Vis spectroscopy and FT-IR spectroscopy is presented.

2.4.1 Differential Scanning Calorimetry

In this project PMMA was removed through calcination where the organic molecules were thermally decomposed and oxidised. In order to understand this process, we applied DSC to monitor the enthalpy change during the thermal decomposition of PMMA. During DSC a sample and a reference are heated over a set temperature range and the heat flow to each is measured (the ordinate on a DSC graph). During transitions within the sample, such as melting or crystallisation, more or less energy will be required, compared to the reference, to keep the temperatures equal. This can be quantitatively seen by an increase or decrease of the heat flow. An increase in heat flow indicates that the sample requires more energy to keep the same temperature as the reference, evidencing an endothermic process. Conversely a decreased heat flow indicates an exothermic reaction. The peaks in a DSC graph represent $\Delta H/\Delta T$, therefore enthalpy information can be gathered from the areas under the peaks, as described by Equation 2.7.

$$\Delta H = KA \tag{2.7}$$

where *K* is the calorimetric constant and *A* is the area under the peak.

When a sample reaches a transition temperature the heat flow will change sharply as the sample cannot continue rising in temperature until the transition has completed; this means the ordinate value is infinite, but this is not seen in practice, instead they are often seen as broad peaks. The broadness of the peaks can give information on the crystallinity of the sample, with a sharper transition indicating higher crystallinity. These are first order transitions because there is a change in heat capacity and latent heat. DSC can also measure changes in heat capacity, which are shown by a change in the baseline, if it rises the heat capacity has increased, this is a second order transition because there is no change in latent heat. Finally, the reverse run can be performed, showing transitions as the sample decreases in temperature. These are performed after the increasing temperature run and will show if any of the transitions are reversible. If the graph shows no peaks during temperature decreasing, then all the transitions seen during heating are non-reversible.[169–171]

In this project DSC was implemented in several samples to highlight transitions, such as the desorption of OH groups from the titania surface, degradation of PMMA and degradation of MMA. Due to the DSC equipment used having a maximum temperature of 425 °C, the crystallisation of TiO_2 could not be observed on this equipment, but was instead examined using X-ray diffraction in Section 2.4.3.

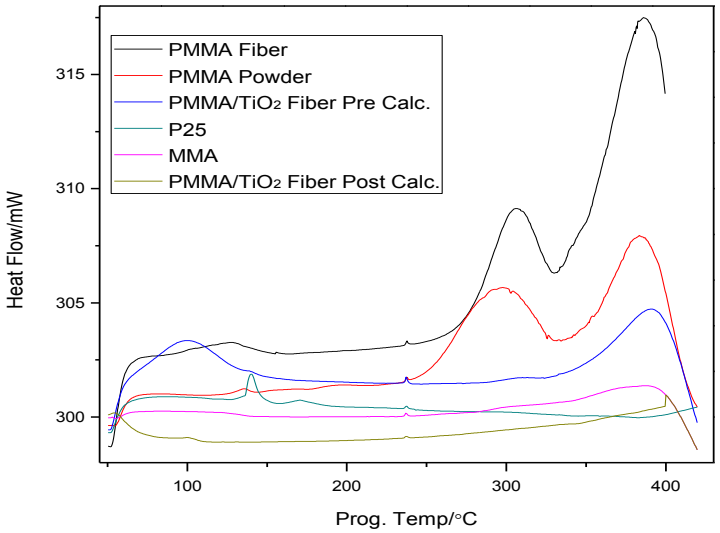

Figure 2.24. DSC endotherms of components of the production of nanofibres. It can be seen that MMA and PMMA do not show the same isotherms, evidence that MMA is not part of the PMMA degradation pathway. Small isotherms at ~150 °C and ~250 °C were both found to be non-reversible. The 250 °C isotherm was determined to be an impurity within the equipment.

Pure powder PMMA (Sigma-Aldrich 996,000 rfm), PMMA nanofibres, PMMA/TiO_2 nanofibres pre-calcination, PMMA/TiO_2 nanofibres post-calcination, P25 powder and MMA were investigated with DSC. Unless otherwise stated, none of the samples had been pre-calcined. Figure 2.24 shows the endotherms of these materials.

The endotherms of PMMA powder and PMMA fibres are almost identical, with transitions beginning at ~260 °C and ~325 °C. Both transitions are first order as there is a change in heat capacity and latent heat of the sample. These transitions are non-reversible as evidenced by the lack of peaks during the reverse scan. It was postulated that the first transition was the degradation of the polymer into the monomer and that the second transition was the degradation of the monomer. To test this a sample of

MMA was run on the DSC. If the second transition was the degradation of the monomer then it would be observed in the MMA results. However, MMA was shown to degrade at 100 °C and no other transitions were observed. This is evidence that MMA is not part of the PMMA degradation pathway.

Studies on the mechanisms of the thermal degradation of PMMA show that the initial step is a mass loss at low temperatures.[172] This weight loss reduces the chain length, increasing the thermodynamic stability. Further investigation of the thermal oxidation degradation details three steps in the process. These processes occur at 165, 260 and 375 °C, and are ascribed to scissions at the head to head linkages, scissions at the polymer chain end and random scissions respectively.[173] The last two processes coincide with the two large transitions observed in the DSC endotherms of PMMA powder and fibres, but at slightly shifted temperatures. The slight difference in endotherms is attributed to the difference in morphology and molecular weight of the PMMA in our studies compared to the reference literature (10,000-320,000 M_w powder compared to 996,000 M_w nanofibres).

The activation energy of the first step, mass loss, is small at ~0.05 j/g^{-1}. This may have been too low to record the change in heat flux using the DSC machine implemented. The measured ΔH values of the PMMA transitions observed in our DSC data were 125 and 234 j/g^{-1} respectively. These positive enthalpies confirm the endothermic nature of the transitions. The melting point and heat of fusion are lower in fibres than in powdered samples, due to the powdered samples having a higher crystallinity than is present in fibres, this is observed as lower temperature endotherms.

In the PMMA and TiO_2 sample of Figure 2.24 there was a large endotherm at ~100 °C, this was possibly due to desorption of water or the desorption of OH groups

from the titanium surface. At ~150 °C there was a small isotherm which has been assigned to some remaining DMF. In all five traces there was a small isotherm at 240 °C, which has been attributed to an impurity, proven by running blank samples and still observing the endotherm. In the P25 sample there was a well defined peak at 150 °C. As there was no DMF in the sample at any point the peak was attributed to surface hydroxyl groups on the titanium. A repeat run was performed on the same sample, in this case the endotherm was no longer observed, this provides evidence for a volatile, non-reversible, surface bound species, such as a hydroxyl group.

2.4.2 UV-Vis Absorption and Infra-Red Spectroscopy

UV-Vis absorption (Figure 2.25) and IR (Figure 2.26) spectra were taken of electrospun PMMA fibres as a function of increasing calcining temperature. PMMA can be observed at λ_{max} =210 nm in UV-Vis and has distinctive peaks at ~3400 and 3000 cm^{-1} in FT-IR. Figure 2.25 shows the maxima absorbance of PMMA as a function of calcining temperature. The plot reveals two separate drops in PMMA concentration, occurring at ~250 °C and 400 °C.

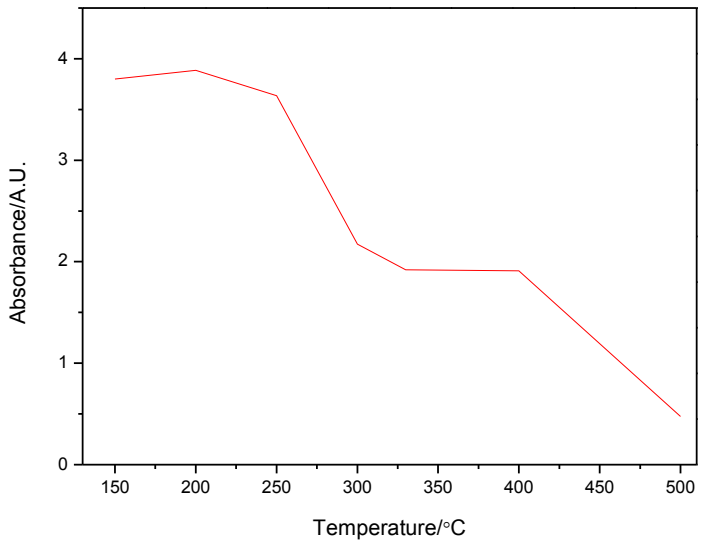

Figure 2.25. The maxima absorbance of PMMA (210 nm) as a function of temperature. The two decreases in concentration of PMMA observed in the UV-Vis spectrum, match those observed with DSC.

These decreases in concentration have been ascribed to polymer chain end scissions and random chain scissions for 250 °C and 400 °C respectively. The initial head to head linkage break does not alter the concentration of PMMA, as it serves to break the polymer up in to smaller polymer sections. As UV-Vis spectroscopy was only tracking concentration, this degradation step was not observed.

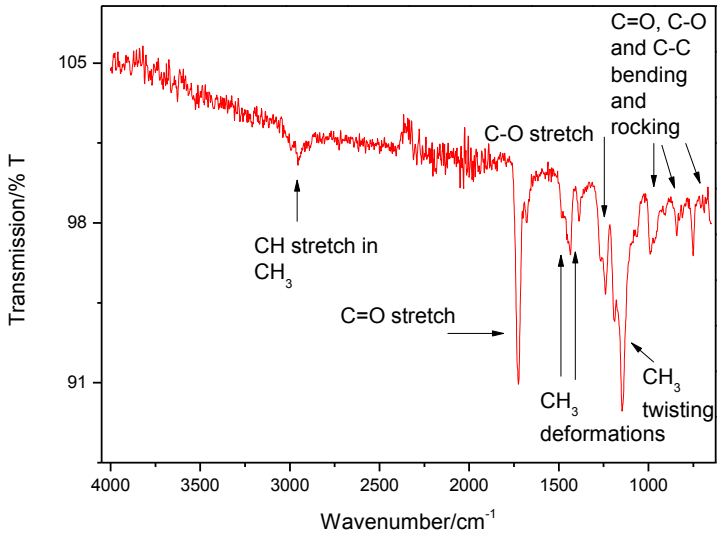

Figure 2.26. FT-IR of electrospun PMMA. Annotations taken from Haris et. al.[52]

A typical FT-IR spectrum of PMMA, with assignments taken from Haris *et al.*, is depicted in Figure 2.26.[52] The stretching mode of the carbonyl ester group, 1727 cm^{-1}, was tracked and used to quantitatively chart the degradation of PMMA. Figure 2.27 shows transmission/% of the carbonyl ester group of PMMA as a function of calcining temperature. Only one transition was observed by FT-IR spectroscopy at ~50-200 °C, compared to the two observed by UV-Vis spectroscopy and DSC, at 250 °C and 390 °C respectively. It is possible the transition observed by FT-IR is the previously unseen scission of head-to-head linkages, as literature values predict head-head linkage scissions occurring within this temperature range.[173] Analysing the CH_2 unit in the backbone of the PMMA would show the greatest evidence of the degradation, elucidating the existing FT-IR data, especially during the backbone fission. However, the clearest resonances for the CH_2 unit are only observable in Raman spectroscopy, which was not available.

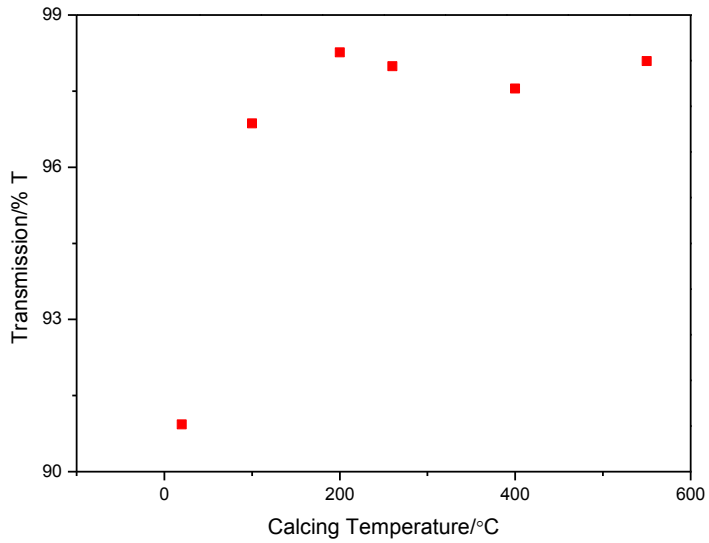

Figure 2.27. Intensities of the 1727 cm^{-1} C=O stretching peak as a function of calcining temperature. Higher intensities indicate more of the incident radiation has been transmitted through the sample and therefore concentrations are lower.

Figure 2.28 shows the FT-IR spectrum of TiO_2 nanofibres calcined at 400 °C, a temperature where TiO_2 is crystalline. Titania has several bands in the IR spectrum. The Ti-O and Ti-O-Ti bands (~600 and ~550 cm^{-1} respectively) could not be observed as they occur outside of the working window of the FT-IR used.[174] The absorbance of water on the surface at 1630 cm^{-1} can be observed. The lack of any observed Ti-OH bands provides evidence that all the $Ti(OH)_2$ formed in the steam treatment step had been converted to TiO_2.

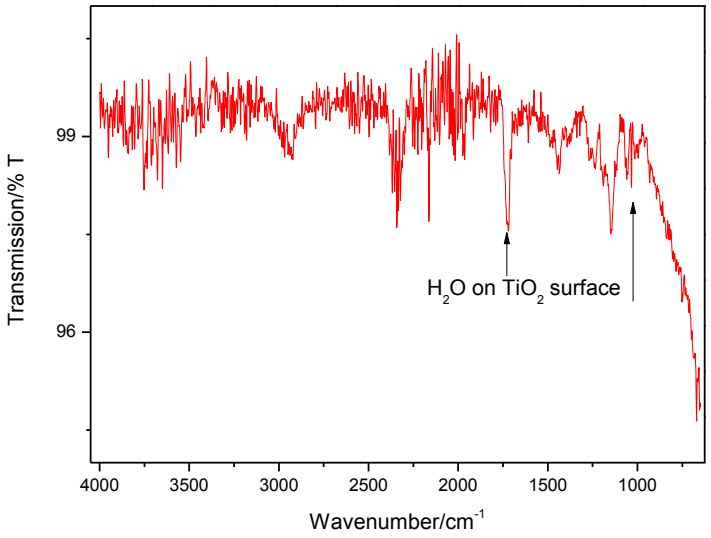

Figure 2.28. FT-IR of TiO_2 fibres calcined at 400 °C. Adsorbed water on the TiO_2 can be observed. The spectrum reveals that no PMMA remains in the sample.

2.4.3 Analysis of the TiO_2 Phase by X-Ray Diffraction

X-ray diffraction was used to investigate the electrospun sample at increasing calcining temperatures. The diffraction patterns were then analysed and compared to photocatalytic activity to determine the influence of crystallinity on photoactivity.

The mat created when electrospinning from TTiP, is a complex mixture of TTiP, $Ti(OH)_2$ and amorphous TiO_2. Steam treatment converts any remaining TTiP to $Ti(OH)_2$, and calcining converts the $Ti(OH)_2$ to TiO_2 and crystallises it. TiO_2 initially crystallises into the anatase phase and then, at higher temperatures, to rutile. There is a third phase, brookite, which crystallises at even higher temperatures at this length scale. Aside from lowering the yield, remaining metal alkoxides can interfere with the crystallisation of the TiO_2, where higher concentrations of alkoxides can result in lower

concentrations of anatase TiO_2. Adding water has been shown to remove these alkoxides and therefore increase the fraction of anatase TiO_2 produced.[138]

It was expected that the powder diffraction patterns for anatase phase TiO_2 would increase in intensity from 350 to 500 °C, and then decrease as the anatase converts to rutile, with a corresponding increase in rutile indexes. Before the crystallisation of the sample, photoactivity was expected to be poor, although some literature suggests that amorphous TiO_2 can be photoactive.[175] No peaks were observed in the X-ray diffraction patterns until 300 °C with the exception of an impurity at 88 θ in the 250 °C sample. From 350 °C, the anatase (101) index can be clearly seen, and rises dramatically at 400 °C (Figure 2.29). At 550 °C, rutile was first observed, evidenced by the (211) and (301) indexes in low concentrations. Above 550 °C, the anatase peaks began to recede, while the intensity of rutile peaks increased.

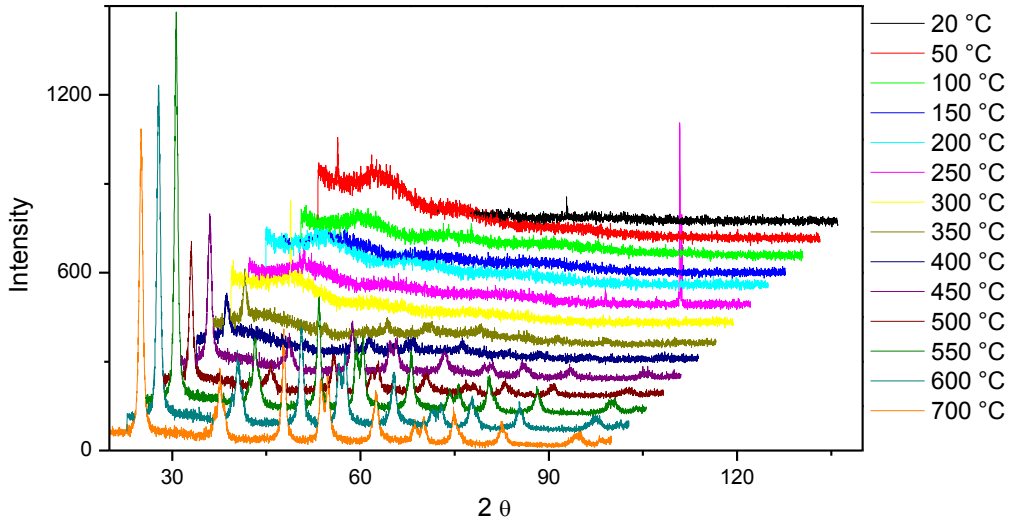

Figure 2.29. XRD diffractograms of TiO_2 nanofibres as a function of calcining temperature. Assignments of peaks are detailed in Figure 1.18. The anatase phase can be observed from 350 °C. At 550 °C the rutile phase begins to crystallise with the commensurate decrease in anatase phase.

The crystallite size was calculated at each temperature that TiO_2 was observed to be crystalline (> 300 °C), by using the Scherrer equation (Equation 1.16). Table 2.1 shows the crystallite sizes of TiO_2 nanofibres as a function of calcining temperature. An increase in crystallite size was observed up until a maximum of 12.9 nm at 550 °C which is in good agreement with several authors.[176,177] Above 550 °C, the crystallite size dropped again as the rutile content increased, which may be attributed to the smaller unit cell of the ruitle phase leading to relatively smaller crystallite sizes.

Table 2.1. Crystallite sizes of TiO_2 as a function of calcining temperature. Crystallite size increases with increasing anatase content. At 550 °C rutile phase begins to crystallise where the crystallite size is observed to decrease and then remain at a constant diameter.

Calcining Temperature/°C	400	450	500	550	600	700
Crystallite Size/nm	10.2	10.9	11.8	12.9	11.8	11.8

SEM images were taken from a sample at each calcining temperature, which revealed the samples to be of a uniformly fibrous and smooth nature at all calcining temperatures. From these images it was determined that calcining within the temperature range 50-700 °C had little effect on the morphology of the fibres (Figure 2.30).

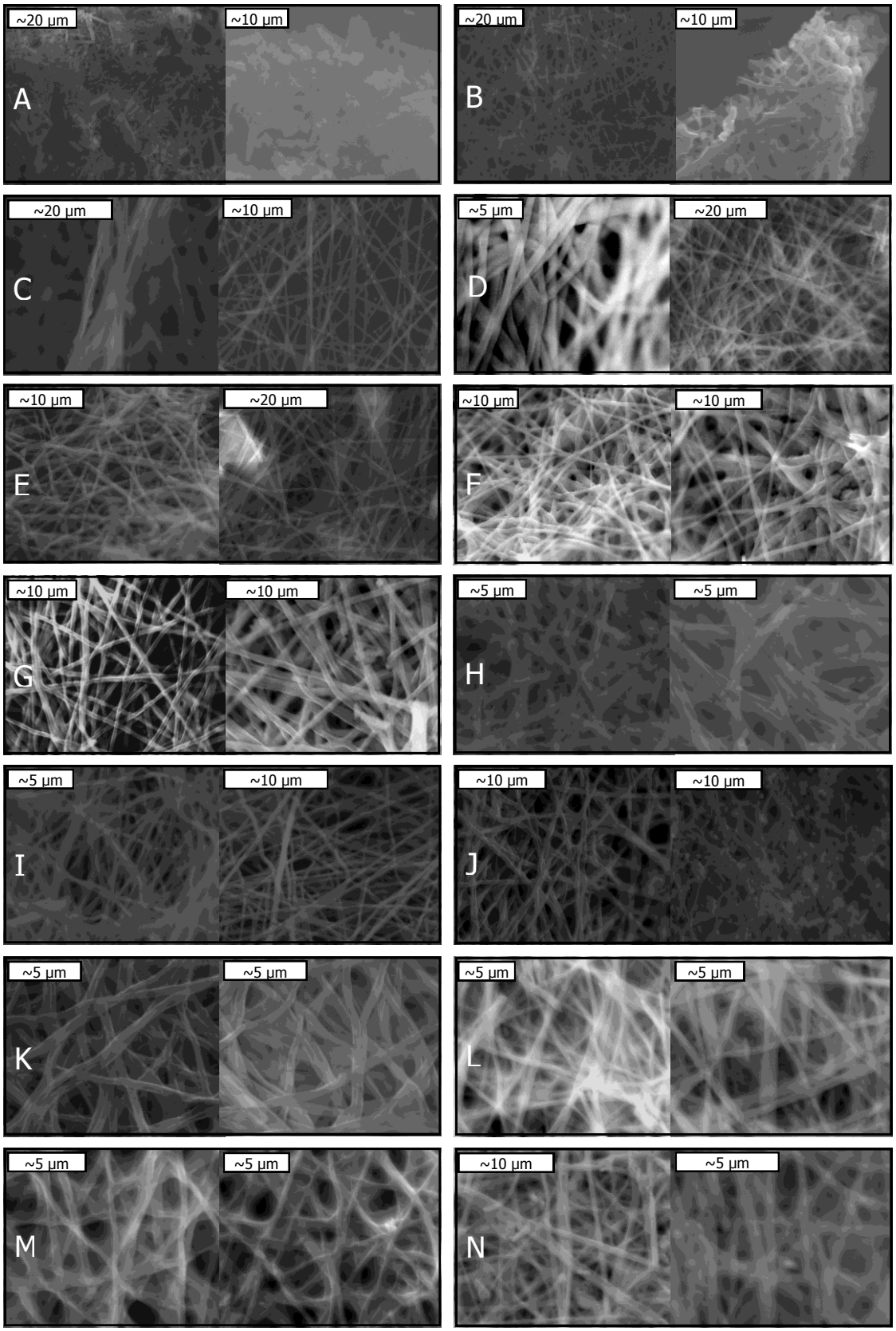

Figure 2.30. SEM images of TiO_2 nanofibres as a function of calcining temperature (°C): A: Uncalcined, B: 50, C: 100, D: 150, E: 200, F: 250, G: 300, H: 350, I: 400, J: 450, K: 500, L: 550, M: 600 and N: 700.

From Figure 2.30 the fibre diameter was estimated (Table 2.2). There was an overall decrease in fibre size as the calcining temperature increased. The largest decrease in fibre diameter was at 200-250 °C, which corresponds to the second transition observed in the degradation of PMMA by DSC, UV-Vis and FT-IR, attributed to polymer chain end scissions.

Table 2.2. Estimated fibre diameter as a function of calcining temperature. The decrease in fibre diameter is attributed to the removal of the PMMA scaffold and the crystallisation of TiO_2 into the anatase phase.

Calcining Temperature/°C	Fibre Diameter/nm
20	1000
50	1000
100	1000
150	800
200	800
250	500
300	500
350	500
400	400
450	500
500	500
550	400
600	400
700	500

Above 300 °C, once the PMMA had been removed, the decrease in fibre size was attributed to decreased particle size caused by the extra thermal energy. The extra thermal energy will reduce the stability of larger particles, encouraging them to form smaller, more thermodynamically stable aggregates.

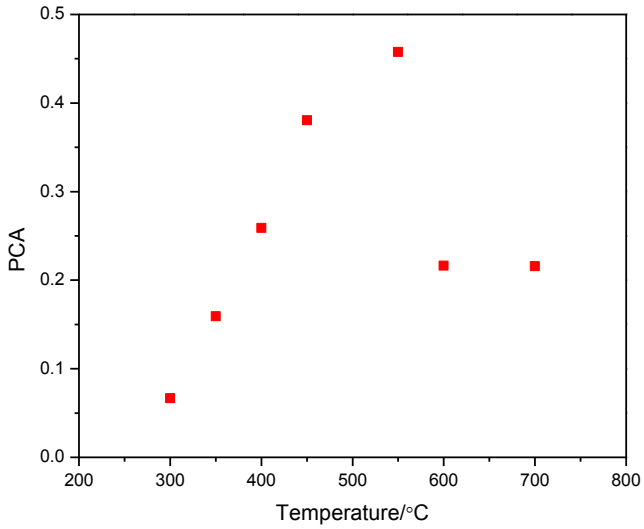

Figure 2.31. Photocatalytic activity of TiO_2 nanofibres as a function of calcining temperature. The photocatalytic activity increases with increasing anatase content, but drops sharply at 550 °C when the rutile phase content becomes non-negligible.

Figure 2.31 shows the photoactivity of TiO_2 nanofibres as a function of calcining temperature, for all the crystalline samples (> 300 °C). It can be observed that from 300-550 °C the photoactivity increased. This is in good agreement with Răileanu *et al*. who observed that photoactivity increased with respect to calcining temperature and found that 500 °C was the optimum calcining temperature for maximum photoactivity.[178] The photoactivity was then observed to decrease at calcining temperatures above 550 °C, which matches the trend of the phase change from anatase

to rutile observed in the X-ray diffraction data. The maximum photoactivity is observed at the same temperature as the maximum anatase composition of the fibres and decreases when the rutile phase content becomes non-negligible. This is good evidence that the photoactivity of TiO_2 is largely dependent on its crystal phase. In our work, it has been shown that almost pure anatase phase TiO_2 nanofibres, with a small amount of rutile, show the highest photoactivity towards the degradation of phenol. Crystallite size was also determined to have an effect on photoactivity, as crystallite size was observed to change following the same trend as photoactivity. However, photoactivity decreases more rapidly above 550 °C than crystallite size, therefore under these conditions it is concluded that the crystallinity of the TiO_2 is more important in determining the photoactivity than fibre diameter or crystallite size.

2.5 Conclusions

It has been shown that TiO_2 nanofibres can be produced by electrospinning a PMMA in DMF solution in a controlled and consistent manner, at a rate of ~0.02 g/hr. The control in the production is achieved by carefully selecting intrinsic and extrinsic variables, all of which will have a non-negligible impact on the morphology and diameter of the product and the ease of production.

Modification of the nozzle diameter alters the fibre diameter, where larger diameter nozzles give rise to less control of the size and morphology of the product. Reducing the nozzle diameter from 1.5 mm to 1.0 mm reduced the deviation of fibre diameter and decreased the beads found in the fibres.

The systematic alteration of voltage was shown to affect the morphology and diameter of the product. At low voltages, the electric field was not strong enough to extrude fibres from the nozzle and high voltages were observed to increase the rate of evaporation of solvent, leading to blockages and beads.

Variation of the distance between nozzle and collector was shown to affect the fibre diameter and morphology. Both inconsistent fibre diameter and a larger concentration of beads were observed at shorter distances, due to the short distance not being sufficient to allow for the evaporation of the solvent before reaching the collector. At longer distances the fibres were unable to reach the collector and, therefore, collected on the nearest grounded surface.

It was found that both diameter and viscosity increased exponentially as a function of PMMA concentration. An exponent of 0.4 was found for the relationship between concentration and fibre diameter. The plot of viscosity as a function of PMMA concentration was found to be biphasic, with exponents of 0.4 and 3.4 for the semi-dilute un-entangled and semi-dilute entangled concentration regions respectively. The critical chain overlap (c*) and critical chain entanglement (c_e) have been observed, and are in good agreement with literature values. Based on these results, it has been determined that the morphology and diameter of the fibres produced directly results from the viscosity of the solution, which is dependent on polymer concentration and molecular weight. As the molecular weight of the polymer remained constant, it can be inferred from my studies that viscosity is solely determined by the concentration of the PMMA.

Having determined the influence of the intrinsic and extrinsic variables; fibre diameter, viscosity, nozzle diameter, concentration, voltage and deposition distance, the

accurate and precise control over length scale and morphology has been achieved. Given that the properties of nanomaterials are dependent on length scale and morphology, the electronic properties and chemical reactivities are expected to be well controlled using this preparation method.

The degradation of PMMA occurs in three steps; polymer head to head scissions, polymer chain end scissions and random scissions. The first two of these were observed by FT-IR spectroscopy. The second two were observed in both UV-Vis spectroscopy and DSC. The temperatures of these transitions were in good agreement with literature, 165, 260 and 375 °C respectively for the three degradation steps.

An optimum calcination temperature of 550 °C was determined by photocatalytic investigations, which is in good agreement with literature. X-ray diffraction analysis as a function of calcining temperature revealed that photocatalytic activity drops at the same temperature that the anatase phase begins to decrease, with the commensurate increase in rutile phase. This optimum sample was majoritively anatase with a small amount of rutile phase. As the change in activity more closely followed the crystal phase of TiO_2 rather than crystallite size or fibre diameter, the change in activity was attributed to be more dependent upon the TiO_2 phase.

3. Photon and Phonon Activated TiO_2 for the Decomposition of Phenol

The photooxidising ability of TiO_2 is well established, due to its inherent abilities as a semiconductor but the excitation of electrons can also be accomplished thermally. In this chapter I quantify the oxidising ability of both photon and phonon activated TiO_2, in two different morphologies, used for the oxidation of phenol. The two chosen morphologies were pristine TiO_2 nanofibres, produced in-house, and P25 powder (Sigma-Aldrich 99.5 %) which were used as the benchmarks in the remainder of this project.

P25 is a 75 % anatase: 25 % rutile TiO_2 powder, with a crystallite size of ~21 nm and a specific surface area of 35-65 m^2/g. The pristine nanofibres prepared were almost 100 % anatase TiO_2 with a small amount of rutile phase present (~ < 1 %), with a fibre diameter of ~400 nm. Specific surface area measurements were unavailable however, He *et al*. found their fibres, of similar dimensions and composition, to have a specific surface area of 15.2 m^2/g.[179] Despite the predicted decrease in surface area, nanofibres are advantageous compared to P25 as they can be synthesised uniformly and with a greater control over the dimensions.

In this chapter, a review of the degradation of phenol by TiO_2 is provided. The photocatalytic results of both pristine TiO_2 nanofibres and commercial P25 powder are compared. The relationship between incident light intensity and photocatalytic activity has also been investigated with respect to the distance between the reactor and the radiation source. Finally, as an alternative to photoactivation, thermal excitation of TiO_2 has been discussed and investigated. The details of the preparation of the catalysts are

discussed in Section 7.2 and the details of the determination of photoactivity are discussed in Section 7.3 and Section 7.4.

3.1 Degradation of Phenol by TiO_2 Nanomaterials

Phenol was chosen as the benchmark volatile organic compound because, like a number of pollutant compounds, it contains an aromatic ring but is itself relatively low cost and non-toxic. The degradation of phenol by photoactivated TiO_2 was initially thought to be first order,

$$r = -\frac{d[PhOH]}{dt} \tag{3.1}$$

or,

$$r = k[PhOH] \tag{3.2}$$

However, more recent evidence has shown that the degradation is pseudo first order,[180,181]

$$r = k[PhOH][O_2] \tag{3.3}$$

when O_2 is in excess it becomes constant and, therefore,

$$r = k'[PhOH] \tag{3.4}$$

Equation 3.4 describes that the concentration of phenol is proportional to rate of the degradation.

Hucthings and Besenbacher proposed that during photocatalysis phenol degrades by one of two pathways, where each require seven oxygen atoms and twenty

eight electrons to completely oxidise phenol (Scheme 3.1).[180] One pathway occurs *via* *p*-benzoquinone and the other *via* hydroquinone. However, there can be inter-conversion between hydroquinone and *p*-benzoquinone *via* redox reactions. For each oxidation of hydroquinone to *p*-benzoquinone two electrons are required, reducing the efficiency of the oxidation of phenol.

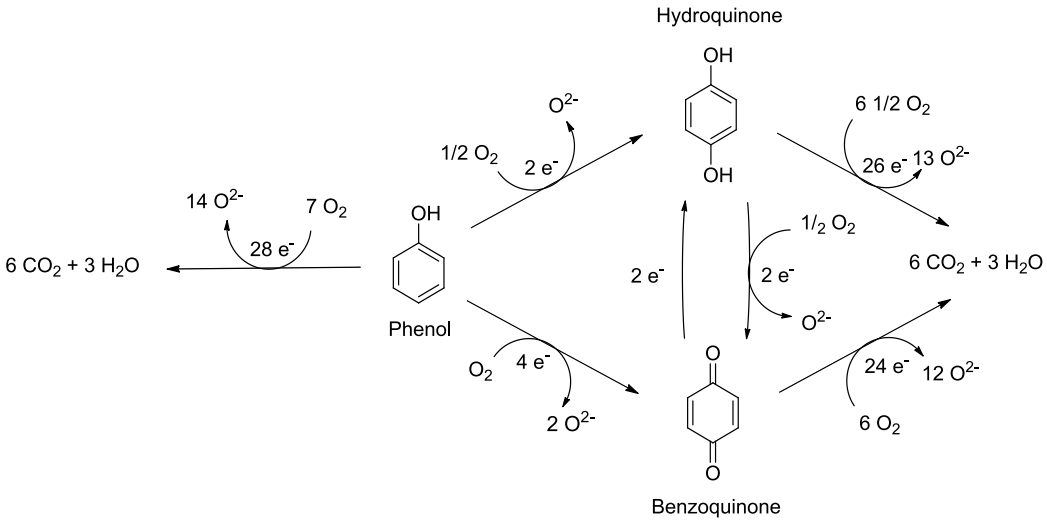

Scheme 3.1. Degradation pathways of phenol. The left pathway shows the direct decomposition of phenol to CO_2 and H_2O. The right pathways show the decomposition of phenol via two derivative compounds. Hydroquinone and benzoquinone can interconvert, where the oxidation of hydroquinone to benzoquinone reduces the efficiency of the decomposition as it requires 2 electrons. [180]

Hutchings and Besenbacher observed hydroquinone to be the dominant side product in the photooxidation of phenol by native TiO_2, reaching a maximum of 25 % of the initial phenol concentration. However, *p*-benzoquinone was found to be the dominant side product when using gold, palladium and gold/palladium loaded TiO_2.[180] This was attributed to the excess of electrons produced by photoactivated TiO_2 driving the equilibrium towards *p*-benzoquinone.

Radical affinity and adsorption on to TiO_2 are partly determined by the substituent groups present on the phenolic compounds.[85] Adsorption onto TiO_2 is determined by the strength of the electron withdrawing groups on the α-carbon, the stronger of which will increase the interaction between Ti-O(H)-Ph.[182] Figure 3.1 shows the rate of adsorption onto TiO_2 of phenol and several of its derivatives.

$$Catechol \gg phenol > resorcinol > m-creosol > o-creosol$$

Figure 3.1. Rate of adsorption onto TiO_2, as determined by the strength of the withdrawing group on the α-carbon.

Phenol adsorbs at the Ti-OH interface where it is then attacked by OH radicals, forming dihydroxybenzenes. The attack can occur at three different positions on the phenol ring. Parra *et al.* found that the photooxidation of the dihydroxybenzenes occur at a faster rate than phenol, this was attributed to the *ortho-para* directing nature of the hydroxyl group.[183] Of the dihydroxybenzenes there are four potential activation sites where OH radicals can be directed towards. In the cases of hydroquinone and catechol OH radicals are directed to all four of these sites. Resorcinol is only activated at three of these sites, however, each of those sites is doubly directed to (by each hydroxy group). Figure 3.2 shows the possible attack sites of phenol and three dihydroxybenzenes, where the arrows indicate the attack sites of the OH radical.

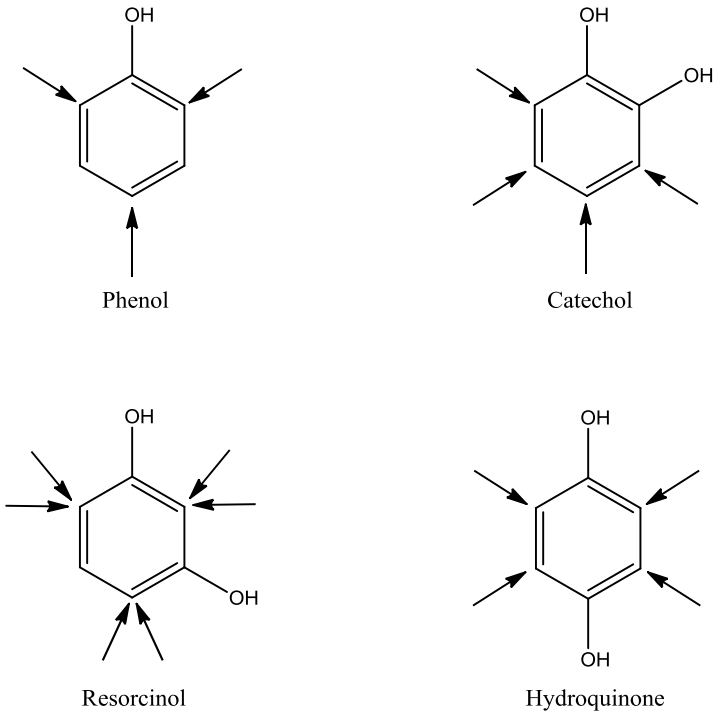

Figure 3.2. Structures of phenol and dihydroxybenzenes, with indicated directing positions.

The degradation of these aromatic compounds by TiO_2 follows the order; resorcinol>hydroquinone>catechol.[183] This provides evidence that the position of substituent is important in the degradation of aromatic compounds. The lower degradation rate of phenol compared to its daughter compounds is because phenol only mono-directs at three sites. This has also been observed in chlorinated phenols, where the initial attack of the hydroxyl radical has the greatest effect on overall degradation, determined by stabilisation of the incoming hydroxyl group.[184] When the system is at pH 5, the rate of degradation of phenol can be increased by the addition of H_2O_2 as it provides more hydroxyl radicals.[88] This is because hydrogen peroxide can be split by UV light to ·OH.[89]

After the addition of an additional hydroxyl group the aromatic ring breaks open into muconic acid, then maleic or fumaric acid (isomers) then oxalic acid which breaks

down into formic acid.[185] Formic acid can then easily be broken down into CO_2 and H_2O – mineralisation.

3.2 Photocatalytic Studies

Photodegradation of phenol was performed by illuminating the TiO_2 catalyst at regular intervals, with a constant gas flow of phenol polluted O_2. The gas stream was captured in a 1 M $NaOH_{(aq)}$ collector at the end of the photoreactor. The purpose of the sodium hydroxide was to trap phenol as sodium phenolate, which is less volatile than phenol, and to provide a more intense UV-Vis spectroscopic handle. The phenol present in the collector was measured at regular intervals by UV-Vis spectroscopy. During illuminated periods the catalyst is considered activated and the increase in concentration of phenol in the collector should be slow, the rate of which will be determined by the effectiveness of the photocatalyst. Conversely, during non-illuminated periods, the catalyst is considered deactivated and the concentration of phenol will increase at a faster rate, determined by the flow rate of the polluted gas stream. The UV-Vis absorption of sodium phenolate was observed at λ_{max} = 288 nm. Absorbances for neither benzoquinone, λ_{max} = 246 nm or hydroquinone, λ_{max} = 270 nm, nor any other intermediates, were observed in this study by UV-Vis spectroscopy. GC-MS analysis of the collector solution and the atmosphere above the solution, further revealed no evidence of any compounds other than sodium phenolate. This was evidence that phenol had been completely mineralised to water and carbon dioxide.

3.2.1 P25

The photocatalytic activity (PCA) of commercial P25 was measured as a benchmark, with SEM analysis to confirm its morphology. SEM images of commercial P25 show that the TiO_2 is uniformly present in powdered crystallite form (Figure 3.3).

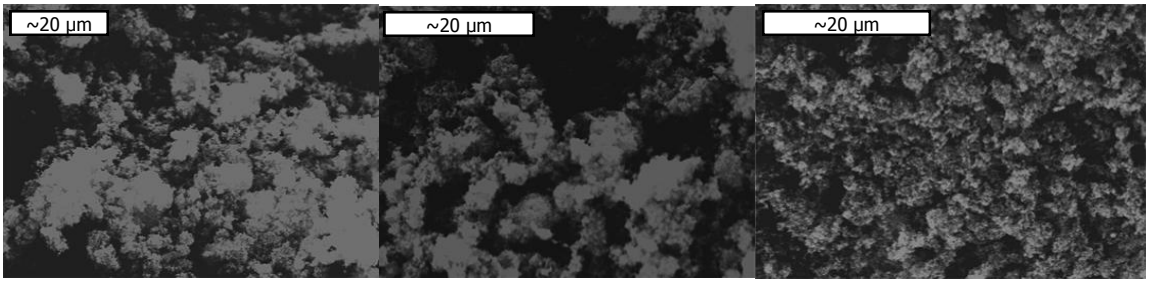

Figure 3.3. SEM images of P25 showing it's powdered morphology.

Figure 3.4 shows the X-ray diffraction pattern of P25 powder. The anatase (a) and rutile (r) indexes can clearly be seen while no presence of any impurity was observed.

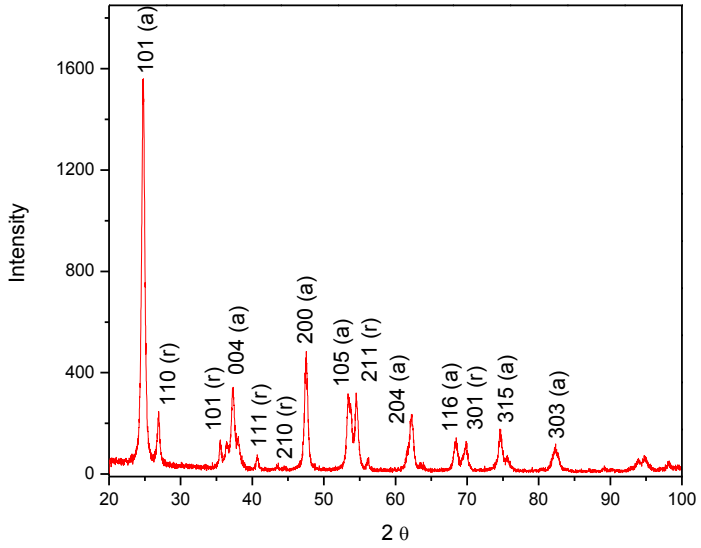

Figure 3.4. Powder diffraction pattern of P25 TiO_2, where the rutile (r) and anatase (a) phases can be distinguished from each other. Obtained at University of Sussex, 2012, Wei Cheet Lee and indexed from ICDD.

Prior to photocatalytic studies, the P25 was dried at 100 ˚C overnight, but was otherwise used as purchased. The catalyst was tested three times, where each test contained a minimum of two on/off cycles of illumination. An average photocatalytic activity was taken of the three tests and a value of 1.13 was determined.

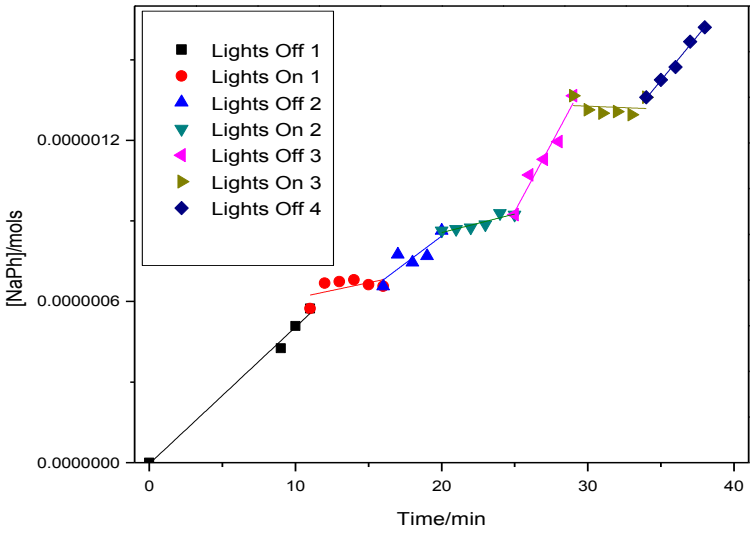

Figure 3.5. Photocatalytic data of P25. The horizontal lines represent the lights on periods, where the catalyst is considered activated and build-up of phenol in the collector is slow. The more vertical lines represent the lights off periods, where the catalyst is considered de-activated and the build-up of phenol of fast. The difference in gradients of the lights on and lights off periods gives rise to the photocatalytic activity (PCA).

In Figure 3.5 the data set for one of the P25 tests is shown, where the more horizontal lines correspond to the periods of UV illumination and the more vertical lines correspond to periods of no UV illumination. Qualitative information on the activity of the catalyst can be determined by the relative slopes of the illuminated and non-illuminated periods: where the closer to horizontal the slope, the higher the rate of phenol degradation. The details of the determination of photocatalytic activity are listed in Chapter 7. When using P25 the slope of the illuminated periods is near to horizontal, indicative of a high level of phenol decomposition.

3.2.2 Pristine TiO_2 Nanofibres

Pristine TiO_2 nanofibres were prepared by electrospinning 10 wt. % TTiP in a 7 wt. % PMMA in DMF solution. The product was steam treated at 80 °C for one hour and calcined at 550 ˚C overnight to yield TiO_2 fibres (Figure 3.6).

Figure 3.6. Picture of TiO_2 nanofibres immediately after electrospinning. The product is a non-woven mat of approximately 2 mm depth.

SEM imaging revealed TiO_2 to be present in the form of interwoven nanofibres of ~400 nm diameter that were found to be smooth and bead free (Figure 3.7).

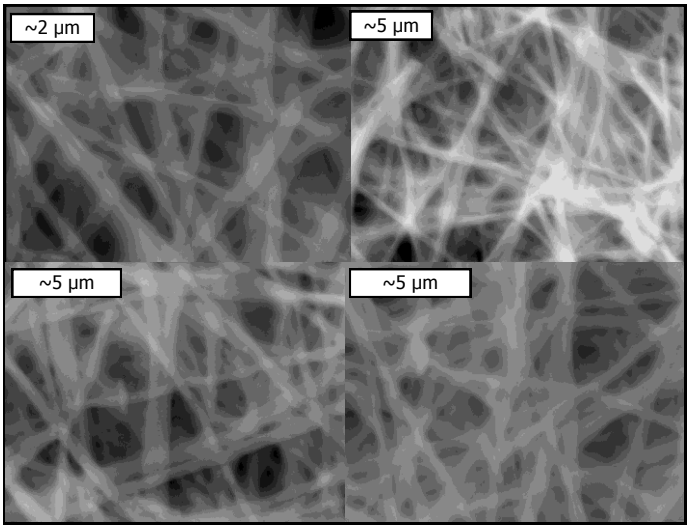

Figure 3.7. SEM images of TiO_2 nanofibres that are uniformly fibrous and ~400 nm diameter.

Figure 3.8 shows the X-ray diffraction pattern of the TiO_2 nanofibres used in these studies. The anatase phase was observed as the dominant crystallinity of TiO_2, however, a small amount of rutile was also observed.

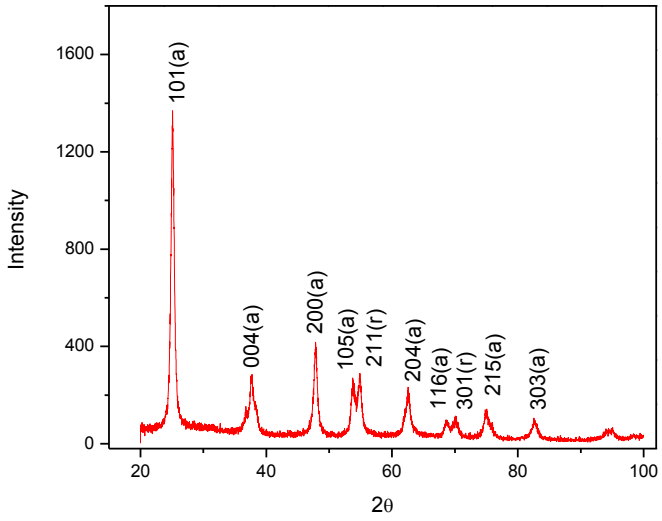

Figure 3.8. X-ray diffraction pattern of TiO_2 nanofibres used in these photocatalytic measurements. The diffraction pattern was indexed from ICDD.

The photoactivity of these fibres was tested three times, where each test contained at least two on/off cycles of illumination. The activity during each test was measured and an average of 0.47 calculated. The activity of TiO_2 nanofibres was found to be less than half that of P25 powder; the reasons for the difference in activity are discussed in Section 3.2.3.

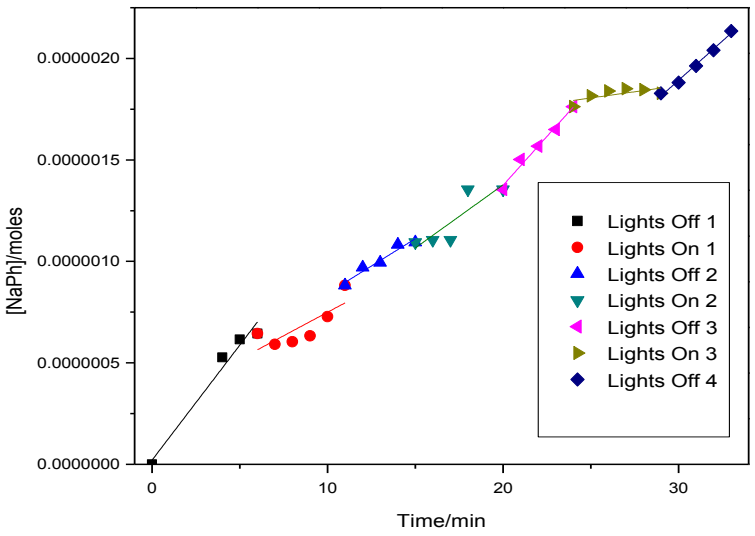

Figure 3.9. Photocatalytic data taken for one run of pristine TiO_2 nanofibres. The horizontal lines represent the lights on periods, where the catalyst is considered activated and build-up of phenol in the collector is slow. The more vertical lines represent the lights off periods, where the catalyst is considered de-activated and the build-up of phenol of fast. The difference in slope between the lights on and lights off periods is smaller than for P25 powder indicating a lower photocatalytic activity.

In Figure 3.9 the data sets for one test of pristine TiO_2 nanofibres can be seen. It can be observed that during the illuminated periods, the gradient is steeper than for P25, qualitatively indicating a lower photoactivity for our TiO_2 nanofibres.

3.2.3 Comparison of P25 and TiO_2 nanofibres

Chemical composition and mass were kept constant between pristine TiO_2 nanofibres and P25, but there were several important differences. P25 powder is a mixture of 75 % anatase and 25 % rutile phase TiO_2, compared to the pristine nanofibres which are nearly 100 % anatase, with the remainder being rutile. In Chapter 2 it was observed that as the rutile content of the nanofibres increased, the photocatalytic activity decreased. As the TiO_2 nanofibres discussed in this chapter have lower rutile content than the P25, it is clear that the difference in photoactivity is not solely determined by the crystal phase.

The crystallite size of P25 was found to be higher than that of the nanofibres, at 16.5 nm compared to 12.9 nm. While a smaller crystallite is associated with a higher surface area, Ying *et al.* found that at crystallite sizes below ~10 nm activity drops as surface recombination of electron–hole pairs becomes prominent.[186] As the crystallite size of the nanofibres is close to this critical size, its rate of recombination is theorised to be higher than that of P25. Finally, the increased surface area of P25 is likely to lead to an increase in photoactivity. Based on literature reports, the specific surface area of ~400 nm diameter TiO_2 fibres is ~15.2 m^2/g,[187] roughly half the specific surface area of the P25 used (35-65m^2/g). From our studies we attribute the increase in photoactivity of P25 to be a combination of increased surface area, leading to more active sites, and a larger crystallite size, reducing the rate of recombination.

3.2.4 Degradation of Other VOCs by TiO_2 Nanofibres

In order to examine the efficacy of titania nanofibres in the decomposition of a broad number of organic compounds, TiO_2 was used to photooxidise acetanilide,

acetone, dimethyl formamide and toluidine blue. Previous decompositions were performed solely using phenol as the target VOC due to its relatively low toxicity, low price and characteristic UV absorbance however, in real applications the photocatalytic reactor will have to remove many other VOC traces.

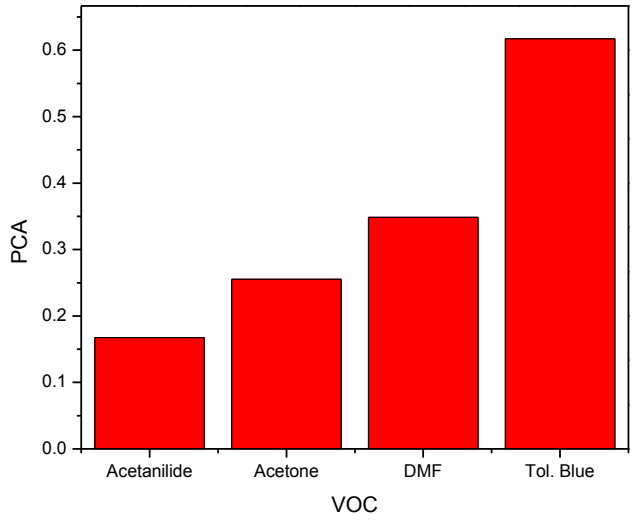

Figure 3.10. Photocatalytic activity of four other VOCs. They have all been shown to decompose non-negligibly by UV light activated TiO_2 nanofibres. The efficiencies of decomposition are thought to be largely due to ease of attack by OH radicals and the volatility of the compounds.

The photooxidation of all four compounds was observed with varying levels of decomposition. To our knowledge neither DMF nor toluidine blue have been used as target molecules for photooxidation. The four compounds were chosen due to their containing a selection of functional groups including amides, ketones and conjugation. TiO_2 showed the lowest affinity towards acetanilide, a sentiment confirmed by Ameta *et al.* in the decomposition of *p*-nitroaniline, *p*-aminophenol and acetanilide, in the presence of CdS and Fenton's reagent.[26] Reasons for low activation are attributed to

acetanilide's low solubility in water and relative low volatility. The photooxidation of acetone by titania has also been observed by Henderson *et al.*, who found good levels of VOC removal.[27,28] The degradation of dyes by semi-conductors is well established and it is likely that TiO_2 showed the same affinity for toluidine blue.

Whilst the effective degradation of each organic compound is unique, it has been shown that UV light activated TiO_2 will decompose a variety of organic compounds. This shows promise for industrial applications where the composition of polluted gas streams will not be restricted to solely phenol.

3.2.4 Photocatalytic Activity as a Function of Incident Light Intensity

To explore the UV illumination influence on the catalytic degradation of phenol, the UV light source was incrementally moved away from the reactor tube and PCA measurements taken. It was predicted that intensity would reduce as a function of distance, at a rate of $1/r^2$, and that the degradation of phenol would follow this trend, indicating a linear relationship between light intensity and photocatalytic activity. This was observed not to be the case, as photooxidation of phenol decreased linearly as a function of illumination distance (Figure 3.11).

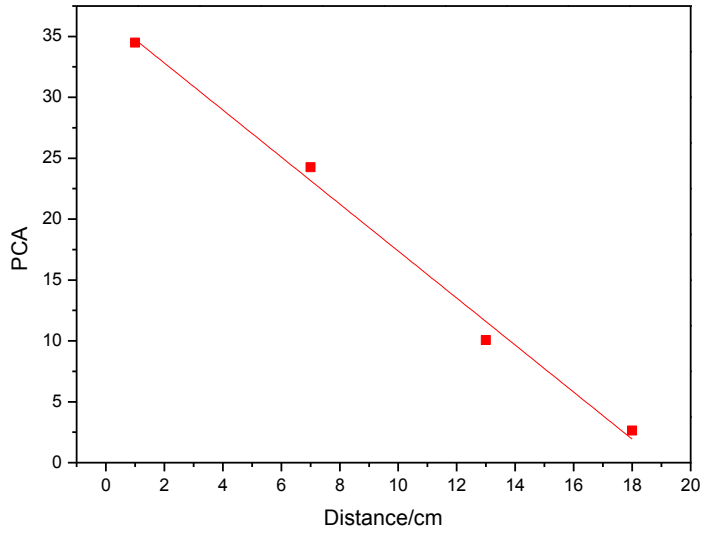

Figure 3.11. Photocatalytic activity as a function of incident light distance. The degradation of phenol with respect to UV light distance was observed to be linear when it was predicted to follow the trend of $1/r^2$. The reason for this unexpected trend is that the absorption of photons is first order.

The decrease in photoactivity is a result of decreased photon flux towards the reactor. This is trend is revealed in Figure 3.12 where it is observed that light intensity decreases linearly with distance. Light intensity usually decreases with $1/r^2$, however, several authors have found at low intensities, this relationship is first order because the absorption of photons is first order.[184,188–190] At higher light intensities there is an excess of photons, therefore the relationship becomes squared due to the creation of more electron hole-pairs which rapidly recombine.[188] At very high intensities the activity becomes independent of increasing intensity because only a maximum amount of photons can be absorbed by a finite amount of catalyst.

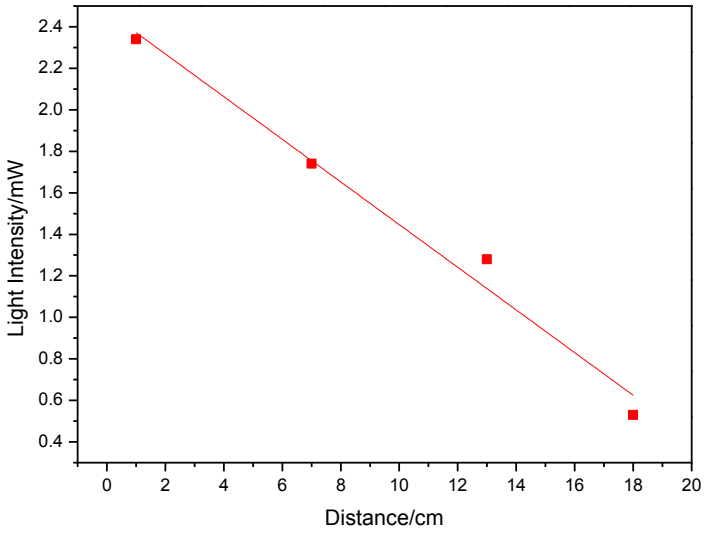

Figure 3.12. Light intensity as a function of incident light distance. The linear trend is due to the absorption of photons being first order.

3.3 Phonon Activated TiO_2 Nanomaterials

3.3.1 Benefits and Physics of Thermal Activation

While the performance of these oxidation and reduction centres can be exceptional, their use in everyday life is hindered by the inefficient activation of TiO_2 by ambient light. TiO_2 activation requires UV radiation of 385 nm, which only accounts for 3 % of natural light, therefore most laboratory experiments require the use of UV lamps.[3] This reduces the efficiency of any catalysis taking place because of the added energy cost of running a light source. As an alternative, thermal excitation can be used to create electron-hole pairs. An advantage of thermal activation is that is does not suffer from issues of light penetration, such as when TiO_2 is impregnated into a support such as a zeolite.

Nearly free electron physics states that thermal excitations can occur in a semiconductor, but to a lesser extent than in a metal, due to the presence of the bandgap. At any temperature above absolute zero, a percentage of the electron population will be above the Fermi level. The number of excited electrons in the bottom level of the conduction band has been shown to be in the order of 10^{-10} for silicon at room temperature. This distribution can be approximated by Fermi-Dirac statistics,[191] where it is assumed that half odd-integer spin particles will not interact in any significant way. This is expressed by the Fermi-Dirac equation (Equation 3.5). It states that as the temperature increases the population of excited electrons increases.

$$n_i = \frac{1}{e^{(e-\mu)/kT}+1} \tag{3.5}$$

where μ is the energy of the Fermi level, or the potential energy of an electron in a crystalline solid k is the Bolztman constant and T is the temperature. Following the Pauli exclusion principle, the effect of thermal excitation is relatively small, as only the top layer of electrons in the valence band are able to be excited. Electrons in lower levels cannot be excited without a much larger activation energy.

As charge carrier mobility is only weakly dependent on temperature, any increase in activity can almost be solely attributed to increased charge carrier concentration.

To compare thermal excitation with UV excitation, the gas phase decomposition of phenol over 0.1 g of TiO_2 nanofibres was investigated in three stages;

1: Using no catalyst and no UV illumination the reactor was heated at increasing temperatures in on-off cycles. This was predicted to show negligible decomposition of the phenol and was used as a baseline.

2: Stage 1 was repeated with the addition of 0.1 g of TiO_2. This was predicted to show the decomposition of phenol with activity increasing with temperature. The baseline was subtracted from these values to show the true effect of thermally activated TiO_2.

3: The reactor was filled with 0.1 g of catalyst and kept at a constant temperature throughout the experiment. The sample was subjected to UV radiation in cycles in order to study the combinatory effects of thermal and UV activation. Based on research by Melosh *et al.* we expect the degradation of phenol to be increased when both activation methods are combined.[192]

3.3.2 Thermal Activation of a TiO_2 Catalyst

A background reading was taken by measuring the thermal degradation of phenol without any catalyst. In order to simulate the presence of a catalyst, the reactor was packed with glass wool and covered with aluminium foil to block out ambient UV light. Without a catalyst or UV illumination very little phenol degradation was observed until 400 °C, where the activity was found to be 0.15. This observed degradation is from the direct thermal decomposition of phenol. The pyrolysis of phenol is well documented,[193,194] where it has been calculated that the temperature of decomposition is 500 °C, however, experimentally it is possible for decomposition to occur at lower temperatures.[195]

Upon the addition of 0.1 g of TiO_2 nanofibres, a significant level of degradation was observed. The degradation of phenol was significantly greater with the TiO_2 catalyst present than without, indicating the thermal activation of semiconductors for

oxidation reactions is possible. Finally, the temperature and UV activation were combined to show their compounded effect.

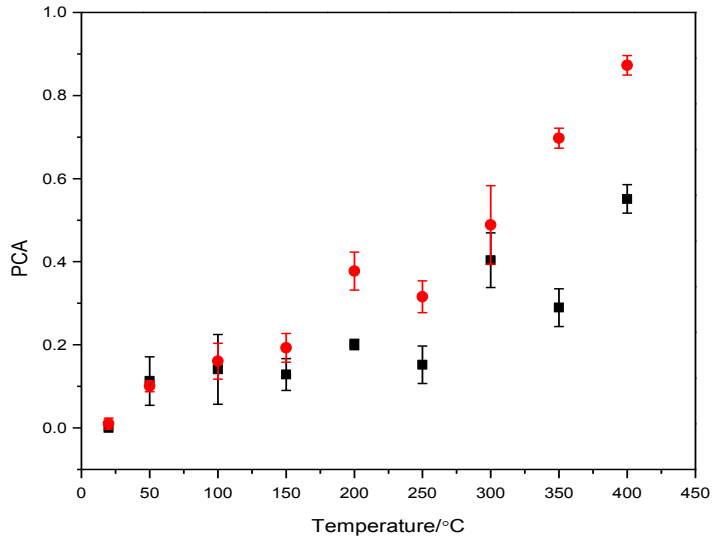

Figure 3.13. Catalytic activity as a function of reaction temperature. Black: thermal activation only. Red: combined thermal and UV activation. The error bars represent the standard deviation of the catalytic activities. The decomposition of phenol but thermally activated TiO_2 is equal to the decomposition of phenol by UV irradiation. When thermal and UV activation methods are combined, the decomposition of phenol is twice as much as either thermal or photo activation separately.

Figure 3.13 shows a linear trend for both thermal activation of TiO_2, and combined thermal and photoactivation of TiO_2. The R^2 value for thermal activation is 0.75, which increased to 0.92 when thermal and photo activation were combined. This indicates a stronger dependence on UV activation compared to thermal activation. However, the activity of only thermal activation is 0.55 compared to 0.47 for only UV activation. The slight decrease in phenol degradation when using photon activated TiO_2

was attributed to inefficient light penetration of the catalyst. When both activation methods are combined there is an increase in activity to 0.87, almost double either photon or phonon activation, which we attribute to photon enhanced thermionic excitations. In solar energy conversion, Melosh *et al.* observed a 70 % increase in efficiency when thermal emissions were photon enhanced,[192] which they also attributed to an increased number of emitted electrons when the two excitation methods were combined.

3.4 Conclusions

TiO_2 has been shown to successfully oxidise phenol under photoactivation using UV lamps as the photon source. The degree of phenol removal was more than twice as effective by P25 as for TiO_2 nanofibres. This was attributed to the increased surface area of P25 powder and the smaller crystallite size of the nanofibres increasing recombination rate. No intermediates or side products of phenol were observed by GC-MS or UV-Vis absorption. This indicates either the complete mineralisation of phenol, to CO_2 and H_2O, or that the concentrations of intermediates and side products are below the detection limits of the analytical method. *In situ* measurements or end of line CO_2 analysis would give more insight into the degradation pathway. If our catalyst system does indeed completely mineralise phenol to CO_2 and H_2O then it is an ideal photocatalytic set-up as there are no toxic by-products, which is desirable for a commercial photocatalyst.

The relationship between photon flux and photocatalytic activity as a function of illumination distance has been determined, where it was found that both of these decreased linearly as distance was increased. This is due to the intensity of light being

first order with respect to distance at low light intensities. This knowledge gives a greater understanding of the photon-catalyst relationship and proves useful in the design of future photocatalytic reactors.

Thermal activation of TiO_2 was shown to be effective for the removal of phenol. At 400 °C a similar rate of degradation was observed compared to UV activation. When thermal activation was combined with UV illumination, the photocatalytic activity increased to double that of either individual activation method. This provides an extra activation method for TiO_2 when UV sources are unavailable. Furthermore, the combined activation methods can increase the removal of VOCs from polluted gas streams.

4. Doped TiO_2 Nanofibres

To excite an electron in titania, radiation of above 375 nm is required, which is in the UVA region of natural light. As this only accounts for 3 % of ambient light, there is a barrier to overcome before TiO_2 photocatalysis can be successfully integrated into everyday life.[196] The inherent inefficiency of photoactivation of TiO_2 by natural light has led to research into the extension of the bandgap, to encompass the visible light response. Thus far, the most popular method for the alteration of the bandgap of TiO_2 is by the addition of dopants into the titania lattice.[55,197] Extensive research has been undertaken towards the loading of other atoms into titania where, aside from altering the electronic properties, increased surface area and more effective electron–hole pair separation have been observed. Dopants are often chosen based on their cost, ease of availability and toxicity. For these reasons, main-group elements and d-block metals are commonly used.

In this chapter the investigation of the photooxidation of phenol by metal oxide doped TiO_2 nanofibres is presented. Six transition metals, which had shown promise in the literature, were chosen as dopants of TiO_2. These were added immediately prior to electrospinning, in concentrations of 0.01-50 mol %, which altered the colour of the precursor polymer solution, the concentration of the dopant influencing the intensity of the colour. After steam treatment and calcination, colour changes were observed, indicating that the precursors had transformed into their metal oxides, and were characterised by SEM imaging and powder X-ray diffraction. Furthermore, powder X-ray diffraction was used to gain information on the location of the dopant, and to determine the crystallite sizes, by the Scherrer equation.

4.1 Methods of Doping

There are two common methods used in the doping of metal oxide semiconductors; dye-sensitisation and lattice doping. In the first, the semiconductor can be sensitised by adding a dye which will absorb in the visible light region, freeing an electron.[198] This electron can then be injected into the conduction band of the bulk material. Alternately the lattice can be impregnated with dopants, which can result in impurity states in between the valence and conduction bands of the bulk material (Figure 4.1). This can result in lower energy bandgaps, where less energy is required to facilitate transitions.[196]

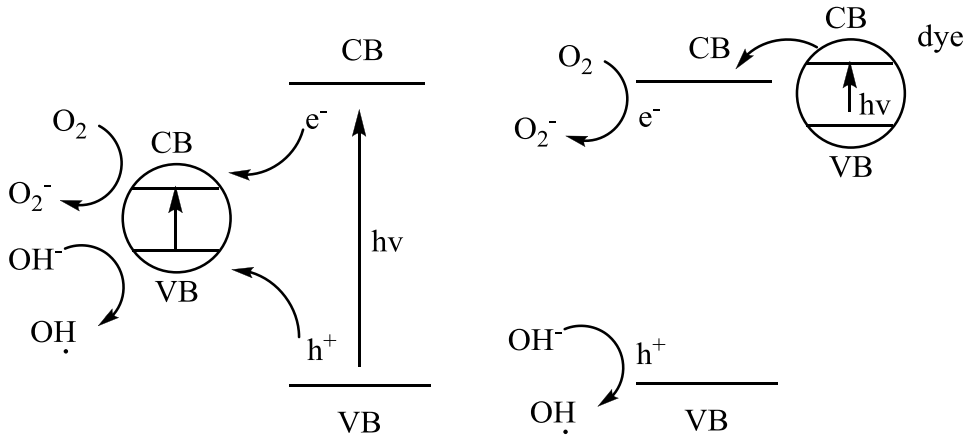

Figure 4.1. From left, impurity state and dye sensitised methods of doping. In impurity state doping an additional energy level is added within the band-gap, reducing the energy required for the excitation of an electron. In dye-sensitised doping a dye absorbs light, usually in the visible region, and injects this electron into the conduction band of the semi-conductor.

Loading transition metals into the lattice of TiO_2 predominantly leads to the formation of impurity states. Figure 4.2 shows the calculated density of states in the bandgap of rutile TiO_2 when doped with a variety of transition metals.[199] The impurity states formed by the dopants can be seen within the bandgaps.

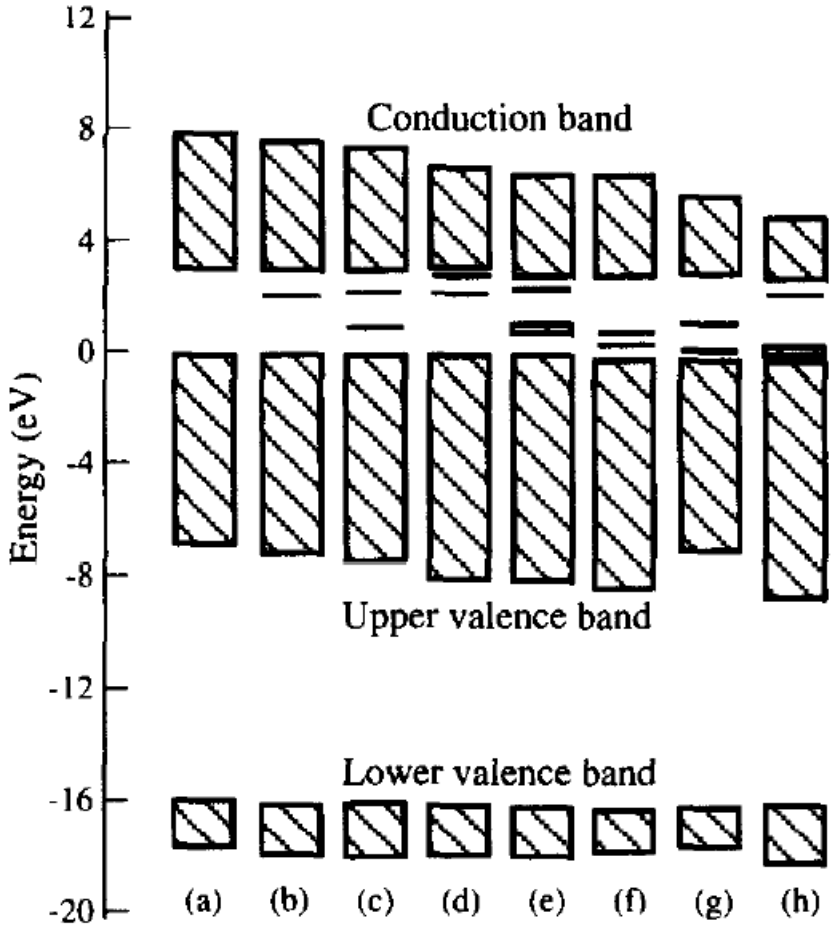

Figure 4.2. Energy bands for transition metal doped rutile titania. (a) undoped, (b) V^{4+}, (c) Cr^{4+}, (d) Ni^{4+}, (e) Mn^{3+}, (f) Fe^{3+}, (g) Co^{3+}, (h) Cu^{3+}.[199] The impurity states can be seen within the bandgaps of the transition metal doped titania.

A change in the bandstructure can be spectroscopically measured, as discussed in Sections 1.8.3 and 1.8.4, where the terms ‘red-shift’ and ‘blue-shift’ are used to refer to lower and higher energy bandgap shifts respectively.

4.2 Electronics of Doping

Band gap modification

The bandgap of TiO_2 can be modified by the addition of a dopant to the lattice, resulting in a red-shift towards the visible light region of the electromagnetic spectrum. For example, Fe_2O_3 loaded TiO_2 nanofibres were found to enhance the photooxidation of methylene blue (MB), which was attributed to a red-shift in the bandgap.[200] Martinez-Arias ascribed the extension of the bandgap to be due to charge transfer from Fe^{3+} 3d electrons to the TiO_2 conduction band and iron *d-d* transitions.[201] Similar results were obtained by Xu and Ao, and Wu and Chen, who found loading titanium with vanadium led to a visible light response and a higher photodegradation, of reactive brilliant red and methylene blue respectively, than an equivalent un-doped sample.[202,203] Wu and Chen attributed this to an extra state inserted between the valence and conduction bands caused by V^{4+} and V^{5+} either substituting Ti^{4+} in the lattice or sitting in vacancies.[10]

Non-metals have also been used to modify the bandgap, for example nitrogen has been observed to replace oxygen in the TiO_2 lattice, sensitising it to visible light.[204] Magrulka *et al.* observed a reduction in the bandgap to 2.65 eV upon lattice doping with nitrogen, which was found to be effective in the degradation of phenol and *o*-chlorophenol.[205]

Blue-shifts of band structure have also been observed. This is exemplified in Sn^{4+} doped TiO_2 nanoparticles, where UV-Vis absorption analysis revealed an increase in the bandgap with increasing tin loading in to the lattice, corresponding to a 0.9 eV shift at 10 % loading.[181] However, despite the continuing increase in bandgap, photoactivity

only improved against pristine TiO_2 up until 0.3 % Sn^{4+} loading, attributed to additional recombination centres formed at higher loadings.

Electron-Hole Pair Recombination

The doping of titania with metals is also thought to improve activity by the dopants providing shallow electron traps, retarding the electron-hole pair recombination rate. Scheme 4.1 details the processes involved in photooxidation of an organic species when Fe^{3+} is loaded into the TiO_2 lattice.[206] Scheme 4.1(a) and (b) are the generation of the electron-hole pair. Scheme 4.1(c) and (d) show the trapping of the charge carriers by the reduction and oxidation of Fe^{3+} respectively. Scheme 4.1(e) is charge migration, reducing $Ti^{4+} \rightarrow Ti^{3+}$, and Scheme 4.1(f) is the reduction of Fe^{4+} by a surface hydroxyl group, converting it to a hydroxyl radical. Scheme 4.1(g-j) detail the regeneration of Fe^{3+} by the hole, a hydroxyl radical, the electron and Ti^{3+} respectively. Finally, Scheme 4.1(k) and (l) show the interfacial charge transfer of the iron trapped electron and hole to an oxidant and reductant respectively.

$$Fe^{3+} + h\nu \rightarrow Fe^{4+} + e^{-} \qquad (a)$$

$$Fe^{3+} + h\nu \rightarrow Fe^{2+} + \quad h^{+} \qquad (b)$$

$$Fe^{3+} + e^{-} \rightarrow Fe^{2+} \qquad (c)$$

$$Fe^{3+} + h^{+} \rightarrow Fe^{4+} \qquad (d)$$

$$Fe^{2+} + Ti^{4+} \rightarrow Fe^{3+} + Ti^{3+} \qquad (e)$$

$$Fe^{4+} +> OH^{-} \rightarrow Fe^{3+} + \cdot OH \qquad (f)$$

$$Fe^{2+} + h^{+} \rightarrow Fe^{3+} \quad (g)$$

$$Fe^{2+} + \cdot OH \rightarrow Fe^{3+} + OH^{-} \quad (h)$$

$$Fe^{4+} + e^{-} \rightarrow Fe^{3+} \quad (i)$$

$$Fe^{4+} + Ti^{3+} \rightarrow Fe^{3+} + Ti^{4+} \quad (j)$$

$$Fe^{2+} + reductant \rightarrow Fe^{3+} + reductant^{-} \quad (k)$$

$$Fe^{4+} + oxidant \rightarrow Fe^{3+} + oxidant^{+} \quad (l)$$

Scheme 4.1. Electronics of iron doped titania. (a) and (b) charge carrier generation. (c) and (d) charge trapping. (e) and (f) charge release and migration. (g-j) charge carrier recombination. (k) and (l) charge transfer, where the oxidant is the organic compound to be oxidised.[206]

If an electron–hole pair separation can be extended beyond the nano-second scale,[207] then the quantum efficiency can be increased. The quantum efficiency is the ratio of the number of electron-hole pairs created compared to incident photons. This is thought to be why amorphous TiO_2 has very little photoactivity, because the non-bridging oxygens facilitate rapid recombination.[208] Li *et al.* argue that the charge trapping steps occur from Fe^{3+} located in different parts of that crystal. By EPR they observed two signals correlating to iron and assigned them to surface Fe^{3+} trapping h^{+}, g = 4.30, and bulk Fe^{3+} trapping e^{-}, g = 1.99.[73]

Physical Changes

As well as modifying the bandgap and slowing the rate of recombination, doping of TiO_2 can also result in a change in surface area,[77,209,210] alteration of the crystallisation temperatures[74–76] and increased surface hydroxyl groups.[211] An increase in surface hydroxyl groups can increase activity by providing more radicals with which to oxidise volatile organic compounds, however, an increase in OH radicals is associated with an increase of vacancies which can act as recombination centres.[212–214]

Combinatory Effects of Doping

There is no clear indication which of the above reasons is responsible for the change in activity observed where dopants have been employed, but it is likely that the effects are due to a complex combination of all the variables. However, it is generally agreed that doping levels above 5 mol. % show a decrease in photoactivity of the sample, attributed to an increased population of recombination centres.[215]

4.3 Photoactivity of Metal Oxide Doped Nanofibres

To determine the efficacy of different transition metal dopants, they were loaded into TiO_2 in concentrations of 0.01–50.00 mol %. The resulting photoactivities were examined as a function of loading of transition metal, and compared to pristine TiO_2 nanofibres and P25 powder. In Figure 4.3 the photo-degradation of phenol as a function of dopant loading concentration is presented for six different transition metal dopants.

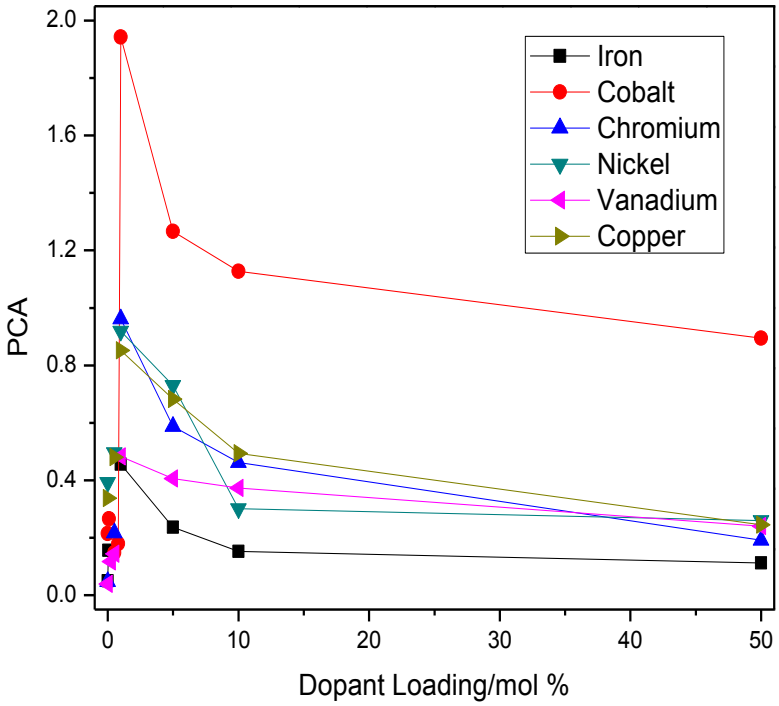

Figure 4.3. Photocatalytic activity as a function of dopant loading. All dopants show their highest activity at 1 mol %. The cobalt doped titania shows the highest activity. Even at 50 mol % loading the cobalt doped titania showed higher activity than undoped TiO_2, leading to a separate investigation of mono-metallic cobalt nanomaterials.

It was found that for all the transition metal doped samples investigated, the maximum efficiency was observed at 1.00 mol % loading. The photoactivities of all six dopants at 1.00 mol % loading can be seen in Table 4.1. At this loading the highest activity was seen for cobalt doped nanofibres at 1.94, four times increased activity compared to pristine TiO_2 nanofibres. The lowest observed activity was for iron loaded nanofibres (0.46), slightly lower than pristine TiO_2 nanofibres.

Table 4.1. Photocatalytic activity of six transition metal dopants at 1.00 mol % loading of titania.

Dopant	Iron	Cobalt	Chromium	Nickel	Vanadium	Copper
PCA (1.00 mol % loading)	0.46	1.94	0.96	0.92	0.48	0.85

At dopant concentrations 0.01-1.00 mol %, the photoactivity of all transition metal doped titania catalysts was lower than that of pristine TiO_2. This is attributed to the dopant retarding the crystallisation of TiO_2 into the anatase phase. As discussed in Section 2.4.3, the phase of TiO_2 was deemed to be of great importance in determining the photoactivity of the sample, where reactivity was observed to be at its highest when the TiO_2 was almost 100 % anatase. At lower loadings the photoactivation was close to that of native TiO_2 nanofibres. As the loading increased from 1.00–50.00 mol % the photoactivity rapidly decreased, until the observed photoactivity was lower than that of pristine TiO_2 nanofibres. Cobalt doped titania was the exception, and continually showed photoactivity higher than pristine TiO_2 nanofibres, even at 50.00 mol % loading. These results led to a separate investigation on mono-metallic cobalt compounds, which are discussed in Section 4.4. The details of the doped catalysts and their photocatalytic activities are discussed in detail in their individual sections.

4.3.1 Cobalt Doped TiO_2 Nanofibres

In order to prepare cobalt doped TiO_2 nanofibres, purple cobalt acetyl acetonate ($Co(AcAc)_2$) was used as the dopant precursor. The fibres prepared were smooth and

defect free at all concentrations, with no change in morphology observed as cobalt loading increased (Figure 4.4). The fibre diameter was ~400 nm and did not change until cobalt loading reached 50.00 mol %, where fibre diameter increased to ~1000 nm.

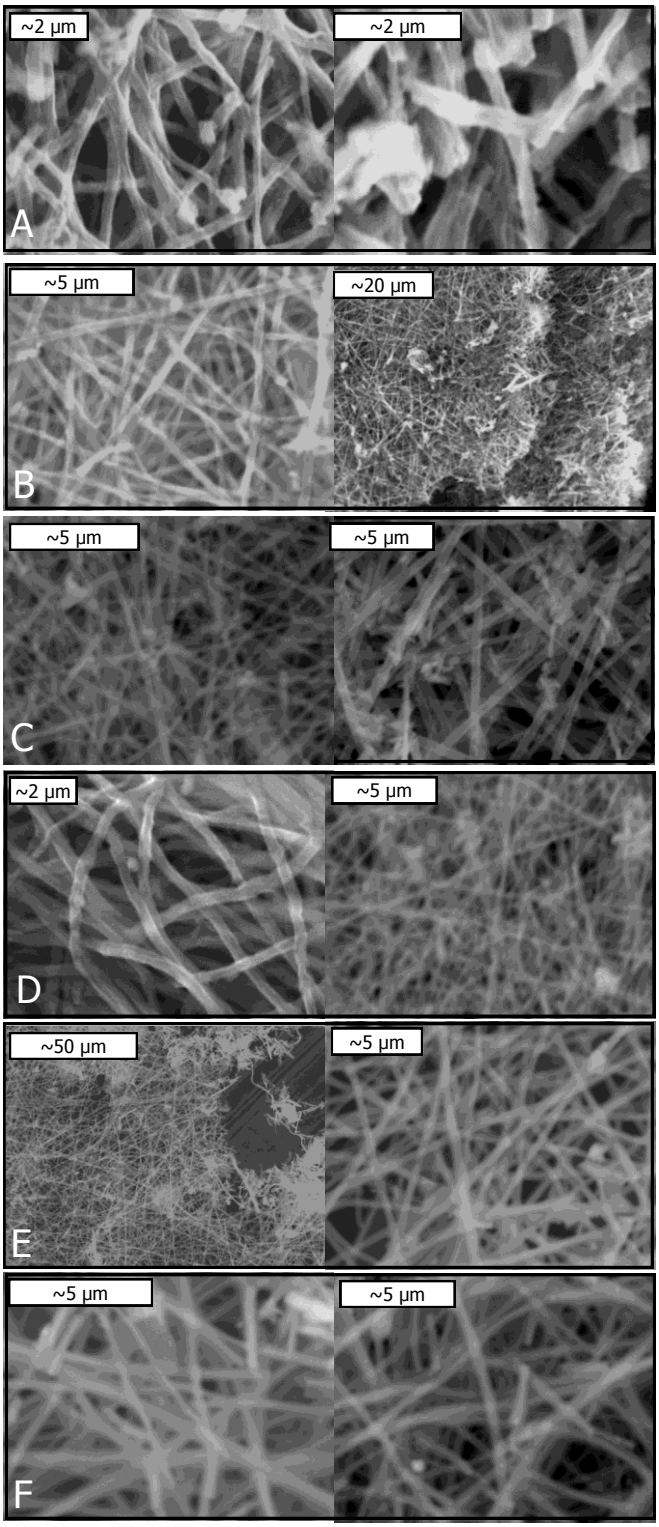

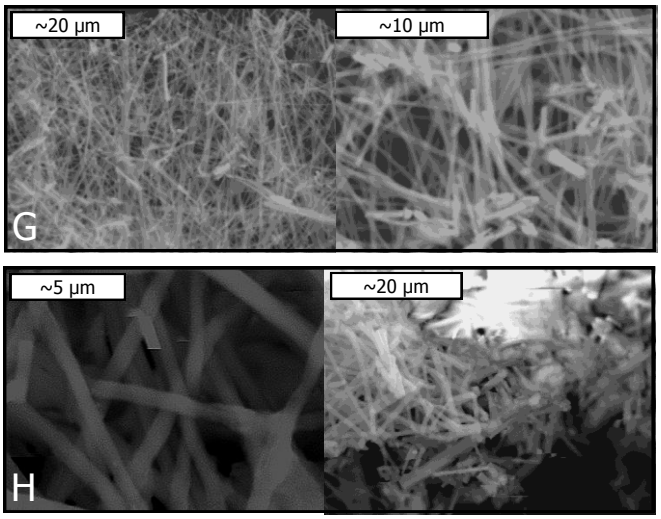

Figure 4.4. SEM images of cobalt doped TiO_2 nanofibres as a function of cobalt loading (mol %). A. 0.01, B. 0.10, C. 0.50, D. 0.80, E. 1.00, F. 5.00, G. 10.00 and H. 50.00. The observed morphology was fibrous at all concentrations of dopant with a diameter of ~400 nm, until 50 mol % loading where the fibre diameter increased to 1000 nm.

The dark green fibres indicated a transformation to CoO. Equation 4.1 details the formation of CoO during the steam treatment of $Co(AcAc)_2$.

$$Co(AcAc)_2 + XS\ H_2O \rightarrow Co(OH)_2 + Heat \rightarrow 2CoO + H_2O + 2AcAcH \qquad (4.1)$$

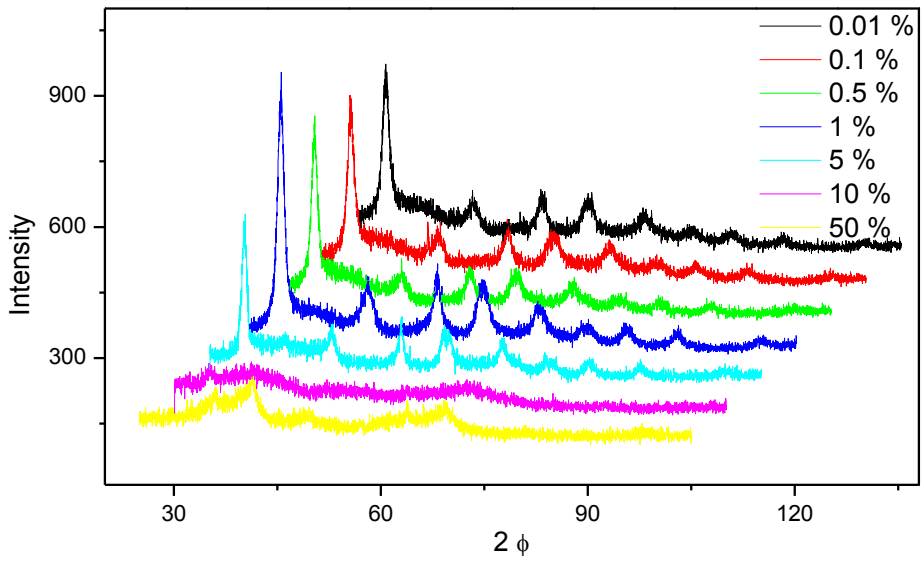

Figure 4.5. X-ray diffraction patterns of cobalt loaded TiO_2 nanofibres. As the loading of cobalt increases, the titania indexes recede and the CoO indexes become more prominent. Below 5 mol % loading, CoO peaks were not observed which is attributed to the Co impregnating into the titania lattice.

X-ray diffraction analysis revealed the presence of CoO, where the peaks were relatively broad, and increased in intensity as the cobalt loading increased (Figure 4.5). However, the cobalt oxide pattern was weak in comparison to that of TiO_2. Below 5.00 % cobalt loading, no CoO patters were observed, however, above 10.00 mol % loading only CoO patterns were observed. Brik *et al.* found Co_3O_4 to be the only cobalt oxide present which was attributed to their production process, where there was no steam treatment to encourage the formation of CoO over Co_3O_4.[216] A small shift in the CoO 440 index by 2.06 % was observed at 50.00 mol % loading. Kuljanin-Jakovljevic *et al.*

attributed shifts of the X-ray diffraction peaks to a distorted titania lattice resulting from the substitution of Ti^{4+} by Co^{2+},[217] a view shared by Choudhury and Choudhury.[218] The lattice substitution of titanium by cobalt, and the creation of an oxygen vacancy, is shown in Equation 4.2. The absence of CoO diffraction patterns until 5.00 mol % loading shows some evidence towards cobalt loading into the lattice of TiO_2 below this concentration.

$$Ti_{Ti}^{x} \rightarrow Co_{Ti}'' + V_o^{\cdot\cdot} \tag{4.2}$$

TiO_2 was determined to only be present in anatase crystallinity with no significant shifting of the titania peaks. The ionic radius of Co^{2+} (79 pm) is slightly smaller than that of Ti^{4+} (81 pm) which may allow for substitution by Co^{2+} without significant lattice perturbation. The intensity of the anatase pattern is higher in the 5.00 mol % loading than the 1.00 mol % loading which disrupts the correlation seen between dopant loading and photocatalytic activity. Therefore this is attributed to be denser packing of the sample on the XRD sample holder.

The crystallite size of the catalysts was calculated using the Scherrer equation, and was found not to increase significantly with doping concentration (Table 4.2). These findings were shared by Iwasaki *et al.*, who found that crystallite size only increased slightly with increased cobalt loading concentration and determined that calcining temperature was more determinate of crystallite size.[176] Compared to un-doped titania, Xu *et al.* observed a smaller crystallite size, 26 nm reduced to 16–18 nm, in cobalt loaded thin films.[219] They attribute the smaller crystallite size to doping causing lattice deformation, reducing crystallite growth. Their findings are in good agreement with our results, where crystallite size was observed to reduce from 12.9 nm to 6.8 nm upon initiation of cobalt loading.

Table 4.2. Crystallite sizes of cobalt doped nanofibres. Upon addition of the dopant, the crystallite size reduces, however, increased loading of Co does little to alter the crystallite size.

Cobalt Loading/mol %	0.01	0.10	0.50	1.00	5.00	10.00	50.00
Crystallite Size/nm	6.8	7.1	8.4	7.5	9.5	No anatase peaks	No anatase peaks

Cobalt doping has been shown to facilitate the conversion of anatase to rutile at lower temperatures, with higher concentrations of cobalt exacerbating the effect.[220] However, in this work, neither of the most intense rutile indexes were observed, (110) and (211), even at the highest cobalt loadings.

Kang *et al.* observed that $CoTiO_3$ was present when they calcined a material containing Co_3O_4 and TiO_2 above 600 °C.[221] At high cobalt loadings, calcined above 450 °C, $CoTiO_3$ can be formed, from CoO or Co_3O_4, and TiO_2, but its presence could not be discerned from our X-ray diffraction patterns as the most intense $CoTiO_3$ peaks are overlapped by the anatase (110), (004) and (200) planes. The formation of cobalt titanate during cobalt loading of titanium dioxide is shown in Equations 4.3 and 4.4.

$$CoO + TiO_2 \rightarrow CoTiO_3 \quad (4.3)$$

$$Co_3O_4 + 3TiO_2 \rightarrow 3CoTiO_3 + 1/2\ O_2 \quad (4.4)$$

The photoactivity of the cobalt doped fibres was determined by measuring the degradation of phenol. It was found that at 0.01 mol % Co loading the activity was 0.21,

around half that of pristine TiO_2 (0.47). This is attributed to incomplete crystallinity of the TiO_2. Increasing the loading to 1.00 mol % boosted the photoactivity to 1.94, four times that of pristine TiO_2. Klabunde and Hamal obtained similar results in their investigations and attributed the enhanced activity to increased surface area, extension of the bandgap into the visible region, increased generation of hydroxyl radicals and greater separation of electron–hole pairs.[222] Based on reduction potentials Co^{2+} (E_0 = -0.28), is more likely to accept electrons than TiO_2 (E_0 = -0.502), which could result in the loading of Co^{2+} decreasing the recombination rate by behaving as an electron trap. At loadings above 1.00 mol % the photoactivity decreased, to 0.89 at 50.00 % cobalt loading. This is double the activity of pristine TiO_2 despite retaining only half of the photoactive TiO_2. This result prompted a separate investigation which will be discussed in Section 4.4.

As well as increasing photoactivity, Co loading has been predicted to extend the bandgap into the visible region. Reddy and Punnoose observed a red-shift in the bandgap, which could allow for visible light activation.[220] Kuljanin-Jakovljevic *et al.* agree, finding a 0.14 eV lowering of the bandgap at ~0.46 % Co, which they attributed to extra states within the TiO_2 bandgap.[217] Choudhury and Choudhury further concluded that cobalt doping lowers the bandgap, observing a shift to 2.55 eV at 0.04 mol Co loading.[218] Iwasaki *et al.* found that this lower energy bandgap was suitable for visible light photooxidation of acetaldehyde.[176]

4.3.2 Iron Doped TiO_2 Nanofibres

To prepare iron doped titania nanofibres, $FeCl_2$ was loaded into a TTiP containing polymer solution, which resulted in brown solutions. After steam treatment

and calcination brown fibres remained, the colour of which was attributed to the presence of Fe_2O_3. The fibres prepared were found to be ~400 nm in diameter, smooth and defect free until 50.00 mol % iron loading (Figure 4.6). At that loading the morphology was observed to be of gelled fibres of ~1000 nm diameter.

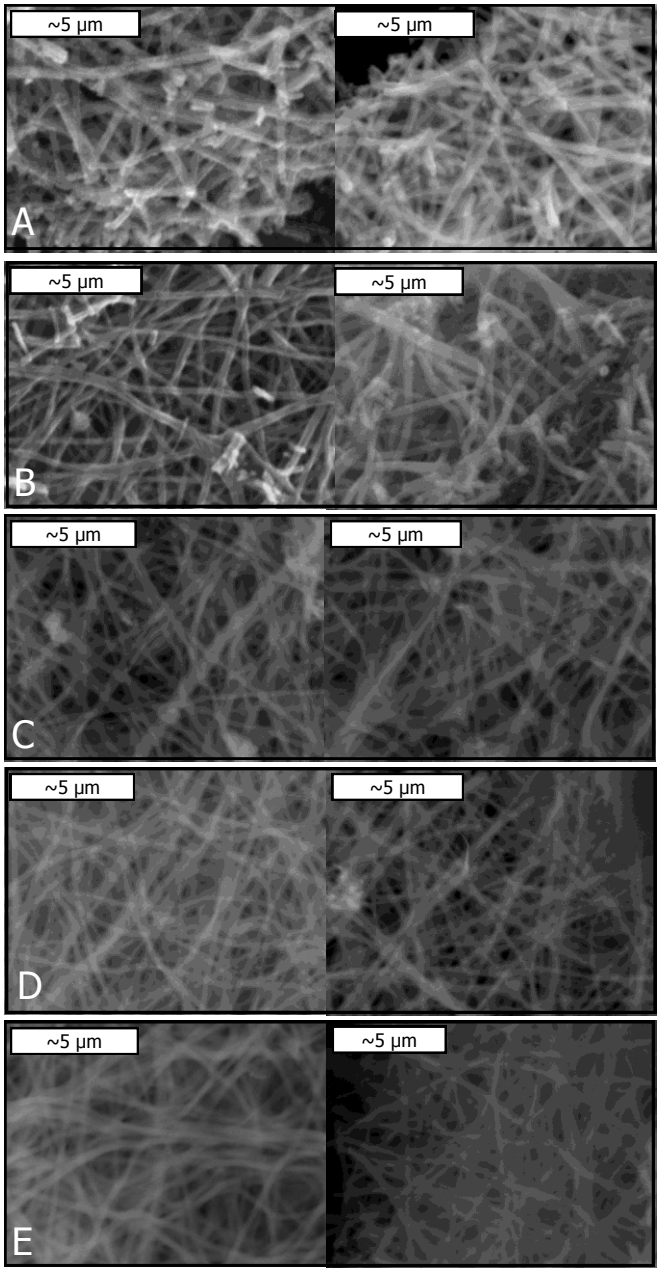

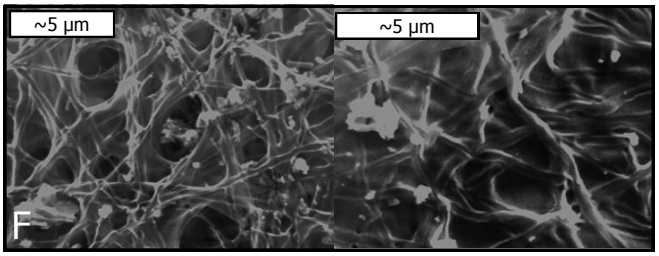

Figure 4.6. SEM images of iron doped TiO_2 nanofibres as a function of iron loading (mol %). A. 0.01, B. 0.50, C. 1.00, D. 5.00, E. 10.00 and F. 50.00. The materials were found to be uniformly fibrous and ~400 nm diameter until 50 mol % loading where the morphology became that of gelled fibres which had increased in diameter to ~1000 nm.

Only the X-ray diffraction patterns of the 0.01 mol % and 50.00 mol % samples are presented as the others were impossible to interpret, containing impurity peaks and inconsistent intensities, attributed to poor sample loading (Figure 4.7). As iron loading increased above 5.00 mol %, features of the XRD were lost. The diffraction patterns observed were those of Fe_2O_3 and anatase TiO_2, however, they were relatively broad and were difficult to assign.

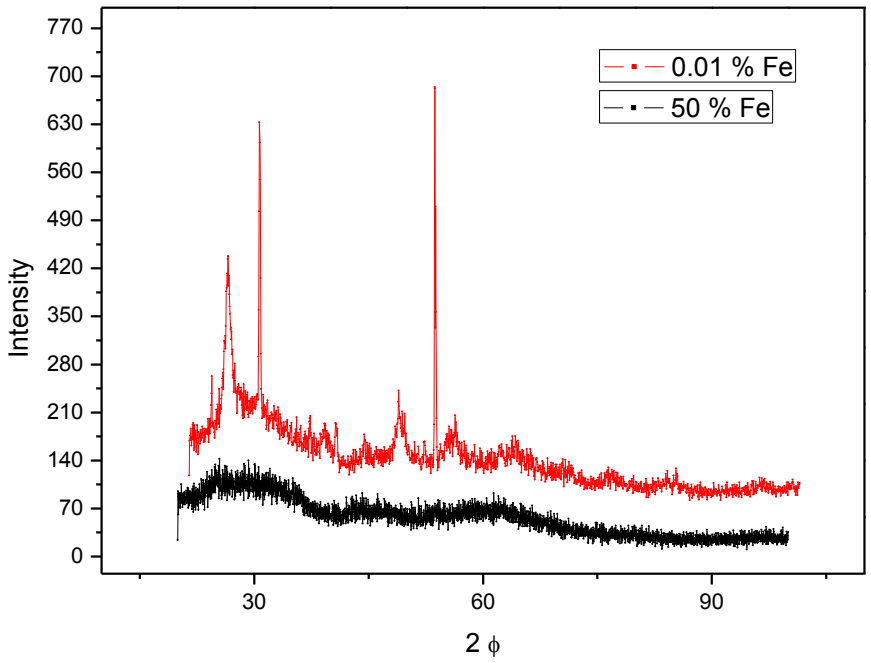

Figure 4.7. X-ray diffraction patterns of 0.01 and 50.00 mol % Fe loaded TiO_2 nanofibres. The titania diffraction patterns become lost as the iron loading reaches 50 mol %. Only two diffraction patterns are presented due to inconsistent loadings of the samples leading to un-interpretable data.

As the dopant loading increased the TiO_2 peaks receded and at 5.00 mol % loading, anatase TiO_2 peaks were no longer observed. Iron has solubility in TiO_2 of about 1.00 mol %, above this loading it is theorised that iron clusters on the surface as Fe_2O_3. A 2.77 % shift of diffraction peaks, at 50.00 mol % iron loading, was observed in the anatase TiO_2 peaks, suggesting that iron oxide had lattice doped the TiO_2, however, the reliability of this value is debated due to the poor quality of the diffraction patterns. Martinez-Arias *et al*. observed only Fe_2O_3 and a corresponding shift in X-ray diffraction peaks which they attributed to a lattice expansion.[201] Despite the smaller ionic radii of Fe^{3+} (75 pm) compared to Ti^{4+} (81 pm), they attributed the lattice

expansion to be a compensating effect from the rearrangement of the lattice due to oxygen vacancies. Viswanathan and Ranjit disagree and believe that the lattice expansion on loading of Fe^{3+} is due to iron forming a solid solution.[223] The lattice replacement of titanium by iron, and the subsequent creation of an oxygen vacancy, is shown in Equation 4.5.

$$Ti_{Ti}^{x} \rightarrow Fe_{Ti}' + V_O^{\cdot} \tag{4.5}$$

Doping titania with iron can result in the formation of $FeTi_2O_5$,[224] however, we did not observe any by X-ray diffraction, which was attributed to the calcination temperature being too low for iron titanate to form.

Incorporation of dopants into the lattice of TiO_2 can force the transformation from anatase to rutile. When doping with iron this is due to the rutile crystal structure being more tolerant of Fe^{3+} incorporation.[73,225] Conversely, Cordischi *et al*. found rutile to be less tolerant of doping than anatase.[226] However, we observed no rutile content, which is confirmed by Ranjit and Viswanathan, and Palmisano *et al.* who observed little transformation to rutile, below 550 °C, even at 5 mol %.[223,227] Seabra *et al.*, however, observed only the rutile crystal phase in un-doped samples at 500 °C, and found that doping with iron decreased the photocatalytic activity of Orange II by nearly half.[228]

The crystallite size within the iron loaded titania fibres was calculated from the X-ray diffraction pattern, using the Scherrer equation. The crystallite size of titania fibres was found to be reduced by over half upon the addition of iron (Table 4.3). Upon increasing the iron concentration, no significant pattern of crystallite size was observed, implying that precise concentration of iron has little effect on crystallite size.

Table 4.3. Crystallite sizes of iron loaded titania. The crystallite size of the iron doped titania decreases once iron has been loaded which was attributed to the iron disturbing the growth of larger cyrstallites.

Iron Loading/mol %	0.01	0.05	1.00	5.00	10.00	50.00
Crystallite Size/nm	11.8	4.3	5.9	7.1	4.1	No anatase peaks

Ying *et al.* investigated the relationship between photocatalytic activity and crystallite size, and found that at sub 6 nm crystallite sizes photoactivity decreases due to an increase in recombination rate caused by the increased surface area that small grains offer.[186] Photoactivity was observed to increase until 1.00 mol % loading of iron, to a value of 0.46, however, even at its maximum efficiency, iron doped TiO_2 was found to be less photoactive than pristine TiO_2 nanofibres, 0.47, which is in good agreement with other published results.[229,230] We attribute this to the small crystallite sizes of iron loaded TiO_2 increasing the rate of recombination. This is in contrast to research that states that iron behaves as a shallow electron trap when doped into titania (Scheme 4.1).[201,206] The reduction potential of Fe_2O_3 (E_0 = 0.16) is higher than that of TiO_2 (E0 = -0.502), giving credence to iron behaving as an electron trap in the photocatalytic mechanism. In further contrast to our findings, Xin *et al*. found that, in the removal of coffee and red wine stains from cloth, Fe^{3+} doped titania performed higher than native TiO_2 in loadings of 0.1-2 wt. %.[215] They also concluded that there was a visible light response from iron doped TiO_2, however, they found that visible light activation was half as efficient as UV activation. It is generally agreed that at loadings of iron above a

critical concentration the activity drops sharply as at high loadings of iron, Fe^{3+} is thought to act as a recombination centre, reducing the photoactivity.[231] We observed this critical concentration to be 1.00 mol % iron, above which we observed the activity to drop rapidly, dropping to a value of 0.11 at 50.00 mol % iron loading. Viswanathan and Rajit argue that the addition of Fe^{3+} forms Fe_2O_3 on the surface which creates a heterojunction,[223] increasing the photocatalytic activity but if this layer of iron oxide becomes too large, then it will effectively block incident UV radiation, preventing activation of the TiO_2. Furthermore they argue that at higher iron loading, an increase in space charge layer will be observed, which will increase the probability of recombination. Cordischi *et al*. found that an excess of iron loading gave rise to Fe_2TiO_5 which they found to be photo-inactive, however, they did agree that minimal iron loading could lead to reduced recombination rates.[226]

These observed differences in photocatalytic activity are believed to come from differing preparation methods, creating different catalysts, and differing testing conditions. Navio and Litter summed up doping titania with iron, stating that at very low concentrations (below 0.5 at. %) there is little effect from Fe^{3+} loading, at slightly higher concentration (~1 at. %) a noticeable increase in activity is observed and at high loadings (above 1 at. %) the catalyst is deactivated by the formation of Fe_2O_3 and/or Fe_2TiO_5.[206] Both of these phases have low lying bandgaps, at 2.2[232] and 2.18[233] eV respectively, with little energy to perform redox reactions.

While visible light activation was not investigated in this work, iron is theorised to be a suitable dopant to allow for activation by ambient light. Martinez-Arias observed a visible light response by UV-Vis diffuse reflectance spectroscopy, with bands observed at 400 nm, from Fe^{3+} 3d electrons to the Ti^{4+} conduction band, and at 500 nm,

from either $^2T_{2g} \rightarrow {}^2A_{2g}, {}^2T_{1g}$ or $d - dFe^{3+} \rightarrow Fe^{2+} + Fe^{4+}$ transitions.[201] Ohno *et al.* found that iron doping red-shifts the bandgap, but with no corresponding photoactivity under visible light illumination, which is evidence towards the red-shift being due to an iron centred redox.[106]

4.3.3 Nickel Doped TiO_2 Nanofibres

In order to prepare nickel doped TiO_2 nanofibres, $NiCl_2$ was added to a TTiP containing polymer solution, resulting in a green solution, which gave rise to green fibres after steam treatment and calcination. The green of the fibres was attributed to the presence of NiO, rather than Ni_2O_3 which is black.

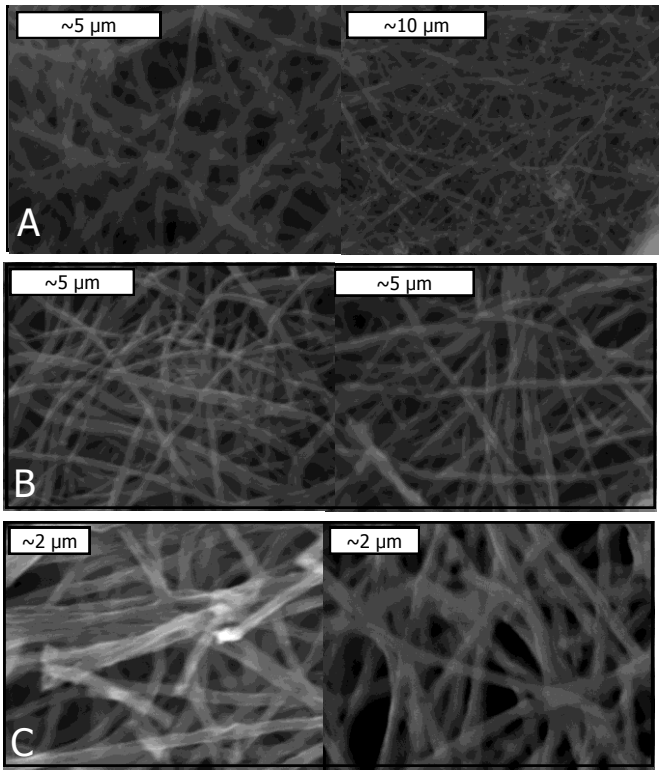

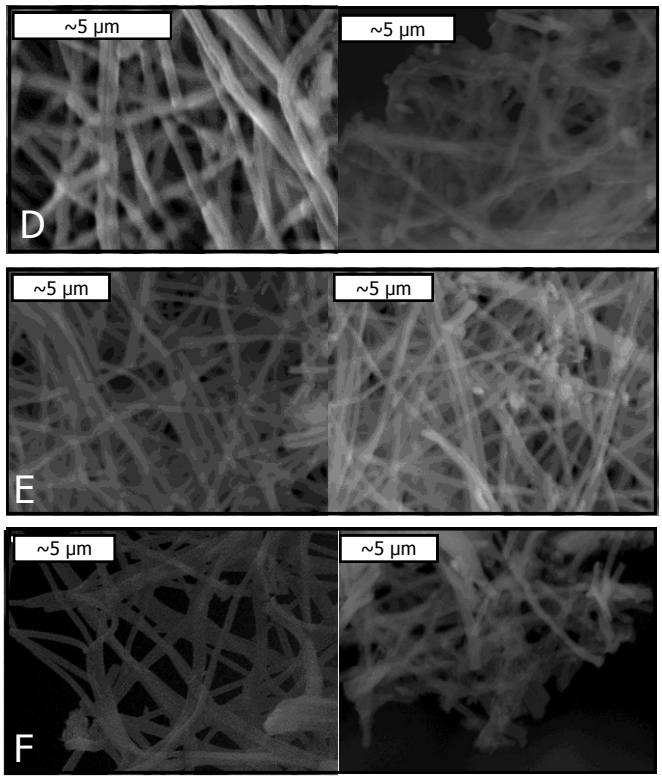

Figure 4.8. SEM images of nickel doped TiO_2 nanofibres as a function of nickel loading (mol %). A. 0.01, B. 0.50, C. 1.00, D. 5.00, E. 10.00 and F. 50.00. The morphology was fibrous in all loadings and the diameters were ~400 nm until 50 mol % loading where the diameter increased to ~1000 nm.

By SEM the formed fibres were observed to be smooth and defect free at all loadings. A fibre diameter of ~400 nm was observed at all concentrations of nickel until 50.00 mol % loading, where the impregnation of nickel resulted in the fibres increasing to ~1000 nm in diameter (Figure 4.8).

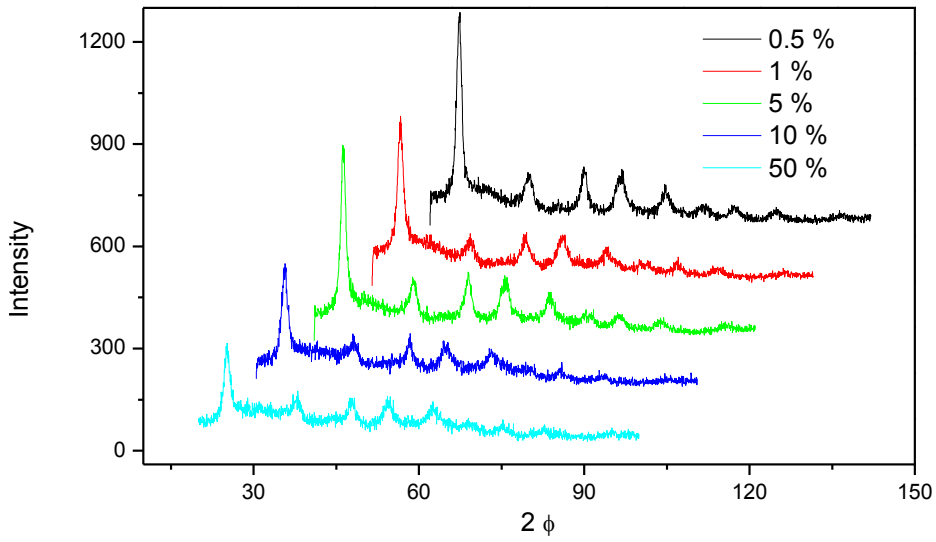

Figure 4.9. X-ray diffraction patterns of NiO doped TiO_2 nanofibres. X-ray diffraction patterns revealed titania to be in the anatase phase, with the intensity decreasing as the nickel loading increased. The NiO peaks were observed from 1 mol % loading, evidence of little tolerance for nickel dissolving into the TiO_2 lattice.

The X-ray diffraction patterns of the nickel doped nanofibres were relatively sharp and all peaks were assigned to either anatase TiO_2 or NiO. XRD confirmed that no other nickel oxides were observed, and NiO was seen at loadings as low as 1 mol % (Figure 4.9). This implies a very low tolerance for lattice doping of TiO_2 by Ni^{2+}, which may be attributed to the slightly larger ionic radius of Ni^{2+} (83 pm). Using the same synthetic method, Peng *et al*. also only observed NiO.[177] However, Karthik *et al.* found that, even at 8 mol % loading of Ni, no peaks other than anatase-TiO_2 were observed in the X-ray diffraction,[234] evidence for lattice replacement of Ti^{4+} by Ni^{2+}, as shown in Equation 4.6.

$$Ti_{Ti}^{x} \rightarrow Ni_{Ti}'' + V_O^{\cdot\cdot} \quad (4.6)$$

TiO_2 is present solely in the anatase phase and is observed clearly, even when nickel loading reached 50.00 mol %. The overlap between several NiO and TiO_2 planes made careful analysis difficult. Our analysis of the crystalline phase of nickel doped TiO_2 was in good agreement with Kisand, who observed only the anatase phase until calcining temperatures above 800 °C.[177] In contrast, Nirmala and Kim found that when preparing Ni doped TiO_2 by electrospinning rutile was the majority phase.[235] A 1.58 % shift of X-ray diffraction peaks of the anatase pattern was observed which may be attributed to lattice doping. Karthik *et al.* confirmed that loading of nickel into TiO_2 shifted the X-ray diffraction peaks to higher d-values, as determined by extent of distortion to the crystal lattice.[234]

The crystallite sizes of nickel loaded titania were calculated from the X-ray diffraction patterns by the Scherrer equation. Upon addition of 0.01 mol % nickel, the crystallite size was found to significantly decrease, from 12.9 nm to 6.5 nm. When the nickel loading increased, from 0.01-50.00 mol %, no significant change in crystallite size was observed (Table 4.4). The observed decrease in crystallite size upon the addition of nickel is in good agreement with Tseng *et al.*[236] and Sharma *et al.*,[237] where Sharma *et al*. attributed the decrease to a difference in charge between Ti^{4+} and Ni^{2+} causing surface TiO_2 to assert a maximum distance.

Table 4.4. Crystallite sizes of nickel doped TiO_2 nanofibres. The crystallite size decreased appreciably upon the addition of nickel, attributed to disruption of the crystallite growth process by the dopant. Further increasing the nickel loading did not significantly change the crystallite size, evidence that crystallite size is independent of nickel loading.

Nickel Loading/mol %	0.01	0.50	1.00	5.00	10.00	50.00
Crystallite Size/nm	6.5	7.1	6.5	8.4	6.5	7.5

The photoactivity of the nickel loaded catalysts was observed to increase up until 1.00 mol % nickel, from 0.39 to 0.91. At this maximum activity, the degradation of phenol is nearly twice as high compared to pristine TiO_2 nanofibres. At loadings above this critical concentration the photooxidation of phenol dropped rapidly, finally reaching 0.26 at 50.00 mol % Ni, roughly half that of pristine titania nanofibres; this was due to the dopant poisoning the TiO_2. Similar results were presented by Sharma *et al*. who found that nickel doping enhanced the activity of TiO_2 until 8 mol % loading. Above this loading they found that the activity dropped sharply, reducing to un-doped activities as soon as 10.00 mol % loading. This was attributed to Ni centres acting as shallow traps, giving a longer life-time to electron-hole pairs.[237] Scheme 4.2 shows the role Ni^{2+} plays in the mechanism of TiO_2 photocatalysis, proposed by Tseng *et al.*.[236] Scheme 4.2(a) is the creation of the charge carriers by UV light. Scheme 4.2(b) is the trapping of the electron by Ni^{2+}, causing the reduction of nickel. Scheme 4.2(c) is the reoxidisation of Ni^{+} to generate super oxide. Scheme 4.2(d) is the reduction of Ti^{4+} by Ni^{+}. The formed Ti^{3+} can then proceed to convert O_2 into superoxide as shown in Scheme 4.2(e).

$$TiO_2 + hv \rightarrow e^- + h^+ \quad (a)$$

$$Ni^{2+} + e^- \rightarrow Ni^+ \quad (b)$$

$$Ni^+ + O_2 \rightarrow Ni^{2+} + O_2^- \quad (c)$$

$$Ni^+ + Ti^{4+} \rightarrow Ni^{2+} + Ti^{3+} \quad (d)$$

$$Ti^{3+} + O_2 \rightarrow Ti^{4+} + O_2^- \quad (e)$$

Scheme 4.2. Nickel behaving as an electron trap.[236] (a) is the creation of the electron hole pair. (b) is the trapping of the excited electron by Ni^{2+}, reducing it to Ni^+. This can then oxidise O_2 to super oxide (c). Ni^+ can also reduce Ti^{4+} (d). This generated Ti^{3+} can go onto reduce O_2 to super oxide.

The reduction potential of Ni^{2+} is E_0 = -0.257 V, which is more likely to accept electrons than TiO_2 (E_0 = -0.502 V), allowing for the trapping of electrons by the nickel dopant, which would reduce the recombination rate of the electron–hole pairs.

The doping of TiO_2 with nickel has also been shown to alter the band structure of the material. For example, Nirmala and Kim observed that when nickel substitutes into the TiO_2 lattice the bandgap was reduced by 0.95 eV, where they suggest it could be activated by visible light and would yield lower rates of recombination.[235] Sharma *et al.* also observed a decrease in bandgap energy, by reflectance UV-Vis spectroscopy, to 425 nm at 10.00 mol % Ni. They attribute this extra UV-Vis band to an energy level in the bandgap of TiO_2 from Ni^{2+}/Ni^+.[237] The reduction in activity as the nickel loading increased was then attributed to the distance between the nickel centres and positive holes decreasing, allowing Ni^+ to behave as a recombination centre, as shown in Equation 4.7.

$$Ni^{+} + h^{+} \rightarrow Ni^{2+} \quad (4.7)$$

4.3.4 Chromium Doped TiO_2 Nanofibres

To prepare chromium doped TiO_2 nanofibres, $CrCl_3$ was added to the TTiP containing polymer solution, yielding a purple solution. Upon steam treatment and calcination, green nanofibres remained. The green colour of the fibres was attributed to the presence of Cr_2O_3, which was previously called viridian. At the calcining temperatures used Cr_2O_3 is the most thermally stable chromium oxide.

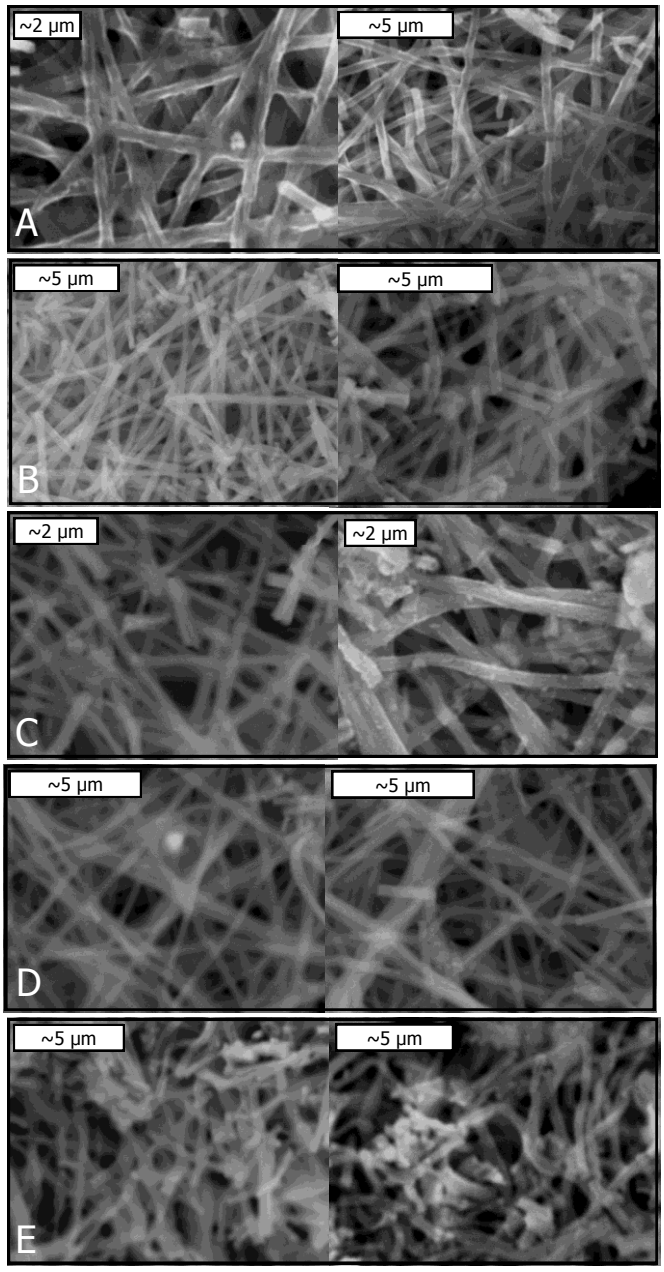

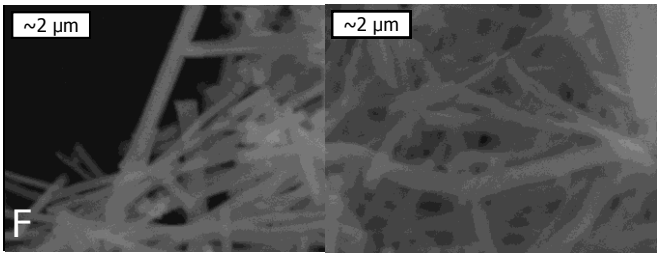

Figure 4.10. SEM images of chromium doped TiO_2 nanofibres as a function of chromium loading (mol %). A. 0.01, B. 0.50, C. 1.00, D. 5.00, E. 10.00 and F. 50.00. The morphology was uniformly fibrous and defect free with a diameter of 500 nm at all loadings.

The prepared fibres were uniformly smooth and defect free (Figure 4.10). The morphology and fibre diameter (~500 nm) were not observed to change as the concentration of chromium loading increased. Therefore we conclude that chromium loading in this methodology has no significant influence on the diameter or morphology of the nanofibres produced.

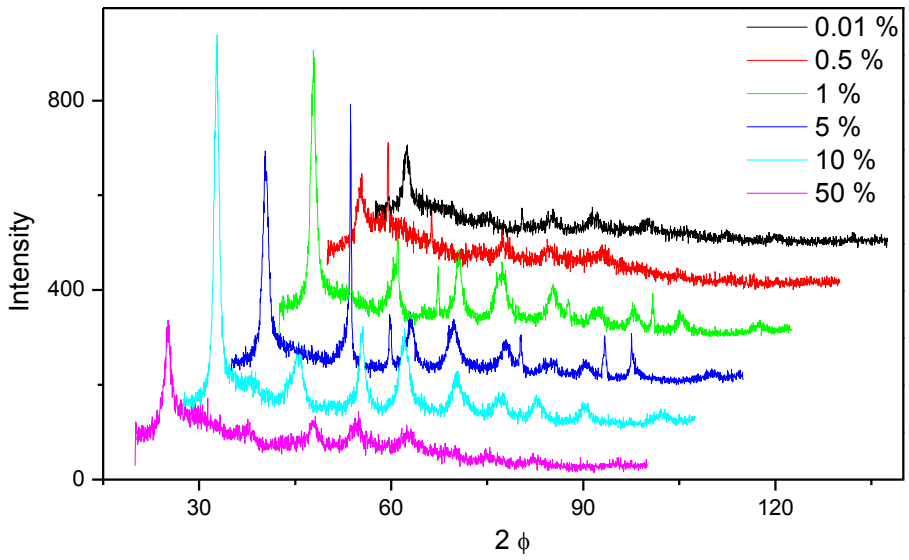

Figure 4.11. X-ray diffraction patterns of chromium oxide doped TiO_2 nanofibres. It appears as though anatase TiO_2 is in lowest concentration in the 0.01 Cr mol % loaded sample, however, this is experimental error from sample loading in the X-ray diffractometer. The anatase diffraction pattern decreases as the chromium loading increases with the commensurate increase in the peaks of Cr_2O_3. The chromium oxide peaks are observed from 1 mol % loading, implying a low tolerance of the TiO_2 for Cr^{3+}.

The X-ray diffraction patterns of the prepared nanofibres show inconsistent intensities due to loading of the powder samples into the diffractometer, however, they confirm the presence of anatase TiO_2 and Cr_2O_3 (Figure 4.11). Cr_2O_3 was observed at all loadings above 1.00 mol %, which is in good agreement with Ciesla *et al.* who also found Cr_2O_3 to be the only chromium oxide present.[63] In contrast, Mardare *et al.* observed some Cr_2O_5 in the X-ray diffraction patterns, however, their product was obtained from a Cr^{6+} precursor.[240] TiO_2 was found to be present only in the crystalline

anatase phase, however, there is overlap between anatase and Cr_2O_3 planes, which made careful analysis difficult. No presence of the rutile phase was observed which contrasts the findings of Tsai and Tseng who observed rutile phase TiO_2 in samples above 10.00 mol % loading.[241] This was despite a lower calcining temperature of 450 °C, which was attributed to a higher concentration of Cr defects favouring the transition to rutile.

A shift in the diffraction peaks of the anatase pattern, by 2.1 %, was observed. Tian *et al.* argue that a shift in d-values is evidence of Cr^{3+} substituting into the TiO_2 lattice, followed by the creation of oxygen vacancies (Equation 4.8), or titanium interstitials (Equation 4.9), to compensate for the charge imbalance.[242] As we observed chromium oxide X-ray diffraction patterns from 1.00 mol % loading, we conclude that the solubility of Cr^{3+} into the TiO_2 lattice is low.

$$Cr_2O_3 \rightarrow 2Cr'_{Ti} + V_O^{\cdot\cdot} \tag{4.8}$$

$$Cr_2O_3 + Ti_{Ti} \rightarrow 4Cr'_{Ti} + Ti_i^{\cdot\cdot\cdot\cdot} \tag{4.9}$$

The lattice expansion caused by lattice substitution of Ti^{4+} by Cr^{3+} was detailed by Choudhury and Choudhury to occur in three stages; initially there is a lattice expansion as Cr^{3+} ion substitutes Ti^{4+}. As the loading increases there is an increase of oxygen vacancies which contract the Ti-O and Cr-O bonds. Finally, at even higher concentrations, there is an excess of Cr^{3+} which cannot substitute into the lattice so lie on interstitial sites, disturbing the lattice.[243] This explanation does not violate Vegard's Law, which states that lattice size changes linearly with dopant.[244]

Using the X-ray diffraction patterns the crystallite size of the Cr doped nanofibres was calculated by the Scherrer equation. The crystallite size reduced from 12.9 nm to 7.1 nm upon addition of 0.01 mol % Cr but was not observed to change

significantly with an increase in dopant concentration (Table 4.5). These findings are in good agreement with Tian *et al.*, who observed little change in the crystallite size of increasingly doped TiO_2.[242] The lower crystallite size of the Cr doped samples was attributed to disruption of the crystal growth by the dopant, however, the extent of the disruption has been shown, in this work, not to be concentration dependent.

Table 4.5. Crystallite sizes of chromium doped TiO_2 nanofibres. The crystallite size decreases significantly upon the addition of Cr^{3+}, however, the crystallite size is independent of concentration of the dopant. The reason for the decreased crystallite size is postulated to be due to disruption of the crystal growth by the Cr^{3+}.

Chromium Loading/mol %	0.01	0.50	1.00	5.00	10.00	50.00
Crystallite Size/nm	7.1	7.1	8.4	7.1	8.4	7.1

The photocatalytic activity of Cr doped TiO_2 nanofibres was assessed by measuring the degradation of phenol under UV activation. The activity of the sample increased up to 0.96 at 1.00 mol % Cr loading. This activity is double that of pristine TiO_2 nanofibres which is attributed to decreased recombination rate, a view shared by Huang and Huang who observed that Cr loading increased the photooxidation of methyl orange, which they attributed to the impurity states reducing electron-hole pair recombination.[245] This activity profile was in good agreement with Guo *et al.*,[246] who found lower loadings to show better photovoltaic activity as increased Cr concentration encouraged the formation of Cr_2O_3,[242] which they argue acts as a recombination centre for electron-hole pairs. The redox potential of Cr^{3+} to Cr^{2+} (E_0 = -0.407 V), is a more

positive potential than that of TiO_2 (E_0 = -0.502 V), which would favour the reduction of chromium. Cr^{3+} could provide an electron trap, reducing the rate of recombination. Above 1.00 mol % Cr loading the photoactivity drops to a low of 0.19 at 50.00 mol % due to the increased recombination centres provided by chromium.

The loading of chromium into TiO_2 can alter the band structure of TiO_2, sensitising it to visible light. Guo *et al.* found that the loading of Cr^{3+}, shifted the band edge towards the visible region, even in doping levels of parts per million.[246] As the loading of Cr increased, Tsai and Tseng observed a bandgap shift into the visible region but a lowered photocatalytic activity.[241] This was thought to be due to the presence of Cr_2O_3 on the surface and the increased rutile content, which is often thought to be less photocatalytically active. Huang and Huang suggested that loading TiO_2 with Cr will add impurity states into the bandgap. They attributed the extra bandgaps to $Cr^{3+} \rightarrow Ti^{4+}$ or $^4A_{2g} \rightarrow ^4T_{1g}$ in an octahedral field at ~450 nm, and d-d transitions from $^4A_{2g} \rightarrow ^4T_{1g}$ of Cr^{3+} at ~800 nm.[245]

4.3.5 Vanadium Doped TiO_2 Nanofibres

In order to prepare vanadium loaded TiO_2 nanofibres, $VOSO_4$ was added to a TTiP containing polymer solution. The resulting blue solution was electrospun, steam treated and calcined at 550 °C to yield blue nanofibres, where the blue colour was indicative of the presence of VO_2. Analysis of the fibres by SEM revealed a smooth, defect free morphology at all concentrations of vanadium loading (Figure 4.12). The fibre diameter was measured to be ~400 nm up until 50.00 mol % loading of vanadium, where the fibre diameter increased to ~1000 nm. We conclude that at low loadings of

vanadium, the dopant has little influence on the morphology or diameter of the nanofibres.

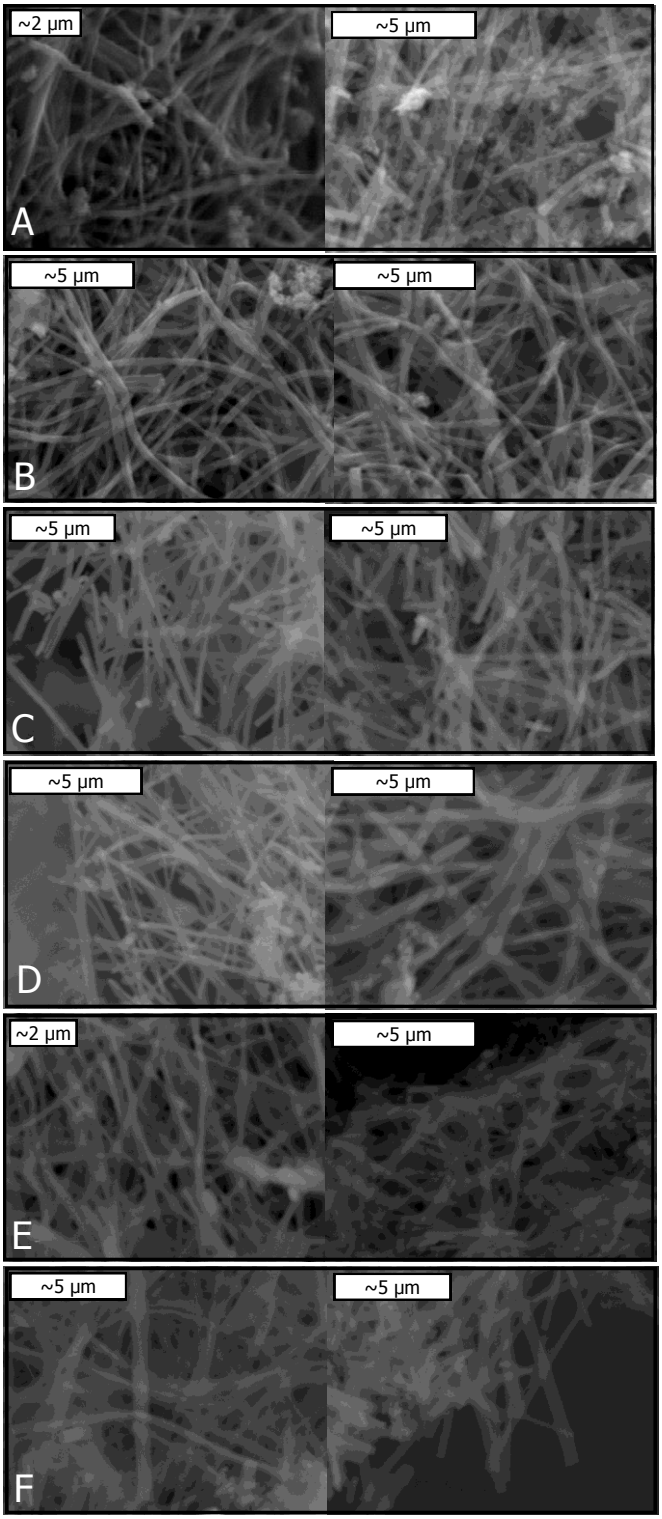

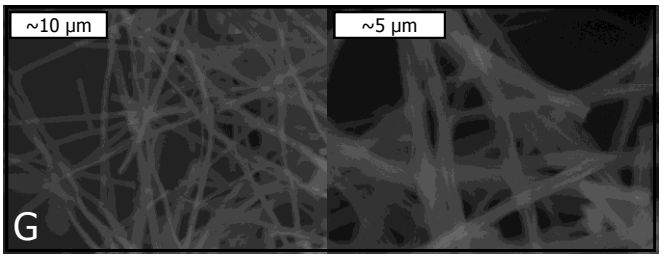

Figure 4.12. SEM images of vanadium doped TiO_2 nanofibres as a function of vanadium loading (mol %). A. 0.01, B. 0.25, C. 0.50, D. 1.00, E. 5.00, F. 10.00 and G. 50.00. The morphology was observed to be uniformly fibrous at all loading concentrations, however, the fibre diameter increased from 500 nm to 1000 nm when the vanadium loading reached 50 mol %.

To determine the composition and phase of the vanadium doped nanofibres, X-ray diffraction was employed. The diffraction patterns observed confirmed the presence of vanadium as VO_2 and TiO_2 in the anatase phase (Figure 4.13). The diffraction patterns of VO_2 and V_2O_5 overlap, leading to the possibility that V_2O_5 could be present. At 0.01 mol % the intensity of the anatase diffraction pattern is lower and broader than expected due to poor packing in the sample holder of the XRD. The sample containing 0.25 mol % vanadium contains a significant amount of rutile. As no other samples show any significant presence of rutile we ascribe this to an error in the calcination process, leading to a higher calcining temperature for that sample, converting the anatase phase to rutile.

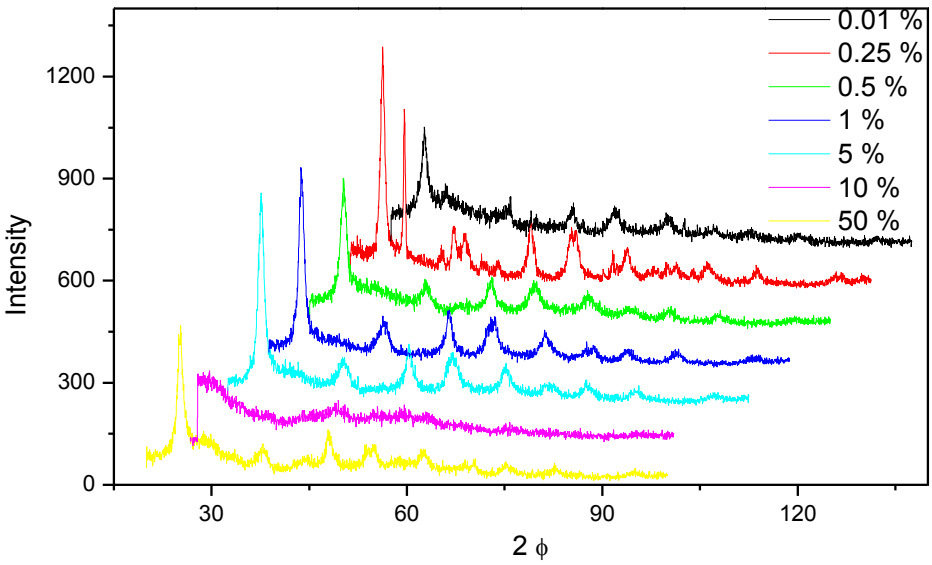

Figure 4.13. X-ray diffraction patterns of vanadium oxide doped TiO_2 nanofibres. TiO_2 is present in the anatase phase. The 0.25 mol % loaded sample contains a significant amount of rutile attributed to higher than predicted calcining temperature and is treated as erroneous. No vanadium oxide (VO_2 orV_2O_5) peaks are observed until 50 mol % loading, evidence that the TiO_2 lattice has a higher tolerance for impregnation by vanadium.

Apart from the 0.25 mol % loaded sample, TiO_2 was found to be crystalline solely in the anatase phase. This finding is in good agreement with Tian *et al.* who observed that, when loading with V^{4+}, there was no change in TiO_2 crystallinity, as the retention of charge balance does not promote any phase change of TiO_2.[242] Wu *et al.* also only observed anatase phase TiO_2, even after calcining at 700 °C, with no evidence of any vanadium oxides, which they attributed to vanadium substitution into the TiO_2 lattice.[203] We observed a 0.75 % shift of the diffraction peaks at 0.10 mol % loading, which may be indicative of lattice substitution. Furthermore, we do not observe the

presence of VO_2 until 50.00 mol % loading, which could also be evidence of lattice doping by vanadium.

Doping V^{5+} into the TiO_2 lattice changes the cell diameter due to the smaller ionic radius of the V^{5+} (68 pm) compared to Ti^{4+} (81 pm), this reduction can be observed by a shift to the left in the X-ray diffraction.[247] Shao *et al.* also attributed this shift to the successful doping of vanadium into the TiO_2 lattice.[248] Equations 4.10 and 4.11 detail the creation of titanium vacancies by V^{4+} and V^{5+} respectively.

$$Ti_{Ti}^{x} + V^{4+} \rightarrow V_{Ti}^{x} \tag{4.10}$$

$$Ti_{Ti}^{x} + V^{5+} \rightarrow V_{Ti}^{\cdot} \tag{4.11}$$

The crystallite size of vanadium doped nanofibres was calculated from the X-ray diffraction data using the Scherrer equation. The crystallite size decreased from 12.9 nm to 7.5 nm upon the addition of 0.01 mol % vanadium, which was attributed to the dopant retarding crystal growth (Table 4.6). This is in contrast to Li *et al* who found that crystallite size increased from 14.8 nm to 19.6 nm on the addition of V^{4+}.[249] Upon increase of vanadium loading we did not observe the crystallite size to alter significantly, showing that crystallite size is not concentration dependent in our catalysts. In opposition to this Wu and Chen found that crystallite size increased with increased vanadium loading,[203] which is in contrast to Chang and Liu who found that crystallite size decreased with high levels of loading due to inhibited crystal growth.[250]

Table 4.6. Crystallite size of vanadium doped TiO_2 nanofibres. Crystallite size decreases noticeably upon the addition of vanadium to TiO_2 nanofibres, attributed to the disruption of the crystallite growth by the dopant, however, upon increasing the vanadium loading, no significant change in crystallite size is observed.

Vanadium Loading/mol %	0.01	0.25	0.50	1.00	5.00	10.00	50.00
Crystallite Size/nm	7.5	10.9	7.9	7.9	7.5	7.9	No anatase peaks

The photooxidation efficiency of vanadium doped TiO_2 nanofibres was investigated by measuring the degradation of phenol. The photoactivity reached a maximum of 0.48 at 1.00 mol %, slightly higher than 0.47 for pristine TiO_2 nanofibres. Wu observed the decomposition of crystal violet and methylene blue by vanadium loaded titania and then, at a critical point, decreased in activity.[203] While they offer no explanation for the increase in activity Higashimoto proposed a V^{5+}/V^{4+} cycle that traps an electron, lowering the rate of recombination and, furthermore, promotes the formation of O_2^- (Scheme 4.3).[251]

$$e^- + V^{5+} \rightarrow V^{4+} \qquad (a)$$

$$V^{4+} + O_2 \rightarrow V^{5+} + O_2^- \qquad (b)$$

Scheme 4.3. V^{5+} behaving as an electron trap and the subsequent reduction of O_2 into superoxide by the V^{4+} species.[251]

Scheme 4.3(a) depicts the reduction of V^{5+} by the excited electron. Scheme 4.3(b) depicts V^{4+} reoxidising to V^{5+} and the subsequent reduction of oxygen to superoxide.

Shao *et al.* suggested an alternative mechanism that involved a two electron cycle, from V^{3+} to V^{5+}, both beginning from V^{4+} (Scheme 4.4).[248] Scheme 4.4(a) and (b) are the reduction and oxidation of V^{4+} respectively. Scheme 4.4(c) and (d) are the reduction of oxygen to superoxide from V^{3+} and the excited electron respectively. Scheme 4.4(e) and (f) describe the formation of hydroxyl radicals from V^{5+} and the hole respectively. These radicals can then to go on to decompose the target VOC.

$$V^{4+} + e^- \rightarrow V^{3+} \quad \text{(a)}$$

$$V^{4+} + h^+ \rightarrow V^{5+} \quad \text{(b)}$$

$$V^{3+} + O_2 \rightarrow V^{4+} + O_2^- \quad (c)$$

$$e^- + O_2 \rightarrow +O_2^- \quad (d)$$

$$V^{5+} + OH^- \rightarrow V^{4+} + \cdot OH \quad (e)$$

$$h^+ + OH^- \rightarrow \cdot OH \quad (f)$$

Scheme 4.4. Proposed mechanism for vanadium redox participation.[248] V^{4+} is shown to trap the electron and hole (a and b). V^{3+} can proceed to reduce O_2 to super oxide (c) as can an excited electron (d), while V^{5+} (e) and h^+ (f) can create hydroxyl radicals from hydroxide ions.

The two electron reduction of V^{5+} to V^{4+} has a reduction potential of 0.957 V, suitably sufficient to behave as an electron trap during photooxidation. While the reduction potential of V^{4+} to V^{3+} (E_0 = 0.337 V), is much less favourable towards as an electron trap than $V^{5+} \rightarrow V^{4+}$, it is still sufficient to display this behaviour.

As the loading of vanadium increased beyond 1.00 mol % the degradation of phenol was observed to decrease, to a minimum of 0.24 at 50.00 mol %. The activity

was half that of pristine TiO_2 nanofibres which was attributed to the distribution of vanadium ions no longer remaining dilute, allowing for the occurrence of electron tunnelling, enhancing recombination.[247]

Further to enhancing the photoactivity, vanadium loading has been shown to modify the TiO_2 bandgap. Wu *et al.* and Kumar *et al.* both observed new bandgap minimums at 2.8 and 2.85 eV respectively.[203,247] This red-shift in bandgap was further confirmed by Xu and Ao who observed a tail in diffuse reflectance spectra, which they attributed to a impurity state within the titania bandgap.[202]

4.3.6 Copper Doped TiO_2 Nanofibres

To prepare copper doped TiO_2 nanofibres, $Cu(NO_3)_2$ was added to a TTiP containing polymer solution, resulting in a blue solution. The solution was electrospun, steam treated and calcined at 550 °C, yielding dark green nanofibres. The green colour was ascribed to be a result of CuO, due to the thermal degradation of copper nitrate readily forming CuO rather than Cu_2O. Furthermore, any copper hydroxide formed in the steam treatment stage will rapidly convert to CuO when heated, with the subsequent formation of water. Equations 4.12 and 4.13 detail the formation of CuO from copper nitrate and copper hydroxide respectively.

$$2Cu(NO_3)_2 \rightarrow 2CuO + 2NO + O_2 \quad (4.12)$$

$$Cu(OH)_2 \rightarrow CuO + H_2O \quad (4.13)$$

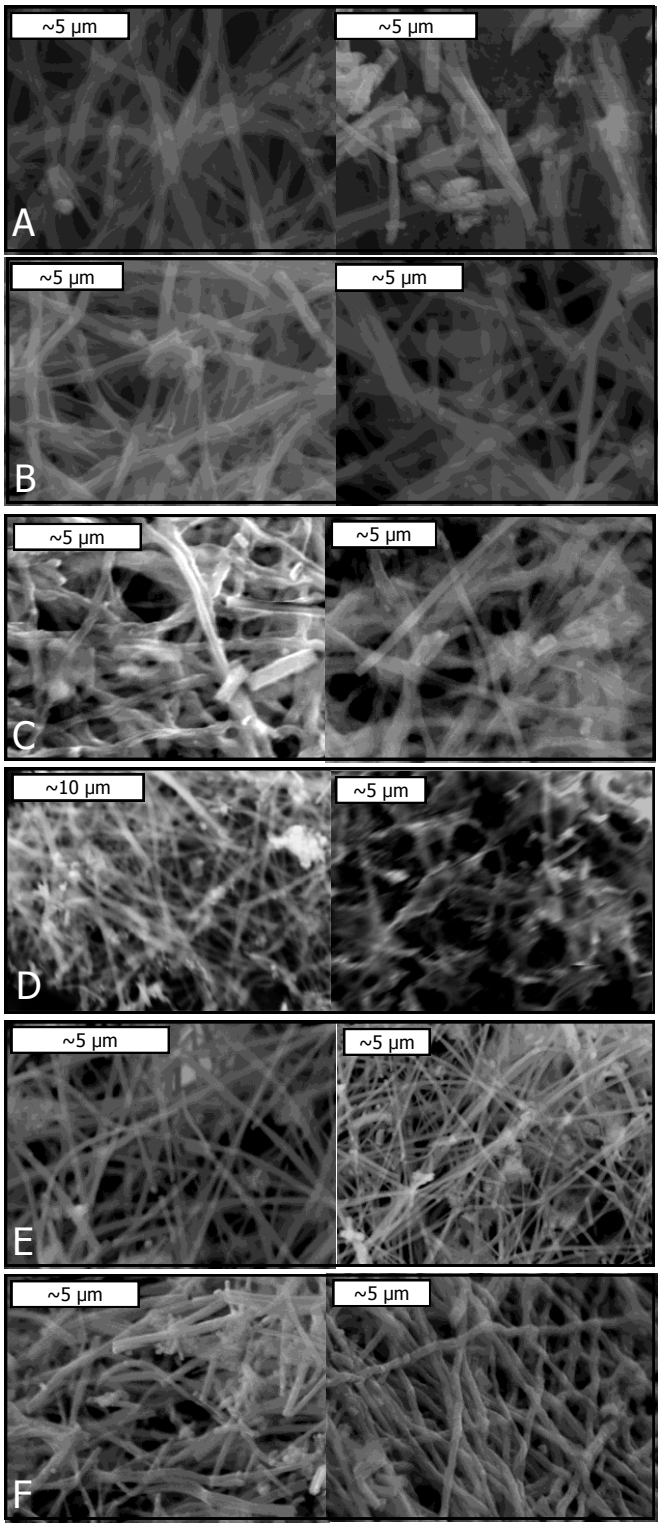

Figure 4.14. SEM images of copper doped TiO_2 nanofibres as a function of copper loading (mol %). A. 0.01, B. 0.50, C. 1.00, D. 5.00, E. 10.00 and F. 50.00. In all loadings of copper the morphology was observed to be fibrous, with little to no defects. The fibre diameter was found to be 500-1000 nm, with no dependence on loading concentration.

SEM analysis of the nanofibres found the fibres to be generally smooth with some aggregates caused by pooling of the electrospinning solution (Figure 4.14). The morphology did not significantly change on the increase of copper loading. The fibre diameter was found to be 500-1000 nm, with little dependence on copper concentration. This is evidence that the copper has not lattice substituted and is instead situated on the fibre surface, however, no evidence of surface coating was observed in these SEM images.

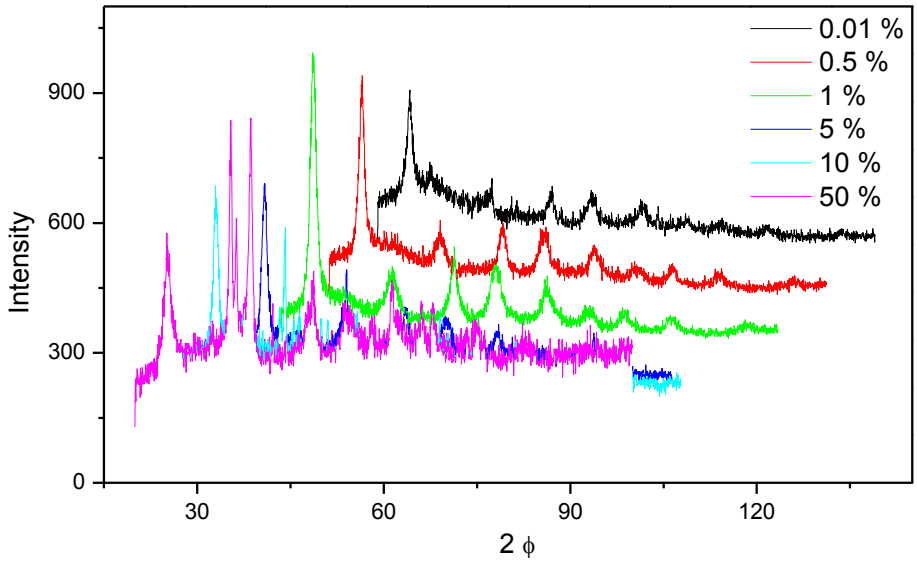

Figure 4.15. X-ray diffraction patterns of copper oxide doped TiO_2 nanofibres. It was found that TiO_2 was present in the anatase phase. CuO was observed from 5 %, showing a small solubility of copper into the titania lattice. As the copper concentration tends towards saturation Cu_2O is also observed, which is thought to lie on the fibre surface.

The composition and phase of the copper doped nanofibres was investigated by X-ray diffraction as a function of loading concentration (Figure 4.15). TiO_2 was

observed only in anatase crystallinity, decreasing in intensity as the concentration of copper increased. The anatase pattern indexes of the 0.01 mol % Cu nanofibres are less intense than expected due to poor loading in the sample holder. Copper was found in the form of CuO, however, at 50.00 mol % copper loading Cu_2O was also observed. This is in good agreement with Kang and Choi, who observed the CuO (111) and (002) faces above 5 mol % copper loading,[252] and proposed copper to be present only on the titania surface. This is contradictory to Larsson and Andersson, who observed only anatase phase TiO_2 when loading with copper, and documented no shift of the peaks, however, they note the overlap between indexes of CuO and anatase TiO_2 could lead to incorrect assignments.[253] Song *et al.* further confirm that copper oxide planes are not visible in X-ray diffraction, which they attribute to copper doping into the TiO_2 lattice.[254] Gomez *et al*. also did not observe any copper materials in the X-ray diffraction patterns of their samples, only a shift of the anatase TiO_2 peaks, which they theorised could be due to the cationic substitution of Cu^{2+} for Ti^{4+}.[255] We also observed a 0.5 % shift in the anatase diffraction patterns which may be attributed to lattice substitution by Cu^{2+}. Equation 4.14 describes the substitution of Ti^{4+} by Cu^{2+} and the subsequent formation of an oxygen vacancy.

$$Ti_{Ti}^{x} \rightarrow Cu_{Ti}'' + V_O^{\cdot\cdot} \tag{4.14}$$

It was theorised that in our nanofibres, below 5 mol % Cu loading, the copper is incorporated into the lattice and that above this loading the lattice becomes saturated and the copper is present as CuO on the surface, resulting in its prominence in the X-ray diffraction patterns.

From X-ray diffraction patterns, the Scherrer equation was used to determine the effect of copper doping on crystallite size. The crystallite size of copper doped titania

nanofibres was observed to be smaller than that of undoped nanofibres, reducing from 12.9 nm to 7.0 nm, which was attributed to disruption of the crystallite growth by the Cu^{2+} (Table 4.7). The crystallite size was not found to be concentration dependent as we did not observe any significant change in crystallite size with increased copper loading. These findings are in good agreement with Larsson et *al.*[256] Both Gomez *et al.*[255] and Song *et al.*[254] also observed a decrease in crystallite size when copper was loaded, which Song *et al.* attributed to doping inhibiting crystallite growth, further corroborating our data.

Table 4.7. Crystallite size of copper doped TiO_2 nanofibres. Crystallite size decreases non-negligibly upon the addition of a copper dopant, attributed to disruption of the crystallite growth by the dopant.

Copper Loading/mol %	0.01	0.50	1.00	5.00	10.00	50.00
Crystallite Size/nm	7.9	8.4	7.1	7.9	10.1	5.9

The photoactivity of copper loaded nanofibres was tested by assessing the degradation of phenol under UV illumination. As the copper loading increased to 1.00 mol % the photoactivity increased to above that of pristine TiO_2 nanofibres, 0.85 compared to 0.47. This was attributed to the copper dopant acting as a shallow electron trap, reducing electron-hole pair recombination, an explanation shared by Gomez *et al.*, who attributed surface CuO oxide clusters to the increased rate of decomposition of 2,4–dichlorophenoxyacetic acid compared to P25 and their prepared pristine TiO_2.[255] Dutta *et al.* ascribed the increase in hydrogen production with copper loaded TiO_2 to be

a facet of the decreased bandgap of the doped material. Kang and Choi, however, argue that the increased reduction potential of CuO, to either Cu_2O (E_0 = 0.153 V) or Cu (E_0 = 0.342 V), is greater than that of TiO_2 (E_0 = -0.502 V), resulting in CuO absorbing electrons, inhibiting recombination.[252,257]

At loadings above 1.00 mol % the photoactivity was observed to decrease, reducing to 0.24 at 50.00 mol %, which was attributed to the higher density of CuO, acting both as a recombination centre and reducing the contact between TiO_2 and CuO, lessening the charge transfer between the two.[255,258]

Furthermore, doping copper into titania has been shown to facilitate a change in the bandgap energies. Gomez *et al.* observed a reduction in bandgap energy, by diffuse reflectance UV-Vis absorption, to 2.81 eV at 5 wt. % loading of Cu, but did not observe any visible light activation of the catalyst. They assigned the apparent reduction in bandgap to the $2E_g \rightarrow 2T_{2g}$ transition of Cu^{2+}.[255] Dutta *et al.*, however, observed an extension of the bandgap into the visible region, 2.4 eV, with a commensurate activation by visible light.[258]

4.4 Cobalt Oxide and Cobalt Phosphate Materials

Based on our previously observed high photoactivities of cobalt doped TiO_2, precedent was found to investigate the photoactivity of monometallic cobalt compounds. Monometallic cobalt compounds have previously been shown to behave as semiconductors by the group of Nocera at MIT. They found that cobalt "pacman" complexes, applied to biochemistry, would completely reduce O_2 into H_2O.[259] In order for a system to perform these transformations, it must be able to provide four electrons

and four protons. Using this knowledge they synthesised a cobalt catalyst that proved very effective in water splitting, by placing Co^{2+} precursors into a phosphate solution that formed a Co-P catalyst *in situ*.[260] The scientific principles that govern a materials ability to split water are the same as those that allow a material to photooxidise volatile organic compounds, which prompted us to investigate $Co_3(PO_4)_2$ and CoO nanomaterials for use in the photodegradation of phenol.

4.4.1 Morphology and Photoactivity of Cobalt Oxide and Cobalt Phosphate Nanomaterials

Cobalt oxide and cobalt phosphate nanomaterials were prepared by five methods and tested for photoactivity by measuring the degradation of phenol under UV illumination. The preparation methods used gave rise to two different morphologies, powder and fibre, in varying degrees of purity. One of the attempted preparation methods resulted in a low yield and therefore was not studied further. Of the four samples analysed, three showed non-negligible photooxidation of phenol (Figure 4.16), however, all values were below the photoactivity of pristine TiO_2 nanofibres. The activity of the fibre compounds, A and C, showed lower activity than the two powdered compounds, B and D, which was attributed to the increased surface area of nanopowders compared to nanofibres: to confirm this conclusion BET studies will be required, which were unavailable at the time of study (Table 4.8).

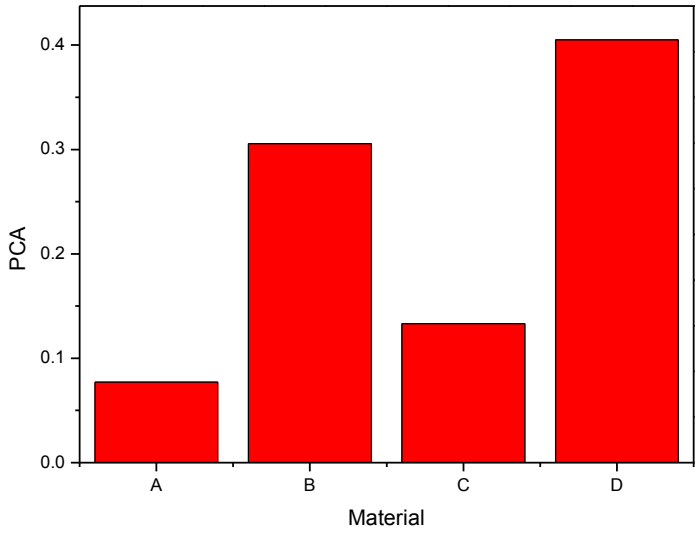

Figure 4.16. Activities of the four cobalt materials. A) CoO fibres, B) CoO from Na_3PO_4, C) $Co_3(PO_4)_2$ from H_3PO_4, D) Electrospun $Co_3(PO_4)_2$. The two powdered samples (B and D) show increased activity compared to the fibrous samples (A and C) which is predicted to be a facet of the higher surface area of powdered samples. Whilst all four catalysts show non-neglidigble photoactivity they are less active than pristine TiO_2.

Table 4.8. Experimental data from cobalt materials.

Material	Morphology	Particle/Fibre Size (nm)	PCA
CoO Fibres	Fibres	500-1000	0.08
CoO from Na_3PO_4	Particulate	400	0.30
$Co_3(PO_4)_2$ from H_3PO_4	Mainly particulate some fibres	Unable to determine	0.13
$Co_3(PO_4)_2$ electrospun	Powder	100	0.40
$Co_3(PO_4)_2$ fibres	Fibres	5000-10000	Not yet run

The individual experimental procedures and SEM and EDX analyses are discussed below.

4.4.1.1 Cobalt Oxide Nanofibres

Cobalt oxide fibres were prepared by electrospinning $Co(AcAc)_2$, yielding fibres of dark green colour and 500-1000 nm diameter. The product was uniformly fibrous and conductive, with no observable defects. This shows that $Co(AcAc)_2$ has significant interactions in the polymer solution to form fibres and retain the morphology after calcination (Figure 4.17). EDX analysis showed the presence of cobalt only, where other peaks were assigned to the stage of the SEM.

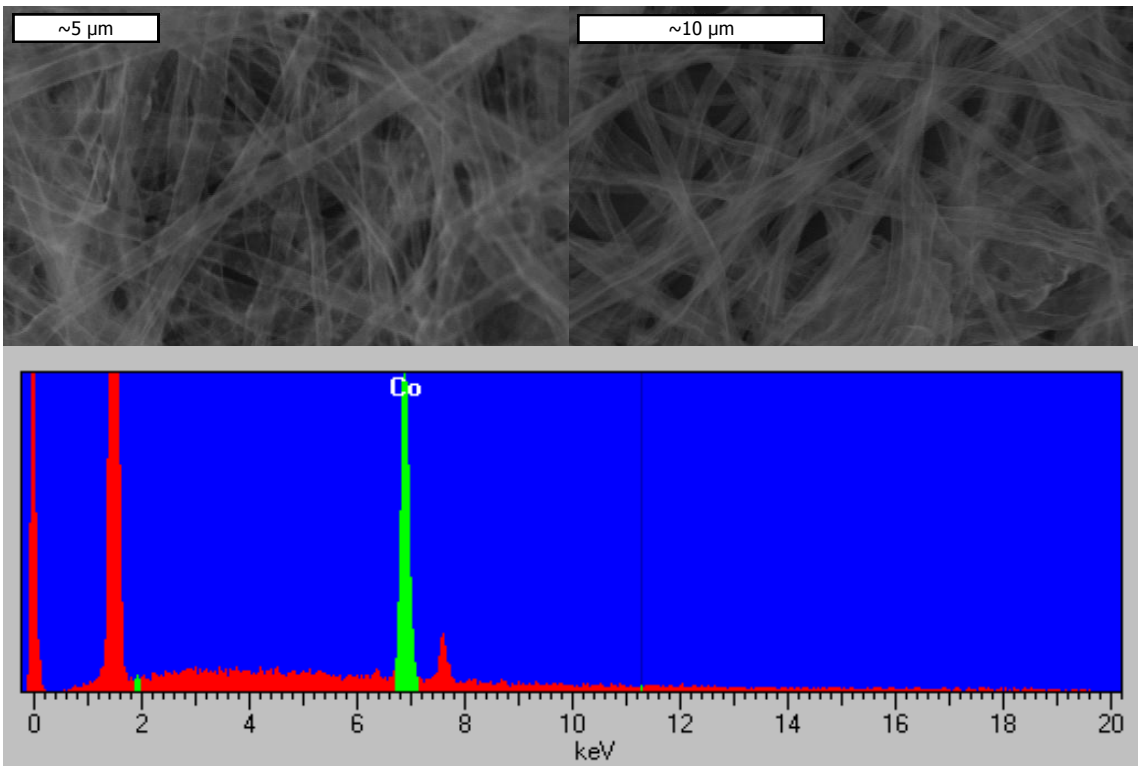

Figure 4.17. SEM images and EDX analysis of CoO nanofibres. Other peaks in the EDX spectrum are from the stage of the SEM. The material was uniformly fibrous and 500-1000 nm diameter.

X-ray diffraction confirmed the presence of cobalt as CoO, where no other materials were observed (Figure 4.18). The observed CoO pattern was relatively sharp and pure.

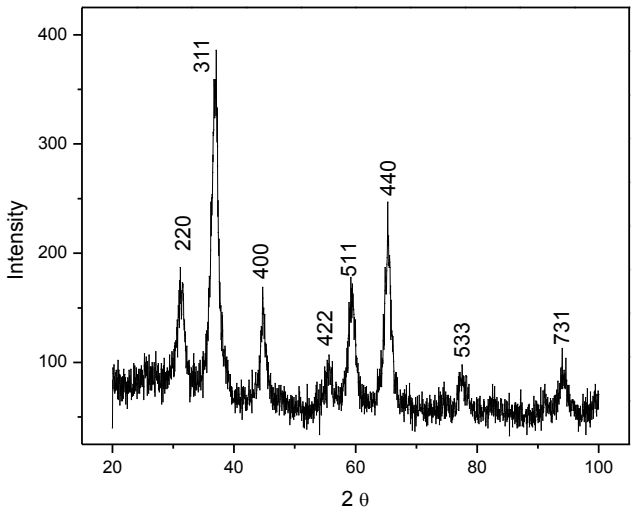

Figure 4.18. X-ray diffraction pattern of cobalt oxide.

The CoO nanofibres were tested for photoactivity by degradation of phenol where the photoactivity was found to be ~5 times lower than pristine TiO_2 nanofibres, 0.08 compared to 0.47. The reduction potential of Co^{2+} is -0.28 V, less than that of TiO_2, -0.502 V, resulting in a lower affinity for the photooxidation of phenol. Furthermore, CoO has a relatively small bandgap of 2.2-2.8 eV,[261] which may not have the redox potential to oxidise phenol. Moreover the measured fibre diameter of the CoO fibres was larger 500-1000 nm than that of TiO_2 nanofibres, 400-500 nm, which would result in a lower surface area for the cobalt fibres, further reducing their comparative photoactivity.

4.4.1.2 Cobalt Phosphate

Method 1: Sodium Phosphate

To prepare cobalt phosphate Na_3PO_4 was added into a polymer solution containing $Co(AcAc)_2$ to convert the cobalt acetyl acetonate to cobalt phosphate *in situ*, however, sodium phosphate was very insoluble in the electrospinning solution resulting in little contact between reactants. After electrospinning the sample was not steam treated as usual to dissuade the material from converting to cobalt hydroxide. The electrospun material was calcined at 550 °C, yielding a black powder. The morphology was examined by SEM revealing some fibrous material but the majority of the morphology was particulate (Figure 4.19). The particle aggregates were found to be ~400 nm, a higher resolution image may reveal smaller sizes. By EDX analysis the material was found to contain cobalt but no phosphorous, indicating that cobalt phosphate had not been formed. Other signals observed in the EDX spectrum were assigned to the stage of the SEM.

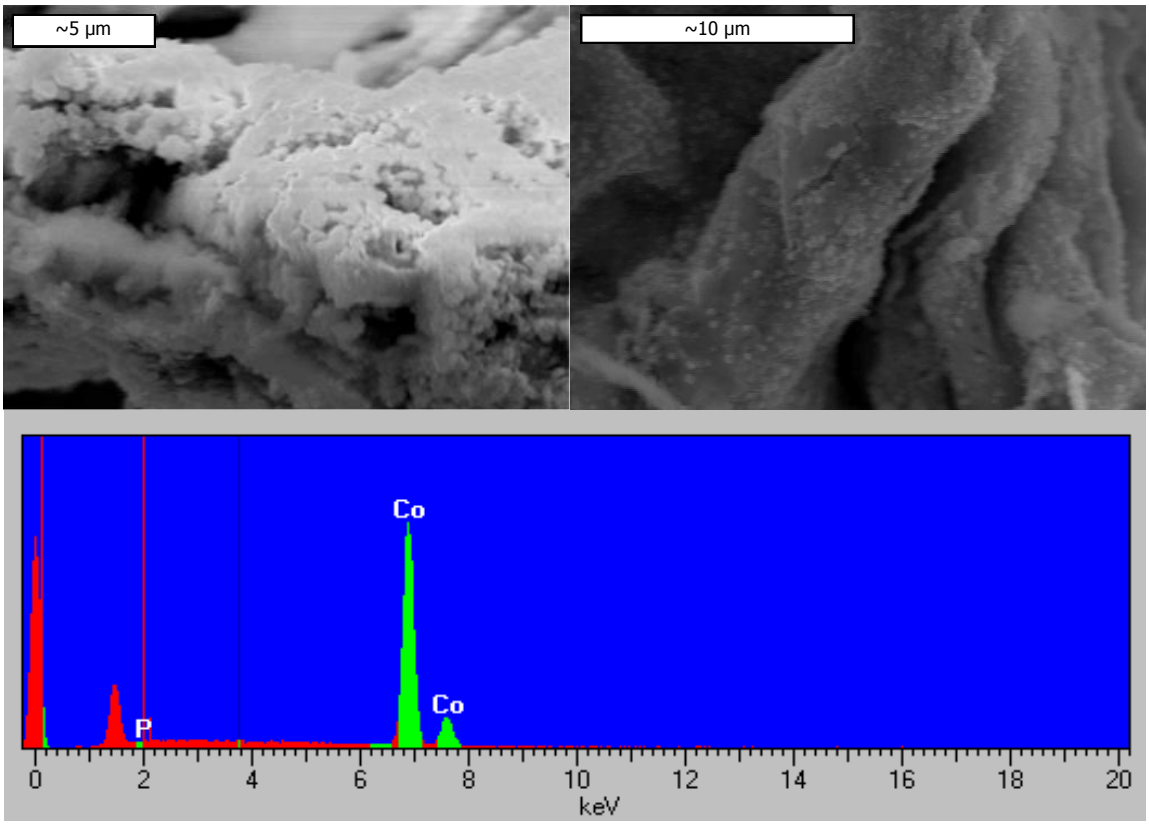

Figure 4.19. SEM images and EDX analysis of CoO from the attempted preparation of $Co_3(PO_4)_2$ from Na_3PO_4. The EDX revealed the phosphorous concentration to be too low for the material to be cobalt phosphate.

X-ray diffraction was used to determine the compound of cobalt present. The diffraction pattern was assigned to CoO, where no presence of any other material was observed (Figure 4.20). The formation of cobalt oxide was attributed to the insolubility of sodium phosphate, not encouraging its reaction with cobalt acetyl acetonate.

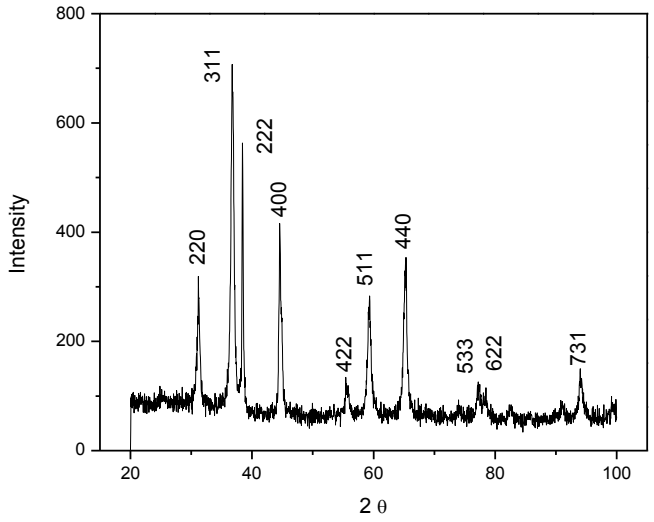

Figure 4.20. X-ray diffraction pattern of attempted preparation of cobalt phosphate from sodium phosphate. The pattern is that of cobalt oxide.

The photoactivity of the CoO powder was determined to be 0.30, four times higher than that of the CoO fibres, which has been attributed to the expected increase in surface area of the nanoparticles. An investigated into surface area is necessary to clarify this. The activity is lower than that of TiO_2 nanofibres, which is attributed to the reasons presented in Section 4.4.1.1.

Method 2: Phosphoric Acid Soak

The preparation of cobalt phosphate was attempted a second time by electrospinning cobalt acetyl acetonate and then immediately soaking the fibres in a 5 % phosphoric acid solution for three days. Green fibres were formed which were then calcined at 550 °C without prior steam treatment. After calcining, only a grey solid remained. Analysis of the morphology by SEM revealed that few fibres were prepared,

with the morphology being predominantly particulate (Figure 4.21). SEM imaging was difficult due to charging effects experienced. In future, gold coating will be required to accurately image the product.

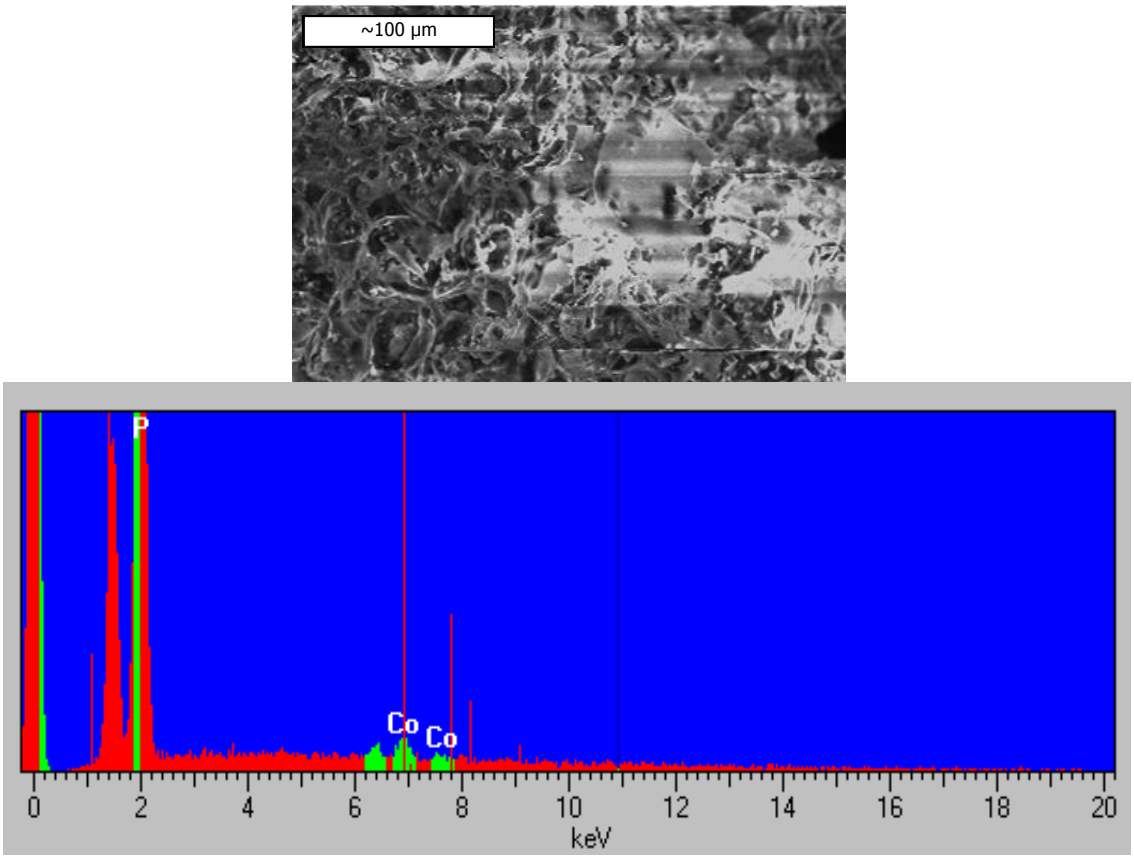

Figure 4.21. SEM image and EDX analysis of the sample. The SEM image is of poor quality due to charging effects from the sample. The EDX spectrum shows large quantities of phosphorous in comparison to cobalt.

Compositional analysis by EDX showed a high content of phosphorous compared to cobalt (19:1), which is in contrast to Nocera, who found this ratio to be 1:2.[259] The elemental composition is not correct to be purely $Co_3(PO_4)_2$, however, the excess phosphorous present is attributed to arise from the reaction of phosphoric acid and aluminium foil (Equation 4.15). Other peaks present were assigned to the stage of the SEM

$$Al + H_3PO_4 \rightarrow AlPO_4 + 1\,{}^{1}/_{2}\,H_2 \quad (4.15)$$

Analysis by X-ray diffraction confirms the presence of $Co_3(PO_4)_2$ and a number of impurity peaks (Figure 4.22). These diffraction patterns were assigned to aluminium phosphate and aluminium oxide, a result of the aluminium foil used as a substrate during electrospinning.

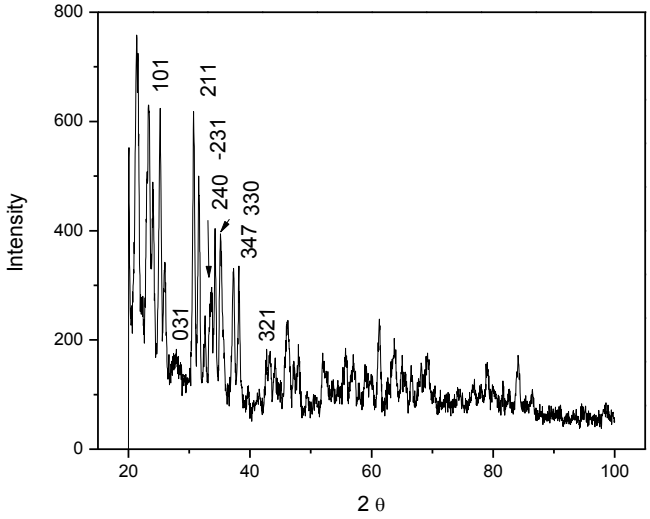

Figure 4.22. X-ray diffraction pattern of cobalt phosphate prepared from phosphoric acid.

The photoactivity of this mixture of compounds was analysed by measuring the decomposition of phenol. The observed photocatalytic activity was 0.13, four times lower than for pristine TiO_2 nanofibres (0.47). Despite retaining the morphology of the sodium phosphate prepared sample, the photoactivity is lower, which is attributed to the presence of aluminium oxide and aluminium phosphate impurities.

By this method, cobalt phosphate nanofibres were readily prepared but, due to the side reactions associated with the aluminium foil, it was determined to be an

unsuitable synthetic route. Modification of the electrospinning process to remove the necessity of an aluminium foil collector may result in the preparation of pure cobalt phosphate nanofibres.

Method 3: Electrospinning Commercially Purchased $Co_3(PO_4)_2$ Powder

The preparation of cobalt phosphate nanofibres was attempted by electrospinning commercially purchased $Co_3(PO_4)_2$. This method yielded pink fibres, retaining the colour of the starting material, which were calcined at 550 °C. Morphological analysis by SEM revealed that, after calcining, only particulate remained, this was attributed to $Co_3(PO_4)_2$ being unable to hold a fibre structure once the polymer scaffold has been removed (Figure 4.23).

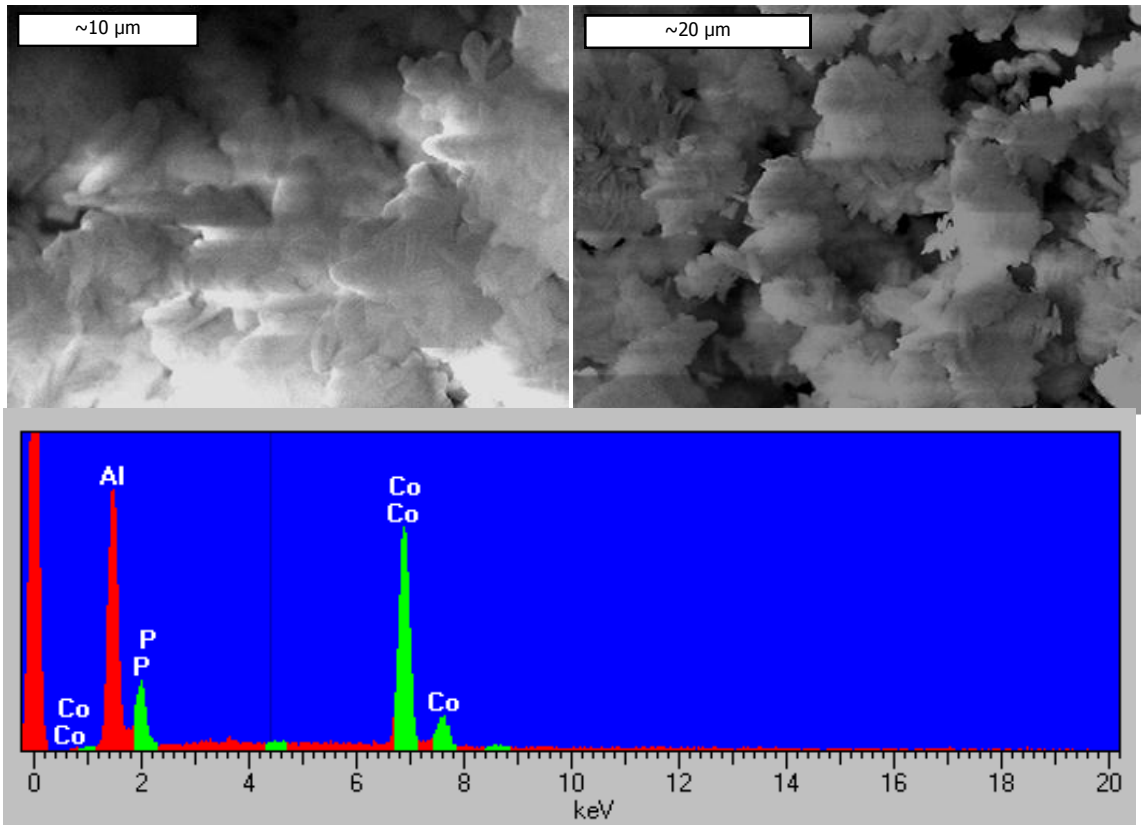

Figure 4.23. SEM images and EDX analysis of attempted production of nanofibres from electrospinning cobalt phosphate. The 1:2 ratio of phosphorous to cobalt is in good agreement with the findings of Nocera *et al.*.[79]

Elemental analysis by EDX found cobalt and phosphorous in ratios consistent with pure cobalt phosphate (Figure 4.23), where the presence of other elements, such as aluminium, were a result of the SEM stage.

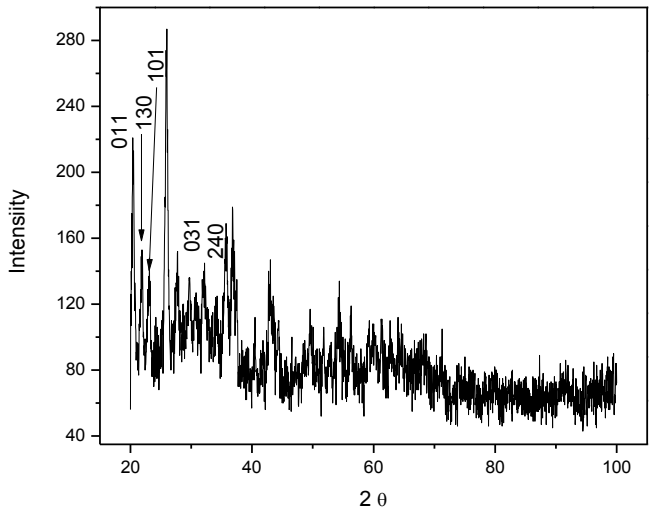

Figure 4.24. X-ray diffraction pattern of electrospun commercially purchased cobalt phosphate powder.

The prepared powder was determined to be $Co_3(PO_4)_2$ by X-ray diffraction, consistent with the EDX data presented in Figure 4.24. The thus far unassigned peaks have been attributed to impurities in commercial cobalt phosphate.

The photoactivity of the cobalt phosphate powder was analysed by measuring the degradation of phenol under UV illumination. The observed photoactivity was found to be 0.405, slightly lower than that of pristine TiO_2 nanofibres, despite the predicted increase in surface area of powders. The lower photoactivity is attributed to the lower bandgap energy of cobalt phosphate, 1.7-3.1,[262] which may not have the reducing power to incite the degradation of phenol. Furthermore the redox potential of Co^{2+} is lower than that of Ti^{4+}, E_0= -0.28 V compared to E_0= -0.502 V, which may also

lead to lower photooxidation activity. This preparation proved the potential application of cobalt phosphate to photooxidation reactions, however, this preparation method was unsuitable for the preparation of nanofibres.

Method 4: Acetone Soak

A further attempt at the preparation of fibrous $Co_3(PO_4)_2$ was performed by electrospinning cobalt acetyl acetonate and soaking this in a 1:1 solution of acetone and water, which was saturated with Na_3PO_4 for three days. The purpose of the acetone solution was to remove the PMMA whilst simultaneously converting the Co(AcAc) to $Co_3(PO_4)_2$, in order to avoid the sample collapsing into a powder. The sample was not steam treated but calcined at 550 °C, yielding dark blue fibres. Morphological analysis by SEM revealed the product had retained its fibrous morphology with a diameter of 1-10 μM (Figure 4.25). The observed fibres were brittle and contained many nodules. These were attributed to the stirring of the soaking solution causing deformities. Elemental analysis by EDX found a 3:1 ratio of phosphorous to cobalt, which is not consistent with pure cobalt phosphate. Thus far the excess phosphorous is attributed to Na_3PO_4 impurities in the fibres, however, further analysis, including X-ray diffraction, will be required for complete characterisation of the material.

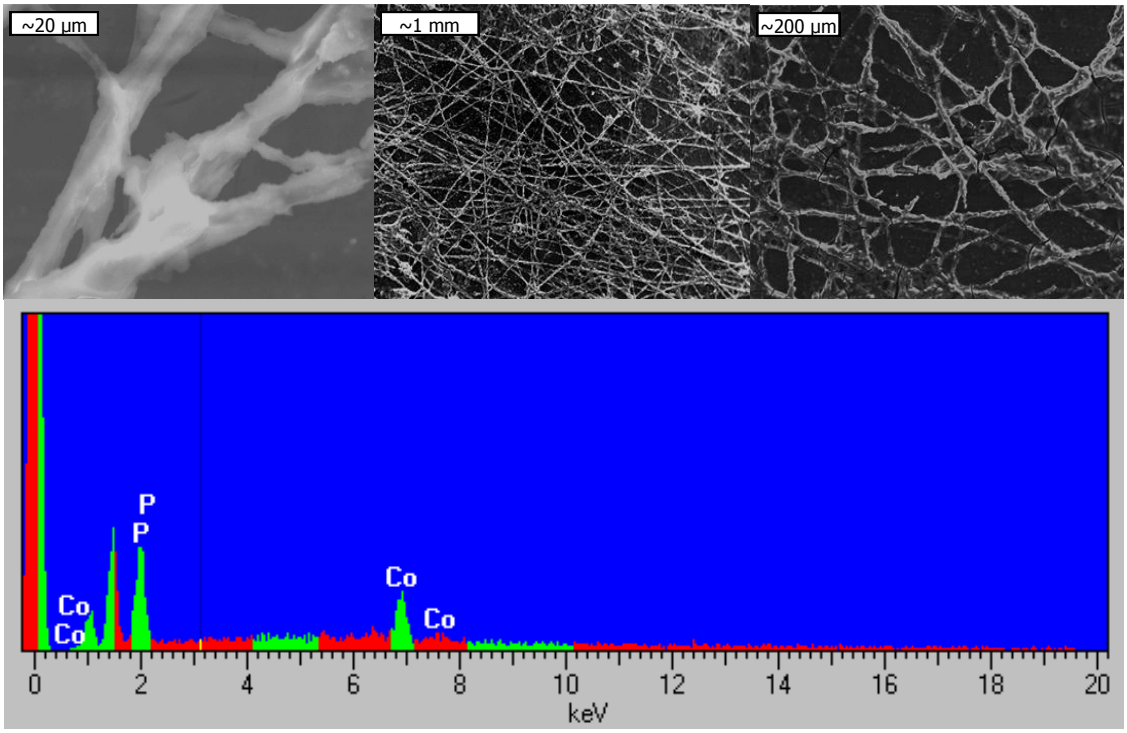

Figure 4.25. SEM images and EDX analysis of fibrous Co:P material assigned to be impure $Co_3(PO_4)_2$.

4.5 Conclusions

It was found that doping nanofibres with metal oxides alters the activity. For all dopants 1 mol % loading yields the highest activity. For all dopants, apart from iron, this activity was higher than that of pristine TiO_2 nanofibres. A maximum photoactivity was achieved by doping TiO_2 nanofibres with cobalt reaching a value of 1.94, compared to 0.47 for undoped TiO_2 nanofibres. This increase in photoactivity has been attributed to the dopant behaving as a shallow electron trap, reducing the electron–hole pair recombination rate. Above 1 mol % loading the activity decreases due to the closer proximity of metal centres allowing them to behave as recombination centres.

No change in TiO_2 phase with dopant loading was observed, but crystallite size was found to decrease upon addition, which was attributed to the inhibition of crystallite

growth by the dopant. Once incorporated into titania, increasing the loading of the dopant did not significantly alter the crystallite size. No change in morphology was observed upon the addition of dopants, all producing defect free nanofibres. Further analysis by surface area measurements and XPS analysis would add insight into the properties of doped titania nanofibres.

Mono-metallic cobalt materials were found to non-negligibly oxidise phenol under UV illumination. Cobalt oxide was found to be less photoactive than cobalt phosphate, which was in turn less active than pristine TiO_2. The smaller bandgaps of CoO and $Co_3(PO_4)_2$ (2.2-2.8 eV and 1.7-3.1 eV respectively[262]), may incite a visible light response from these catalysts. While more investigations are required, including surface area measurements and XPS, monometallic cobalt materials show promise in the field of photocatalysis.

5. Supported Catalysis

P25, a powdered mix of 75 % anatase and 25 % rutile TiO_2, has been shown to have one of the highest activities with regard to photocatalytic degradation, but its morphology carries an inherent disadvantage. While P25 has a large surface area (35-65 m^2/g), powders lack mechanical strength and can result in pressure drops in continuous flow reactors. Because of this drawback, much research has been focused on the development of supports for TiO_2, where silica materials are a popular choice.[263–265] Silica supports are advantageous for several reasons; the starting materials are generally cheap, safe and abundant, they combine well with TiO_2, are inert to photoreactions themselves (and to VOCs), there are a number of morphologies that can be made from them, such as zeolites,[266,267] fibres[268] and spheres[269] and finally, in certain structures, there is the possibility they can perform as wave guides for light.

In this chapter, an investigation into the development of three types of supports; zeolites, glass fibres and TiO_2 nanofibres is presented. All three were investigated with respect to synthesis, morphology and photocatalytic activity.

5.1 Zeolites

Discovery

Zeolites are a group of man-made and naturally occurring, porous aluminasilicates. In 1756 renowned mineralogist Axel Fredrik Cronstedt observed a material that could absorb a large amount of water, *via* intumescence.[270] This material was later revealed to be the mineral stellerite, containing an amount of stilbite; he named this novel material a zeolite, from the greek *zeo* (to boil) and *lite* (stone). From

the initial discovery the next century was spent investigating the adsorption properties of these new materials and their syntheses. It was during this time that the faujasite structured zeolite Y was first discovered in Germany. By the 1930s the first single crystal structure had been obtained[271] and by the 1950s Union Carbide and Mobil had begun to synthesise and use zeolites for a variety of applications including; drying gas,[272] separation and purification,[273] and hydrogen cracking.[274,275] During the 1980s and 1990s there was an increase in zeolite research because of the modification of zeolite Y to sodium-Y,[276] and Mobil's MCM zeolites.

MCM, or Mobil composition of matter, are a series of mesoporous, inorganic polymers created by Mobil in 1992.[277] MCM41-S is the amorphous silica variant of the 41st incarnation and MCM41-AS is the alumina silicate variant of the same incarnation. MCM41-S is 100 % SiO_2 whereas MCM41-AS is SiO_2 with ~ 3 % Al_2O_3.[278] Sodium zeolite Y is an alumina silicate with a faujasite structure and sodium counter-ion. It has a much higher content of Al_2O_3 than MCM41-S, by around 30 %.[279] These zeolites have extremely large surface areas where MCM41-AS has a specific surface area of 900-1000 m^2/g and Na-Y has a specific surface area of 900 m^2/g, however, MCM has a pore size of ~1.6-10 nm[278] to zeolite Y's ~0.6-0.8 nm.[280] The crystal structures of MCM41 and zeolite Y are shown in Figure 5.1.

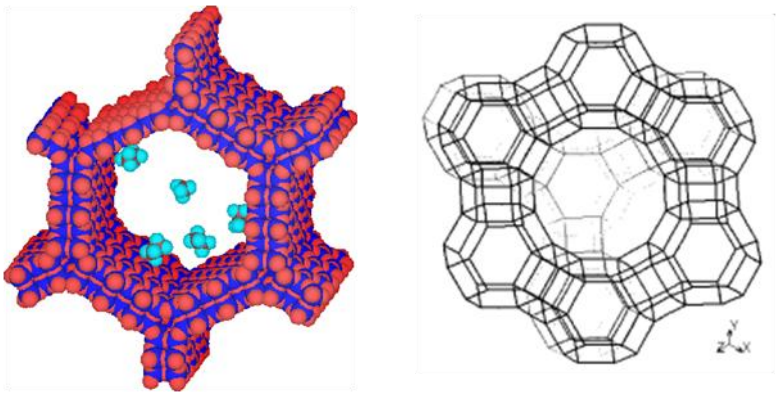

Figure 5.1. From left: structures of MCM41[15] and zeolite Y.[265]

Applications

The high porosity of zeolites renders them ideal candidates for molecular sieves and filters. A series of synthetic and natural zeolites were studied to determine their sorption affinity to d-block metals for the treatment of electroplating waste water, where it was found that the zeolites adsorbed ~20-61 mg/g of the pollutant.[281] Leinonen and Lehto also found that zeolites were suitable for waste water remediation, with selectivity of the d-block pollutant.[266] Both groups found that two mechanisms were possible; sorption of the pollutant *via* hydroxyl groups or cation exchange, with different pollutants favouring one mechanism or the other. Querol *et al*. found that while zeolites did not perform as highly as precipitation processes in the cleaning of polluted well-water, the zeolites were a passive remediation technique.[282] Castaldi *et al.* have shown the applications of zeolites towards solid waste remediation using a natural zeolite, clinoptilolite. They compared a zeolite, compost and calcium hydroxide to prevent the uptake of heavy metal pollutants from soil to lupin plants. They also found selectivity of the zeolite towards particular metals, namely cadmium, while zinc and

lead were more efficiently removed by compost and calcium hydroxide.[283] Zeolites have also been extensively used in the gas phase for both the separation and purification of products. Ackley *et al.* provide an excellent review of patents for gas phase purification using zeolites.[284]

Zeolites have also been applied to the field of catalysis for example, conversion of hydrocarbon based molecules has been observed over zeolites. Froment *et al.* provide extensive examples of many zeolites, and the conditions required, to catalytically convert methanol to gasoline.[285] Furthermore, *n*-butane has been converted over H-ZSM5 (zeolite Socony Mobil) under acidic conditions and was proposed to occur *via* carbonium ions.[286] Similarly conversion of 1-butene to propene was observed over several synthetic zeolites and the conversion was found to be dependent on the pore size of the zeolite.[287]

Zeolites can also be modified to contain other elements within their structure. Of particular relevance is the inclusion of titanium due to the possibility of photoactivation. Okubo *et al.* synthesised TS-1 (titanium silicate) by two different methods. The first involved a one-pot synthesis using titanium tetra *n*-butoxide (TBOT), tetraethyl*ortho*silicate (TEOS), tetrapropylammonium hydroxide (TPAOH), hydrogen peroxide and water.[288] The second used a titanium-peroxo complex as a replacement for the alkoxide complex. The two mechanisms gave rise to silicon and titanium rich zeolites respectively. Xia and Tatsumi synthesised Ti-β incorporated into a zeolite by several methods and found that some of these zeolites decomposed cyclohexane substantially more than TS-1.[289] They attributed this to the higher crystallinity of the Ti-β, where less crystalline samples are more hydrophilic, which reduces hydrocarbon oxidation. Furthermore, the Ti-β zeolite had a larger pore size, allowing diffusion for

larger molecules. This sentiment was shared by Corma *et al.* who synthesised a titanium silicate based on the MCM-41 structure, using a hydrothermal method with titanium tetraethoxide.[290] They found that surface area and pore size did not change appreciably from the native zeolite, 932 m^2/g and 0.2 nm respectively. They found that the pore size of Ti-MCM-41 allowed for selective transformation of large organic molecules. Moreover, titanium can also be inserted into zeolite structures post-synthesis. Mohamed *et al.* showed that Titanium was incorporated into zeolite Y by ion exchange, using potassium titanooxalate.[291]

Zeolites have also been used as supports for photoactive species, such as TiO_2, for use in photooxidation reactions. They are good choices for photocatalysis supports as they are commonly transparent above ~280 nm,[292] allowing for UV light penetration. Furthermore, it is thought that zeolites will accept an electron and keep it delocalised around the entire structure, decreasing the recombination rate.[293] As early as 1997 TiO_2 was coated on zeolites Y, X and MCM-41 for the liquid phase photooxidation of acetophenone.[294] The zeolites were made in-house, with differing pore sizes and alumina to silica ratios, and then coated with TiO_2. However, Langford and Xu predicted that using a solution preparation, the titanium particles would be too large to diffuse into the zeolite pores, therefore they modified the preparation by careful temperature and mixing control, to create 2-4 nm particles. They found that the smaller TiO_2 particles generally gave rise to catalysts with a lower surface area, which is consistent with the filling of the zeolite pores. Conversely, the larger TiO_2 particles gave rise to catalysts with surface areas similar to that of the native zeolites, this provides evidence of surface coating. Photocatalytic efficiency of the surface coated samples was

typically higher than for the pore loaded samples, which was attributed to greater light adsorption and unblocked zeolite pores.

TiO_2 coated on a zeolite, using titanium tetrabutoxide, has been shown to degrade formaldehyde in the gas phase at higher efficiencies than native TiO_2 powder, attributed to an increase in surface area and adsoprtion.[295] Jasra *et al.* achieved similar results by coating zeolites HY and NaY with TiO_2 using a TTiP solution.[296] Tanaka and Hisanaga also coated zeolites by this method in large loadings, 30-60 wt. % of TTiP to zeolite.[297] All TiO_2 loaded catalysts showed superior activity to native TiO_2 in the gas phase degradation of benzene, however, they attributed this not just to higher adsorption of the pollutant onto the zeolite but also the increased adsorption of water.

TiO_2 has been surface coated on to zeolites by plasma chemical vapour deposition (PCVD) of TTiP, where the coating amount was controlled by reaction time.[298] It was found that lower coatings of TiO_2 provided higher conversion of NO and SO_2, which was attributed to the pores of the zeolite remaining exposed.

TiO_2 has also been coated onto zeolites HY, Hβ and H-ZSM by stirring the zeolite with P25 in acetone where titania coated the surface and entered the pores, as evidenced by a decrease in surface area.[299] The photooxidation of 2,4–dichloro phenoxyacetic acid was increased twofold by zeolite supported TiO_2 which was attributed to the higher surface area and adsorption. For these reasons, low TiO_2 loadings (< 3 wt. %) show the highest activity as they maximise the use of the zeolites pores and surface area.

In the remainder of this section, investigations towards the combination of the large surface area of zeolites with the photoactivity of TiO_2 are presented. Two methods

were used to accomplish this; firstly, zeolite powders of Na-Y and MCM41-S were dipped into solutions of TTiP in DMF to facilitate the loading of TiO_2 into the pores of the zeolites. Secondly, Na-Y, MCM41-S and MCM41-AS zeolites were added to polymer solutions and electrospun to create novel zeolite:TiO_2 nanofibres and determine the critical amount of TTiP required to form nanofibres.

5.1.1 Photoactivity of Zeolite/Titania Materials

The photocatalytic activity of the zeolite/titania catalysts was tested by measuring the degradation of phenol in their presence. The experimental details of the photocatalytic measurement method are described in Section 7.3. The zeolites used in this work show no activity of their own, < 0.04, (Figure 5.2), therefore all degradation must come from TiO_2, with any increase in activity above the standards a result of the zeolites influence.

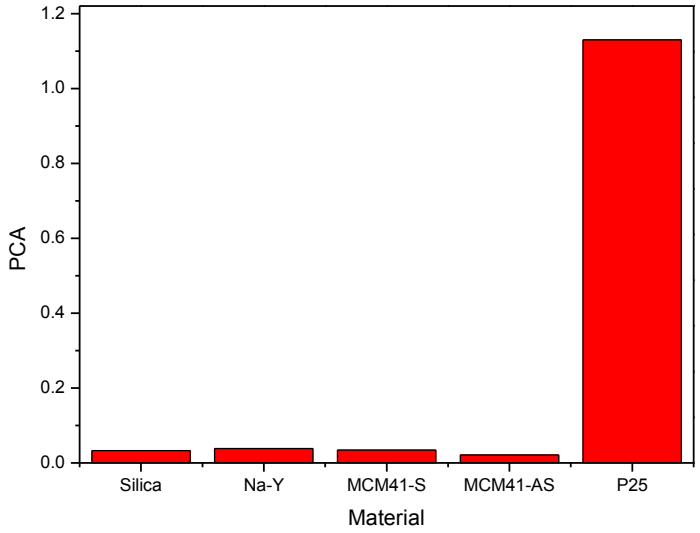

Figure 5.2. Catalytic activity of sodium zeolite-Y, MCM41-S and MCM41-AS starting materials and silica gel. It can seen that the starting materials do not show any activity of their own.

The X-ray diffraction patterns of the four supports were taken and were found to be in good agreement with literature patterns (Figure 5.3). MCM41-S, MCM41-AS and silica gel show little of interest in their diffraction patterns due to their lack of long range order.

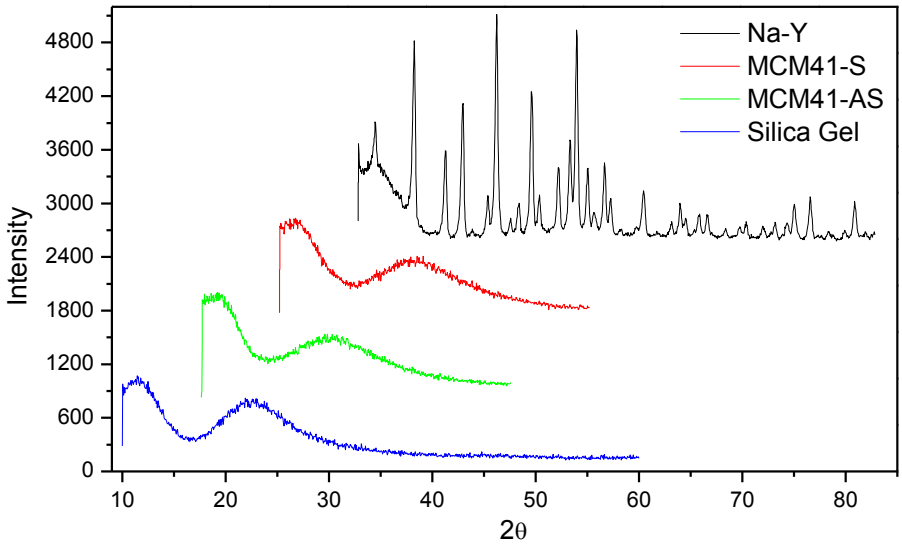

Figure 5.3. Typical X-ray diffraction patterns of Na-Y, MCM41-S, MCM41-AS and silica gel. MCM41-S, MCM41-AS and silica gel have no long range order so have little of interest in their X-ray diffraction patterns.

5.1.1.1 Dip Coated Zeolites

In order to prepare dip-coated zeolites, MCM41-S and Na-Y zeolites were soaked in solutions of TTiP in DMF, in concentrations of 0.001-1 M for 24 hours. After steam treatment (80 °C) and calcination (550 °C), powdered nanomaterials remained. The morphology and composition of the powders, as a function of TiO_2 loading, were analysed by SEM and EDX (Figure 5.4). The samples were powdered, however, the particulate size was unable to be determined due to low resolution of the images. Furthermore, SEM was unable to determine whether TiO_2 was present on the surface or in the pores of the zeolites.

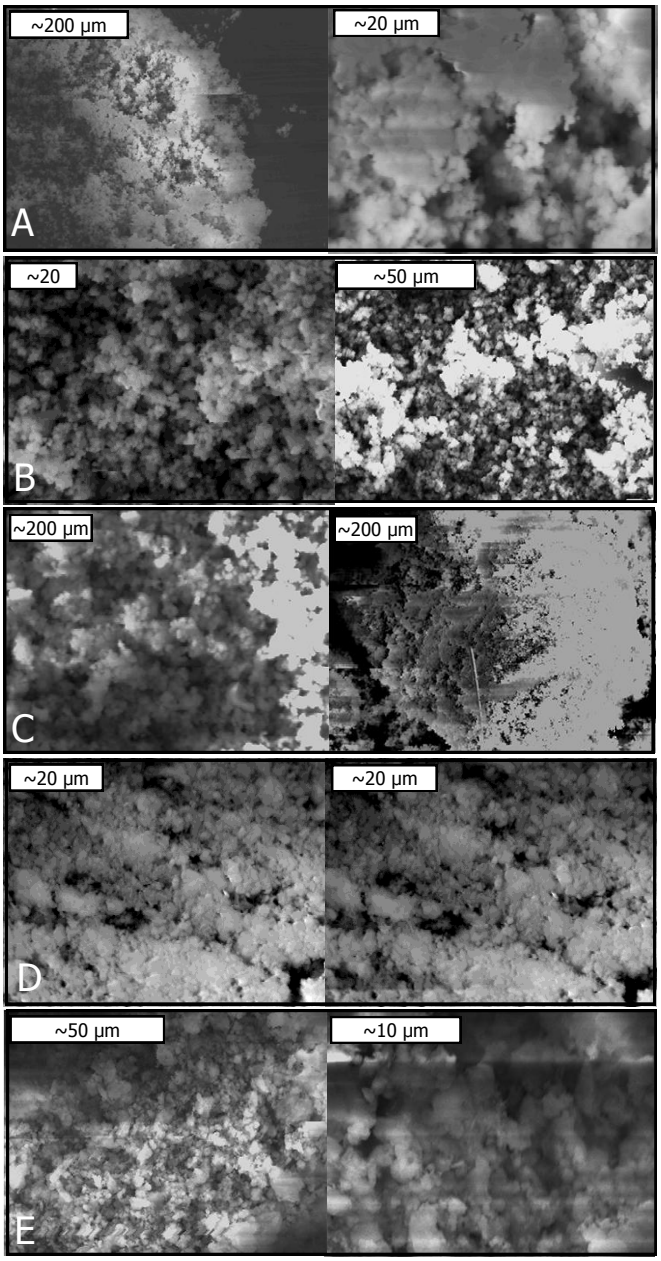

Figure 5.4. SEM images of dip-coated titania zeolites as a function of titanium loading (at. %), as determined by EDX spectroscopy. A. 0.35, B. 1.30, C. 2.74, D. 4.10 and E. 5.60.

The diffraction patterns of the prepared samples match the diffraction patterns of the zeolite starting materials. No shift of diffraction patterns was observed for any of the coated zeolites, which provides evidence that there was no change in lattice for either the zeolites or TiO_2 (Figure 5.5). This is evidence that the TiO_2 has entered the pores or

resides on the surface of the zeolites. In the Na-Y loaded zeolites, the anatase 101 peak can be observed clearly, with the peak intensity increasing with TiO_2 loading. The 101 peak is not observed in the diffraction patterns of MCM-41 despite the higher loadings, this could be caused by the zeolites destroying the long rang order of TiO_2. There is no presence of any TiO_2 species other than anatase, indicating that the presence of the zeolites does not alter the crystallisation of the titania.

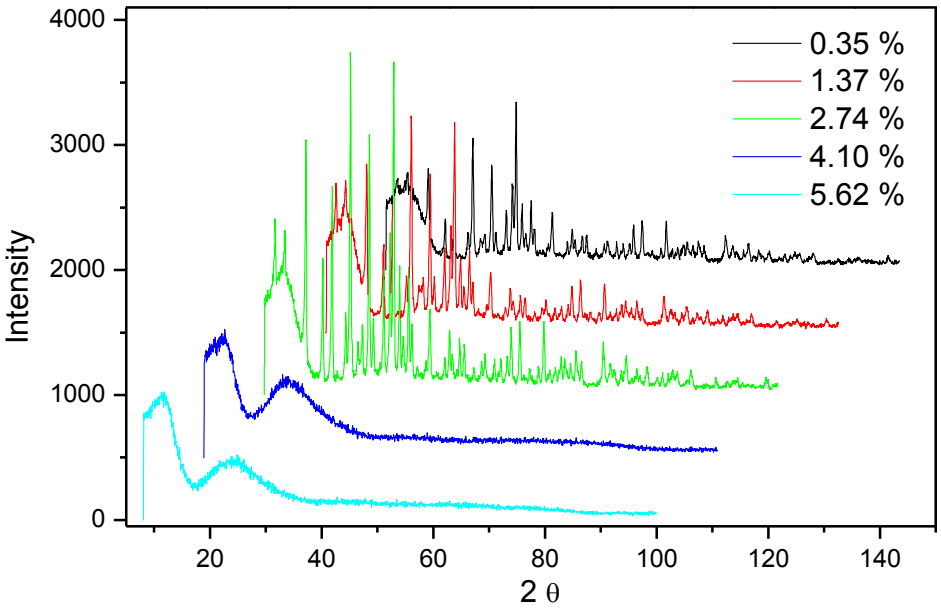

Figure 5.5. X-ray diffraction patterns of dip coated zeolites. Anatase peaks are not observed in the MCM-41 samples which is thought to be due to the zeolites destroying the long range order.

The photocatalytic activity of the dip-coated zeolites was tested by measuring the degradation of phenol under UV activation. It was found that the photoactivity increased linearly with titania loading (Figure 5.6). At 0.35 at. % the activity was 0.10, but by ~2.74 at. % the activity raised to 0.49, higher than that of pristine TiO_2 nanofibres. By 5.60 at. % loading of TiO_2, the activity had almost reached that of P25 (1.13), reaching 1.10. These findings are in contrast to Cheng *et al.*, who found that zeolite supported TiO_2 actually decreased the efficiency compared to pristine TiO_2 when degrading phenol, however, this was due to hydrophilicity of the zeolites preferentially adsorbing H_2O over phenol during a liquid phase reaction.[300]

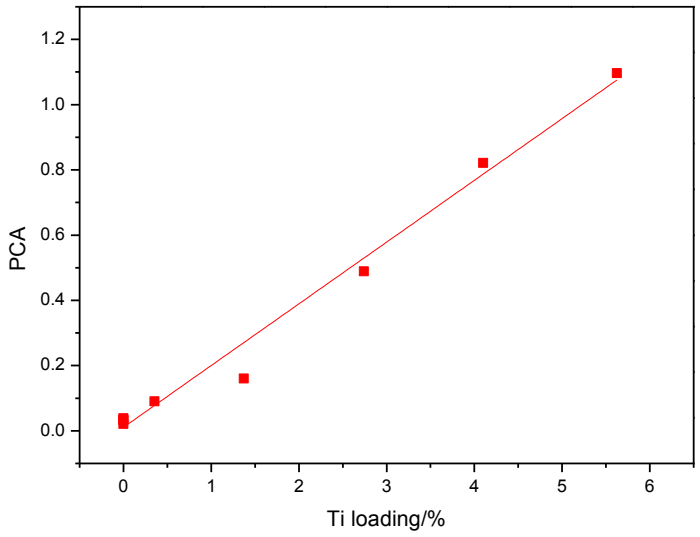

Figure 5.6. Photocatalytic activity of dip coated zeolites. The photoactivity increases linearly with TiO_2 loading, this is unsurprising as TiO_2 is the photoactive material. Despite the lower TiO_2 than pristine titania nanofibres, the activity is nearly as high as for P25. This is attributed to the high surface area, better absorption and electron delocalisation that comes from the presence of the zeolite.

The activity of the highest performing dip-coated zeolite is 20 times higher per gram of TiO_2 than for pristine TiO_2 nanofibres. There are three explanations for this increase in activity; the loaded zeolites will most likely have an increased surface area compared to native TiO_2, zeolites have been shown to have a high level of adsorption, increasing the contact time between TiO_2 and the pollutant and finally, zeolites are thought to act as electron sinks, decreasing the electron–hole pair recombination. Which one, or combination of these reasons, best describes the increase in activity is unclear, BET, sorption studies and spectroscopic analysis would be required to determine the precise explanation.

5.1.1.2 Electrospun Zeolites

To combine the activity of loaded zeolites with mechanical strength of nanofibres, zeolites were loaded into a TTiP containing polymer solution and electrospun. In low concentrations of TTiP, the fibrous morphology was lost after calcining, and the material collapsed into powder. This was due to the fibre structure being produced from the viscous polymer solution, which is removed when calcined. The inorganic components can remain as fibres after calcining only if they have enough interactions to retain the structure of the scaffold. Zeolites will not keep the fibrous structure on their own, therefore TTiP is required to act as a linker. In the synthesis of zeolite fibres it has been determined that when the TTiP to zeolite ratio is high enough, the morphology will remain fibrous after calcining. The morphology of these materials was analysed by SEM as a function of TiO_2 content, determined by EDX (Figure 5.7). Fibres were observed from 4.6 at. % Ti loading, and their presence increased as the titanium loading increased, however, it was not until 94.0 at. % loading that only

negligible amounts of particulate remained. Where fibres were observed they were found to be 500-1000 nm in diameter. Their surface structure was difficult to analyse due to the presence of large amounts of particulate.

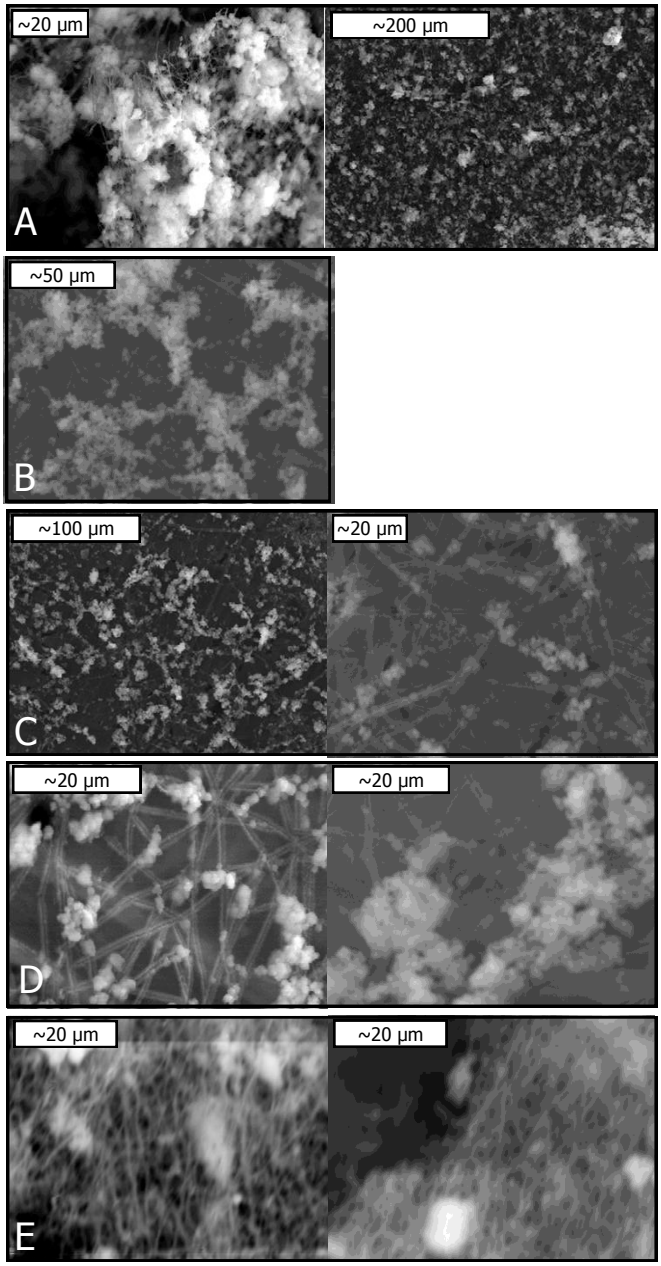

Figure 5.7. SEM images of electrospun zeolite:TiO_2 materials as a function of titanium content (at. %) as a determined by EDX spectroscopy. A. 4.6, B. 14.7, C. 18.8, D. 26.1 and E. 94.0. Fibres were observed from loadings of TTiP as low as 4.6 at. %, however, fibres did not become the dominant morphology until ~19 at. %.

The electrospun zeolite:TiO_2 composites were analysed by X-ray diffraction in order to determine any changes in the crystal structure (Figure 5.8). X-ray diffraction of the electrospun zeolite:TiO_2 materials indicated only the presence of anatase TiO_2 and the zeolite, with no significant shift of the diffraction patterns compared to the starting materials. As with dip-coated zeolites, the presence of zeolites did not affect the crystallisation of the titania.

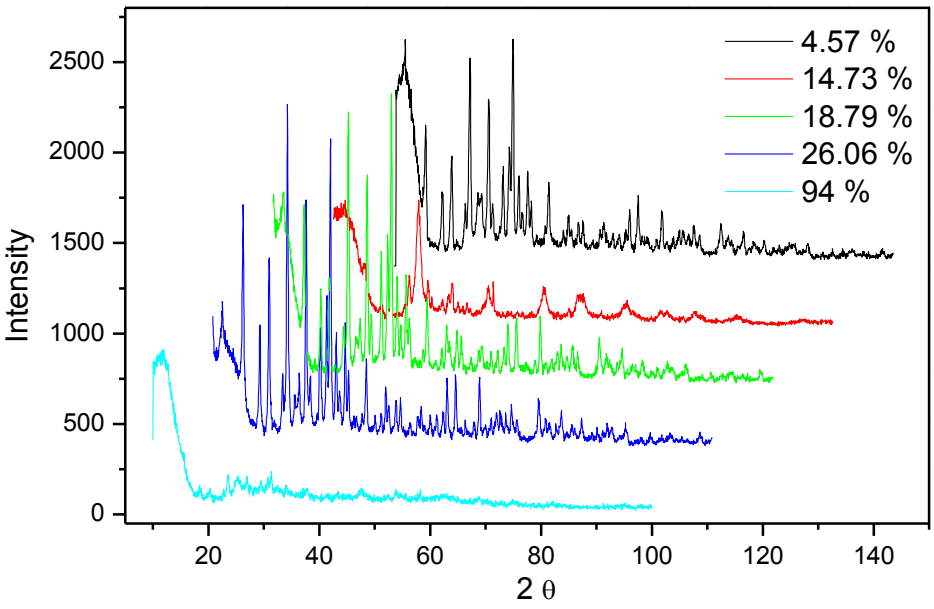

Figure 5.8. X-ray diffraction patterns of zeolites electrospun with TTiP.

The photocatalytic activity was examined in the same manner as for the dip coated zeolites. It was found that the photoactivity increased linearly with TiO_2 loading (Figure 5.9). At 5.57 at. % loading the activity was found to be 0.20, less than half that of pristine TiO_2, which was attributed to the much lower TiO_2 content. At 94.0 at. %

TiO_2, the activity had increased to 0.62, which is higher than that of pristine TiO_2 nanofibres, despite containing 6 % less TiO_2. The increased activity is thought to come from increased surface area, a higher adsorption of VOCs and the zeolite delocalising excited electrons. The high TiO_2 to zeolite ratio would render these effects minimal and potentially block the pores of zeolite, reducing the surface area and adsorption, hence the lower activity than found for dip-coated zeolites.

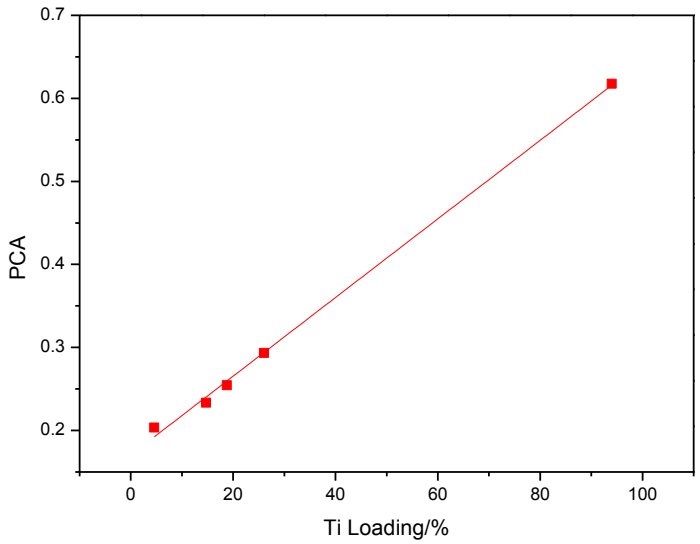

Figure 5.9. Photocatalytic activity of electrospun zeolite:titania composites as a function of titanium loading. The activity increases linearly with TiO_2 as titania is the photoactive medium. The activity is higher than for pristine TiO_2 nanofibres which is thought to be due to the predicted increase in surface area, the better adsorbtion properties of zeolites retarding the flow of the VOC and the delocalisation of the excited electrons.

5.3 Glass Fibres

Glass fibres are a suitable choice of support for TiO_2 largely due to their very low cost, thermal stability and chemical inertness. As well as offering a mechanically strong structure, they can be used to reduce the pressure drop in continuous flow reactors. Furthermore, there is the possibility that glass fibres will act as optical channels, or wave guides, allowing the more efficient flow of UV light. [270,303,304] Wave guides prevent the degradation of the wave over distance (normally $1/r^2$) by making use of total internal reflection. For a material to act as a wave guide it must have a width of the same magnitude as the wave, this means that certain materials are only applicable to certain waves. A more efficient flow of UV light may lead to higher activation of the TiO_2 catalyst and therefore, higher levels of photocatalytic activity.

Glass fibres have previously been used to immobilise transition elements, for example palladium has been coated onto glass fibre cloths to reduce the pressure drop in reactors when using densely packed catalysts,[303] and platinum has been immobilised on glass fibres for the thermal oxidation of propane.[304] Glass fibres have also been used to support TiO_2 for the liquid phase removal of benzamide by photooxidation.[305,306] The glass fibres were dip-coated and calcined where they found an increase in mechanical strength and decrease in pressure drop, however, the fibres were less efficient than pristine P25 powder. Chung *et al.* also found that while TiO_2 coated glass fibres were less efficient in the photooxidation of organic compounds than anatase powder, the catalyst was more durable.[307] Brezova and Blazkov *et al.* also found that glass fibres can be successfully coated in TiO_2 by dip-coating and, moreover, that dopants can be successfully incorporated by this method.[308,309] They found that in the liquid phase photooxidation of phenol, Pt^0 doping was highly efficient. Furthermore, TiO_2 coated

glass fibres have also been successfully used in the gas phase for removal of pollutants from indoor air.[310] Glass fibres containing oxides have successfully been prepared by the sol-gel method, because of their potential improvements over pure silica glass, for example ZrO_2 to increase the resistance to alkaline solutions.[311] TiO_2:SiO_2 composite fibres can also be readily prepared by the co-condensation of silicon and titanium alkoxides by the sol-gel method. The addition of SiO_2, even in relative low concentrations (< 20 %), has been shown to increase the mechanical strength of the fibres, rendering them less brittle.[312] These polytitanosiloxanes have higher TiO_2 crystallisation temperatures, where crystallisation into the anatase phase does not occur until *ca.* 800 °C, dependant on the silica to titania ratio.[313,314] Core-shell silica-titania fibres have been prepared by co-axial electrospinning,[315] and P25 has been immobilised inside silica fibres.[314] The immobilised P25 showed some photooxidation of acetaldehyde at half the efficacy of the corresponding amount of pure P25, however, powder samples are often of higher activity than fibres due to the increased surface area.

5.2.1 Photoactivity of TiO_2 Coated Glass Fibres

To prepare TiO_2 coated glass fibres, glass wool, 1 g, was soaked in solutions of PMMA in DMF, containing TTiP, 0.01–1.00 g. The polymer solution preparation gave rise to good adhesion of the TTiP to the substrate. The morphology of these materials was analysed by SEM but, due to charging effects, the samples had to be gold coated first (Figure 5.10).

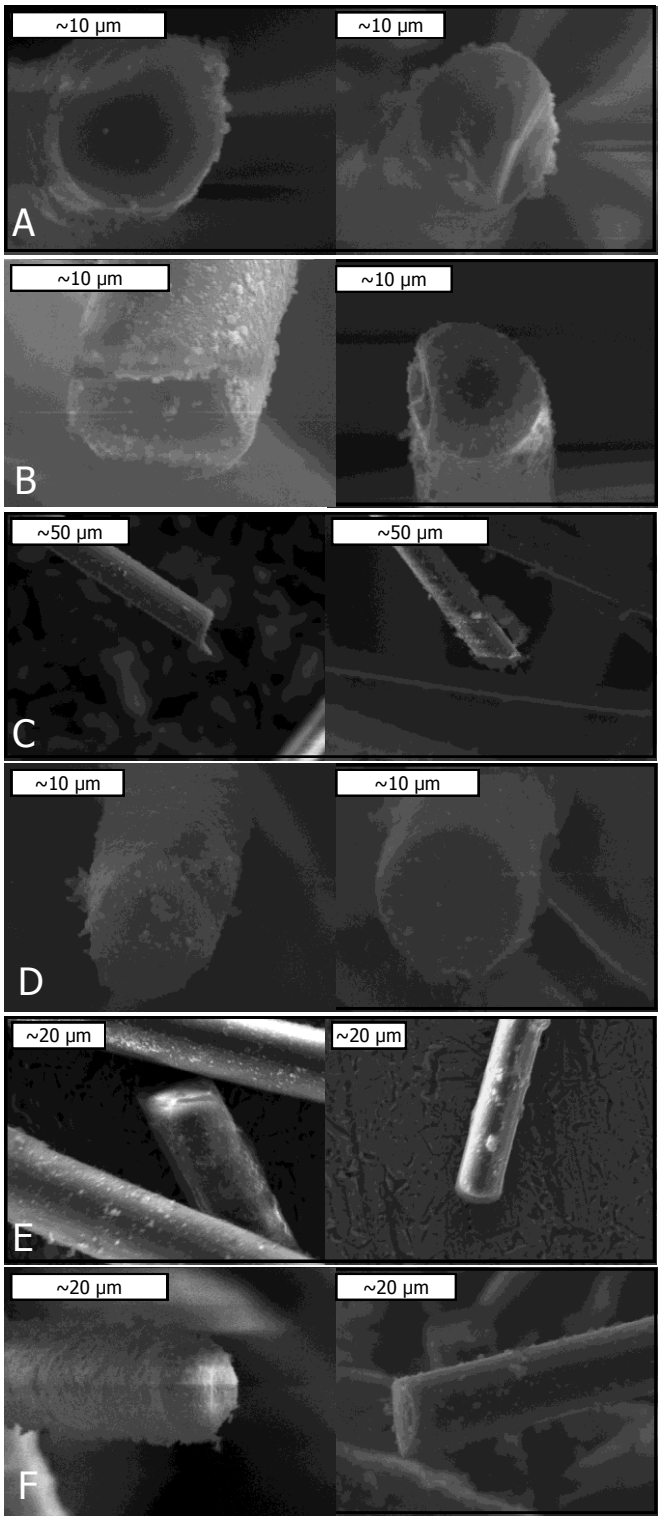

Figure 5.10. SEM images of TiO_2 coated glass fibres as a function of polymer solution loading (g/TTiP). A. 0.01, B. 0.10, C. 0.30, D. 0.50, E. 0.80 and F. 1.00. The coating diameter increases as the concentration of TTiP in the precursor solution increased.

An increase in coating diameter as concentration of TTiP solution increased was observed by SEM, as shown in Table 5.1. At 0.01 g TTiP, the coating is not homogenous as there is not enough TiO_2 to completely coat the glass fibres, where the average size of the aggregates was ~100 nm. Increasing the loading to 0.10 g TTiP proved sufficient to uniformly coat the glass fibres. As the loading increased, the structure no longer had the mechanical strength to support the full load. It is predicted that there is a maximum concentration above which no further increase in coating diameter will be observed as the load will be at its maximum. The surface area of glass fibres, 0.5 m^2/g, is around 100 times lower than the predicted surface area of TiO_2 nanofibres, 15.2 m^2/g.[179]

Table 5.1. Coating diameters of TiO_2 on glass fibres. Charging effects made analysis of the 0.3 and 0.8 g samples difficult. The coating diameter can be seen to increase as the loading of TTiP in the precursor solution increased.

TTiP /g	Estimated diameter of coating
0.01	100 nm non-homogeneous
0.10	100 nm homogeneous
0.30	Images not clear enough
0.50	200 nm
0.80	Images not clear enough
1.00	300 nm

The photoactivity of the coated glass catalysts was tested by way of measuring phenol degradation under UV illumination. The photoactivity was found to increase with concentration of the coating polymer solution (Figure 5.11). The activity was not observed to be linear as the method coating of the fibres was not completely optimised.

The coated glass fibres show exceptional photoactivity, from 0.09 at 0.01 g TTiP increasing to 1.63 at 1.00 g TTiP. The 1.00 g loading shows higher activity than for P25 powder despite the much higher surface area of P25. The increased activity is postulated to be due to the glass fibres are acting as wave guides for UV light, which would result in more efficient catalyst activation. The inference of wave guide effects can be tested by synthesising a glass fibre that is not optically active and comparing their photoactivity to dip-coated glass fibres.

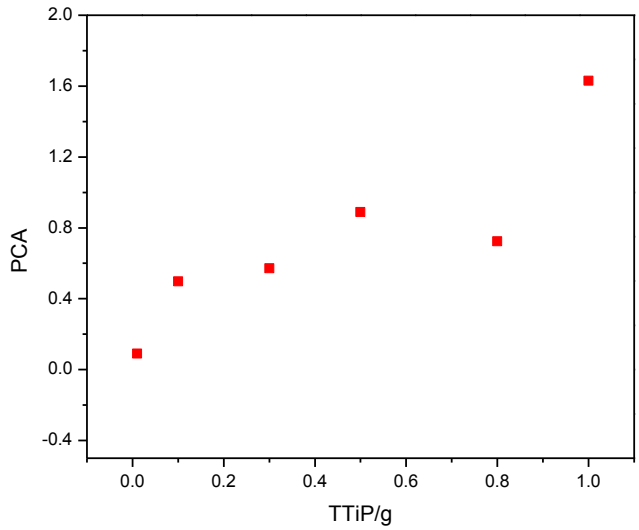

Figure 5.11. Photocatalytic activity as a function of TTiP concentration for dip-coated glass fibres. There is a general trend of activity increasing with TiO_2 loading, as it is the active species, however, the activity far surpasses that of even P25 powder. The increase in activity is postulated to be due to the glass fibres behaving as waveguides for the UV light.

5.4 Particulated Fibres

Using the high surface area of P25 powder and the comparatively high mechanical strength of TiO_2 nanofibres, it was the aim to create a novel material which combined the properties of both morphologies. This will allow for the creation of a photoactive support for TiO_2.

5.4.1 Morphology and Photoactivity of Particulated Fibres

To prepare these composite materials, 0.8 g of TTiP and P25 was loaded into a PMMA solution, where the P25 loading was between 0.05–0.70 g, and the remainder compiled of TTiP. The solution was stirred for two hours to ensure good mixing and then electrospun. The resulting materials were steam treated and then calcined revealing particulated fibres. The prepared materials were analysed by SEM to assess their morphology (Figure 5.12). It was observed that as the concentration of P25 in the polymer solution increased, the electrospun fibres became more particulated. It was found that P25 does not retain the fibrous morphology of the polymer scaffold; as the PMMA was removed the fibres crumbled to powder. By the addition of TTiP, to act as a linking agent, the fibrous morphology could be preserved.

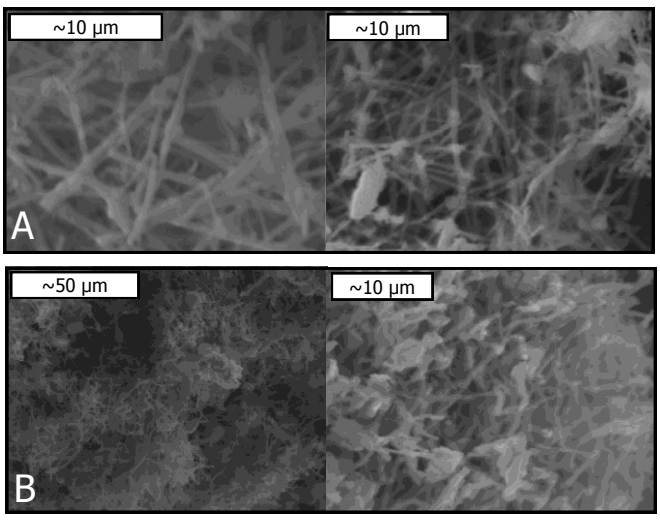

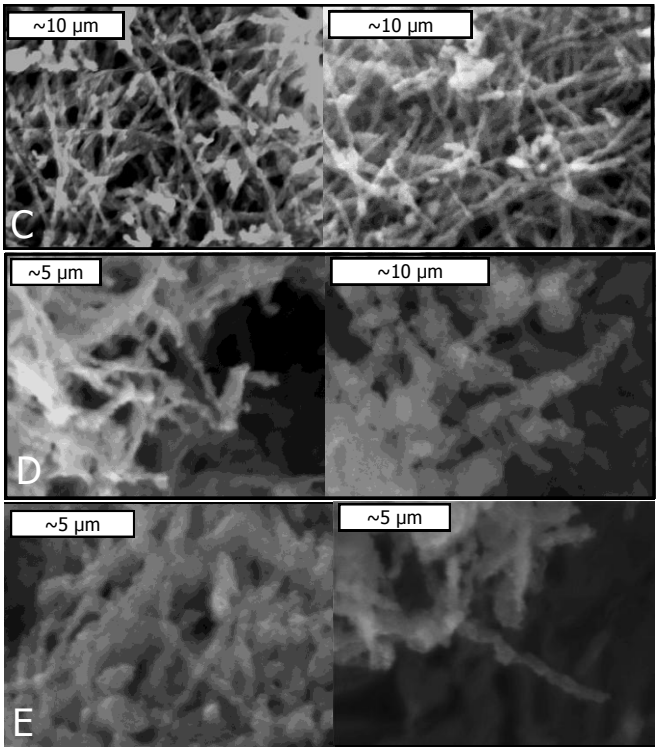

Figure 5.12. SEM images of fragmented fibres as a function of P25 loading (g). A. 0.06, B. 0.09, C. 0.40, D. 0.66 and E. 0.70 g. The level of particulation can be seen increasing as the P25 content increases, as P25 will not hold the fibre scaffold of its own accord.

The fibre diameter was not observed to change significantly upon increase of P25 loading, increasing from ~500 nm at 0.06 g P25 to ~800 nm at 0.70 g P25. We conclude that the ratio of TTiP to P25 has little effect on fibre diameter, and the electrospinning process is the biggest factor in determining their size.

The photoactivity of the particulated fibres was tested by measuring the decomposition of phenol under UV activation. It was found that as the P25 loading increased, the activity increased, which was attributed to the predicted increase in surface area (Figure 5.13). The maximum activity was observed for 0.70 g P25 loading (1.15), marginally higher than that of P25 (1.13). Despite the predicted higher surface area of pure P25, the higher than predicted activity of the particulated fibres is attributed

to increased light penetration due to the less dense packing of TiO_2 in the fibres compared to the powder.

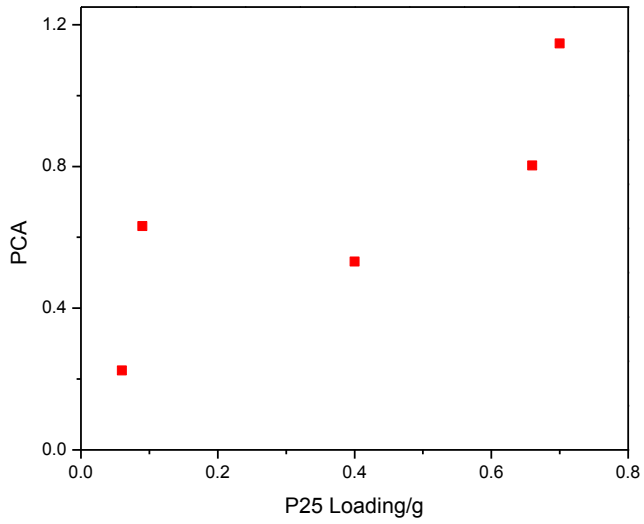

Figure 5.13. PCA of catalysts as a function of P25 loading. The activity increases as the P25 content increases. The activity increases to around the same level as pristine P25 powder, despite the morphology being partially fibrous. This has been attributed to the better contact with UV light of fibres as they are less densely packed than fibres.

As P25 is composed of 25 % rutile and 75 % anatase while the native TiO_2 nanofibres are pure anatase, the diffraction patterns of rutile TiO_2 can be used to reap more information on the composition of particulated fibres. Rutile content was observed to increase as P25 loading increased (Figure 5.14). The 0.09 g loaded sample shows higher than predicted rutile content and also higher than predicted photocatalytic activity, therefore it was concluded that for the 0.09 g loaded sample the P25 content was higher than the loading amount. P25 is not soluble in DMF, and the suspension created is not homogeneous leading to inconsistent P25 content in the particulated

fibres. No change in diffraction peak angles was observed of the catalysts, indicating no change in the TiO_2 lattice.

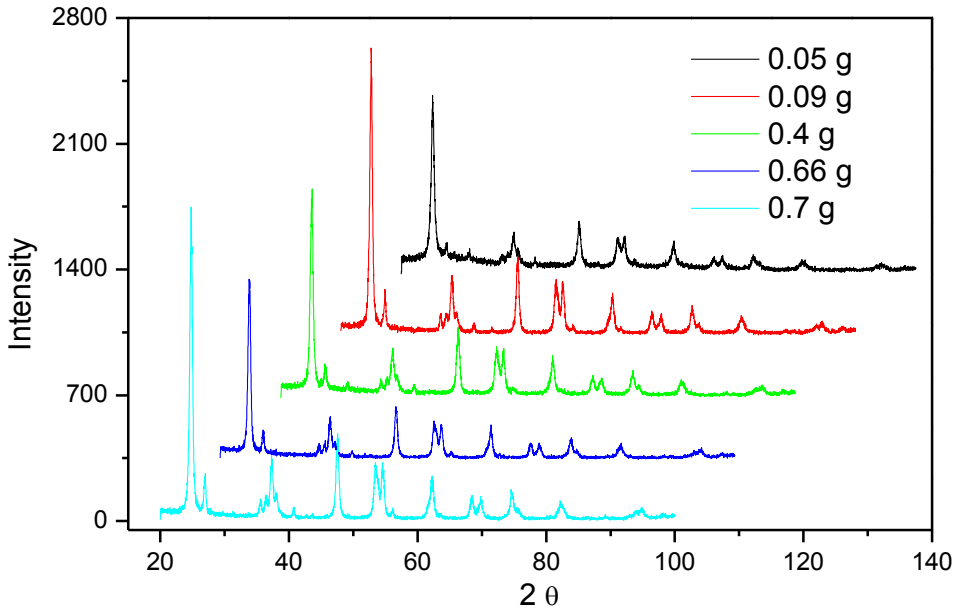

Figure 5.14. X-ray diffraction patterns of particulated fibres. The titania nanofibres are wholly anatase whilst P25 is a 75 % 25 % anatase to rutile mix. Therefore, rutile content can be used to document the composition of the fibres.

To further analyse the particulated fibres, crystallite sizes were calculated from the X-ray diffraction data using the Scherrer equation (Table 5.2). Crystallite sizes were observed to increase as the P25 content increased, which could offer an alternative explanation for the increase in photoactivity as small crystallite sizes are thought to encourage recombination. Ying *et al.* observed a decrease in photoactivity as crystallite

size decreased towards 10 nm, which they attributed to a higher rate of recombination, caused by the higher surface area.[186]

Table 5.2. Crystallite sizes of P25 loaded nanofibres. 0.8 g sample is pure P25 powder.

P25 Loading/g	0	0.05	0.09	0.4	0.66	0.7	0.8
Crystallite Size/nm	12.9	12.9	14.2	14.2	14.2	15.8	16.5

5.5 Conclusions

Four supports for TiO_2, dip-coated zeolites, TiO_2:zeolite fibres, dip-coated glass fibres and P25 loaded TiO_2 fibres have been successfully prepared. Figure 5.15 shows the best performing of each support, along-side the non-photoactive starting materials, for comparison. It can be seen that the coated glass fibres show the highest photocatalytic activity of all the samples.

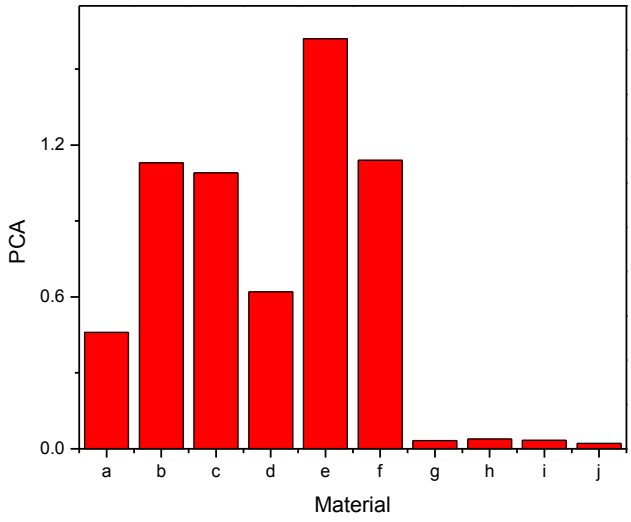

Figure 5.15. Photoactivities the best performing of; a. TiO_2 nanofibres, b. P25, c. dip-coated zeolite, d. electro spun zeolite, e. glass fibres, f. particulated fibres, g. silica gel, h. NaY, i. MCM41-S, and j. MCM41-AS.

It has been shown that using a simple dip-coating methodology, MCM-41 and NaY zeolites can be successfully coated with TiO_2, creating a zeolite:titania powder. While BET would be required to confirm this, it is believed that TiO_2 has, at least partially, entered into the zeolites pores. There is an associated increase in the photooxidation of phenol when using dip-coated zeolites compared to pristine P25. The justification of the increase in activity is that zeolites have a large surface area, a higher adsorption than TiO_2 and finally, can delocalise an electron, reducing the rate of electron–hole pair recombination.

Furthermore the minimum amount of TTiP required to create zeolite:titania nanofibres (> 5 wt. %), has been successfully determined, where the created fibres are of lower photoactivity than dip-coated zeolites but have higher mechanical strength. Per gram of TiO_2 the best performing dip coated catalyst is ~10 times more effective

than the best performing electrospun zeolite:titania catalyst. Despite this, zeolite:titania nanofibres show increased photooxidation of phenol over pristine TiO_2 nanofibres, attributed to the same three factors as for dip-coated zeolites. The novel combination of zeolites and titania is effective for photooxidation of organic pollutants and offers benefits over pristine TiO_2 nanofibres and P25 powder, however, more quantitative studies are required to qualify the increased activity.

TiO_2 has been successfully coated onto glass fibres using a TTiP polymer solution with control of the coating layers by altering the concentration of the TTiP in the polymer solution. The TiO_2 coated glass fibres showed high activity towards the photooxidation of phenol. A TTiP loading as small as 1 wt. % of the glass fibre is sufficient to surpass the activity of native TiO_2 fibres and a loading of 80 wt. % surpassed the activity of P25 powder. While the reason for this increase is not yet proven, it is possibly due to the glass fibres acting as a wave guide for the UV light. Creating a glass material of the same dimensions as the glass fibres used, but with an Urbach edge (absorption tail) short enough that the material will not act as a wave guide for UV light would provide more evidence whether any increased activity comes from a wave guide effect. The increased mechanical strength of the material, the low cost of production and the high photocatalytic activity make TiO_2 coated glass fibres a suitable catalyst for photooxidation of volatile organic compounds.

Particulated fibres offer the high photoactivity of P25 and the mechanical strength of TiO_2 nanofibres prepared from TTiP. The addition of P25 to the polymer solution creates a material where the particulate is held in fibre form, however, the insolubility of P25 in DMF leads to inhomogeneous mixing with TTiP, resulting in unpredictable loadings. The photoactivity increased as the P25 loading increased, which

is attributed to the increase in surface area and crystallite size, however, BET analysis is required for further proof. The photoactivity of the highest performance sample is close to that of P25 powder, but with the addition of higher mechanical strength and lower pressure drop in continuous flow reactors.

6. Conclusions and Further Work

The aim of this project was to create a semiconductor catalyst based on TiO_2 nanomaterials, for the removal of volatile organic compounds from biogas. At present P25, a powdered mix of anatase and rutile TiO_2, is seen as the benchmark for photocatalysis but is rarely used in industry due to its lack of mechanical strength, pressure drop and separation problems. In this project, nanofibres were the chosen morphology due to their compromise between high surface area and relatively high mechanical strength. Furthermore, their preparation by electrospinning polymer solutions is simple, easy to control and allows for uniform doping of other metal oxides. It has been shown that TiO_2 nanofibres can be created easily by electrospinning polymer solutions, and the morphology carefully controlled. Furthermore, an analysis of the calcination procedure was performed where it was found that the PMMA is removed in three stages, head to head scissions, chain end scissions and random scissions. An optimum calcining temperature of 550 °C was also discerned and, with X-ray diffraction, it was found that photoactivity was largely due to the crystal phase of TiO_2: this was found to be majority anatase with a low percentage of rutile. At temperatures above 550 °C the rutile phase begins to crystallise in significant concentrations, reducing the photoactivity.

The prepared fibres show photooxidation of phenol where no side products were found during the decomposition, by GC-MS. The photoactivity of titania nanofibres (0.47) was found to be around half that of P25 powder (1.13) which is predicted to be due to the lower surface area of the fibres.

It has also been shown that TiO_2 nanofibres can be activated by thermal energy, as determined by Fermi-Dirac statistics. This offers an alternative for when UV illumination is not a suitable method of catalyst activation. At 400 °C the activity is slightly increased over UV activation (0.55). When the two methods are combined (0.87) there is an almost 50 % increase in activity than using UV activation on its own, attributed to photon enhanced thermionic excitations.

TiO_2 nanofibres were loaded with six metal oxides, CoO, Fe_2O_3, NiO, Cr_2O_3, VO_2 and CuO, to assess any increased activity, where it was found that five out of the six surpassed the activity of pristine TiO_2 nanofibres at 1.00 mol % loading. These photoactivities are presented in Table 6.1. Iron oxide showed no increase in activity however, it may be that the iron loaded TiO_2 is visible light active, which was not investigated. The increase in activity upon doping is likely from the metal centres acting as shallow electron traps, retarding the electron–hole pair recombination rate. However, at higher loadings (> 1.00 mol %) these centres become close enough together to act as recombination centres, reducing the efficiency. Analysis by XPS and diffuse reflectance UV-Vis would be required to further elucidate the electronic structures of the doped nanofibres.

Table 6.1. Photoactivities of 1.00 mol % transition metal doped TiO_2 nanofibres.

Dopant	Iron	Cobalt	Chromium	Nickel	Vanadium	Copper
PCA (1.00 mol % loading)	0.46	1.94	0.96	0.92	0.48	0.85

The activity of the cobalt loaded nanofibres was much higher than the other dopants and prompted an investigation of the photoactivity of the mono-metallic cobalt

materials CoO and $Co_3(PO_4)_2$. Table 6.2 shows the photoactivity of these materials. While these were found to be non-negligibly photoactive, their activities were less than that of pristine TiO_2 nanofibres. Further investigation into these materials is required, but they offer an alternative to TiO_2 semiconductors.

Table 6.2. Photocatalytic activities of mono metallic cobalt catalysts.

Material	Photocatalytic Activity
CoO fibres	0.08
CoO from Na_3PO_4	0.30
$Co_3(PO_4)_2$ from H_3PO_4	0.13
Electrospun commercial $Co_3(PO_4)_2$	0.40
$Co_3(PO_4)_2$ fibres	Not yet analysed

Supported catalysts were investigated to enhance the activity, mechanical strength and industrial applicability of TiO_2 nanomaterials.

Dip coated zeolites showed a maximum photoactivity of 1.10, almost equal to that of P25, despite the lower TiO_2 content. Zeolite:TiO_2 nanofibres can be prepared when a critical concentration of TTiP is supplied, a minimum of ~5 at. %. At their maximum activity these composite fibres surpassed the activity of pristine TiO_2 nanofibres, reaching 0.62, despite 6 % less TiO_2 content. In both of these cases the increase in activity is believed to arise from a combination of increased surface area, increased adsorption of phenol and the electron delocalisation ability of the zeolites. To further clarify these materials, BET measurements will be required.

Glass wool was dipped in TTiP to prepare TiO_2 coated glass fibres. The coating diameter increased with TTiP loading, but not linearly. The activity increased linearly with TiO_2 loading, where the best performance sample surpassed the activity of P25 by 150 % per gram, reaching 1.63 for 1.00 g of material. The increase in activity is thought to be because of the glass acting as a wave guide for the UV light, increasing the activation efficiency. Preparing glass fibres of similar dimensions that cannot behave as a wave guide and performing photocatalytic studies is required to further analyse these materials.

Finally, to combine the high activity of P25 with the relative mechanical strength of TiO_2 nanofibres, P25 was placed into a TTiP containing polymer solution and electrospun. This produced particulated fibres, where the fibres became less smooth and more brittle as the P25 loading increased. The photooxidation of phenol increased with P25 loading where the best performing sample marginally surpassed the activity of P25, to 1.15. This was attributed to the combination of the high surface area of P25 with the improved light penetration of nanofibres.

Figure 6.1 shows the comparative activities of the best performing catalysts from each category along-side P25 powder and pristine TiO_2 nanofibre benchmarks.

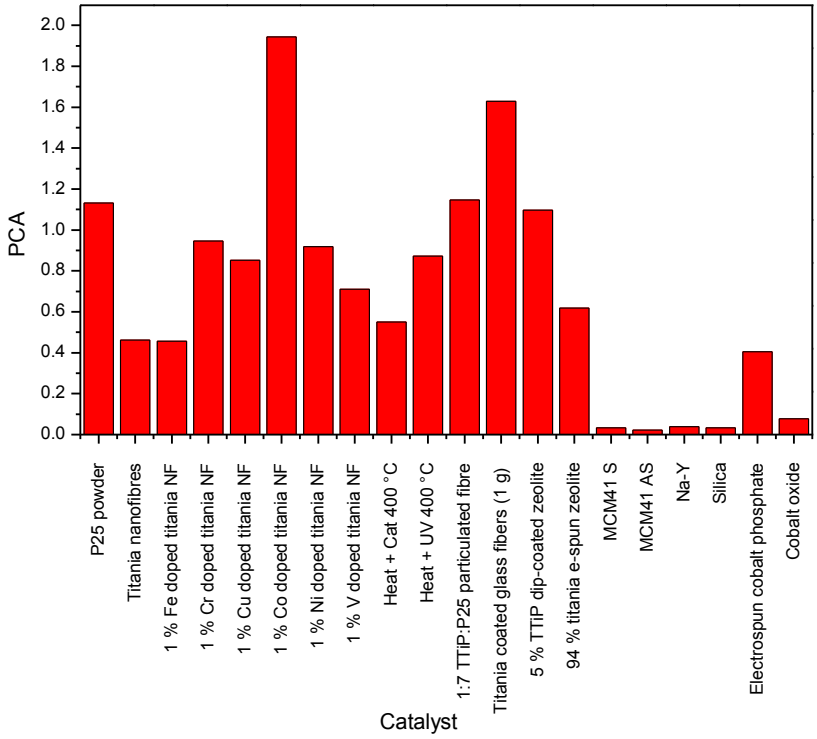

Figure 6.1. Collated activities of the best performance catalyst of each series of catalyst.

Thus far all catalytic studies have been performed in laboratory conditions using phenol in O_2 as a representation of a polluted gas stream. Before these catalysts can be implemented in real waste gas treatment facilities there will need to be analysis under real world conditions. Specifically this means that the gas stream must be a sample from a real polluted gas stream which is likely to contain, amongst other things, aromatics, hydrocarbons, halogenated organics and silicon based compounds. A worry for industrial reactors is that siloxanes found in waste gas will coat the catalyst, blocking its active sites, dramatically reducing the efficiency of the catalyst. Investigating a real

polluted gas stream is difficult to accomplish in laboratory conditions because of the range of compounds present in the mixture, requiring the need for an alternative method of analysis. Investigations proposed for the future are to use a polluted gas cylinder as the gas feed and bypass the VOC reservoir. Instead of collecting into an aqueous collector and sampling for UV-Vis, gas tight syringes can be used to inject samples into a GC-MS. This allows for quantitative analysis of a variety of compounds, where lights off and lights on concentrations can be compared.

Even though development is required before these catalysts can be used in industrial reactors, extensive progress has been made in producing a range of catalysts that will remove selected volatile organic compounds from biogas.

7. Experimental Techniques

7.1 Materials and Equipment

O_2 was supplied by BOC Gases UK. Phenol, titanium tetraisopropoxide (TTiP) (97 %), poly(methyl methacrylate) (PMMA) (996,000 average molecular weight, analytical standard), methyl methacrylate (MMA) (98.5 %), cobalt acetyl acetonate ($Co(AcAc)_2$) (97 %), iron chloride and acetyl acetone (99 %) were supplied by Sigma–Aldrich. Nickel chloride hexahydrate (97 %) was supplied by BDH. Vanadium oxy-sulfate (99.5 %) was supplied by Riedel de Haen. Chromium chloride anhydrous (99 %) was supplied by Venton. Sodium hydroxide (analytical grade) was supplied by Fisher Scientific. Dimethyl formamide (DMF) (99 %) was supplied by Acros Organics.

SEM imaging was performed on a Jeoul M820 SEM with EDX attachment. Light intensity measurements were made with a Melles Griot broadband power/energy meter 13PEM001. ICP-MS was performed on a with a laser ablation attachment. GC-MS were run on a Perkin Elmer Tubomass MS with a Perkin Elmer Autosystem XL GC. FT-IR were measured on a Perkin Elmer Spectrum 1 spectrometer using both ATR mode and NaCl plates. DSCs were measured on a Perkin Elmer DSC 4000 with a blank pot as a standard. UV-Vis absorption was measured on a Biowave and a Thermospectronic UV 300. X-ray diffraction was measured on a Siemens Kristalloflex diffractometer using powder plates. Samples were calcined in a Carbolite OAF 1000 furnace. Solution viscosities were measured at room temperature using an Ostwald viscometer (PSL tube viscometer, BS/U type) with a 4 mm capillary

7.2 Electrospinning

Unless specified otherwise, the polymer solution was prepared by dissolving 7 wt. % PMMA in DMF and left to stir for four hours. 30 minutes before electrospinning, the desired precursor(s) was added and stirred to form a homogenous solution. Prior to electrospinning, 0.15 wt. % acetyl acetone was added to the polymer solution and shaken for one minute. This was to prevent aggregation of the additional precursors in the electrospinning process which could cause blockages. The electrospinning apparatus was set-up as shown in Figure 7.1 and, unless specified otherwise, the nozzle-tip to collector distance was set at 20 cm. The polymer solution was added to a 20 ml BD plastic syringe and placed in a syringe pump (Zivac P2000) set at 2 ml hr^{-1} flow rate. Unless specified otherwise, a 25 gauge needle was placed on the end of the syringe and a high voltage wire, set at 15 kV, was attached to the end of the needle. The fibres were collected on a square sheet of aluminium foil on a ground, rotating collector. All experiments were carried out at room temperature, stabilised at 22 ˚C with a relative humidity of 35 %. Once collected, 1 ml of deionised water was spilled on the fibres and the foil was placed in a boat inside a water bath and heated at 80 °C for one hour. The steam treatment was to convert any remaining precursor to the hydroxide form. The purpose of this was to minimise any loss of precursor during the calcining process. Post steam treatment, the fibres were placed in a furnace and heated to 550 °C at a 1 °C a minute ramping rate. All fibres produced were analysed by SEM, with an operating voltage of 10-30 kV. In order to determine fibre diameter, fibres were measured in 10 distinct regions and averaged. The error bars in the fibre diameter plots correspond to the diameter distribution.

Figure 7.1. Electrospinning apparatus. A high voltage bias is applied to a needle attached to a syringe. A syringe pump is used to maintain a constant flow of electrospinning solution. The electrospun fibres are collected on aluminium foil on a rotating drum (off screen).

7.3 Photocatalysis

The photocatalytic experimental set up (Figure 7.2) was comprised of a quartz tube of 5 cm length and 7 mm inner diameter. This tube was filled with 0.1 g of catalyst packed into the centre with glass wool. The tube was connected at one end to an O_2 cylinder, at 2 ft^3 hr^{-1} flow rate, *via* a concentrated aqueous phenol reservoir, and at the other end to a 250 ml round bottom flask collector containing 12 ml 1 M NaOH. The tube was placed inside a Nail-Art gel-curing UV-lamp apparatus, containing 4x9 W lamps, with the reactor tube secured at a 1 cm distance from the UV lamps, unless

stated otherwise. UV illumination was alternated on and off at regular intervals to simulate catalyst activation and non-activation. 3 ml aliquots were taken regularly and analysed for sodium phenolate concentration using a portable BioWave UV spectrometer at 290 nm wavelength. Concentrations were determined *via* the Beer-Lambert equation using 2028.93 as the molar extinction coefficient, calculated *via* standard solutions of sodium phenolate. When required, a 3 cm by 3 cm metal block, powered by a 200 V supply, was placed underneath the quartz tube so that the two were touching. Measurements of temperature were taken from the block using an electronic thermometer. All reactor runs were performed with at least three on-off cycles of either UV illumination or heating.

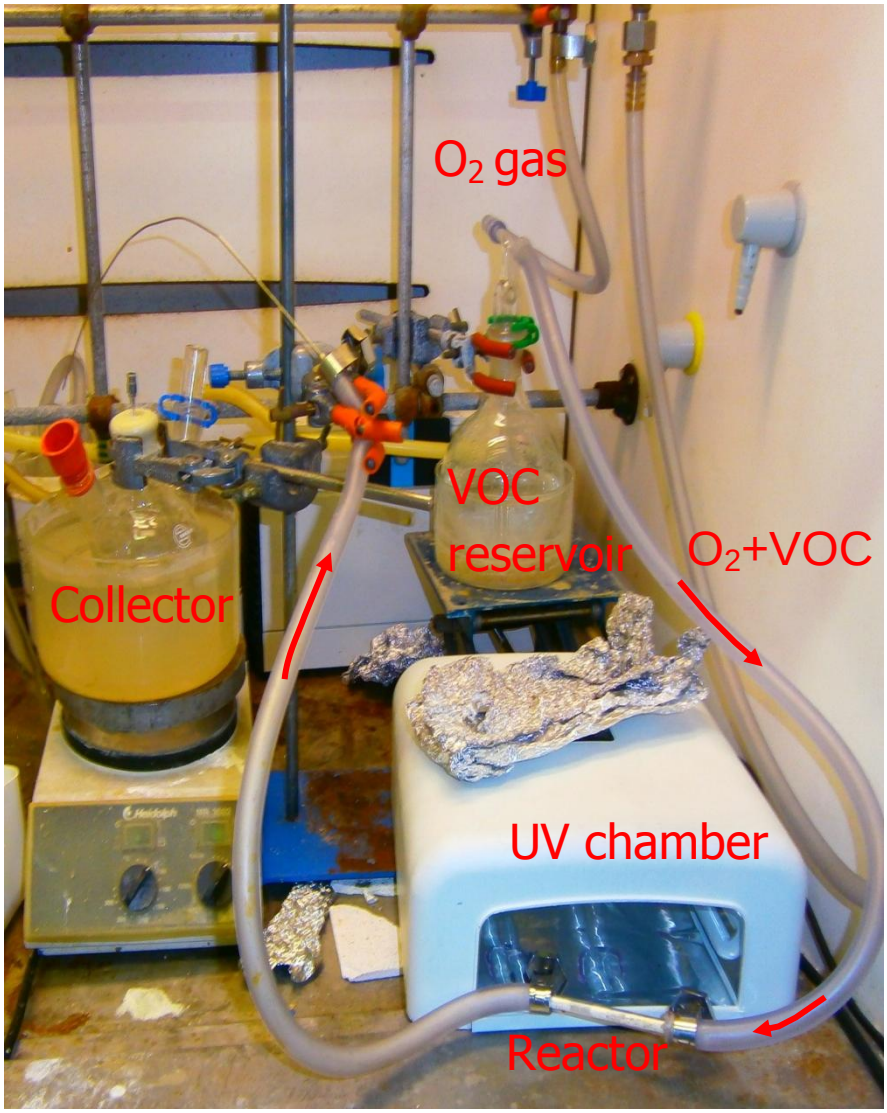

Figure 7.2. Photocatalytic reactor. The reservoir contains phenol dissolved in deionised water. This is carried through the reactor towards a collector containing a solution of NaOH. The NaOH will trap phenol as the less volatile NaOPh.

7.4 Determination of Photocatalytic Activity

During the catalytic runs, the build up of sodium phenolate in the collector was tracked. During the lights off section, the build up of sodium phenolate is directly proportional to the flow rate,

$$k_{[NaPh]} = k_{[PhOH]} \tag{7.1}$$

During the lights on section the rate of build up is determined by the efficiency of the catalyst,

$$k_{[NaPh]} = k_{[PhOH]} - k_{TiO_2 activity} \tag{7.2}$$

A high efficiency catalyst will result in a slower rise in concentration. On a plot of [NaPh] as a function of time, the lights on section will yield a shallower slope than the lights off section.

Each slope is *dC/dT*, the gradient of which is a rate in mol $dm^{-3}/m^{-1}/0.1\ g^{-1}$. This was converted to $mol/m^{-1}/0.1\ g^{-1}$. The sum of the lights on gradients is subtracted from the sum of the lights off gradients. While 0.1 g of the catalyst is loaded into the reactor every use, the exact laying of the catalyst affects the pressure drop, filling the catalyst in exactly the same manner every time was impossible, even more so given the fact that most catalysts will have a slightly different structure from each other. Because of this the phenol flow rate was not precisely the same for every activity test. To account for this the gradient difference was divided by the flow rate of phenol, in mol/m^{-1}, to give a comparable activity per 0.1 g.

7.5 Doped TiO_2 Nanofibres

Samples were prepared as described in Section 7.2. Dopants were added to the polymer solution in concentrations of 0.01-50 mol %. The precursors to these dopants were as follows: Chromium – $CrCl_3$, Cobalt – $Co(AcAc)_2$, Copper – $Co(NO_3)$, Iron – $FeCl_2$, Nickel – $NiCl_2.6H_2O$ and Vanadium – $VOSO_4{\cdot}5H_2O$.

7.6 Monometallic Cobalt Nanomaterials

7.6.1 Cobalt Oxide Nanofibres

10 wt. % of Co(AcAc) was added to 7 % PMMA in DMF and stirred for 30 minutes. Immediately prior to electrospinning, 0.15 % acetyl acetone was added and agitated for 30 seconds. The electrospun sample was water treated for one hour in an 80 °C steam bath and then calcined at 550 °C.

7.6.2 Cobalt Phosphate Nanomaterials

Method 1: Sodium Phosphate

10 wt. % of Co(AcAc) and an equal amount of Na_3PO_4 were added to 7 wt. % PMMA in DMF and stirred for 30 minutes. This yielded a purple slurry. The solution was electrospun under conditions described in Section 7.2 and then calcined at 550 °C, without prior steam treatment. This left a black powder which EDX showed to contain high quantities of cobalt but no measureable amount of phosphorous. The sample was determined to be CoO by X-ray diffraction.

Method 2: Phosphoric Acid Soak

10 wt. % Co(AcAc) was added to 7 wt. % PMMA in DMF and left to stir for 30 minutes. This was electrospun without added acetyl acetone, under conditions described in Section 7.2. After electrospinning the sample was placed in a 5 % phosphoric acid solution for three days to convert the Co(AcAc) to $Co_3(PO_4)_2$. After calcining at 550 °C a grey powder remained which was found to be composed of 95 % P to 5 % Co by EDX

elemental analysis. It was determined to be $Co_3(PO_4)_2$ with aluminium oxide and aluminium phosphate impurities, by X-ray diffraction.

Method 3: Electronspinning of Commercially Purchased Cobalt Phosphate

10 wt. % $Co_3(PO_4)_2$ hydrate (Sigma-Aldrich) was added to 7 wt. % PMMA in DMF and was left to stir for 30 minutes. This was electrospun without added acetyl acetone, under conditions described in Section 7.2. After electronspinning, the sample was calcined at 550 °C without steam treatment. A purple powder remained which was found to be a 2:1 ratio of cobalt to phosphorous and was determined by x-ray diffraction to be pure $Co_3(PO_4)_2$.

Method 4: Acetone Soak

10 wt. % Co(AcAc) was added to 7 wt. % PMMA in DMF and left to stir for 30 minutes. This was electrospun without added acetyl acetone, under conditions described in Section 7.2. The sample was placed in 500 ml of 1:1 acetone to deionised water containing 10 g of Na_3PO_4. After three days, the sample was removed and placed in a furnace at 550 °C for 24 hours. The sample was dark blue and was found to be fibres of 1-10 μM in diameter with a composition of 1:3 cobalt to phosphorous, as determined by EDX elemental analysis.

7.7 Zeolites

7.7.1 Dip-coated Zeolites

TTiP was added to DMF in concentrations of 0.1-0.001 M and mixed well. 1 g of MCM41-S and Na-Y zeolites were separately added to the TTiP solutions and left to soak for 24 hours to encourage maximum soaking of TTiP into the zeolite pores. After 24 hours soaking the samples were filtered and the solid phase steam treated above an 80 °C water bath for one hour before being placed in a 550 °C furnace for 12 hours.

7.7.2 Electrospun Zeolites

A 7 wt. % solution of PMMA in DMF was prepared to which 0.8 g of ratios of 8:1-1:8 of zeolite to TTiP were added. The solutions were stirred for 30 minutes prior to electrospinning and, immediately before electrospinning, two drops of acetyl acetone were added. The solutions were electrospun under conditions described in Section 7.2. The materials were steam treated above an 80 °C water bath for one hour before being placed in a 550 °C furnace for twelve hours.

7.8 Dip-coated Glass Fibres

Glass wool was stirred in NaOH(aq) at 40 °C overnight to clean the glass and to increase the hydrophilicity. The glass wool was washed with deionised water and dried in an oven at 200 °C for two hours. 1 g of glass wool was submerged in 10 ml of DMF containing 0.01–1.00 g of TTiP. The samples were stirred for two hours and then steam treated for 30 minutes at 80 °C above a water bath. The materials were then calcined for two hours in a furnace. This was repeated three times. The finished samples were cut

into small pieces and 0.1 g was placed in a tube reactor. Due to the conductivity of glass, the catalysts were gold coated for three minutes with an Edwards S150 Sputter Coater, before being examined by SEM.

7.9 Particulated Fibre Experimental

Ratios of TTiP and P25 were placed in 7 % PMMA in DMF, totalling 0.8 g of titanium materials. The polymer solution was stirred for two hours to ensure good mixing. Acetyl acetone was added immediately prior to electrospinning. The solutions were electrospun under conditions described in Section 7.2, and then steam treated above a water bath at 80 °C for one hour before being calcined at 550 °C for twelve hours.

References

1. Euro Legislation, http://eur-lex.europa.eu/LexUriServ/LexUriServ.do?uri=CELEX:32004L0042:EN:NOT. 2004
2. Government Legislation, http://www.legislation.gov.uk/uksi/2005/2773/made, 2005.
3. Georg Schwedt, *The Essential Guide to Environmental Chemistry*, Wiley, 1st edn., 2002.
4. M. R. Hoffmann, S. T. Martin, W. Choi, and D. W. Bahnemann, *Chem Rev*, 1995, **95**, 69–96.
5. Siemens, http://www.environmental-expert.com/articles/former-manufactured-gas-plant-mgp-chooses-siemens-and-activated-carbon-system-for-voc-removal-202369, 2013
6. PpTek LTD, http://www.pptek.co.uk/index.php, 2013
7. A. Berenjian, N. Chan, and H. J. Malmiri, *Am. J. Biochem. Biotechnol.*, 2012, **8**, 220–229.
8. R. Feynman, http://www.zyvex.com/nanotech/feynman.html 1959.
9. D. McMullan, *Scanning*, 1995, **17**, 175–185.
10. Z. L. Wang, *Adv. Mater.*, 2003, **15**, 1497–1514.
11. T. Ando, *Nanotechnology*, 2012, **23**, 062001.
12. H. Yang, Y. Wang, S. Lai, H. An, Y. Li, and F. Chen, *J. Food Sci.*, 2007, **72**, R65–R75.
13. Nobel Prize in Physics 1986, _http://www.nobelprize.org/nobel_prizes/physics/laureates/1986/, 1986.
14. H. W. Kroto, J. R. Heath, S. C. O'Brien, R. F. Curl, and R. E. Smalley, *Publ. Online 14 Novemb. 1985 Doi101038318162a0*, 1985, **318**, 162–163.
15. S. Iijima, *Publ. Online 07 Novemb. 1991 Doi101038354056a0*, 1991, **354**, 56–58.
16. Euro Legislation, http://eur-lex.europa.eu/LexUriServ/LexUriServ.do?uri=CELEX:32011H0696:EN:NOT, 2011
17. R. A. Zsigmondy, http://www.nobelprize.org/nobel_prizes/chemistry/laureates/1925/zsigmondy-lecture.pdf 1925.
18. H. W. C. Postma, T. Teepen, Z. Yao, M. Grifoni, and C. Dekker, *Science*, 2001, **293**, 76–79.
19. C. Rutherglen and P. Burke, *Nano Lett.*, 2007, **7**, 3296–3299.
20. J. Xiang, W. Lu, Y. Hu, Y. Wu, H. Yan, and C. M. Lieber, *Nature*, 2006, **441**, 489–493.
21. X. Zong, H. Bien, C. Chung, L. Yin, D. Fang, B. Hsiao, B. Chu, and E. Entcheva, *Biomaterials*, 2005, **26**, 5330–5338.
22. B. A. Kairdolf, A. M. Smith, T. H. Stokes, M. D. Wang, A. N. Young, and S. Nie, *Annu. Rev. Anal. Chem.*, 2013, **6**, 143–162.
23. X. Gao, Y. Cui, R. M. Levenson, L. W. K. Chung, and S. Nie, *Nat. Biotechnol.*, 2004, **22**, 969–976.
24. W. E. Moerner and D. P. Fromm, *Rev. Sci. Instrum.*, 2003, **74**, 3597.
25. S. Sharma and M. Madou, *Philos. Trans. R. Soc. Math. Phys. Eng. Sci.*, 2012, **370**, 2448–2473.
26. Z. Dai, L. Xu, G. Duan, T. Li, H. Zhang, Y. Li, Y. Wang, Y. Wang, and W. Cai, *Sci. Reports*, 2013, **3**.

27. S. Rather, N. Mehrajuddin, R. Zacharia, S. Hwang, A. Kim, and K. Nahm, *Int. J. Hydrog. Energy*, 2009, **34**, 961–966.
28. A. Mishra, S. Banerjee, S. K. Mohapatra, O. A. Graeve, and M. Misra, *Nanotechnology*, 2008, **19**, 445607.
29. R. Kler and Q. Chen, *Un-Published. Results*, 2012.
30. X. Cheng, Z. Shi, N. Glass, L. Zhang, J. Zhang, D. Song, Z.-S. Liu, H. Wang, and J. Shen, *J. Power Sources*, 2007, **165**, 739–756.
31. J. Lu, C. J. Brigham, C. S. Gai, and A. J. Sinskey, *Appl. Microbiol. Biotechnol.*, 2012, **96**, 283–297.
32. S. C. Roy, O. K. Varghese, M. Paulose, and C. A. Grimes, *Acs Nano*, 2010, **4**, 1259–1278.
33. C. Wang, M. Shen, H. Huo, H. Ren, and M. Johnson, *Aip Adv.*, 2011, **1**, 042124–042124.
34. O. Carp, *Prog. Solid State Chem.*, 2004, **32**, 33–177.
35. D. M. Mittleman, R. W. Schoenlein, J. J. Shiang, V. L. Colvin, A. P. Alivisatos, and C. V. Shank, *Phys. Rev. B*, 1994, **49**, 14435.
36. A. N. Goldstein, C. M. Echer, and A. P. Alivisatos, *Science*, 1992, **256**, 1425–1427.
37. M. Perez, *Scr. Mater.*, 2005, **52**, 709–712.
38. M. G. Rossmann and E. Arnold, in *International Tables for Crystallography*, ed. U. Shmueli, International Union of Crystallography, Chester, England, 1st edn., 2006, vol. B, pp. 235–263.
39. J. Tao, T. Luttrell, and M. Batzill, *Nat. Chem.*, 2011, **3**, 296–300.
40. A. Rao, M. Schoenenberger, E. Gnecco, T. Glatzel, E. Meyer, D. Brändlin, and L. Scandella, *J. Phys. Conf. Ser.*, 2007, **61**, 971–976.
41. Y.-Y. Kim, K. Ganesan, P. Yang, A. N. Kulak, S. Borukhin, S. Pechook, L. Ribeiro, R. Kröger, S. J. Eichhorn, S. P. Armes, B. Pokroy, and F. C. Meldrum, *Nat Mater*, 2011, **10**, 890–896.
42. K. Thamaphat, P. Limsuwan, and B. Ngotawornchai, *Kasetsart Jnat Sci*, 2008, **42**, 357–361.
43. T. Akita, P. Lu, S. Ichikawa, K. Tanaka, and M. Haruta, *Surf. Interface Anal.*, 2001, **31**, 73–78.
44. H. Tan, J. Verbeeck, A. Abakumov, and G. Van Tendeloo, *Ultramicroscopy*, 2012, **116**, 24–33.
45. Z. L. Wang, J. S. Yin, and Y. D. Jiang, *Micron*, 2000, **31**, 571–580.
46. F. Cosandey, D. Su, M. Sina, N. Pereira, and G. G. Amatucci, *Micron*, 2012, **43**, 22–29.
47. G. A. Sawatzky and J. W. Allen, *Phys. Rev. Lett.*, 1984, **53**, 2339–2342.
48. M. Ghaffari, H. Huang, O. K. Tan, and M. Shannon, *CrystEngComm*, 2012, **14**, 7487–7492.
49. W. Göpel, J. A. Anderson, D. Frankel, M. Jaehnig, K. Phillips, J. A. Schäfer, and G. Rocker, *Surf. Sci.*, 1984, **139**, 333–346.
50. J. Lüning, J. Rockenberger, S. Eisebitt, J. E. Rubensson, A. Karl, A. Kornowski, H. Weller, and W. Eberhardt, *Solid State Commun.*, 1999, **112**, 5–9.
51. C. L. Dong, C. Persson, L. Vayssieres, A. Augustsson, T. Schmitt, M. Mattesini, R. Ahuja, C. L. Chang, and J. H. Guo, *Phys. Rev. B*, 2004, **70**, 195325.
52. M. R. H. M. Haris, S. Kathiresan, and S. Mohan, *Pharma Chem.*, 2010, **2**, 316–323.
50. L. Atkinson, Masters Project Presentation, University of Sussex, 2008.
54. R. López and R. Gómez, *J. Sol-Gel Sci. Technol.*, 2012, **61**, 1–7.
55. M. Anpo, *Pure Appl. Chem.*, 2000, **72**, 1787–1792.

56. J. Hwang, E.-G. Kim, J. Liu, J.-L. Brédas, A. Duggal, and A. Kahn, *J. Phys. Chem. C*, 2007, **111**, 1378–1384.
57. Y. Park, Y. So, S. J. Chung, and J. I. Jin, *J.-Korean Phys. Soc.*, 2000, **37**, 59–63.
58. D. Gall, M. Städele, K. Järrendahl, I. Petrov, P. Desjardins, R. T. Haasch, T. Y. Lee, and J. E. Greene, *Phys. Rev. B*, 2001, **63**, 125119.
56. University of Cambridge, *Fermi Dirac Distrib.*, *http://www.doitpoms.ac.uk/tlplib/semiconductors/fermi.php, 2013_*
57. Food Standards Agency, http://www.food.gov.uk/policy-advice/additivesbranch/enumberlist#.UG2R8U2HLcJ, 2012
61. E. Keidel, *Farben-Ztg.*, 1929, **34**, 1242.
62. A. Fujishima and K. Honda, *Publ. Online 07 July 1972 Doi101038238037a0*, 1972, **238**, 37–38.
63.H. Honda, A. Ishizaki, R. Soma, K. Hashimoto, and A. Fujishima, *J Illum Eng Soc*, 1998, **42**.
64.S. N. Frank and A. J. Bard, *J. Am. Chem. Soc.*, 1977, **99**, 303–304.
65.S. Ye, Q. Tian, X. Song, and S. Luo, *J. Photochem. Photobiol. Chem.*, 2009, **208**, 27–35.
66.W. H. Baur, *Acta Crystallogr.*, 1961, **14**, 214–216.
67.D. T. Cromer and K. Herrington, *J. Am. Chem. Soc.*, 1955, **77**, 4708–4709.
68.S.-D. Mo and W. Y. Ching, *Phys. Rev. B*, 1995, **51**, 13023–13032.
69.R. Thompson, Ed., *Industrial Inorganic Chemicals: Production and Uses*, Royal Society of Chemistry, 1995.
70.T. Mitsuhashi and O. J. Kleppa, *J. Am. Ceram. Soc.*, 1979, **62**, 356–357.
71.H. Zhang and J. F. Banfield, *J. Phys. Chem. B*, 2000, **104**, 3481–3487.
72.K.-N. P. Kumar, K. Keizer, A. J. Burggraaf, T. Okubo, H. Nagamoto, and S. Morooka, *Publ. Online 02 July 1992 Doi101038358048a0*, 1992, **358**, 48–51.
73.X. Li, P.-L. Yue, and C. Kutal, *New J. Chem.*, 2003, **27**, 1264.
74.R. D. Shannon and J. A. Pask, *J. Am. Ceram. Soc.*, 1965, **48**, 391–398.
75.S. Vargas, R. Arroyo, E. Haro, and R. Rodríguez, *J. Mater. Res.*, 1999, **14**, 3932–3937.
76.R. Rodríguez-Talavera, S. Vargas, R. Arroyo-Murillo, R. Montiel-Campos, and E. Haro-Poniatowski, *J. Mater. Res.*, 1997, **12**, 439–443.
77.R. Zheng, Y. Guo, C. Jin, J. Xie, Y. Zhu, and Y. Xie, *J. Mol. Catal. Chem.*, 2010, **319**, 46–51.
78.C. Magne, S. Cassaignon, G. Lancel, and T. Pauporté, *ChemPhysChem*, 2011, **12**, 2461–2467.
79.X. Chen and S. S. Mao, *Chem. Rev.*, 2007, **107**, 2891–2959.
80.K. Tanaka, M. F. V. Capule, and T. Hisanaga, *Chem. Phys. Lett.*, 1991, **187**, 73–76.
81.T. Kawahara, Y. Konishi, H. Tada, N. Tohge, J. Nishii, and S. Ito, *Angew. Chem. Int. Ed.*, 2002, **41**, 2811–2813.
82.D. C. Hurum, A. G. Agrios, K. A. Gray, T. Rajh, and M. C. Thurnauer, *J. Phys. Chem. B*, 2003, **107**, 4545–4549.
83.J.-M. Herrmann, *J. Photochem. Photobiol. Chem.*, 2010, **216**, 85–93.
84.H. Gerischer and A. Heller, *J. Phys. Chem.*, 1991, **95**, 5261–5267.
85.Z. He, L. Xie, J. Tu, S. Song, W. Liu, Z. Liu, J. Fan, Q. Liu, and J. Chen, *J. Phys. Chem. C*, 2010, **114**, 526–532.
86.C. D. Jaeger and A. J. Bard, *J. Phys. Chem.*, 1979, **83**, 3146–3152.
87.Y. Mao, C. Schoeneich, and K. D. Asmus, *J. Phys. Chem.*, 1991, **95**, 10080–10089.
88.F. Akbal and A. Nur Onar, *Environ. Monit. Assess.*, 2003, **83**, 295–302.
89.G. R. Peyton and W. H. Glaze, *Environ. Sci. Technol.*, 1988, **22**, 761–767.

90.M. W. Peterson, J. A. Turner, and A. J. Nozik, *J. Phys. Chem.*, 1991, **95**, 221–225.
91.M. de O. Melo and L. A. Silva, *J. Braz. Chem. Soc.*, 2011, **22**, 1399–1406.
90. James Dyson Awards 2012, http://www.jamesdysonaward.org/Projects/Project.aspx?ID=2480&RegionId=8&Winindex=0, 2012 .
93.J. H. Carey, J. Lawrence, and H. M. Tosine, *Bull. Environ. Contam. Toxicol.*, 1976, **16**, 697–701.
94.A. L. Pruden and D. F. Ollis, *J. Catal.*, 1983, **82**, 404–417.
95.C.-Y. Hsiao, C.-L. Lee, and D. F. Ollis, *J. Catal.*, 1983, **82**, 418–423.
96.Y. Ku and C.-B. Hsieh, *Water Res.*, 1992, **26**, 1451–1456.
97.R. W. Matthews, *Water Res.*, 1986, **20**, 569–578.
98.N. Mera, T. Hirakawa, T. Sano, K. Takeuchi, Y. Seto, and N. Negishi, *J. Hazard. Mater.*, 2010, **177**, 274–280.
99.F. Denny, E. Permana, J. Scott, J. Wang, D. Y. H. Pui, and R. Amal, *Environ. Sci. Technol.*, 2010, **44**, 5558–5563.
100.C. Akly, P. A. Chadik, and D. W. Mazyck, *Appl. Catal. B Environ.*, 2010, **99**, 329–335.
101.D. M. Tobaldi, A. Tucci, A. S. Škapin, and L. Esposito, *J. Eur. Ceram. Soc.*, 2010, **30**, 2481–2490.
102.J. Hernández-Fernández, R. Zanella, A. Aguilar-Elguezabal, R. D. Arizabalo, S. Castillo, and M. Moran-Pineda, *Mater. Sci. Eng. B*, 2010, **174**, 13–17.
103.T. An, L. Sun, G. Li, and S. Wan, *J. Mol. Catal. Chem.*, 2010, **333**, 128–135.
104.S. Suárez, T. L. R. Hewer, R. Portela, M. D. Hernández-Alonso, R. S. Freire, and B. Sánchez, *Appl. Catal. B Environ.*, 2011, **101**, 176–182.
105.M. D. Hernández-Alonso, I. Tejedor-Tejedor, J. M. Coronado, and M. A. Anderson, *Appl. Catal. B Environ.*, 2011, **101**, 283–293.
106.V. M. Menéndez-Flores, D. W. Bahnemann, and T. Ohno, *Appl. Catal. B Environ.*, 2011, **103**, 99–108.
107.D. Gong, C. Grimes, O. K. Varghese, W. Hu, R. S. Singh, Z. Chen, and E. C. Dickey, *J. Mater. Res.*, 2001, **16**, 3331–3334.
108.Zainab T Y Al-Abdullah and Qiao Chen, *Un-Publ. Results*, 2012.
109.Z. T. Y. Al-Abdullah, Y. Shin, R. Kler, C. C. Perry, W. Zhou, and Q. Chen, *Nanotechnology*, 2010, **21**, 505601.
110.R. Hahn, M. Stark, M. S. Killian, and P. Schmuki, *Catal. Sci. Technol.*, 2013.
111.Y. V. Kolen'ko, K. A. Kovnir, A. I. Gavrilov, A. V. Garshev, J. Frantti, O. I. Lebedev, B. R. Churagulov, G. Van Tendeloo, and M. Yoshimura, *J. Phys. Chem. B*, 2006, **110**, 4030–4038.
112.A. Nakahira, T. Kubo, and C. Numako, *Acs Appl. Mater. Interfaces*, 2010, **2**, 2611–2616.
113.X. Jiang, Y.-B. Jiang, and C. J. Brinker, *Chem. Commun. Camb. Engl.*, 2011, **47**, 7524–7526.
114.J.-Y. Ji, P.-H. Shih, C. C. Yang, T. S. Chan, Y.-R. Ma, and S. Y. Wu, *Nanotechnology*, 2010, **21**, 045603.
115.C. S. Cundy and P. A. Cox, *Microporous Mesoporous Mater.*, 2005, **82**, 1–78.
116.A. C. Walker, *J. Am. Ceram. Soc.*, 1953, **36**, 250–256.
117.H. Feng, M.-H. Zhang, and L. E. Yu, *Appl. Catal. Gen.*, 2012, **413-414**, 238–244.
118.T. Putta, M.-C. Lu, and J. Anotai, *J. Environ. Manage.*, 2011, **92**, 2272–2276.
119.V. N. Nguyen, N. K. T. Nguyen, and P. H. Nguyen, *Adv. Nat. Sci. Nanosci. Nanotechnol.*, 2011, **2**, 035014.

120.Z. Wu, F. Dong, W. Zhao, H. Wang, Y. Liu, and B. Guan, *Nanotechnology*, 2009, **20**, 235701.
121.G. Che, B. B. Lakshmi, C. R. Martin, E. R. Fisher, and R. S. Ruoff, *Chem. Mater.*, 1998, **10**, 260–267.
122.P. C. Chang, Z. Fan, D. Wang, W. Y. Tseng, W. A. Chiou, J. Hong, and J. G. Lu, *Chem. Mater.*, 2004, **16**, 5133–5137.
123.T. T. Kang, X. Liu, R. Q. Zhang, W. G. Hu, G. Cong, F. A. Zhao, and Q. Zhu, *Appl. Phys. Lett.*, 2006, **89**, 071113–071113.
124.I. P. Parkin, *Chem. Vap. Depos.*, 2012, **18**, 87–88.
125.C. Sarantopoulos, A. N. Gleizes, and F. Maury, *Thin Solid Films*, 2009, **518**, 1299–1303.
126.S. J. Kim, K. Xu, H. Parala, R. Beranek, M. Bledowski, K. Sliozberg, H.-W. Becker, D. Rogalla, D. Barreca, C. Maccato, C. Sada, W. Schuhmann, R. A. Fischer, and A. Devi, *Chem. Vap. Depos.*, 2013, **19**, 45–52.
127.D. E. Wolfe and J. Singh, *Surf. Coatings Technol.*, 2000, **124**, 142–153.
128.B. A. Movchan, *Surf. Eng.*, 2006, **22**, 35–46.
129.L. González-García, G. Lozano, A. Barranco, H. Míguez, and A. R. González-Elipe, *J. Mater. Chem.*, 2010, **20**, 6408.
130.Ebelmen, *Justus Liebigs Ann. Chem.*, 1846, **57**, 319–355.
129.W. Geffen and E. Berger, Deutsch. Reichspatent No. 736411, 1939.
132.S. Sakka and K. Kamiya, *J. Non-Cryst. Solids*, 1982, **48**, 31–46.
133.E. A. Barringer and H. K. Bowen, *J. Am. Ceram. Soc.*, 1982, **65**, C–199–C–201.
134.R. Roy, *J. Am. Ceram. Soc.*, 1956, **39**, 145–146.
135.Rustum Roy and Della M. Roy, *Am. Miner.*, 1954, 957.
136.R. Roy, *J. Am. Ceram. Soc.*, 1969, **52**, 344–344.
137.E. Traversa, G. Gnappi, A. Montenero, and G. Gusmano, *Sensors Actuators B Chem.*, 1996, **31**, 59–70.
138.K. Terabe, K. Kato, H. Miyazaki, S. Yamaguchi, A. Imai, and Y. Iguchi, *J. Mater. Sci.*, 1994, **29**, 1617–1622.
139.L. Miao, S. Tanemura, S. Toh, K. Kaneko, and M. Tanemura, *J. Cryst. Growth*, 2004, **264**, 246–252.
140.P. S. Archana, R. Jose, T. M. Jin, C. Vijila, M. M. Yusoff, and S. Ramakrishna, *J. Am. Ceram. Soc.*, 2010, **93**, 4096–4102.
141.T. Maiyalagan, B. Viswanathan, and U. V. Varadaraju, *Bull. Mater. Sci.*, 2006, **29**, 705.
142.B. Ding, C. K. Kim, H. Y. Kim, M. K. Seo, and S. J. Park, *Fibers Polym.*, 2004, **5**, 105–109.
143.M. Maeda and T. Yamada, *J. Phys. Conf. Ser.*, 2007, **61**, 755–759.
144.John Zeleny, *Phys. Rev.*, 1917, **10**, 1–7.
145.G. Taylor, *Proc. R. Soc. Math. Phys. Eng. Sci.*, 1969, **313**, 453–470.
146.G. Taylor, *Proc. R. Soc. Lond. Ser. Math. Phys. Sci.*, 1964, **280**, 383–397.
147.P. K. Baumgarten, *J. Colloid Interface Sci.*, 1971, **36**, 71–79.
146.C. Hendrick, in *Archive Set 1*, American Institute of Aeronautics and Astronautics, 1963.
149.J. J. Feng, *Phys. Fluids*, 2002, **14**, 3912–3926.
150.D. H. Reneker, A. L. Yarin, H. Fong, and S. Koombhongse, *J. Appl. Phys.*, 2000, **87**, 4531–4547.
151.V. G. Drozin, *J. Colloid Sci.*, 1955, **10**, 158–164.

152.J. M. Deitzel, J. Kleinmeyer, D. Harris, and N. C. Beck Tan, *Polymer*, 2001, **42**, 261–272.
153.P. Gupta, C. Elkins, T. E. Long, and G. L. Wilkes, *Polymer*, 2005, **46**, 4799–4810.
154.M. G. McKee, G. L. Wilkes, R. H. Colby, and T. E. Long, *Macromolecules*, 2004, **37**, 1760–1767.
155.R. H. Colby, L. J. Fetters, W. G. Funk, and W. W. Graessley, *Macromolecules*, 1991, **24**, 3873–3882.
156.N. G. McCrum, C. P. Buckley, and C. B. Bucknall, *Principles of Polymer Engineering*, OUP Oxford, 2nd edn., 1997.
157.J. E. Mark, Ed., *Physical Properties of Polymers Handbook*, Springer, 2nd ed., 2007.
158.A. Potdevin, G. Chadeyron, D. Boyer, and R. Mahiou, *J. Sol-Gel Sci. Technol.*, 2006, **39**, 275–284.
159.A. Lecomte, A. Dauger, and P. Lenormand, *J. Appl. Crystallogr.*, 2000, **33**, 496–499.
160.J. Macossay, A. Marruffo, R. Rincon, T. Eubanks, and A. Kuang, *Polym. Adv. Technol.*, 2007, **18**, 180–183.
161.K. Kanjanapongkul, S. Wongsasulak, and T. Yoovidhya, *J. Appl. Polym. Sci.*, 2010, 1821–1829.
162.H. Homayoni, S. A. H. Ravandi, and M. Valizadeh, *Carbohydr. Polym.*, 2009, **77**, 656–661.
163.A. K. Kundu, J. Gelman, and D. R. Tyson, *Biotechnol. Bioeng.*, 2011, **108**, 207–215.
164.Weidner,St, G. Kuhn,, J. Friedrich, and H. Schroeder, *Rapid Commun. Mass Spectrom.*, 1996, **10**, 40–46.
165.T. Kashiwagi, T. Hirata, and J. E. Brown, *Macromolecules*, 1985, **18**, 131–138.
166.R. V. Lapshin, A. P. Alekhin, A. G. Kirilenko, S. L. Odintsov, and V. A. Krotkov, *J. Surf. Investig. X-Ray Synchrotron Neutron Tech.*, 2010, **4**, 1–11.
167.M. L. Beasley and R. L. Collins, *Science*, 1970, **169**, 769–770.
169.Sigma Aldrich, http://www.sigmaaldrich.com/analytical-chromatography/analytical-products.html?TablePage=9640723, 2013.
169.S. C. Mraw, *Rev. Sci. Instrum.*, 1982, **53**, 228.
170.M. J. O'neill, *Anal. Chem.*, 1964, **36**, 1238–1245.
171.E. S. Watson, M. J. O'neill, J. Justin, and N. Brenner, *Anal. Chem.*, 1964, **36**, 1233–1238.
172.T. Hirata, T. Kashiwagi, and J. E. Brown, *Macromolecules*, 1985, **18**, 1410–1418.
173.T. Kashiwagi, A. Inaba, J. E. Brown, K. Hatada, T. Kitayama, and E. Masuda, *Macromolecules*, 1986, **19**, 2160–2168.
174.B. Braconnier, C. A. Páez, S. Lambert, C. Alié, C. Henrist, D. Poelman, J.-P. Pirard, R. Cloots, and B. Heinrichs, *Microporous Mesoporous Mater.*, 2009, **122**, 247–254.
175.J. Huang, Y. Liu, L. Lu, and L. Li, *Res. Chem. Intermed.*, 2012, **38**, 487–498.
176.M. Iwasaki, M. Hara, H. Kawada, H. Tada, and S. Ito, *J. Colloid Interface Sci.*, 2000, **224**, 202–204.
177.V. Kisand, U. Joost, V. Reedo, R. Pärna, T. Tätte, J. Shulga, A. Saar, L. Matisen, A. Kikas, and I. Kink, *Appl. Surf. Sci.*, 2010, **256**, 4538–4542.
178.M. Răileanu, M. Crişan, N. Drăgan, D. Crişan, A. Galtayries, A. Brăileanu, A. Ianculescu, V. S. Teodorescu, I. Niţoi, and M. Anastasescu, *J. Sol-Gel Sci. Technol.*, 2009, **51**, 315–329.
179.G. He, Y. Cai, Y. Zhao, X. Wang, C. Lai, M. Xi, Z. Zhu, and H. Fong, *J. Colloid Interface Sci.*, 2013, **398**, 103–111.

180.R. Su, R. Tiruvalam, Q. He, N. Dimitratos, L. Kesavan, C. Hammond, J. A. Lopez-Sanchez, R. Bechstein, C. J. Kiely, G. J. Hutchings, and F. Besenbacher, *Acs Nano*, 2012, **6**, 6284–6292.
181.Y. Zhao, J. Liu, L. Shi, S. Yuan, J. Fang, Z. Wang, and M. Zhang, *Appl. Catal. B Environ.*, 2011, **103**, 436–443.
182.J. Araña, E. Pulido Melián, V. M. Rodríguez López, A. Peña Alonso, J. M. Doña Rodríguez, O. González Díaz, and J. Pérez Peña, *J. Hazard. Mater.*, 2007, **146**, 520–528.
183.S. Parra, J. Olivero, L. Pacheco, and C. Pulgarin, *Appl. Catal. B Environ.*, 2003, **43**, 293–301.
184.J. C. D'Oliveira, G. Al-Sayyed, and P. Pichat, *Environ. Sci. Technol.*, 1990, **24**, 990–996.
185.B. Roig, C. Gonzalez, and O. Thomas, *Spectrochim. Acta. A. Mol. Biomol. Spectrosc.*, 2003, **59**, 303–307.
186.Z. Zhang, C. C. Wang, R. Zakaria, and J. Y. Ying, *J. Phys. Chem. B*, 1998, **102**, 10871–10878.
187.W. Zhang, R. Zhu, L. Ke, X. Liu, B. Liu, and S. Ramakrishna, *Small*, 2010, **6**, 2176–2182.
188.D. Bahnemann, D. Bockelmann, and R. Goslich, *Sol. Energy Mater.*, 1991, **24**, 564–583.
189.R. Terzian and N. Serpone, *J. Photochem. Photobiol. Chem.*, 1995, **89**, 163–175.
190.C. Kormann, D. W. Bahnemann, and M. R. Hoffmann, *Environ. Sci. Technol.*, 1991, **25**, 494–500.
191.J. R. Hook and H. E. Hall, *Solid State Physics*, Wiley-Blackwell, 2nd edn., 1991.
192.J. W. Schwede, I. Bargatin, D. C. Riley, B. E. Hardin, S. J. Rosenthal, Y. Sun, F. Schmitt, P. Pianetta, R. T. Howe, Z.-X. Shen, and N. A. Melosh, *Nat. Mater.*, 2010, **9**, 762–767.
193.R. Cypres and B. Bettens, *Tetrahedron*, 1974, **30**, 1253–1260.
194.A. M. Scheer, C. Mukarakate, D. J. Robichaud, M. R. Nimlos, H.-H. Carstensen, and G. Barney Ellison, *J. Chem. Phys.*, 2012, **136**, 044309.
195.Z. F. Xu and M. C. Lin, *J. Phys. Chem. A*, 2006, **110**, 1672–1677.
196.S. Bingham and W. A. Daoud, *J. Mater. Chem.*, 2011, **21**, 2041.
197.A. Fuerte, M. D. Hernández-Alonso, A. J. Maira, A. Martínez-Arias, M. Fernández-García, J. C. Conesa, and J. Soria, *Chem. Commun.*, 2001, 2718–2719.
198.Y. Park, S.-H. Lee, S. O. Kang, and W. Choi, *Chem. Commun.*, 2010, **46**, 2477.
199.L. B. Lin and D. L. Lin, *J. Phys. Chem. Solids*, 1994, **55**, 1309–1313.
200.S. Zhan, J. Yang, Y. Liu, N. Wang, J. Dai, H. Yu, X. Gao, and Y. Li, *J. Colloid Interface Sci.*, 2011, **355**, 328–333.
201.C. Adán, A. Bahamonde, M. Fernández-García, and A. Martínez-Arias, *Appl. Catal. B Environ.*, 2007, **72**, 11–17.
202.J. Xu, Y. Ao, M. Chen, D. Fu, and C. Yuan, *Thin Solid Films*, 2010, **518**, 4170–4174.
203.J. C.-S. Wu and C.-H. Chen, *J. Photochem. Photobiol. Chem.*, 2004, **163**, 509–515.
204.R. Asahi, T. Morikawa, T. Ohwaki, K. Aoki, and Y. Taga, *Science*, 2001, **293**, 269–271.
205.P. A. Mangrulkar, S. P. Kamble, M. M. Joshi, J. S. Meshram, N. K. Labhsetwar, and S. S. Rayalu, *Int. J. Photoenergy*, 2012, **2012**, 1–10.
206.M. I. Litter and J. A. Navio, *J. Photochem. Photobiol. Chem.*, 1996, **98**, 171–181.
207.S. T. Martin, H. Herrmann, W. Choi, and M. R. Hoffmann, *J. Chem. Soc. Faraday Trans.*, 1994, **90**, 3315.

208.S. Buddee, S. Wongnawa, U. Sirimahachai, and W. Puetpaibool, *Mater. Chem. Phys.*, 2011, **126**, 167–177.
209.G. Colón, M. C. Hidalgo, and J. A. Navío, *Appl. Catal. Gen.*, 2002, **231**, 185–199.
210.R. Bacsa, J. Kiwi, T. Ohno, P. Albers, and V. Nadtochenko, *J. Phys. Chem. B*, 2005, **109**, 5994–6003.
211.J. Zhu, J. Yang, Z.-F. Bian, J. Ren, Y.-M. Liu, Y. Cao, H.-X. Li, H.-Y. He, and K.-N. Fan, *Appl. Catal. B Environ.*, 2007, **76**, 82–91.
212.Y. Wu, M. Xing, J. Zhang, and F. Chen, *Appl. Catal. B Environ.*, 2010, **97**, 182–189.
213.H. Tong, Q. Chen, Z. Yin, H. Hu, D. Wu, and Y. Yang, *Trans. Nonferrous Met. Soc. China*, 2009, **19**, 1483–1488.
214.G. Yang, Z. Jiang, H. Shi, M. O. Jones, T. Xiao, P. P. Edwards, and Z. Yan, *Appl. Catal. B Environ.*, 2010, **96**, 458–465.
215.K. Qi, B. Fei, and J. H. Xin, *Thin Solid Films*, 2011, **519**, 2438–2444.
216.Y. Brik, *J. Catal.*, 2001, **202**, 118–128.
217.J. Kuljanin-Jakovljević, M. Radoičić, T. Radetić, Z. Konstantinović, Z. V. Šaponjić, and J. Nedeljković, *J. Phys. Chem. C*, 2009, **113**, 21029–21033.
218.B. Choudhury and A. Choudhury, *J. Lumin.*, 2012, **132**, 178–184.
219.J. Xu, S. Shi, L. Li, X. Zhang, Y. Wang, X. Chen, J. Wang, L. Lv, F. Zhang, and W. Zhong, *J. Appl. Phys.*, 2010, **107**, 053910.
220.K. M. Reddy and A. Punnoose, *J. Appl. Phys.*, 2007, **101**, 09H112.
221.Guo-Wei Zhou, Don Keun Lee, Young Hwan Kim, Chang Woo Kim, and Young Soo Kang, *Bull Korean Chem Soc*, 2006, **27**, 368.
222.D. B. Hamal and K. J. Klabunde, *J. Phys. Chem. C*, 2011, **115**, 17359–17367.
223.K. T. Ranjit and B. Viswanathan, *J. Photochem. Photobiol. Chem.*, 1997, **108**, 79–84.
224.W.-C. Hung, S.-H. Fu, J.-J. Tseng, H. Chu, and T.-H. Ko, *Chemosphere*, 2007, **66**, 2142–2151.
225.Z. M. Wang, G. Yang, P. Biswas, W. Bresser, and P. Boolchand, *Powder Technol.*, 2001, **114**, 197–204.
226.D. Cordischi, N. Burriesci, F. D'Alba, M. Petrera, G. Polizzotti, and M. Schiavello, *J. Solid State Chem.*, 1985, **56**, 182–190.
227.L. Palmisano, M. Schiavello, A. Sclafani, C. Martin, I. Martin, and V. Rives, *Catal. Lett.*, 1994, **24**, 303–315.
228.M. P. Seabra, I. M. M. Salvado, and J. A. Labrincha, *Ceram. Int.*, 2011, **37**, 3317–3322.
229.E. Piera, *Appl. Catal. B Environ.*, 2003, **46**, 671–685.
230.A. Di Paola, E. García-López, G. Marcì, C. Martín, L. Palmisano, V. Rives, and A. Maria Venezia, *Appl. Catal. B Environ.*, 2004, **48**, 223–233.
231.N. Serpone, D. Lawless, J. Disdier, and J. M. Herrmann, *Langmuir*, 1994, **10**, 643–652.
232.M. P. Dare-Edwards, J. B. Goodenough, A. Hamnett, and P. R. Trevellick, *J. Chem. Soc. Faraday Trans. 1*, 1983, **79**, 2027.
233.D. S. Ginley and M. A. Butler, *J. Appl. Phys.*, 1977, **48**, 2019.
234.K. Karthik, S. K. Pandian, and N. V. Jaya, *Appl. Surf. Sci.*, 2010, **256**, 6829–6833.
235.R. Nirmala, H. Y. Kim, C. Yi, N. A. M. Barakat, R. Navamathavan, and M. El-Newehy, *Int. J. Hydrog. Energy*, 2012, **37**, 10036–10045.
236.H.-H. Tseng, M.-C. Wei, S.-F. Hsiung, and C.-W. Chiou, *Chem. Eng. J.*, 2009, **150**, 160–167.
237.S. D. Sharma, D. Singh, K. K. Saini, C. Kant, V. Sharma, S. C. Jain, and C. P. Sharma, *Appl. Catal. Gen.*, 2006, **314**, 40–46.

238.Y. Li, W. Wlodarski, K. Galatsis, S. H. Moslih, J. Cole, S. Russo, and N. Rockelmann, *Sensors Actuators B Chem.*, 2002, **83**, 160–163.
239.V. Shutthanandan, S. Thevuthasan, T. Droubay, S. M. Heald, M. H. Engelhard, D. E. McCready, S. A. Chambers, P. Nachimuthu, and B. S. Mun, *Nucl. Instruments Methods Phys. Res. Sect. B Beam Interactions Mater. Atoms*, 2006, **242**, 198–200.
240.D. Mardare, F. Iacomi, N. Cornei, M. Girtan, and D. Luca, *Thin Solid Films*, 2010, **518**, 4586–4589.
241.C.-C. Tsai and H. Teng, *Appl. Surf. Sci.*, 2008, **254**, 4912–4918.
242.B. Tian, C. Li, and J. Zhang, *Chem. Eng. J.*, 2012, **191**, 402–409.
243.B. Choudhury and A. Choudhury, *Mater. Chem. Phys.*, 2012, **132**, 1112–1118.
244.A. R. Denton and N. W. Ashcroft, *Phys. Rev.*, 1991, **43**, 3161.
245.Y.-H. Peng, G.-F. Huang, and W.-Q. Huang, *Adv. Powder Technol.*, 2012, **23**, 8–12.
246.Y. Xie, N. Huang, S. You, Y. Liu, B. Sebo, L. Liang, X. Fang, W. Liu, S. Guo, and X.-Z. Zhao, *J. Power Sources*, 2013, **224**, 168–173.
247.S. Songara, M. K. Patra, M. Manoth, L. Saini, V. Gupta, G. S. Gowd, S. R. Vadera, and N. Kumar, *J. Photochem. Photobiol. Chem.*, 2010, **209**, 68–73.
248.Z. Zhang, C. Shao, L. Zhang, X. Li, and Y. Liu, *J. Colloid Interface Sci.*, 2010, **351**, 57–62.
249.K. Chen, J. Li, W. Wang, Y. Zhang, X. Wang, and H. Su, *Appl. Surf. Sci.*, 2011, **257**, 7276–7285.
250.S. Chang and W. Liu, *Appl. Catal. B Environ.*, 2011, **101**, 333–342.
251.S. Higashimoto, W. Tanihata, Y. Nakagawa, M. Azuma, H. Ohue, and Y. Sakata, *Appl. Catal. Gen.*, 2008, **340**, 98–104.
252.H. Choi and M. Kang, *Int. J. Hydrog. Energy*, 2007, **32**, 3841–3848.
253.P.-O. Larsson and A. Andersson, *J. Catal.*, 1998, **179**, 72–89.
254.K. Song, J. Zhou, J. Bao, and Y. Feng, *J. Am. Ceram. Soc.*, 2008, **91**, 1369–1371.
255.R. López, R. Gómez, and M. E. Llanos, *Catal. Today*, 2009, **148**, 103–108.
256.P.-O. Larsson, A. Andersson, L. R. Wallenberg, and B. Svensson, *J. Catal.*, 1996, **163**, 279–293.
257.P. Vanysek, *Crc Handb. Chem. Phys. Crc Press Boca Raton*, 1998.
258.L. S. Yoong, F. K. Chong, and B. K. Dutta, *Energy*, 2009, **34**, 1652–1661.
259.C. J. Chang, Z.-H. Loh, C. Shi, F. C. Anson, and D. G. Nocera, *J. Am. Chem. Soc.*, 2004, **126**, 10013–10020.
260.M. W. Kanan and D. G. Nocera, *Science*, 2008, **321**, 1072–1075.
261.J. Wöllenstein, M. Burgmair, G. Plescher, T. Sulima, J. Hildenbrand, H. Böttner, and I. Eisele, *Sensors Actuators B Chem.*, 2003, **93**, 442–448.
262.Y. Wang, Y. Wang, R. Jiang, and R. Xu, *Ind. Eng. Chem. Res.*, 2012, **51**, 9945–9951.
263.Z. Altıntaş, E. Çakmakçı, M. V. Kahraman, N. K. Apohan, and A. Güngör, *J. Sol-Gel Sci. Technol.*, 2011, **58**, 612–618.
264.R. Sasikala, A. R. Shirole, V. Sudarsan, V. S. Kamble, C. Sudakar, R. Naik, R. Rao, and S. R. Bharadwaj, *Appl. Catal. Gen.*, 2010, **390**, 245–252.
265.K. Cendrowski, X. Chen, B. Zielinska, R. J. Kalenczuk, M. H. Rümmeli, B. Büchner, R. Klingeler, and E. Borowiak-Palen, *J. Nanoparticle Res.*, 2011, **13**, 5899–5908.
266.H. Leinonen, *Removal of harmful metals from metal plating waste waters using selective ion exchangers*, University of Helsinki, 1999.
267.V. Y. Gusev, X. Feng, Z. Bu, G. L. Haller, and J. A. O'Brien, *J. Phys. Chem.*, 1996, **100**, 1985–1988.
268.E. M. Rabinovich, D. W. Johnson, J. B. MacChesney, and E. M. Vogel, *J. Non-Cryst. Solids*, 1982, **47**, 435–439.

269.W. Stöber, A. Fink, and E. Bohn, *J. Colloid Interface Sci.*, 1968, **26**, 62–69.
270.C. Colella and A. F. Gualtieri, *Microporous Mesoporous Mater.*, 2007, **105**, 213–221.
271.L. Pauling, *Proc. Natl. Acad. Sci. U. S. A.*, 1930, **16**, 453.
274.G. C. H. Lee and G. C. H. Lee, US-Patent No. 95/141; 502/64, 1975.
275.R. M. Milton and R. M. Milton, US Patent No. 20810454 1957.
274.P. B. Weisz and V. J. Frilette, *J. Phys. Chem.*, 1960, **64**, 382–382.
275.G. T. Kerr and G. C. Johnson, *J. Phys. Chem.*, 1960, **64**, 381–382.
276.M. E. Davis and R. F. Lobo, *Chem. Mater.*, 1992, **4**, 756–768.
277.J. S. Beck, J. C. Vartuli, W. J. Roth, M. E. Leonowicz, C. T. Kresge, K. D. Schmitt, C. T. W. Chu, D. H. Olson, and E. W. Sheppard, *J. Am. Chem. Soc.*, 1992, **114**, 10834–10843.
278.C. T. Kresge, M. E. Leonowicz, W. J. Roth, J. C. Vartuli, and J. S. Beck, *Nature*, 1992, **359**, 710–712.
279.D. H. Olson, *J. Phys. Chem.*, 1970, **74**, 2758–2764.
280.S. Kulprathipanja and Wiley InterScience (Online service), *Zeolites in industrial separation and catalysis*, Wiley-VCH, Weinheim, 2010.
281.E. Álvarez-Ayuso, *Water Res.*, 2003, **37**, 4855–4862.
282.N. Moreno, X. Querol, C. Ayora, C. F. Pereira, and M. Janssen-Jurkovicová, *Environ. Sci. Technol.*, 2001, **35**, 3526–3534.
283.P. Castaldi, L. Santona, and P. Melis, *Chemosphere*, 2005, **60**, 365–371.
284.M. Ackley, *Microporous Mesoporous Mater.*, 2003, **61**, 25–42.
285.G. F. Froment, W. J. H. Dehertog, and A. J. Marchi, *Catalysis*, 1992, **9**.
286.J. A. Lercher, R. A. Van Santen, and H. Vinek, *Catal. Lett.*, 1994, **27**, 91–96.
287.Y. Iwase, Y. Sakamoto, A. Shiga, A. Miyaji, K. Motokura, T. Koyama, and T. Baba, *J. Phys. Chem. C*, 2012, **116**, 5182–5196.
288.M. Tamura, W. Chaikittisilp, T. Yokoi, and T. Okubo, *Microporous Mesoporous Mater.*, 2008, **112**, 202–210.
289.Q.-H. Xia and T. Tatsumi, *Mater. Chem. Phys.*, 2005, **89**, 89–98.
290.A. Corma, M. T. Navarro, and J. P. Pariente, *J. Chem. Soc. Chem. Commun.*, 1994, 147.
291.R. M. Mohamed, I. A. Mkhalid, M. Abdel Salam, and M. A. Barakat, *Desalination Water Treat.*, 2013, 1–8.
292.A. Corma and H. Garcia, *Chem. Commun.*, 2004, 1443.
293.H. García and H. D. Roth, *Chem. Rev.*, 2002, **102**, 3947–4008.
294.Y. Xu and C. H. Langford, *J. Phys. Chem. B*, 1997, **101**, 3115–3121.
295.B. Dong and S. Lan, *J. Phys. Conf. Ser.*, 2013, **418**, 012121.
296.R. J. Tayade, R. G. Kulkarni, and R. V. Jasra, *Ind. Eng. Chem. Res.*, 2007, **46**, 369–376.
297.T. Hisanaga and K. Tanaka, *J. Hazard. Mater.*, 2002, **93**, 331–337.
298.A. Nasonova and K.-S. Kim, *Catal. Today*, 2013, **211**, 90–95.
299.M. V. Shankar, S. Anandan, N. Venkatachalam, B. Arabindoo, and V. Murugesan, *Chemosphere*, 2006, **63**, 1014–1021.
300.Y. H. Hsien, C. F. Chang, Y. H. Chen, and S. Cheng, *Appl. Catal. B Environ.*, 2001, **31**, 241–249.
301.K. Susa, I. Matsuyama, S. Satoh, and T. Suganuma, *Electron. Lett.*, 1982, **18**, 499–500.
302.E. M. Rabinovich, J. B. MacChesney, D. W. Johnson, J. R. Simpson, B. W. Meagher, F. V. Dimarcello, D. L. Wood, and E. A. Sigety, *J. Non-Cryst. Solids*, 1984, **63**, 155–161.

303.Y. Matatov-Meytal, V. Barelko, I. Yuranov, L. Kiwi-Minsker, A. Renken, and M. Sheintuch, *Appl. Catal. B Environ.*, 2001, **31**, 233–240.
304.L. Kiwi-Minsker, I. Yuranov, E. Slavinskaia, V. Zaikovskii, and A. Renken, *Catal. Today*, 2000, **59**, 61–68.
305.A. Piscopo, D. Robert, C. Marzolin, and J. V. Weber, *J. Mater. Sci. Lett.*, 2000, **19**, 683–684.
306.D. Robert, A. Piscopo, O. Heintz, and J. . Weber, *Catal. Today*, 1999, **54**, 291–296.
307.Y. San You, K.-H. Chung, J.-H. Kim, and G. Seo, *Korean J. Chem. Eng.*, 2001, **18**, 924–929.
308.A. Blaková, L. Csölleová, and V. Brezova, *J. Photochem. Photobiol. Chem.*, 1998, **113**, 251–256.
309.Brezova V., Blazkova A., Karpinsky L., Groskova J., Havlinova B., Jorik V., and Ceppan M., *J. Photochem. Photobiol. Chem.*, 1997, **109**, 177–183.
310.P. Pichat, J. Disdier, C. Hoang-Van, D. Mas, G. Goutailler, and C. Gaysse, *Catal. Today*, 2000, **63**, 363–369.
311.K. Kamiya, S. Sakka, and Y. Tatemichi, *J. Mater. Sci.*, 1980, **15**, 1765–1771.
312.B. G. Muralidharan and D. C. Agrawal, *J. Sol-Gel Sci. Technol.*, 1997, **9**, 85–93.
313.T. Gunji, Y. Nagao, T. Misono, and Y. Abe, *J. Non-Cryst. Solids*, 1989, **107**, 149–154.
314.B. Ding, H. Kim, C. Kim, M. Khil, and S. Park, *Nanotechnology*, 2003, **14**, 532.
315.S. Zhan, D. Chen, X. Jiao, and Y. Song, *Chem. Commun.*, 2007, 2043.

Bibliography

1.P. W. Atkins and J. De Paula, *Atkins' Physical chemistry*, 8th Ed., W.H. Freeman, New York, 2006.
2.J. K. Burdett, *Chemical bonding in solids*, 1st Ed., Oxford Univ. Press, New York, 1995.
3.A. K. Cheetham and Day, *Solid state chemistry: techniques*, 1st Ed., Clarendon Press, Oxford, 1988.
4.W. Clegg, *Crystal structure determination*, 1st Ed., Oxford Univ. Press, Oxford, 1998.
5.P. A. Cox, *The electronic structure and chemistry of solids*, 1st Ed., Oxford University Press, Oxford, New York, 1987.
6.S. R. Elliott, *The physics and chemistry of solids*, 2nd Ed., Wiley, Chichester [u.a., 2000.
7.W. A. Harrison, *Electronic structure and the properties of solids: the physics of the chemical bond*, 2nd Ed., Dover Publications, New York, 1989.
8.G. Herzberg, *Atomic spectra and atomic structure*, 2nd Ed., Dover Publications, New York, 1945.
9.J. Keeler and P. Wothers, *Chemical structure and reactivity: an integrated approach*, 1st Ed., Oxford University Press, Oxford, 2008.
10.D. M. Smyth, *The defect chemistry of metal oxides*, 1st Ed., Oxford University Press, New York, 2000.
11.L. Solymar and D. Walsh, *Lectures on the electrical properties of materials*, 2nd Ed., Oxford University Press, Oxford; New York, 1979.